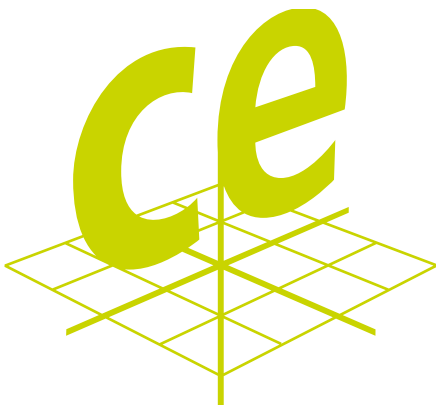


# 3rd Workshop on Computational Engineering 2014

Book of Abstracts



October 6 - 10, 2014

Stuttgart, Germany

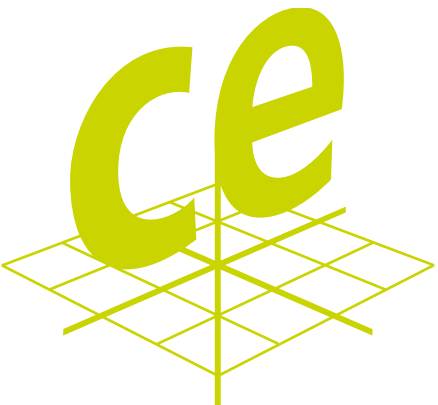
# Sponsors



Cluster of Excellence in Simulation Technology and Graduate School GS SimTech, Universität Stuttgart



Informatik Forum Stuttgart



Graduate School Computational Engineering, Technische Universität Darmstadt



International Graduate School in Science and Engineering, Technische Universität München

# Contents

<b>Invited Talks</b>	<b>5</b>
I Simulation of Unsteady Flows and Fluid-Structure Interactions . . . . .	6
II Parallel Algorithms for Kernel Sums in Computational Science and Statistical Inference .	7
III Coupled Multi-Field Continuum Methods for Porous Media Fracture . . . . .	9
IV Efficient Solution of Optimization Problems with PDEs and Pointwise Constraints . . . .	14
V Computational Bone-Mechanics on Orthopedists Cell Phone . . . . .	16
<b>Minisymposia</b>	<b>22</b>
I Dummy Models Retired? Active Digital Human Models for Automotive Safety Research .	23
I.1 Using Hill-Type Muscles to Drive Active Human Models Brings Low Level Motor Control for Free . . . . .	24
I.2 A Comparison Between Dummy and Human Models for Crash Simulations of Side Impacts . . . . .	29
I.3 Uncertainty Quantification Associated with the Mechanical Response of Femurs .	34
I.4 Vehicle Safety Using the THUMS™ Human Models . . . . .	40
I.5 THUMS User Community - Harmonising the Validation of Human Models for Crash Simulation . . . . .	45
I.6 Modeling Active Human Muscle Responses during Driver and Autonomous Avoidance Maneuvers . . . . .	46
I.7 On the Route to “Autonomous Driving” - A New Quality of Passive Safety and Its Numerical Development & Assessment Tools . . . . .	52
II Get in Shape - Algorithms and Data Structures for Complex, Changing Domains on Adaptive Cartesian Meshes . . . . .	56
II.1 Coupling and Boundary Constraints for a NURBS-Based Immersed Boundary Approach . . . . .	57
II.2 A Task-Based Finite Cell Implementation on Xeon Phi . . . . .	61
II.3 Mesh-to-Particle Coupling for Hybrid Molecular-Continuum Simulations . . . . .	65
II.4 Local Time-Stepping Along Coastlines for Tsunami Simulations . . . . .	70
II.5 Spacetime-Based Adaptive Meshing of Complex Geometries . . . . .	75
II.6 Multi-Scale High-Performance Fluid Flow Simulations Through Porous Media . . .	79
III Towards Exascale Simulations and Applications . . . . .	85
III.1 Towards a Fault-Tolerant, Scalable Implementation of GENE . . . . .	86
III.2 New Approaches to Nonlinear Domain Decomposition . . . . .	92
III.3 Towards Fluid-Acoustics Interaction on Massively Parallel Systems . . . . .	97
III.4 Node-Level Performance Optimization of the Fast Multipole Method . . . . .	103
III.5 Node-Level Performance Engineering for an Advanced Density Driven Porous Media Flow Solver . . . . .	109
IV Optimal Control Based on Reduced Order Models . . . . .	114
IV.1 Optimal Flow Control Based on POD and MPC and an Application to the Cancellation of Tollmien-Schlichting Waves . . . . .	115
IV.2 Parameter Identification for Nonlinear Elliptic-Parabolic Systems . . . . .	120
IV.3 A-Posteriori Error Analysis and Optimality-System POD for Constrained Optimal Control . . . . .	125

IV.4	Interfacing between Dynamics and Optics for Reduced Models of Deformable Optical Elements . . . . .	130
IV.5	Fast Evaluation of Implied Volatility Surfaces with Reduced Order Models . . . . .	135
IV.6	Certified Parameter Optimization for Parametrized PDEs with Reduced Basis Surrogate Models . . . . .	141
V	High Order Methods for Unsteady Flows . . . . .	146
V.1	On the Aliasing of Discrete Kinetic Energy in a Nodal Discontinuous Galerkin Method	147
V.2	GPU-Accelerated High-Order Aeroacoustics Using the Flux Reconstruction Approach	152
V.3	Development of a High-Resolution, Scalable DGM Solver for DNS and LES of Turbomachinery Flows . . . . .	157
V.4	An Application of High-Order DGSEM to Large Eddy Simulation . . . . .	162
VI	Simulation-based Identification . . . . .	167
VI.1	Optimization of the Strainer Design in the Extrusion Process of Visco-Plastic Materials . . . . .	168
VI.2	Wavelet Methods for a Weighted Sparsity Penalty for Region of Interest Tomography	176
VI.3	Colored Buzz, or Glottal Inverse Filtering . . . . .	181
VI.4	A Resolution Guarantee for Anomaly Detection within a Realistically Modeled EIT Setting . . . . .	186
<b>Contributed Talks</b>		<b>191</b>
1	Extrapolation in Time in Thermal Fluid Structure Interaction . . . . .	192
2	Parallel Algorithm for Solution-Adaptive Grid Movement in the Context of Fluid Structure Interaction . . . . .	197
3	Simulation of Wave Propagation and Impact Damage in Brittle Materials Using the Peridynamics Technique . . . . .	202
4	Using Instancing to Efficiently Render Super Carbon Nanotubes . . . . .	205
5	An Efficient Algorithm to Include Sub-Voxel Information in FFT-Based Homogenization .	210
6	A Multi Scale Model for Mass Transport in Arteries and Tissue . . . . .	215
7	Centralized Adaptive Observation Strategy for Atmospheric Dispersion Process Estimation Using Mobile Sensors . . . . .	220
8	Metaheuristic Based Methods for Optimum Design . . . . .	225
9	Source Transformation for the Optimized Utilization of the Matlab Runtime System for Automatic Differentiation . . . . .	230
10	Dynamic Two-Way Parallelization of Non-Intrusive Methods for Uncertainty Quantification	235
11	Data-Driven Uncertainty Quantification with Adaptive Sparse Grids in Subsurface Flow Simulations . . . . .	240
<b>List of Authors</b>		<b>244</b>

# Invited Talks

# **I Simulation of Unsteady Flows and Fluid-Structure Interactions**

Authors: Bijl, Hester

No pdf yet.  
Hester Bijl  
Aerodynamics Laboratory, TU Delft

## **II Parallel Algorithms for Kernel Sums in Computational Science and Statistical Inference**

Authors: Biros, George

---

# Parallel Algorithms for Kernel Sums in Computational Science and Statistical Inference

George Biros

**Abstract** Kernel sums (also known as N-body algorithms) are the computational cornerstone for many problems in mathematical physics. In this talk, I will present (1) a brief history of N-body algorithms and their application to multiscale problems; (2) give a brief overview of the most basic N-body algorithm, the Barnes-Hut method; (3) expand the notion of N-body problems to high-dimensional problems and statistical inference; (4) conclude with applications of N-body algorithms to physics (fluid mechanics) and statistics (supervised learning).

---

G. Biros  
201 East 24th St, Austin, Texas  
Tel.: +1-512-232-9566  
Fax: +1-512-471-8694  
E-mail: [biros@ices.utexas.edu](mailto:biros@ices.utexas.edu)

# **III Coupled Multi-Field Continuum Methods for Porous Media Fracture**

Authors: Markert, Bernd, Heider, Yousef

---

# Coupled multi-field continuum methods for porous media fracture

Bernd Markert · Yousef Heider

**Abstract** Numerical modeling of fracture in fluid-saturated heterogeneous materials, such as in saturated rocks, soils, metal foam and biological tissues, can be properly carried out using extended continuum porous media theories, which account for the crack nucleation and propagation, deformation of the solid matrix and change in the flow of the interstitial fluid. In this, fluid-saturated porous materials basically represent volumetrically interacting solid-fluid aggregates, which are modeled using the Theory of Porous Media. The hydraulic- or tension-induced fractures occur in the solid matrix and are modeled using a phase-field approach. This way of fracture treatment adds a partial differential equation for the phase-field evolution to the coupled solid-fluid problem, which requires special stabilization techniques in the numerical calculation.

**Keywords** Fracture · Phase field · Porous media · Hydraulic fracture · TPM

## 1 Introduction

The theoretical and numerical prediction of failure mechanisms due to crack initiation and propagation in solids has ever since been of great importance in engineering. Following the pioneering work of Griffith [1], cracks propagate if the energy release rate reaches a critical value. In particular, the Griffith theory of brittle fracture in elastic solids provides a criterion for crack propagation, but can neither describe curving and branching cracks nor predict crack initiation. These deficiencies have been overcome by different developments ranging from sharp crack discontinuity as, e.g., in Moes and Belytschko

---

B. Markert · Y. Heider  
Institute of General Mechanics, RWTH Aachen University, Germany  
Tel.: +49-241-8094600  
Fax: +49-241-8092231  
E-mail: markert@iam.rwth-aachen.de, heider@iam.rwth-aachen.de

[2], over cohesive-zone as in Remmers and de Borst [3] to diffusive interface and phase-field models, see, e.g., Bourdin et al. [4], Francfort and Marigo [5] and Kuhn and Müller [6]. Recently, the latter approach has been proven to be well suited for the description of complex multi-dimensional, mixed-mode fracture scenarios including dynamic effects and crack branching, see, e.g., Borden et al. [7] and Miehe et al. [8] for more details and references. The current treatment of fracture in multi-phase saturated porous materials is based on the diffusive phase-field approach within a thermodynamically consistent framework using the continuum Theory of Porous Media (TPM), see also Markert and Ehlers [10].

## 2 Theoretical basics

In the framework of the TPM, a macroscopic description of general immiscible multiphase aggregates  $\varphi$  is introduced, where the individual constituents  $\varphi^\alpha$  (here:  $\alpha = S$  : solid,  $\alpha = F$  : fluid) are considered to be in a state of ideal disarrangement over a homogenized representative volume element (RVE) in the sense of superimposed and interacting continua. In this regard, volume fractions  $n^\alpha := dv^\alpha/dv$  of  $\varphi^\alpha$  are defined as the local ratios of the partial volume elements  $dv^\alpha$  with respect to the total volume element  $dv$  of  $\varphi$ , where the saturation condition  $n^S + n^F = 1$  holds. This yields that the partial density  $\rho^\alpha$  is related to the effective density  $\rho^{\alpha R}$  via  $\rho^\alpha = n^\alpha \rho^{\alpha R}$ , where the material incompressible is associated with  $\rho^{\alpha R} = \text{const.}$ , cf. e.g. [9]. Concerning the kinematics of the considered problem, the motion of  $\varphi^S$  is characterized by a Lagrangean description of the solid matrix via the solid displacement  $\mathbf{u}_S$  and velocity  $\mathbf{v}_S$ , however, the pore-fluid flow is expressed either in Eulerian description using the fluid velocity  $\mathbf{v}_F$  or in modified Eulerian settings via the seepage velocity vector  $\mathbf{w}_F = \mathbf{v}_F - \mathbf{v}_S$ .

The current treatment of biphasic model excludes dynamic effects (quasi-static), thermal effects as well as any mass exchanges (inert  $\varphi^\alpha$ ) and proceeds from intrinsically incompressible constituents ( $\rho^{\alpha R} = \text{const.}$ ). In particular, the arising purely mechanical, binary model with  $\alpha = \{S, F\}$  is governed by the following strongly coupled constituent balance equations (see, e.g. [12]):

– Partial mass balance  $\rightarrow$  partial volume balance:

$$0 = (\rho^\alpha)'_\alpha + \rho^\alpha \text{div } \mathbf{v}_\alpha \quad \rightarrow \quad 0 = (n^\alpha)'_\alpha + n^\alpha \text{div } \mathbf{v}_\alpha \quad (1)$$

– Partial momentum balance:

$$\mathbf{0} = \text{div } \mathbf{T}^\alpha + \rho^\alpha \mathbf{b} + \hat{\mathbf{p}}^\alpha. \quad (2)$$

Herein,  $\text{div}(\cdot)$  is the divergence operator related to  $\text{grad}(\cdot)$ ,  $\mathbf{T}^\alpha = (\mathbf{T}^\alpha)^T$  is the symmetric partial Cauchy stress tensor assuming non-polar constituents,  $\mathbf{b}$  is the mass-specific body force acting on the overall aggregate, and  $\hat{\mathbf{p}}^\alpha$  denotes the direct momentum production, which can be interpreted as the volume-specific local interaction force between the percolating pore fluid and the solid skeleton.

With regard to the energy approach for brittle fracture in heterogeneous porous media, the global potential energy function  $\mathcal{F}$  of a cracked linear elastic, isotropic body can be defined as the sum of the elastic strain energy  $\bar{\Psi}_e^S$  integrated over the whole spatial domain  $\Omega$ , and the critical fracture energy  $\bar{\Psi}_{\text{crack}}^S$  (equal to the energy required to create a unit area of fracture surface) integrated along the crack path  $\Gamma_c$ , cf. [1]:

$$\mathcal{F}(\boldsymbol{\varepsilon}_{S_e}, \Gamma_c) = \int_{\Omega} \bar{\Psi}_e^S(\boldsymbol{\varepsilon}_{S_e}) \, dv + \int_{\Gamma_c} \bar{\Psi}_{\text{crack}}^S \, da \quad (3)$$

Following this, the phenomenological phase-field variable  $\phi^S$  is introduced to distinguish between the cracked ( $\phi^S = 0$ ) and the unbroken states ( $\phi^S = 1$ ) of the material, yielding  $\mathcal{F}(\boldsymbol{\varepsilon}_{S_e}, \Gamma_c) \approx \mathcal{F}(\boldsymbol{\varepsilon}_{S_e}, \phi^S, \text{grad } \phi^S)$ . The next step is to derive the stress and the phase-field evolution relations. In particular, the solid stress tensor is defined as  $\mathbf{T}^S = \partial \mathcal{F} / \partial \boldsymbol{\varepsilon}_{S_e} - p \mathbf{I}$  with  $p$  being the pore-fluid pressure. The non-conserved phase-field evolution is derived using the well-known Allen-Cahn diffusion model [11], which describes the process of phase separation (here crack formation) via a reaction-diffusion equation. Thus, the phase-field evolution is given by

$$\frac{\partial \phi^S(\mathbf{x}, t)}{\partial t} = -M \frac{\partial \mathcal{F}}{\partial \phi^S} \quad (4)$$

with  $M$  being a kinetic parameter related to the interface mobility.

### 3 Numerical treatment

For the numerical solution of an initial-boundary value problem, the Finite Element Method (FEM) treatment is carried out in two steps: Firstly, deriving the weak or variational statements of the governing balance equations and, secondly, using the finite element discretization for the approximate solution of the variational equations. In particular, the governing set of partial differential balance equations (1, 2 and 4) with primary unknowns  $\mathbf{u}_S$ ,  $\mathbf{v}_F$ ,  $p$ ,  $\phi^S$  is treated in a fully coupled manner and discretized in time using an appropriate implicit-monolithic time integration scheme.

### 4 Numerical example

In order to give a qualitative benchmark example, the proposed diffusive porous media fracture model is applied to a two-dimensional IBVP, where the fracture-induced changes to the fluid percolation are investigated. In particular, a rectangular porous material with moderate permeability and included low-permeability barriers is subjected to a pressure gradient from bottom-left high-pressure (red) inflow to top-right low-pressure (blue) outflow (Fig. 1, left). The double-notched porous medium is then set under tension inducing typical

mode 1 fracture. The changes to the permeability (from low/blue to high/red) and the flow path are observed while the cracks propagate. As expected, the model predicts the permeability increase in the degraded or cracked material, thereby strongly affecting the pore-fluid flow regime (see Fig. 1, right). From the streamlines indicating the flow path, it is apparent that the nature of the flow changes completely from the unbroken porous matrix to the finitely opened cracks.

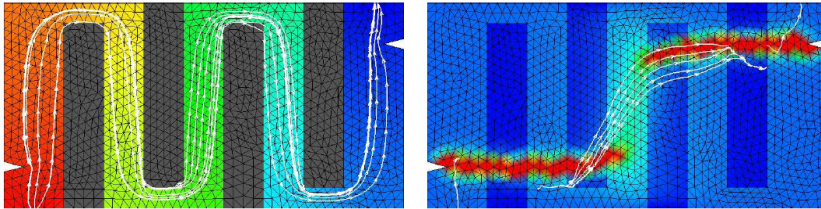


**Fig. 1** Fracture-induced changes of the flow path in a perfused, heterogeneous porous medium

## References

1. Griffith AA, The phenomena of rupture and flow in solids, *Phil. Trans. Roy. Soc. Lond. A*, 221, 163–198 (1921)
2. Moes N and Belytschko T, Extended finite element method for cohesive crack growth, *Eng. Fract. Mech.*, 69, 813–833 (2002)
3. Remmers JJC and de Borst R and Needleman A, A cohesive segments method for the simulation of crack growth, *comp. mech.*, 31, 69–77 (2003)
4. Bourdin B and Francfort GA and Marigo JJ, *The Variational Approach to Fracture*, Springer, Berlin (2008)
5. Francfort GA and Marigo JJ, Revisiting brittle fracture as an energy minimization problem, *J. Mechan. and Phys. Solids*, 46, 1319–1342 (1998)
6. Kuhn C and Müller R, A continuum phase field model for fracture, *Eng. Fract. Mech.*, 77, 3625–3634 (2010)
7. Borden MJ and Verhoosel CV and Scott MA, Hughes TJR and Landis CM, A phase-field description of dynamic brittle fracture, *Comput. Method. Appl. M.*, 217220, 77–95 (2012)
8. Miehe C and Hofacker M and Welschinger F, A phase field model for rate-independent crack propagation: Robust algorithmic implementation based on operator splits, *Comput. Method. Appl. M.*, 199, 2765–2778 (2010)
9. Ehlers W, Challenges of porous media models in geo- and biomechanical engineering including electro-chemically active polymers and gels, *Int. J. Adv. Eng. Sci. Appl. Math.*, 1, 1–24 (2009)
10. Markert B and Ehlers W, A phase-field approach to hydraulic fracturing, 5th International Conference on Porous Media and Annual Meeting, 21 - 24 May, Prague, Czech Republic (2013)
11. Allen SM and Cahn JW, A microscopic theory for antiphase boundary motion and its application to antiphase domain coarsening, *Acta Met.*, 27, 1085–1095 (1979)
12. Markert B, Heider Y, Ehlers W, Comparison of monolithic and splitting solution schemes for dynamic porous media problems, *Int. J. Numer. Meth. Eng.*, 82, 1341–1383 (2010)

# **IV Efficient Solution of Optimization Problems with PDEs and Pointwise Constraints**

Authors: Ulbrich, Michael

---

# Efficient Solution of Optimization Problems with PDEs and Pointwise Constraints

Michael Ulbrich

**Abstract** In the recent past, significant advances have been made in the development and analysis of efficient methods for inequality constrained optimization problems governed by PDEs. We discuss several central aspects of solving this class of problems, putting a focus on second order methods (semismooth Newton and interior point algorithms). Pointwise constraints arise, e.g., as bounds on state or control, in many applications. We address the particular challenges caused by them and describe how they can be addressed. The talk aims at providing a balanced mix of theoretical insights, computational aspects, and illustrative model applications, including seismic tomography.

---

M. Ulbrich  
Boltzmannstr. 3  
85748 Garching b. München  
Tel.: +49-89-289-17929  
Fax: +49-89-289-17932  
E-mail: mulbrich@ma.tum.de

# **V Computational Bone-Mechanics on Orthopedists Cell Phone**

Authors: Yosibash, Zohar

---

# Computational bone-mechanics on orthopedists cell phone

Zohar YOSIBASH

**Abstract** Verified and validated simulation of the human's femur mechanical response, aimed at diagnosis and optimal treatment in clinical orthopedic practice were recently introduced. These are based on CT-scans and high-order finite element methods ( $p$ -FEMs). We describe the methods for creating  $p$ -FEM models of patient-specific femurs and the in-vitro experiments used to assess the validity of the simulation results. Finally, because the orthopedic surgeons need such analyses in a short time-scale, preferably displayed on their cellular phones, we present the implementation of the methods using multi-threading and Java.

**Keywords** High order FEMs · Femurs · Patient-specific

## 1 Introduction

Quantitative computer tomography, (qCT) allows an accurate description of a patient-specific femur's geometry, and its material inhomogeneous properties [1,3–5]. Utilizing qCT scans in conjunction with  $p$ -FEMs [2] we herein provide a systematic method for performing reliable FE simulations of the human femur, validated by in-vitro tests on the large cohort of fresh-frozen femurs.

Once the  $p$ -FE analyses are finalized (the entire process for one patient-specific femur lasts less than 3-hours) and the results are verified so the numerical error is assured to be controlled, we validate the results by a set of in-vitro

---

Study supported in part by grant no. 3-00000-7375 from the Chief Scientist Office of the Ministry of Health, Israel and by the Technical University of Munich - Institute for Advanced Study, funded by the German Excellence Initiative.

---

Z. Yosibash  
Department of Mechanical Engineering, Ben-Gurion University, Beer-Sheva, Israel  
Tel.: +972-8-6477103  
Fax: +123-45-678910  
E-mail: zohary@bgu.ac.il

experiments on a large cohort of healthy and diseased human fresh-frozen femurs. The validity of the presented methods is demonstrated by comparison between the experimental and the predicted results - both strains and displacements.

We discuss and demonstrate some potential applications of patient-specific  $p$ -FE analyses in daily clinical practice: Predicting risk of fracture of femurs with metastatic tumors and selecting the optimal prosthesis for a total hip replacement.

Finally, we present a parallel, Java based  $p$ -FE implementation of the methods described and their intended use on cellular devices.

## 2 Patient-specific $p$ -FE model of femurs from qCT-scans

Patient-specific qCT scans of a femur are *automatically* manipulated by in-house Matlab programs. Exterior, interface and interior boundaries are traced representing different boundaries of a given slice. These slices are manipulated to generate a surface representation of the femur and subsequently a solid model. Large surfaces are generated, which are essential for the  $p$ -mesh generator. The resulting 3D solid is thereafter auto-meshed by tetrahedral high-order elements. The entire algorithm (qCT to FE) is schematically illustrated in Figure 1.

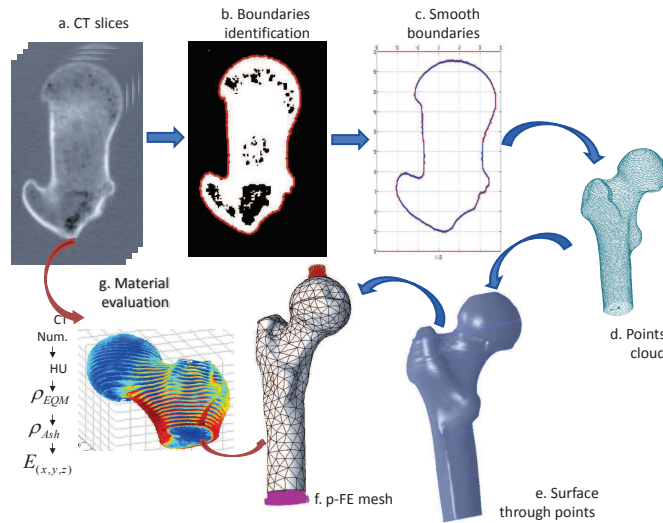


**Fig. 1** Schematic flowchart describing the generation of the  $p$ -FE model from qCT scans. a - Typical CT-slice, b. - Contour identification, c. - Smoothing boundary points, d. - Points cloud representing the bone surface, e. - Bone surface, f. -  $p$ -FE mesh and g. - Material evaluation from CT data.

The material properties at each integration point are determined by the qCT scan.  $K_2HPO_4$  phantoms are placed near each femur and are used to correlate the known mineral density and HU. The ash density  $\rho_{ash}$  is then determined based on empirical connections:

$$E_{cort} = 10200 \times \rho_{ash}^{2.01} [MPa], \rho_{ash} \geq 0.486 \quad (1)$$

$$E_{trab} = 2398 [MPa], \quad 0.3 < \rho_{ash} < 0.486 \quad (2)$$

$$E_{trab} = 33900 \times \rho_{ash}^{2.2} [MPa], \rho_{ash} \leq 0.3 \quad (3)$$

while Poisson's ratio was fixed at  $\nu = 0.3$ .

### 3 Verification of the $p$ -FE model and validation by in-vitro experiments

The  $p$ -FE results are being verified so to ensure that the numerical error is under a specific tolerance. Convergence is realized by keeping a fixed mesh and increasing the polynomial degree of the approximated solution  $p$  until the relative error in energy norm is small, and the strains at the points of interest converge to a given value - see for example Figure 2. Each of the femurs's FE

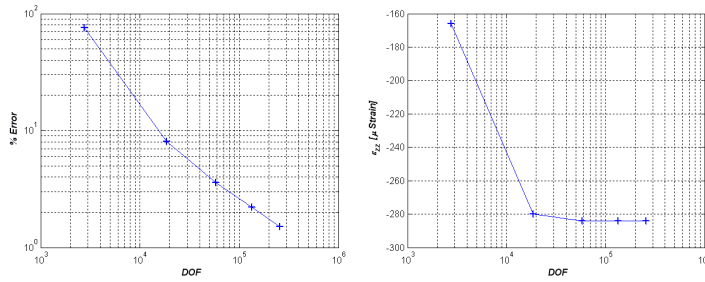


**Fig. 2** Convergence in energy norm and  $\epsilon_{zz}$  at a representative point of interest in a femur.

model consists between 3500 to 4500 elements ( $\sim 150,000$  degrees of freedom (DOFs) at  $p = 4$  and  $\sim 300,000$  DOFs at  $p = 5$ ).

The validation of the  $p$ -FE simulations is performed by comparing them to in-vitro biomechanical experiments on seventeen fresh-frozen human cadaver femurs. In these experiments a simple stance position configuration was considered in which the femurs were loaded through their head while inclined at different inclination angles (0, 7, 15 and 20 degrees). Vertical and horizontal displacements of femur's head and strains along their surface were measured, see Fig. 3.

A total of 102 displacements and 161 strains on the 17 femurs were used to assess the validity of the  $p$ -FE simulations. In Figure 4 the pooled FE strains and displacements are compared to the the experimental observations.

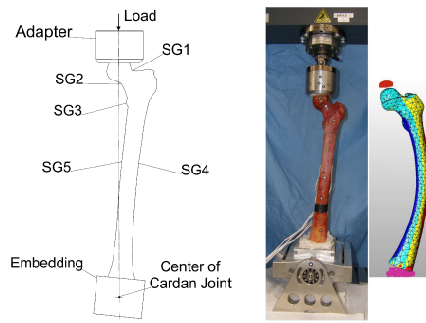


**Fig. 3** (a-left) Sketch of the frontal plane of an embedded and instrumented left femur. (b-right) Experimental setup with the optical markers on an instrumented left femur and its corresponding deformed (magnified) FE model.

*Remark 1* Note that for twelve of the seventeen femurs a blinded comparison was performed, i.e. the group that performed the experiments did not know the FE results, and vice-versa, the experimental results were not known by the group that performed the analysis.

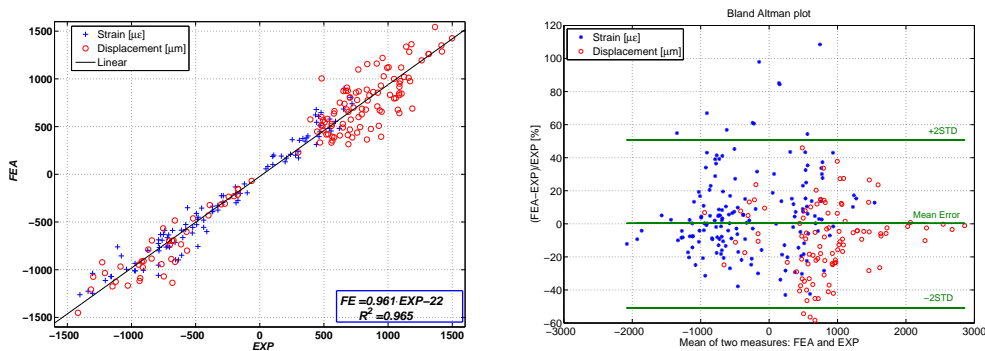


**Fig. 4** Comparison of the computed strains +, \* and displacements o to the experimental observations normalized to 1000 N load. (Left) Linear regression, (Right) Bland-Altman plot.

One may notice the match between the predicted and measured data for femurs under stance position loading: the slope and  $R^2$  of the linear regression are very close to 1, and the average error in the Bland-Altman is zero.

#### 4 $p$ -FE Java implementation

The simulation algorithm presented is being implemented using Java programming language because of its numerous advantages: it is object-oriented, it

allows execution on multiple platforms and supports parallel computing on multiple threads. In Figure 5 the application on an iPhone and the speedup when using multiple threads is shown.

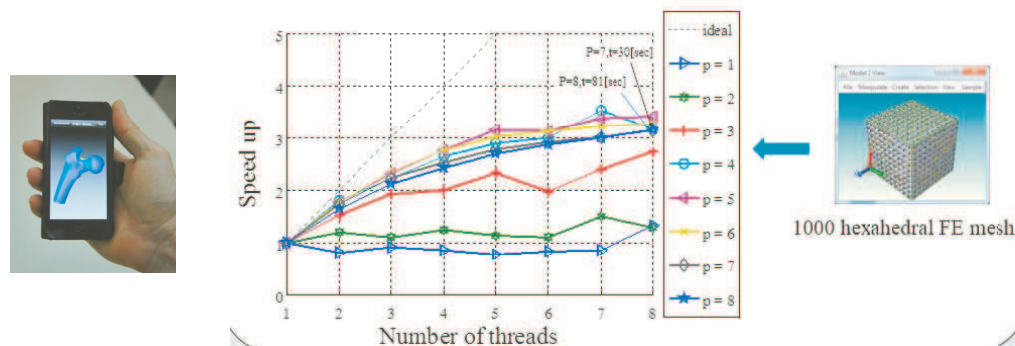


**Fig. 5** (Left) A  $p$ -FE simulation of a femur displayed on an iPhone. (Right) The speedup of the stiffness matrix generation using multiple threads.

**Acknowledgements** I would like to thank past and present graduate students Dr. Nir Trabelsi and Mr. Yosi Levi for their contribution.

## References

1. J. H. Keyak, J. M. Meagher, H. B. Skinner, and Jr. C. D. Mote. Automated three-dimensional finite element modelling of bone: A new method. *ASME Jour. Biomech. Eng.*, 12:389–397, 1990.
2. B. A. Szabó and I. Babuška. *Finite Element Analysis*. John Wiley & Sons, New York, 1991.
3. N. Trabelsi, Z. Yosibash, and C. Milgrom. Validation of subject-specific automated  $p$ -FE analysis of the proximal femur. *Jour. Biomech.*, 42:234–241, 2009.
4. N. Trabelsi, Z. Yosibash, C. Wutte, R. Augat, and S. Eberle. Patient-specific finite element analysis of the human femur - a double-blinded biomechanical validation. *Jour. Biomech.*, 44:1666 – 1672, 2011.
5. Z. Yosibash, R. Padan, L. Joscowicz, and C. Milgrom. A CT-based high-order finite element analysis of the human proximal femur compared to in-vitro experiments. *ASME Jour. Biomech. Eng.*, 129(3):297–309, 2007.

# Minisymposia

**MS I Dummy Models Retired?  
Active Digital Human Models for  
Automotive Safety Research**

MS I.1: Using Hill-Type Muscles to Drive Active  
Human Models Brings Low Level Motor Control for  
Free

Authors: Blaschke, Julian, Schmitt, Syn

## **Abstract**

### **Using Hill-type muscles to drive active human models brings low level motor control for free - work in progress**

Julian Blaschke<sup>1</sup>, Syn Schmitt<sup>1,2</sup>

<sup>1</sup>Research Centre for Simulation Technology, University Stuttgart

<sup>2</sup>Department of Sports and Movement Science, University Stuttgart

The volume of road traffic has risen sharply in the last two decades. Improved and new safety systems in cars are needed, to maintain the occupant safety. Since conventional dummies are limited by their ability to map occupant movement during a broad variety of crash-scenarios and volunteer-tests are only feasible to a certain degree of physical load, it is even more important to use computer-based approaches. Digital models of humans are already in development for years and they are getting increasing attention, since the digitalisation of the production process of cars is irreversible.

Yet, for the typical application during the crash phase, human body models already exist and are being validated against available data from literature or individual tests. Recently, the time period before the instant of crash gained particular attention. State-of-the-art crash simulations start at  $t=t_0$ , which corresponds to the first contact between car and obstacle (which could be also another car). However, the very short period of time in advance of  $t_0$  almost entirely predefines the following crash phase and the severity of the following crash. Then, the car eventually slides on the road, braking manoeuvres are accomplished and the passenger's body position has not necessarily to be in a neutral position.

Active safety systems, like for example belt tensioners or airbags are responsible for the posture and position of the occupant in the car. Therefore, it is their task to ensure that the occupants are in the best possible position at the

moment of impact. Since the position and kinematics at the moment of impact are crucial for the safety of the occupants, it is even more important to reflect the reality in the simulation. A crucial factor is that humans actively try to resist a forward displacement during a strong braking manoeuvre by activating their muscles through reflex and voluntary activation. Conventional human body models achieve that only partially. In contrast, active human body models including muscle-like activation and control are needed to account for a higher bio-fidelity.

Commercially available human body models, like, for example, the THUMS (Total Human Model for Safety) developed by Toyota in 2000 and further developed and used by other automobile manufacturers like Daimler, often don't offer satisfying possibilities of activating muscles in a physiological manner. Muscle behavior in these models is very often passive and based on over-simplified spring and damper systems. Active muscle contraction in biology, however, is a well-coordinated interaction of the muscle and its control. Particularly in the pre-crash phase, where only small accelerations in the range of about  $1g$  occur, muscles have high influence on the kinematics of the human body. We hypothesize, therefore, that the implementation of established models of the biological muscle into human models developed for automotive applications a. will enhance the bio-fidelity of the human models and b. will introduce already low-level motor control without the need of further tuning control parameters.

In this work we present a literature based Hill-type model of a biological skeletal muscle parameterised within a commercially available simulation framework (LS-Dyna®, Livermore Software Technology Corporation/USA). A parametric study was executed to best fit the muscle model (Fig. 1) to previously published literature results (Fig. 2). The commercial framework LS-Dyna® provides already a Hill-type muscle model, the material Mat-Muscle (MAT\_156), which is based on the former S15-Hill-Type-Muscle material. With this, several typical muscle experiments, the quick-release test, an eccentric contraction tests and a concentric contraction tests, were executed numerically to develop and validate the muscle model. For validation purposes in crash-test

scenarios it is recommended to use the concentric test, a test in which a muscle is constrained at one end and loaded at the other end (Fig. 1). The muscle shortens concentrically when activated as soon as the muscle force exceeds the load.

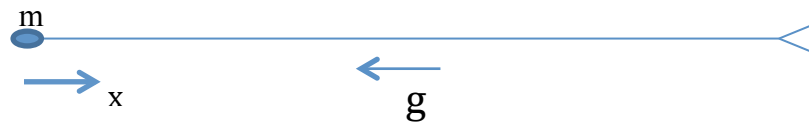


Figure 1: Muscle model for contraction test

The result of the simulation was compared to experimental time versus shortening-velocity curves. It was found, that applying different loads result in different time curves, as expected and can be seen in figure 2. The smaller the

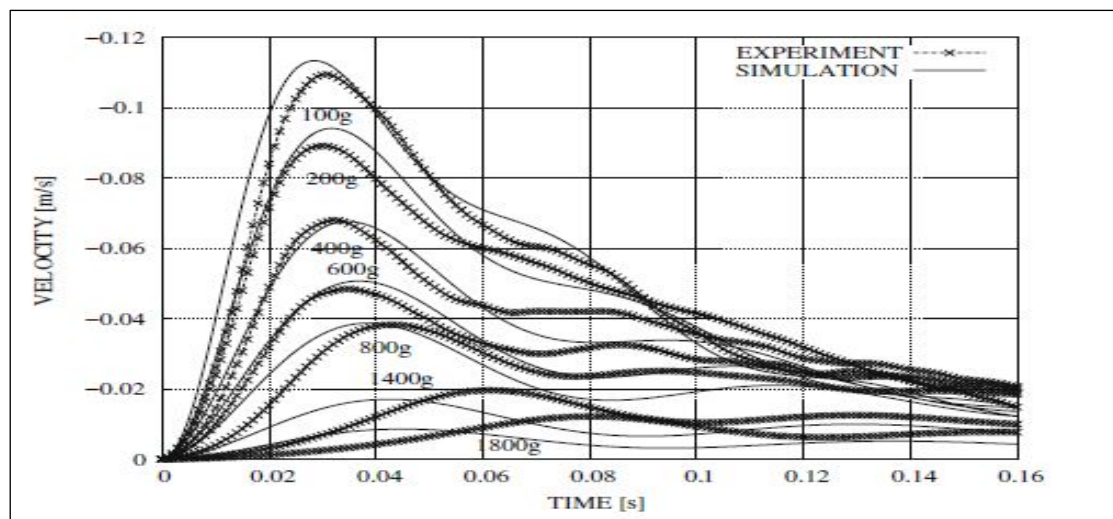


Figure 2: Time vs. velocity curve for the concentric contraction of a one-day old piglet muscle for different loads. Experimental data is plotted with crosses, the simulation result with the solid line. (Günther, Schmitt, & Wank, 2007)

load the faster the contraction and the bigger the displacement. This is also pictured in figure 3, the results of the contraction test with LSDyna® muscle, Mat-Muscle (MAT\_156).

Currently, the activation of the muscle has to be described as a time-dependent function. In the future a more sophisticated solution for the activation is targeted at. Therefore further studies will be made on the activation dynamics in form of differential equations, dependent on, for example, head acceleration or velocity. It is necessary to use time independent muscle activation in order to replicate all relevant crash scenarios and, thus, to develop proper safety systems, since the level of muscle activation is state-dependent rather than time-dependent, explicitly described by a function of time.

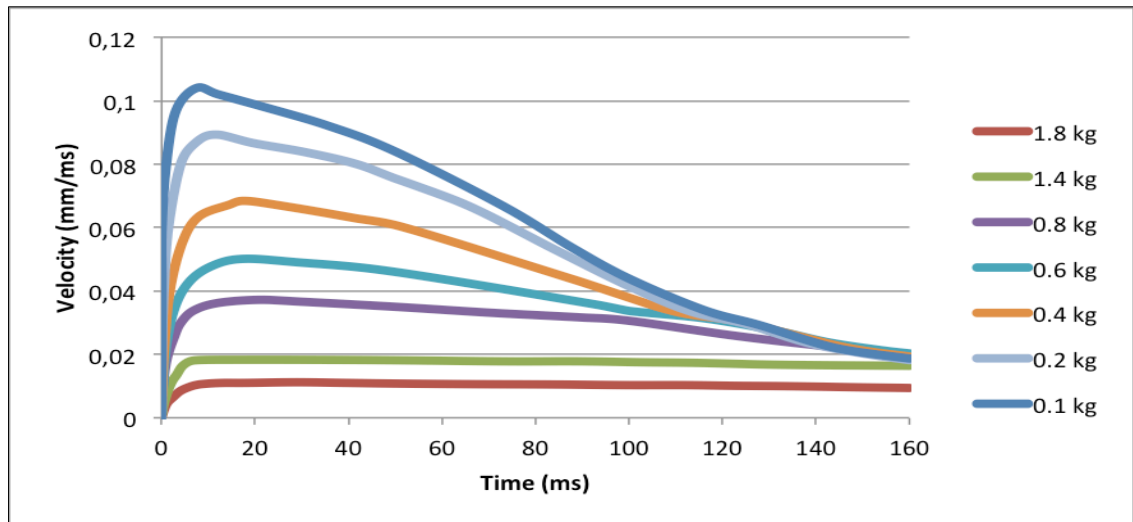


Figure 3: Time vs. velocity curve for the contraction test of LSDyna(R) Mat-muscle (MAT\_156).

#### References

Günther M, Schmitt S, Wank V. High-frequency oscillations as a consequence of neglected serial damping in Hill-type muscle models. *Biol Cybern.* 2007 97(1):63–79.

MS I.2: A Comparison Between Dummy and  
Human Models for Crash Simulations of Side Impacts

Authors: Kleinbach, Christian, Fehr, Jörg

---

# A Comparison Between Dummy and Human Models for Crash Simulations of Side Impacts

Christian Kleinbach · Jörg Fehr

**Abstract** In this paper an anthropometric test devices (ATD) and a human model are compared in a simulation of a standardized side impact scenario. By comparing the injury values of the most important body regions, both models are evaluated.

**Keywords** Side Impact · Dummy Model · Human Model

## 1 Introduction

In 2012, side impacts made up the second largest collision type for passenger cars in the US ([2],[5]). More than 3.8 million collisions with motor vehicles in transport are reported in [5]. In 21.3 % of these collisions, the first harmful contact happens at an angle. This is the second largest type of collision besides rear end, front end, sideswipe and other collisions. When looking only at fatal accidents, being defined as one with at least one dead person within 30 days after the crash, this type of collision is by far the most likely one. Fatal accidents with the first contact at an angle are approximately three times as likely as fatal rear end accidents and about twice as likely as fatal head on accidents.

Side collisions are dangerous, mostly because of the small space available between the outer shell of the vehicle and the occupants. The narrow space

---

C. Kleinbach  
Universität Stuttgart, Institute of Engineering and Computational Mechanics  
Tel.: +49-711-685-66490  
Fax: +49-711-685-66400  
E-mail: christian.kleinbach@itm.uni-stuttgart.de

J. Fehr  
Universität Stuttgart, Institute of Engineering and Computational Mechanics  
Tel.: +49-711-685-66392  
Fax: +49-711-685-66400  
E-mail: joerg.fehr@itm.uni-stuttgart.de

makes crumple zones impossible and results in short time frames available for the deployment of safety devices. Contrary to the more symmetric load in front impacts, the deformation of the door during the collision exposes the human body to an asymmetric load in side impacts. High strain is put onto the thoracic region, especially the ribs, by the intruding parts of the door.

Regarding the mechanical design of the body parts for the ATDs, high demands result from the complex load case described above. This can also be seen in history of the development of ATDs for side impacts. In many cases, the biofidelity was questioned, which led to the development of new or improved dummy models. The transmission of forces from the upper limbs over the shoulder region to the spine, the introduction and construction of single ribs or their coupling to the spine are just some of the problems.

For crash simulations, finite element models of the ATDs can be acquired from various sources. The simulation of crash scenarios with ATDs is necessary during the development of new vehicles and safety systems but it transfers the problems of the mechanical modeling to the finite element models. In order to avoid these problems the intermediate mechanical model can be ignored, and a finite element model of the human body is created directly. The Total human model for safety (THUMS), from Toyota Company, is such a model.

Our aim is the comparison between the ES-2re and the THUMS model in a standardized side impact scenario. The maximum rib deflection and the vicious criterion of both models are compared with each other.

## 2 Test setup

The ES2-re dummy and the THUMS model are compared in a side impact setup shown in figure 1. This setup is defined in the ECE R95 regulations with a moving deformable barrier (MDB EEVC, 950 kg) impacting the car at a  $90^\circ$  angle at a speed of  $50 \frac{\text{km}}{\text{h}}$ . The FE model of the barrier is provided by the Livermore Software Technology Corporation (LSTC).

### 2.1 Vehicle model

The vehicle model used in the simulations is a 2001 Ford Taurus, for which the FE model is publicly available through the Finite Element Model Archive at the National Crash Analysis Center [4]. The FE model has a detailed interior suitable for occupant simulations. However, it comes with the seats positioned for a 5th percentile female dummy. Therefore, the seats are positioned for a 50th percentile dummy with information available in [7]. No airbags but a seat belt with a retractor is installed in the Taurus model.

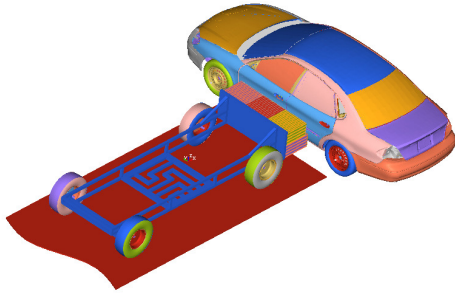


Fig. 1 ECE R95 test setup for side impact.

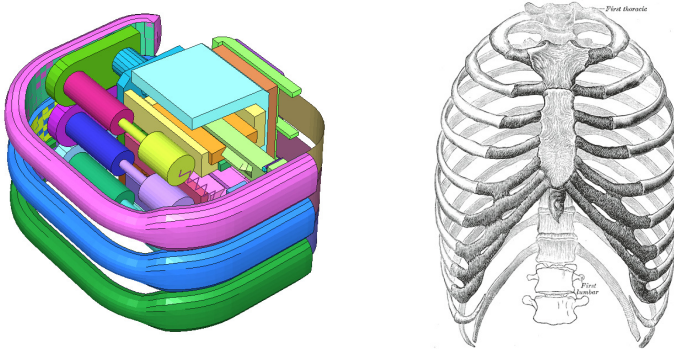


Fig. 2 rib cage of the ES-2re Dummy model next to a human rib cage [1].

## 2.2 Dummy and human model

In side impacts, the thorax is one of the most important body regions. Due to the complex structure, its modelling is difficult. Figure 2 shows the thorax design of the ES-2re dummy next to a human ribcage. The ribcage of the dummy is modelled with three separate ribs, which are mounted with a spring damper combination to the central body representing the spine. The ribs are made of steel and are covered with foam and a rubber layer. They have extensions reaching to the backplate on the impact side. The extensions are steel stripes, which are supported by a needle bearing system in the backplate. This creates a new load path from the spine to the ribs and is intended to cause more realistic rib deflections. The FE model of the ES-2re dummy is provided by Dynamore GmbH.

The THUMS is a detailed FE model of the human body. It contains the skeletal structure, numerous organs, ligaments and other soft tissues. The

model was validated successfully in various impact simulations, as an occupant [6] as well as a pedestrian model [3]. The thorax, being modeled with all organs and a detailed rib cage, is expected to show deformations in a side impact very close to those of a human body. Therefore, a comparison with the ES2-re dummy will show the differences of a human model in crash simulations.

**Acknowledgements** The 2001 Ford Taurus model has been developed by The National Crash Analysis Center (NCAC) of The George Washington University under a contract with the FHWA and NHTSA of the US DOT. The authors would like to thank the German Research Foundation (DFG) for financial support of the project within the Cluster of Excellence in Simulation Technology (EXC 310/1) at the University of Stuttgart.

## References

1. Gray, H.: Anatomy of the human body. Lea & Febiger, Philadelphia (1918)
2. Insurance Institute for Highway Safety: Passenger vehicle occupants - fatality facts 2012. (2014). URL <http://www.iihs.org/iihs/topics/t/general-statistics/fatalityfacts/passenger-vehicles#Crash-types>
3. Iwamoto, M., Omori, K., Kimpara, H., Nakahira, Y., Tamura, A., Watanabe, I., Miki, K., Hasegawa, J., Oshita, F., Nagak, A.: Recent advances in thums: development of individual internal organs, brain, small female and pedestrian model. In: Proceedings of 4th European LS-DYNA Users Conference, pp. 1–10 (2003)
4. National Crash Analysis Center: Finite element model archive. URL <http://www.ncac.gwu.edu/vml/models.html>
5. National Highway Traffic Safety Administration: Traffic safety facts 2012. DOT HS **812 032** (2014)
6. Oshita, F., Omori, K., Nakahira, Y., Miki, K.: Development of a finite element model of the human body. In: 7th International LS-DYNA Users Conference, vol. 14, pp. 205–212 (2002)
7. PMG Technologies Test and Research Centre: Compliance frontal impact cmvss 208/212/301: Ford taurus 2000. NHTSA Test No. 4135 (August 2000)

MS I.3: Uncertainty Quantification Associated with  
the Mechanical Response of Femurs

Authors: Wille, Hagen, Yosibash, Zohar, Ruess, Martin, Rank, Ernst

---

# Uncertainty quantification associated with the mechanical response of femurs

Hagen Wille · Zohar Yosibash ·  
Martin Ruess · Ernst Rank

**Abstract** We consider material and loading uncertainties within the context of patient-specific finite element analyses of human femurs. The influence of the combined uncertainties on the predicted mechanical response is quantified using a truncated polynomial chaos expansion and Smolyak integration. This non-intrusive approach is demonstrated by the finite cell method as a black-box solver. Numerical results are presented and compared to a Monte Carlo simulation.

**Keywords** femur · uncertainty quantification · polynomial chaos expansion · finite cell method

## 1 Introduction

Patient-specific finite element (FE) models of human femurs are based on data extracted from quantitative computed tomography (qCT) scans. The main difficulty is to determine reliably the inhomogeneous material properties [1]. Moreover, most FE analyses are aimed at demonstrating their accuracy with respect to in-vitro experimental observations, where a well-defined load is applied mimicking the hip contact force [2–4]. When used for clinical studies, however, both the physiological load of a patient and its specific material properties are uncertain. Quantifying the influence of the combined uncertainties is of importance, especially since these nonlinearly affect the mechanical response. Our objective is to incorporate material and loading uncertainties into a patient-specific FE analysis of a human

---

H. Wille, E. Rank  
Chair for Computation in Engineering, Technische Universität München, Germany  
E-mail: {wille,rank}@bv.tum.de

Z. Yosibash  
Department of Mechanical Engineering, Ben-Gurion University of the Negev, Israel  
E-mail: zohary@bgu.ac.il

M. Ruess  
Chair of Aerospace Structures and Computational Mechanics, Delft University of Technology, Netherlands  
E-mail: m.ruess@tudelft.nl

femur, and to interpret the stochastic response clearly enough for biomechanical applications.

## 2 Material and Methods

The deterministic mechanical response of a femur was shown to be well predicted by the finite cell method (FCM) [5–7]. The FCM embeds the voxel-based geometry of the femur in a simulation domain of high-order hexahedral cells following a regular Cartesian grid. Figure 1 illustrates this concept, which omits a computational expensive segmentation and meshing procedure. The femur’s material behavior is assumed to be linear elastic and isotropic. This requires two material constants: Poisson’s ratio  $\nu = 0.3$  and Young’s modulus  $E$ . The latter is related to a local densitometric measure  $\rho_{\text{ash}}$  that is computed from the qCT scan of the femur. Note that this approach accounts for the heterogeneous nature of bone tissue.

Because the relation between density and elasticity properties is based on experimental studies with a large scatter, we are uncertain about the correct conversion for the specific femur under investigation. Therefore, we consider a stochastic  $E$ - $\rho_{\text{ash}}$  relation [8]:

$$E = 12000 \rho_{\text{ash}}^{1.45} \cdot X_E \quad E \text{ in [MPa]}, \rho_{\text{ash}} \text{ in [g/cm}^3\text{]} \quad (1)$$

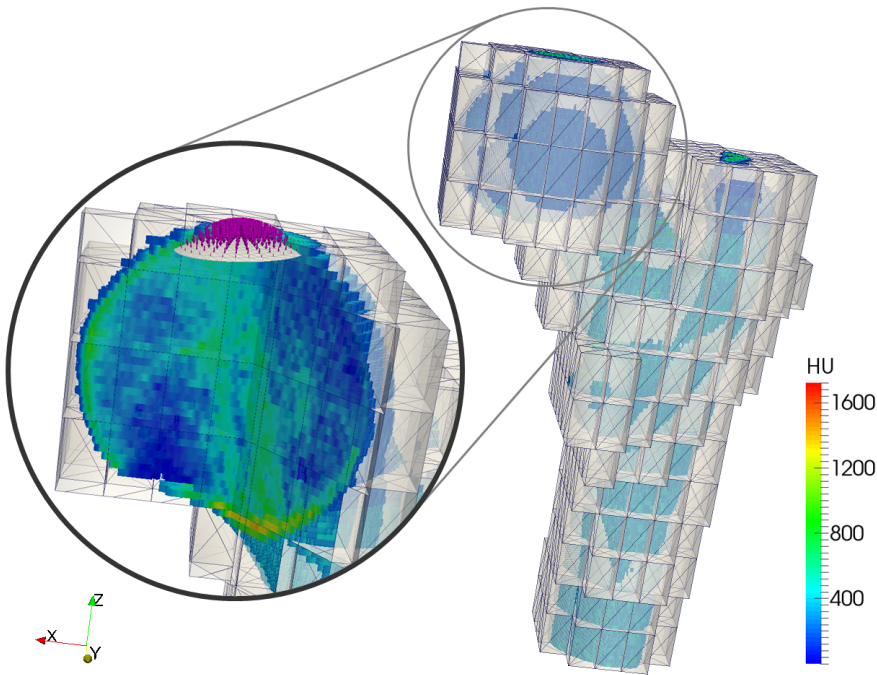


**Fig. 1** Deterministic simulation model of a human femur using the finite cell method. Dirichlet boundary conditions are chosen such that the distal part of the shaft is clamped. The hip contact force is applied as distributed load on a spherical cap resembling the shape of the femoral head. Material constants are computed from the heterogeneous CT values (HU) with the relations from [8].

where  $X_E \sim \ln\mathcal{N}(0, 0.316^2)$  is a log-normal random variable whose distribution characterizes the scatter of the experimental data around the estimated trend. Additionally, we consider a stochastic loading of the femur [9], which describes the variability of hip contact forces measured in-vivo during going upstairs [10]. The stochastic loading is characterized by three independent normal random variables:

$$X_F \sim \mathcal{N}(0.97 \cdot \text{BodyWeight} + 1465, 277^2) \quad F, \text{BodyWeight in [N]} \quad (2)$$

$$X_{A_x} \sim \mathcal{N}(15.25, 3.38^2) \quad A_x \text{ in [deg]} \quad (3)$$

$$X_{A_y} \sim \mathcal{N}(19.69, 6.49^2) \quad A_y \text{ in [deg]} \quad (4)$$

with  $F$ ,  $A_x$ , and  $A_y$  denoting the magnitude of the peak hip contact force and its two corresponding angular directions, respectively.

As a result of the combined material and loading uncertainties, the patient-specific simulation described above is stochastic. Denoting the deterministic model by  $\mathcal{M}$  and the input uncertainties by  $\mathbf{X} = \{X_E, X_F, X_{A_x}, X_{A_y}\}$ , we are interested in the model response  $Y = \mathcal{M}(\mathbf{X})$ . Here, the random variable  $Y$  describes a specific scalar quantity of interest, e.g. the total displacement or the largest principle strain at a specific location. We approximate the distribution of  $Y$  with a truncated polynomial chaos expansion (PCE) [11, 12]:

$$Y = \mathcal{M}(\mathbf{X}) = \sum_{\alpha \in \mathcal{A}} y_\alpha \Psi_\alpha(\mathbf{Z}) \quad (5)$$

where  $\Psi_\alpha$  denotes an orthogonal basis of multivariate Hermite polynomials and  $\mathcal{A}$  represents a finite set of multi-indices. The independent standard normal random variables  $\mathbf{Z}$  are directly related to  $\mathbf{X}$  through an isoprobabilistic transform  $\mathcal{T}$ , i.e.  $\mathbf{X} = \mathcal{T}(\mathbf{Z})$ . In order to determine the unknown PCE coefficients  $y_\alpha$ , the orthogonality of the basis is used. It holds that:

$$y_\alpha = \mathbb{E}[Y \Psi_\alpha(\mathbf{Z})] = \int_{\mathcal{D}_Z} \mathcal{M}(\mathcal{T}(z)) \Psi_\alpha(z) f_Z(z) dz \quad (6)$$

with  $f_Z$  denoting the joint probability density function (PDF) of  $\mathbf{Z}$ . The multidimensional integral is to be numerically evaluated over the corresponding support space  $\mathcal{D}_Z$ . At this point, a sparse quadrature scheme like Smolyak integration [13] proves highly beneficial, as it circumvents the curse of dimensionality. Thus, the computational model  $\mathcal{M}$  needs to be evaluated only at a few Smolyak quadrature points, each leading to a deterministic simulation of the femur with different stiffness, load magnitude, and load direction.

Once the coefficients are determined, statistical quantities of interest can be post-processed from Eq. (5). Mean and variance of  $Y$  are directly computed from the PCE coefficients, because  $\hat{\mu}_Y \equiv \mathbb{E}[Y] = y_0$  and  $\hat{\sigma}_Y^2 \equiv \text{Var}[Y] = \sum_{\alpha \in \mathcal{A} \setminus 0} y_\alpha^2$ . In general, the PCE serves as a surrogate model and a sample set of response quantities is generated by Monte Carlo techniques. These response samples are then used to obtain an estimate of the PDF  $f_Y$  by kernel smoothing [11, pp. 67]. In combination with a limit state function also a probability of failure can be approximated from these samples.

### 3 Results and Discussion

Based on the qCT-scan of a fresh-frozen femur of a 56 year old male donor [14] a FCM model was created. Assuming a body weight of 800 N, we are interested in the PDF of the largest principle strain at 884 post-processing points distributed all over the femur. For every point the stochastic response is approximated by a polynomial chaos of order  $p = 4$  containing 70 coefficients. The corresponding Smolyak quadrature scheme with accuracy level  $p + 1$  consists of 385 quadrature points. Hence, only 385 deterministic simulation runs are necessary for quantifying the stochastic response. This is significantly less than a Monte Carlo simulation, which requires over 10,000 runs for being converged. In Figure 2 we compare the approximated PDF of the PCE with the histogram of such an extensive Monte Carlo simulation. Moreover, probabilities of failure are computed using a yield strain of  $7300 \mu$  as limit state [15].

The femoral neck region exhibits both the largest strains and failure risks during going upstairs, just as the distal part of the femur shaft, which we assume to be affected by the clamped boundary condition. However, all probabilities of failure are very small (order of  $10^{-4}$ ). This is reasonable given that the donor had no skeletal disease.

**Acknowledgements** The authors acknowledge the generous support of the Institute for Advanced Study of the Technische Universität München, funded by the German Excellence Initiative. We thank Dr. Iason Papaioannou from the Engineering Risk Analysis group at Technische Universität München for helpful discussions on non-intrusive methods for uncertainty propagation.

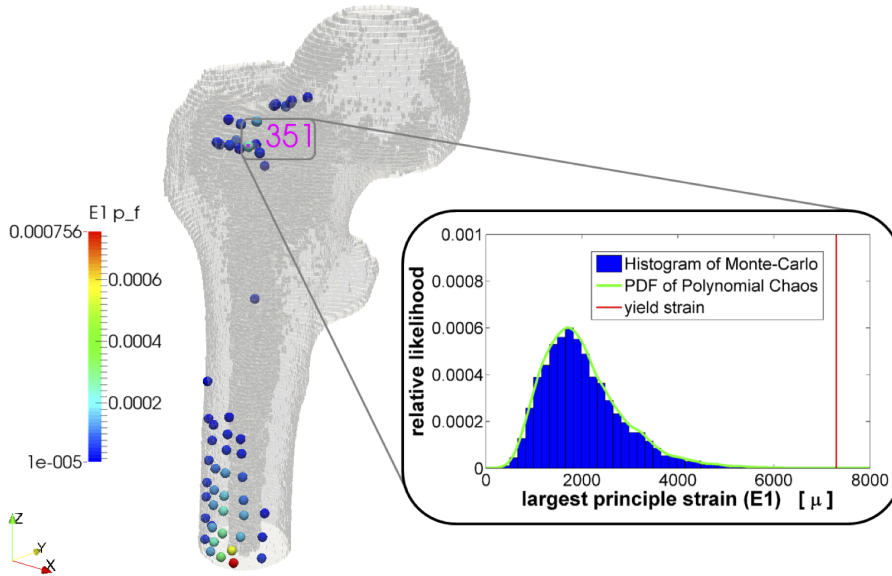


**Fig. 2** Post-processing example: at selected point in space the distribution for the largest principle strain ( $E1$ ) is approximated by a PCE. Colored spheres represent locations where the probability of exceeding the yield strain is larger than  $10^{-5}$ .

---

## References

1. B. Helgason, E. Perilli, E. Schileo, F. Taddei, S. Brynjólfsson, M. Viceconti, *Clinical Biomechanics* **23**(2), 135 (2008)
2. Z. Yosibash, N. Trabelsi, C. Milgrom, *Journal of Biomechanics* **40**(16), 3688 (2007)
3. L. Cristofolini, E. Schileo, M. Juszczyk, F. Taddei, S. Martelli, M. Viceconti, *Philosophical transactions. Series A, Mathematical, physical, and engineering sciences* **368**(1920), 2725 (2010)
4. N. Trabelsi, Z. Yosibash, C. Wutte, P. Augat, S. Eberle, *Journal of Biomechanics* **44**(9), 1666 (2011)
5. A. Düster, J. Parvizian, Z. Yang, E. Rank, *Computer Methods in Applied Mechanics and Engineering* **197**(45-48), 3768 (2008)
6. Z. Yang, M. Ruess, S. Kollmannsberger, A. Düster, E. Rank, *International Journal for Numerical Methods in Engineering* **91**(5), 457 (2012)
7. M. Ruess, D. Tal, N. Trabelsi, Z. Yosibash, E. Rank, *Biomechanics and Modeling in Mechanobiology* **11**(3-4), 425 (2012)
8. H. Wille, E. Rank, Z. Yosibash, *Journal of Biomechanics* **45**(7), 1140 (2012)
9. Z. Yosibash, H. Wille, E. Rank, submitted to *Journal of Orthopaedic Research* (2014)
10. G. Bergmann, G. Deuretzbacher, M.O. Heller, F. Graichen, A. Rohlmann, J. Strauss, G. Duda, *Journal of Biomechanics* **34**(7), 859 (2001)
11. B. Sudret, *Uncertainty propagation and sensitivity analysis in mechanical models – Contributions to structural reliability and stochastic spectral methods. Habilitation à diriger des recherches, Université Blaise Pascal, Clermont-Ferrand, France* (2007)
12. D. Xiu, *Communications in Computational Physics* **5**(2), 242 (2009)
13. F. Heiss, V. Winschel, *Journal of Econometrics* **144**(1), 62 (2008)
14. Z. Yosibash, A. Katz, C. Milgrom, *Medical Engineering & Physics* **35**(7), 978 (2013)
15. H.H. Bayraktar, E.F. Morgan, G.L. Niebur, G.E. Morris, E.K. Wong, T.M. Keaveny, *Journal of Biomechanics* **37**(1), 27 (2004)

MS I.4: Vehicle Safety Using the THUMS™  
Human Models

Authors: Fressmann, Dirk

---

# Vehicle Safety using the THUMS<sup>TM</sup> Human Models

Dirk Fressmann, DYNAmore GmbH

**Abstract** The Total Human Model for Safety (THUMS<sup>TM</sup>) is a computational model of the human body suitable for crash simulations for pedestrian and occupant safety applications. The following presentation will discuss some aspects and primarily focus on a brief comparison between the THUMS model version 3 and the recent model version 4. Geometric details are given and some applications are presented.

**Keywords** Human Modeling · THUMS · Active and Passive Safety · Simulation

## 1 Introduction

The THUMS<sup>TM</sup> Human Models are actively developed by Toyota Motor Corporation (TMC) and Toyota Central R&D Labs Inc. in cooperation with additional research institutes like the Wayne State University since approx. 2000.

Reproducing the anatomical geometry and basic biomechanical properties of the human body (e.g. skeletal structure, joints, bone stiffness or skin flexibility), the THUMS models represent an additional tool to evaluate injury risks and support the development of passive and active safety systems. Older model versions are primarily used to simulate the kinematical behavior of the human body or evaluate stress and strain distributions within the bones and joints. The most recent model version 4 shows a much more detailed modeling technique and can thus additionally be used to analyze more complex injury mechanisms.

In the following, the main focus should be given on a comparison of the recent model version 4 and the previous version 3 which is still in heavy use

---

D. Fressmann  
DYNAmore GmbH, Industriestrasse 2, 70565 Stuttgart  
Tel.: +49-711-45960023  
E-mail: dirk.fressmann@dynamore.de

by various car manufacturers. Details and properties of the THUMS models are presented and some example crash situations for pedestrian and occupant safety simulations are addressed.

## 2 Model Versions and Variants

### 2.1 Model Variants

The model is available as an occupant and a pedestrian model version and - in its standard size - represents a 50%ile adult male (AM50).

The occupant model is primarily used in occupant simulation environments, e.g. for seat, belt and airbag development in a driver and co-driver posture and the evaluation of injury risks in various crash situations (frontal, lateral and rear). Newer applications are also addressing a pre-crash phase, where the human model is used to estimate the motion of the human driver prior to the actual crash phase, e.g. during a lane change or a braking maneuver. However this is still under heavy development since it requires a stabilized human model and a reactive muscle behavior of the model.

The pedestrian models on the other side are used for pedestrian safety simulations, where especially the impact location and time of the head on the engine bonnet or the windscreen is of interest to develop active and passive pedestrian safety systems. Here a variety of different postures, stances and also model sizes can be taken into account. Especially the small female (5%ile female model AF05), the 6 year-old child (6YO) or the large male (95%ile male AM95) are frequently used and are also partly available in the THUMS model family.

### 2.2 Model Versions

Currently available and in active use are the model versions 3 (2008) and 4 (2010 - update to version 4.01 in 2012) - see [1] and [2].

The model version 3 is a simplified representation of the human body, covering mainly the skeletal structure, joints, the flesh, simplified organs and a very detailed head (cf. Fig. 1). The geometry is mainly based on literature data, whereas the head structure was gained from medical CT scan data. The model is primarily used for kinematical evaluations in various crash situations, where the kinematical sequence of the human body is of interest. Additionally, stress and strain evaluations can possibly be performed for the bones and the joints and due to the fine representation of the head, skull and brain injury evaluations might also be possible, depending on the validation basis.

The current model version 4 on the other side is a completely new model based on medical CT scans of a 39year old male (cf. Fig 2). Thus the model represents a very realistic geometry and the detailing of joints, the head, skin and flesh layers was considerably increased. New developments involve a very



**Fig. 1** THUMS Version 3 Model Details

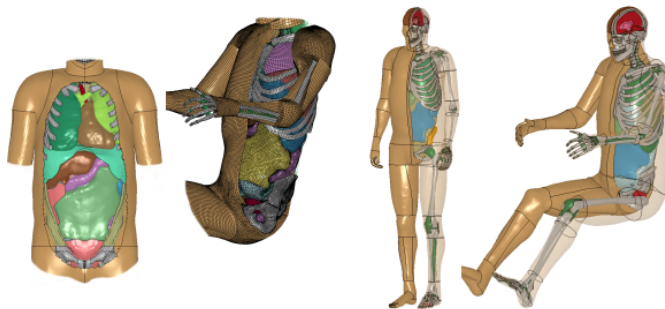


**Fig. 2** THUMS Version 4 Model Details

fine internal organ modeling, 3D ligaments and improved materials, such that not only the kinematical response of the human body can be investigated but also a deeper analysis of injury mechanisms in various areas of the human body is now possible.

### 3 Applications

In the meantime, both model variants and versions are widely used in different pedestrian and occupant safety simulations.

Pedestrian simulations (cf. Fig. 3) are typically used to evaluate the kinematics of the human body on the bonnet during a pedestrian crash situation. Active and passive safety systems can be tested and improved. Efforts to establish the human models within regulatory testing procedures are on the way.

In occupant safety simulations (cf. Fig. 4), the THUMS models are used together with seat and belt models, as well as airbag models. The efficiency of these safety systems can be tested and improved, as well as possible injuries can be evaluated.

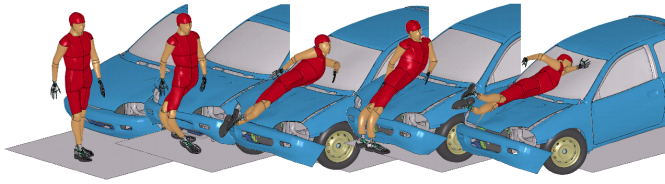


**Fig. 3** Example for a typical pedestrian crash situation



**Fig. 4** Example for a typical occupant crash situation

## 4 Summary

To summarize, model version 3 is a simple, but computationally very efficient model of the human body with limited evaluation possibilities. If one is only interested in the kinematical behavior of the human body in various crash situations, this model is completely sufficient. Model version 4 on the other hand represents a new generation of human models, where the human body is captured in much more detail. This eventually leads to a rather fine model, which is computationally much more expensive and also sets higher demands on the engineers knowledge about biomechanics and possible result extraction possibilities. Both models are actively used and have their own strenghts and limitations.

Further information can be found in [3], [4], [5], [6] and references therein.

## References

1. Toyota Motor Corporation, Toyota Central R&D Labs., Inc., Users guide of Computational Human Model THUMS (Total HUMAN Model for Safety), Version 3.0, March 2008
2. Toyota Motor Corporation, Documentation - Total Human Model for Safety (THUMS), Version 4.0, November 2010
3. JSOL Corporation, THUMS - Total Human Model for Safety, <http://ls-dyna.jsol.co.jp/en/thums/index.html>
4. Iwamoto M, Tamura A, Furusu K, Kato C, Miki K, Hasegawa J, Yang K, Development of a Finite Element Model of the Human Lower Extremity for Analyses of Automotive Crash Injuries, SAE Paper 2000
5. Yasuki T, Yamamae Y, Validation of Kinematics and Lower Extremity Injuries Estimated by Total Human Model for Safety in SUV to Pedestrian Impact Test, Journal of Biomechanical Science and Engineering, Vol 5 No 4, 2010
6. Fressmann, D.; Muenz, T.; Graf, O.; Schweizerhof, K., FE Human Modeling in Crash - Aspects of the numerical Modeling and current Applications in the Automotive Industry, 6. LS-Dyna Anwenderforum, Frankenthal 2007

MS I.5: THUMS User Community - Harmonising  
the Validation of Human Models for Crash Simulation

Authors: Peldschus, Steffen, Fuchs, Therese

No pdf yet.

Steffen Peldschus\*, Therese Fuchs\*\*

\* Lehrgebiet Angewandte Mechanik, Hochschule Furtwangen University

\*\* Institut für Rechtsmedizin, LMU München

MS I.6: Modeling Active Human Muscle Responses  
during Driver and Autonomous Avoidance Maneuvers

Authors: Östh, Jonas, Ólafsdóttir, Jóna Marín, Brolin, Karin

---

# Modeling Active Human Muscle Responses during Driver and Autonomous Avoidance Maneuvers

Jonas Östh · Jóna Marín Ólafsdóttir · Karin Brolin

**Abstract** Integration of pre-crash and in-crash safety systems has a potential to further reduce car occupant fatalities and to mitigate injuries. However, the introduction of integrated safety systems creates new requirements for Human Body Models (HBMs) as occupant kinematics must be predicted for a longer period of time, in order to evaluate the effect of systems activated before the crash phase. For this purpose, a method to model car occupant muscle responses in a finite element (FE) HBM have been developed, utilizing feedback control of Hill-type muscle elements. The model has been applied to study occupant kinematics under the influence of autonomous and driver braking deceleration. Ongoing work aims at extending the model to be able to also capture human responses to lateral and oblique pre-crash loading.

**Keywords** active muscle · occupant kinematics · feedback postural control · human body model · finite element

---

Jonas Östh  
Applied Mechanics, Chalmers University of Technology  
Tel.: +46-31-772 15 36  
E-mail: jonas.osth@chalmers.se

Jóna Marín Ólafsdóttir  
Applied Mechanics, Chalmers University of Technology  
Tel.: +46-31-772 36 53  
E-mail: jona.olafsdottir@chalmers.se

Karin Brolin  
Applied Mechanics, Chalmers University of Technology  
Tel.: +46-31-772 15 09  
Fax: +123-45-678910  
E-mail: karin.brolin@@chalmers.se

## 1 Introduction

With increasing computational power available, numerical simulation has become an important tool for all types of product development, especially in the automotive industry. To evaluate the risk of injury in a simulated vehicle crash, models of the occupants are needed. In physical testing this task is performed by mechanical models of the human, anthropomorphic test devices (ATD). Numerical models of ATD exist and are used extensively, but more detailed responses can be evaluated if the occupants are represented by an HBM, directly representing the anatomical structures and materials of the human body.

Even though HBMs more closely resemble the actual human body, many aspects of the human anatomy and mechanical properties of living tissue remains to be incorporated. One such feature is the inclusion of active musculature and control of the muscles, which has only to a limited extent been included in HBMs to date [1,3,4].

Emerging integrated safety systems has the potential to decrease impact severity through, for instance, autonomous braking [2,15] or steering [5]. Furthermore, sensory information and decision algorithms enable occupant restraint activation to start before impact [6,16]. The duration of and load level present in the pre-crash phase requires human active muscle responses to be taken into account as they will have a major influence on the kinematic response of the occupants. For the evaluation of these types of integrated safety systems, there is a need for the inclusion of actively controlled muscles in HBM.

## 2 Method

In our work, the THUMS version 3.0 AM50 occupant model [17] is used. Its anthropometry is based on the 50th percentile male reported by Robbins et al. [14] and it consists of approximately 68 100 solid elements, 75 700 shell elements and 3400 one-dimensional elements. The model contains rigid bodies (e.g., the vertebrae) and deformable bodies (e.g., the intervertebral discs, ribs, skin, and internal organs). For the simulations, the explicit FE solver LSDYNA (LSTC Inc., Livermore, CA, USA) is used.

### 2.1 Muscle Implementation

A total of 394 Hill-type line muscle elements have been added to the THUMS; 178 for the cervical spine, 110 for the lumbar spine, 14 abdominal, and 23 for each upper and lower extremity (Figure 1). For each of the muscles, active muscle stress is computed according to [9]:

$$\sigma = (N_a(t) * f_v(v) * f_l(l) + f_{pe}(l)) * \sigma_{max} + \sigma_d \quad (1)$$

where  $N_a(t)$  is the muscle activation level determined by the controllers, described in Section 2.2.

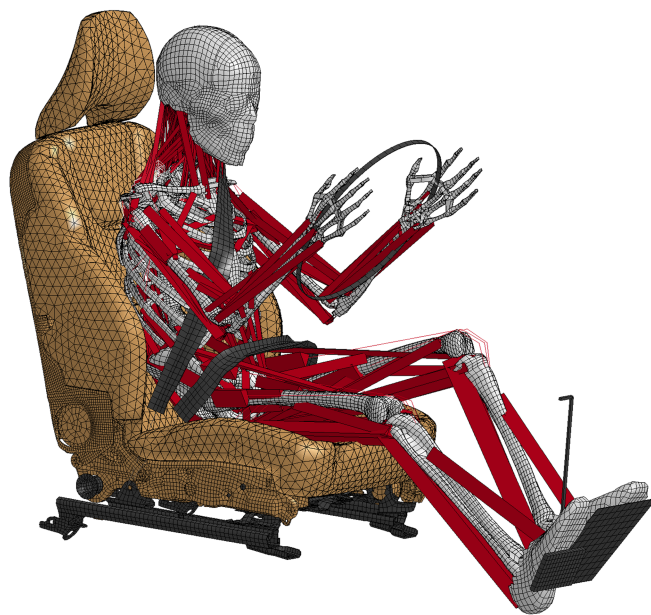


**Fig. 1** Active HBM in a driver braking simulation [13], picture adapted from [9]. The soft tissues not shown to disclose the musculoskeletal structure of the model.

## 2.2 Muscle Implementation

In the maintenance of a reference position, postural control, the human central nervous system employs a feedback control strategy, i.e. stabilizing muscle activations are generated in response to external perturbations [7]. This is implemented for the FE HBM through the use of seven proportional, integral, and derivative (PID) controllers, as generic representations of muscle spindle feedback and vestibular reflexive stabilization.

The controllers use the angle of the head, neck, lumbar spine, and humerus shoulder relative to the vertical axis, and for the elbows between the ulna and humerus, to generate the control signals  $u(t)$ . These are torque requests that are actuated by the muscles of each controlled body segment, which are grouped as either flexors or extensors, and each receive a muscle activation level  $Na(t)$  determined through closed loop control [9].

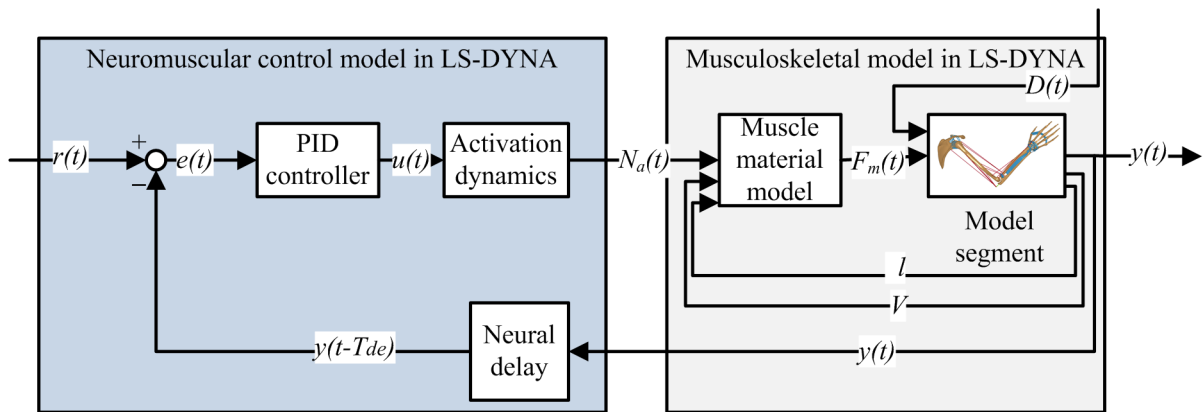


**Fig. 2** Schematic representation of the neuromuscular feedback control model used in the Active HBM. Adapted from Östh [9].

### 3 Applications

The Active HBM and the feedback control method has been applied to study the response of the upper arm to impact-like perturbations [12], for modeling of car passenger responses in medium braking interventions [11]. Furthermore, the Active HBM was used to study driver responses to unexpected autonomous braking interventions in combination with reversible pre-tensioned restraints[10] and in driver voluntary braking [13].

### 4 Ongoing Work

The next step in this work is to extend the controller implementation to simulate postural control in omnidirectional load cases such as autonomous steering and braking interventions. This task is not trivial as it is not as clear in these load cases, in particular for the neck and trunk, which muscles are agonists and which are antagonists. Current research on volunteer muscle activation patterns in multi-directional perturbations show that various neck muscles have distinct directional dependence and muscle specific contraction levels [8]). It might be a feasible solution to modify the control signal so as to regulate actuation by individual muscles rather than agonist and antagonist groups. To validate the response of the modified HBM, volunteer experiments will be performed to gather data on the human kinematic and muscle response during steering and combined steering and braking maneuvers.

### References

1. Chancey VC, Nightingale RW, Van Ee CA, Knaub KE, Myers BS (2003) Improved Estimation of Human Neck Tensile Tolerance: Reducing the Range of Reported Tolerance

- using Anthropometrically Correct Muscles and Optimized Physiologic Initial Conditions. *Stapp Car Crash Journal* 47:135–153.
2. Coelingh E, Jakobsson L, Lind H, Lindman M (2007) Collision Warning with Auto Brake – A Real-life Safety Perspective. *Proceedings of the 20th ESV Conference*; Lyon, France.
  3. de Jager MKJ (1996) *Mathematical Head-Neck Models for Acceleration Impacts*. Ph.D. Thesis; Eindhoven University of Technology, Eindhoven, the Netherlands.
  4. Deng YC, Goldsmith W (1987) Response of a Human Head/Neck/Upper-Torso Replica to Dynamic Loading – II. Analytical/Numerical Model. *Journal of Biomechanics* 20(5):487–497.
  5. Eidehall A, Pohl J, Gustafsson F, Ekmark J (2007) Toward Autonomous Collision Avoidance by Steering. *IEEE Transactions on Intelligent Transportation Systems* 8(1):84–94.
  6. Mages M, Seyffert M, Class U (2011) Analysis of the Pre-Crash Benefit of Reversible Belt Pre-tensioning in Different Accident Scenarios. *Proceedings of the 22nd ESV Conference*; Washington, D.C., USA.
  7. Massion J (1992) Movement, Posture and Equilibrium: Interaction and Coordination. *Progress in Neurobiology* 38:35–56.
  8. Ólafsdóttir JM, Brolin K, Blouin J-S, Siegmund GP (2014) Dynamic Spatial Tuning of Cervical Muscle Reflexes to Multi-directional Seated Perturbations. Submitted for publication.
  9. Östh J (2014) *Muscle Responses of Car Occupants: Numerical Modeling and Volunteer Experiments under Pre-Crash Braking Conditions*. Ph.D. Thesis, Chalmers University of Technology, Gothenburg, Sweden.
  10. Östh J, Brolin K, Bråse D (2014b) A Human Body Model with Active Muscles for Simulation of Pre-Tensioned Restraints in Autonomous Braking Interventions. *Traffic Injury Prevention*, in press. <http://dx.doi.org/10.1080/15389588.2014.931949>
  11. Östh J, Brolin K, Carlsson S, Wismans J, Davidsson J (2012b) The Occupant Response to Autonomous Braking: A Modeling Approach that Accounts for Active Musculature. *Traffic Injury Prevention* 13(3):265–277.
  12. Östh J, Brolin K, Happee R (2012a) Active Muscle Response using Feedback Control of a Finite Element Human Arm Model. *Computer Methods in Biomechanics and Biomedical Engineering* 15(4):347–361.
  13. Östh J, Eliasson E, Happee R, Brolin K (2014a) A Method to Model Anticipatory Postural Control in Driver Braking Events. *Gait and Posture*, in press. <http://dx.doi.org/10.1016/j.gaitpost.2014.07.021>
  14. Robbins DH, Schneider LW, Snyder RG, Pflug M, Haffner M (1983) Seated Posture of Vehicle Occupants. *Proceedings of the 27th Stapp Car Crash Conference*; San Diego, CA, USA.
  15. Schittenhelm H (2009) The Vision of Accident Free Driving – How Efficient are We Actually in Avoiding or Mitigating Longitudinal Real World Accidents. *Proceedings of the 21st ESV Conference*; Stuttgart, Germany.
  16. Schöneburg R, Baumann K-H, and Fehring M (2011) The Efficiency of PRE-SAFE® Systems in Pre-braked Frontal Collision Situations. *Proceedings of the 22nd ESV Conference*; Washington, D.C., USA.
  17. Toyota (2008) *Users' Guide of Computational Human Model THUMS® – AM50 Occupant Model: Version 3.0-080225*. Toyota Motor Corporation, Toyota Central Labs Inc, Toyota City, Aichi, Japan.

MS I.7: On the Route to “Autonomous Driving” -  
A New Quality of Passive Safety and Its Numerical  
Development & Assessment Tools

Authors: Mayer, Christian

## Abstract

Christian Mayer, Daimler AG, Sindelfingen

### On the route to „Autonomous Driving“ – A New Quality of Passive Safety and it's numerical development & assessment tools.

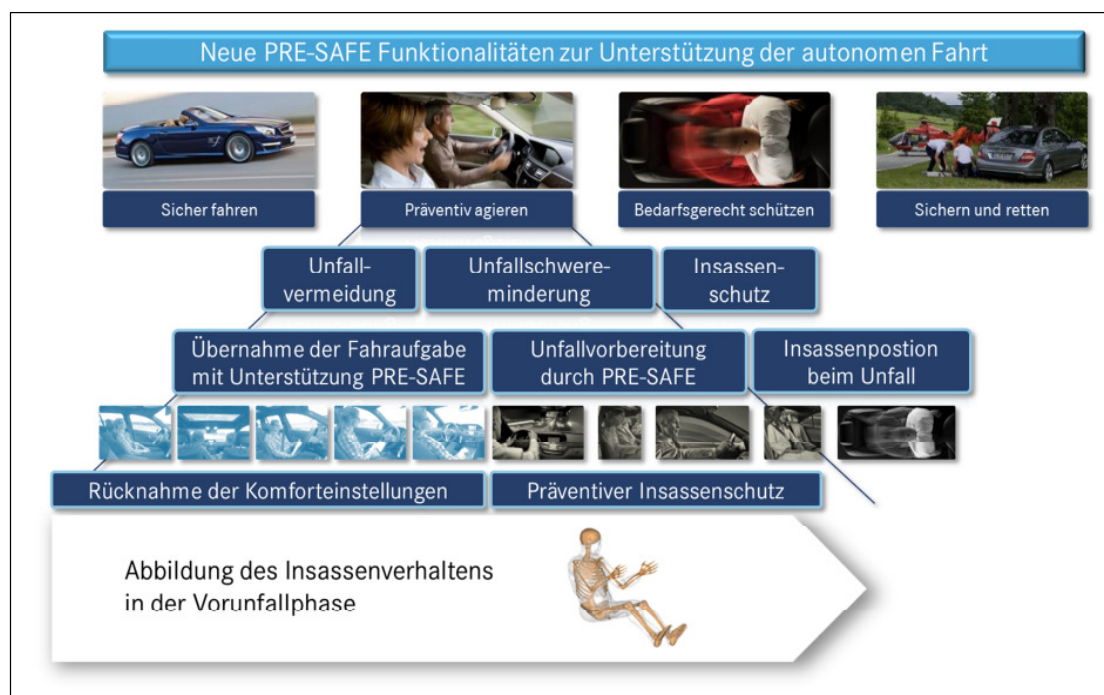
Currently the term „Autonomous Driving“ is often considered as a synonym for a successful implementation of “Vision Zero” or the “Vision of accident free driving”.

The first part of this paper will therefore discuss latest development and also the general framework of different levels of „Autonomous Driving“ and it's system characteristics. Also the human factor and the influence on vehicle and traffic safety are presented. We will show that on the one hand systems which will offer autonomous driving in certain areas and specific use cases are very close to market introduction and on the other hand accident free driving will still be a vision for more than one decade.



This means, that also Passive Safety and related systems and development tools will play an indispensable role within an Integrated Safety approach and the next vehicle generations.

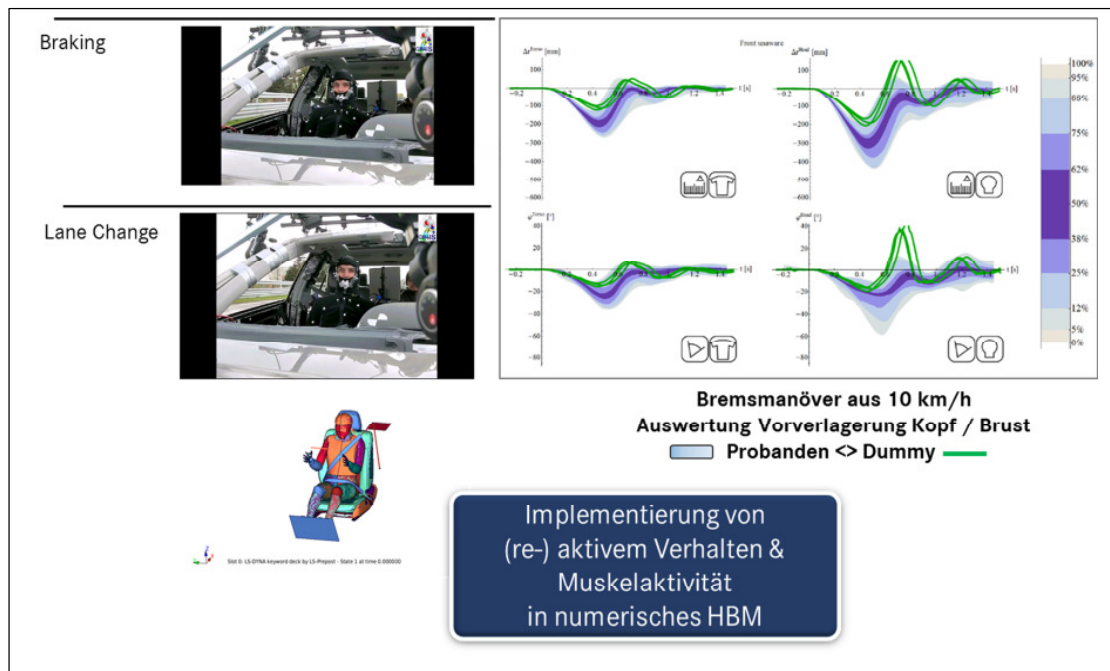
However, these new systems, technologies and driving conditions will open up also potential for a New Quality of Passive Safety. The pre-crash phase and related preventive safety systems and functions will be much more extended towards normal driving conditions respectively autonomous or semi-autonomous driving phases. Safety systems which will interact with the occupant in operating conditions “comfort”, “preventive” and finally “adaptive protection” characterize this new functionality. Especially this area and the needs for evaluation and development tools also for these systems opens up now new applications for numerical and virtual methods.



The second part of this paper will therefore highlight the – at times dramatic progress of these development tools in the field of vehicle and occupant safety within the last decade and will finally show, that now numerical human models offer greatest potential.

As a tool for the development and the assessment of automotive safety systems dummies, also known as ATD – Anthropomorphic Test Dummy/Device-, are used over the last 50 years – successively updated in terms of mechanical design, injury criteria and, most relevant, biofidelity. Meanwhile also numerical dummy models are

established and widely used. As a next step in the field of numerical simulation and “Virtual Testing”, and this is, of course, widely commented, numerical human models will be used as a supplemental tool to investigate the biomechanical impact of safety and restraint systems much more in detail. They, in principal, offer especially in the field of “real life safety” or “individual safety” potential for specific and dedicated improvement.



Application of these human models within the evaluation of a “New Quality of Passive Safety” demands now also the implementation of active muscles and human behavior. First results from related research projects and volunteer studies clearly show, that only virtual human models will offer potential for further development and applicability in this area.

**MS II Get in Shape - Algorithms  
and Data Structures for Complex,  
Changing Domains on Adaptive  
Cartesian Meshes**

MS II.1: Coupling and Boundary Constraints for a  
NURBS-Based Immersed Boundary Approach

Authors: Ruess, Martin, Guo, Yujie

---

# Coupling and boundary constraints for a NURBS-based immersed boundary approach

Martin Ruess · Yujie Guo

## 1 Introduction

Over the past few years isogeometric methods have emerged to be serious competitors in the various fields of numerical simulation, e.g., solid mechanics, fluid dynamics and various multi-physics problems. In comparison to established concepts based on finite elements, isogeometric methods have proven their superiority in many respects by a large number of benchmark problems and proofs-of-concepts, revealing an increased accuracy per degree-of-freedom and unique higher order approximation and continuity capabilities. Within this context, the initial idea to bridge the gap between computer aided geometric design (CAGD) and finite element analysis (FEA) by supporting a more tightly connected interaction of design and analysis faces the challenge of a simple and flexible model generation for complex industry-relevant problems, often assembled from numerous trimmed and non-conforming NURBS patches. The inherent need for multi-domain coupling in isogeometric methods has been addressed in a number of researches following several concepts adapted from, and often extending, domain decomposition methods developed in the framework of large-scale finite element simulations [1–3]. Considering the coupling of domains as a problem of mutually depending essential boundary condition problems, in general, allows the use of the same conceptual approach for a reliable enforcement of the constraints of both problems [3]. Besides a strong enforcement of boundary condition and coupling constraints, weak formulations have a long tradition commonly providing a much higher degree of flexibility in the geometric modeling process at the price of an increased complexity of the mathematical model and the associated solution process.

---

M. Ruess, Y. Guo  
Aerospace Structures & Computational Mechanics  
Faculty of Aerospace Engineering  
Delft University of Technology, The Netherlands  
Tel.: +31-15-278-1629  
E-mail: {m.ruess,y.guo}@tudelft.nl



**Fig. 1** Geometry principles of isogeometric analysis and the finite cell approach (left), composed adaptive numerical integration scheme for immersed boundaries (right).

With this contribution we give an overview about recent developments for the weak enforcement of boundary conditions and coupling constraints in isogeometric methods [5,6]. In particular, we focus on the coupling of thin-walled shell models with partly immersed boundaries and/or models assembled from trimmed and non-conforming patches, cf Figure 1. The trimming problem is one of the central problems in isogeometric analysis which requires a powerful analysis concept to avoid further domain decomposition or re-parametrization.

We propose a fictitious domain extension to isogeometric analysis based on the principles of the finite cell method (FCM), the NURBS-version FCM [7, 4]. The main ingredients of the FCM include adaptive integration towards the immersed physical boundary of the model, the use of higher order NURBS basis functions and the weak enforcement of coupling and boundary constraints. Originally developed for embedding domains on Cartesian grids the presented NURBS-version FCM exploits the smoothness and exactness of the computer-aided-design (CAD) based geometric model description.

We will highlight the challenges, the potential and the limitations of the NURBS-version FCM for thin-walled structures and Kirchhoff-Love shell models. We will further demonstrate a Nitsche-based extension of the equations governing the elasticity problem that turns out to be well-suited for both, weakly enforced essential boundary conditions and weakly enforced coupling constraints. We will show that the adaptive integration scheme is a suitable and powerful concept to tackle any geometric complexity of the conforming and non-conforming trimmed patches at reasonable costs. We study the accuracy, reliability and convergence properties of the proposed approach with several benchmark problems and examples from engineering practice.

## References

1. J. Dolbow and I. Harari. An efficient finite element method for embedded interface problems. *International Journal for Numerical Methods in Engineering* 78, pp. 229–252, 2009.
2. S. Kollmannsberger, A. Reali, A. Özcan, M. Ruess, J. Baiges and E. Rank. Parameter free weak boundary and coupling conditions for IGA. In: Proc. III South-East European Conf. On Comput. Mechanics, Kos, Greece, 2013.

3. M. Ruess, D. Schillinger, A.I. Özcan and E. Rank. Weak coupling for isogeometric analysis of non-matching and trimmed multi-patch geometries, *Computer Methods in Applied Mechanics and Engineering* 269, pp. 46–71, 2014.
4. D. Schillinger and M. Ruess. The Finite Cell Method: A review in the context of higher-order structural analysis of CAD and image-based geometric models. *Archives of Computational Methods in Engineering*, DOI:10.1007/s11831-014-9115-y, 2014.
5. M. Ruess, D. Schillinger, Y. Bazilevs, V. Varduhn and E. Rank. Weakly enforced essential boundary conditions for nurbs-embedded and trimmed nurbs geometries on the basis of the finite cell method. *International Journal for Numerical Methods in Engineering* 95(10), pp. 811–846, 2013.
6. Y. Guo and M. Ruess. Nitsches Method for a Blended Coupling of Isogeometric Shell Structures. submitted to *Computer Methods in Applied Mechanics and Engineering*, 2014.
7. E. Rank, M. Ruess, S. Kollmannsberger, D. Schillinger and A. Dster. Geometric modeling, isogeometric analysis and the finite cell method. *Computer Methods in Applied Mechanics and Engineering* 249252, pp. 104–115, 2012.

MS II.2: A Task-Based Finite Cell Implementation  
on Xeon Phi

Authors: Weinzierl, Tobias

---

# A Task-based Finite Cell Implementation on Xeon Phi

Tobias Weinzierl

## 1 Introduction

Spacetrees as generalisation of the quadtree/octree concept [6,8] have established themselves as mature paradigm to realise structured adaptive mesh refinement (AMR) codes in high performance computing architectures. Fictitious domain methods such as the finite cell method (FCM) [5] have established themselves as mature paradigm to realise solvers for partial differential equations (PDEs) on complicated domains. Both rely on a Cartesian paradigm. One strength of FCM is that it overcomes the  $\mathcal{O}(h)$  accuracy constraint of Cartesian grids that are not aligned to the boundary. At the same time, it preserves the simplicity of the Cartesian mesh. One strength of spacetrees is that they overcome administrative overhead for adaptive grids that change throughout the solution. At the same time, they preserve the simplicity of recursive Cartesian representations. Consequently, a merger is a promising approach to bridge the gap from PDEs on complicated domains to supercomputers for elliptic problems discretised with higher order finite elements.

Our work relies on some recently published techniques embedding small regular Cartesian meshes into a spacetree [7]. These patches are surrounded by a ghost layer. This allows computational kernels to evaluate shape functions per patch without interfering with neighbouring patches once they are properly initialised. The patches plus the kernels define computational tasks. Within the patches, FCM integration can replace unmodified B-spline integration straightforwardly. Our work briefly discusses a choice of minimal patch and ghost layer sizes for a given B-spline order to preserve the no-overhead characteristics of spacetree codes. Starting from such a basis, we focus on matrix-free matrix-vector product evaluations, i.e. matrix-vector product evaluations that can be done in one grid sweep and do not rely on an explicit assembling of a system matrix. This is an important building block of many iterative solvers such as multigrid or Krylov methods; in

---

Tobias Weinzierl  
School of Engineering and Computing Sciences, Durham University, Stockton Road, Durham  
DH13LE, Great Britain  
E-mail: tobias.weinzierl@durham.ac.uk

particular if the solver is very sophisticated and requires only few matrix-vector evaluations to convergence or before the grid is refined. Four algorithmic aspects dominate our work.

First, we discuss a generalisation of the bi-subdivision property of B-splines to arbitrary partitioning factor. It is well-known that a B-spline of order  $p$  on a mesh of mesh width  $h$  can be constructed from two B-splines of order  $p - 1$  on a mesh of mesh width  $h$  in  $1d$ . Higher dimensions then result from tensor products. It is also well-known that a B-spline of order  $p$  on a mesh of mesh width  $h$  can be constructed from B-splines of order  $p$  on a mesh of mesh width  $h/2$  [1]. While the formal proof of the extension is basically a technical exercise, arbitrary subdivision numbers allow us to formalise Cartesian embeddings on the spacetree that break the  $k$  restriction for a spacetree relying on  $k$ -partitioning. We can choose Cartesian embeddings per grid level flexibly and thus tailor our grid layout to problem needs.

Second, we discuss an application of the MLAT/HTMG idea [2,3] to matrix-free B-spline/spacetree finite element spaces. MLAT reduces an AMR matrix-vector product to simple  $d$ -linear interpolation and injection plus compute kernels acting on regular Cartesian subgrids, i.e. patches. It relies on overlapping nested grids, kind of a generating system [3], which picks up an inherent property of spacetrees. With MLAT, the major building block of an AMR code remains the regular grid matrix-vector kernel, augmented by a second kernel realising the  $d$ -linear interpolation according to the B-spline subdivision properties discussed. The scheme thus is even simpler than similar techniques proposed [1,4,5]. An application of this technique yields plain matrix-free AMR.

Third, we discuss the interplay of a proper Cartesian patch size choice with current hardware architectures. Following [7], we reiterate that the smaller the embedded grids the better the ratio of solution accuracy to memory footprint. However, small Cartesian grids do not anticipate recent hardware trends. Manycore architectures in particular require high arithmetic intensity on big regular data structures. And the overhead to administer floods of very small tasks is in general not neglectable. While high order B-splines yield high arithmetic intensity, the architectures' hunger for big data structures contradicts a low global memory footprint. We thus pick up the block fusion concept from [7] and tailor it to our FCM kernels. A tailoring allows us to specify our matrix-free solver on very small Cartesian patches. This yields a good accuracy to memory ratio. In subregions of the computational domain that are resolved by regular spacetree grids, i.e. by assemblies of patches of the same resolution, the algorithm automatically fuses these patches into a bigger patch and thus yields a higher throughput. In terms of multicore tasks, tasks are merged.

Finally, we discuss the interplay of FCM's adaptive integration and multicore architectures within the proposed spacetree paradigm. We start from the observation that a spacetree yields the required adaptive integration grid, if we allow spacetree levels that are refined further than the actual compute grid. The compute grid, i.e. the patches, is embedded into the spacetree and do not necessarily reside exclusively on the spacetree leaves anymore. Furthermore, we observe that iterative schemes do not necessarily require perfectly integrated operators—they may start with an approximation of the operator. While multiple iterative sweeps are performed, we then can improve the operator as well. As a consequence, we propose a temporarily overlapping integration/matrix-vector evaluation scheme where a spacetree traversal on the one hand evaluates the matrix-vector prod-

uct. On the other hand, it spawns additional tasks working on the same meshing paradigm. These tasks integrate the operator better and better and feed the result of this improved integration back into subsequent matrix-vector evaluations.

## References

1. P.B. Bornemann and F. Cirak. A subdivision-based implementation of the hierarchical b-spline finite element method. *Computer Methods in Applied Mechanics and Engineering*, 253:584–598, 2013.
2. A. Brandt. Multi-level adaptive technique (mlat) for fast numerical solution to boundary value problems. In *Proceedings of the Third International Conference on Numerical Methods in Fluid Mechanics*, number 18 in Lecture Notes in Physics, pages 82–89, 1973.
3. M. Griebel. *Zur Lösung von Finite-Differenzen- und Finite-Element-Gleichungen mittels der Hierarchischen-Transformations-Mehrgitter-Methode*, volume 342/4/90 A. SFB-Bericht, Dissertation, Technische Universität München, 1990.
4. E. Rank. Adaptive remeshing and h-p domain decomposition. *Comput. Methods Appl. Mech. Eng.*, 101(1-3):299–313, 1992.
5. D. Schillinger and M. Ruess. The finite cell method: A review in the context of higher-order structural analysis of cad and image-based geometric models. *Archives of Computational Methods in Engineering*, pages 1–65, 2014.
6. T. Weinzierl. *A Framework for Parallel PDE Solvers on Multiscale Adaptive Cartesian Grids*. Verlag Dr. Hut, 2009.
7. T. Weinzierl, M. Bader, K. Unterwiesing, and R. Wittmann. Block fusion on dynamically adaptive spacetime grids for shallow water waves. *Parallel Processing Letters*, 2014. accepted.
8. T. Weinzierl and M. Mehl. Peano – A Traversal and Storage Scheme for Octree-Like Adaptive Cartesian Multiscale Grids. *SIAM Journal on Scientific Computing*, 33(5):2732–2760, 2011.

MS II.3: Mesh-to-Particle Coupling for Hybrid  
Molecular-Continuum Simulations

Authors: Neumann, Philipp

---

# Mesh-to-Particle Coupling for Hybrid Molecular-Continuum Simulations

Philipp Neumann

**Abstract** We revise the design of our macro-micro-coupling tool for hybrid molecular-continuum simulations in fluid dynamics. A particular focus lies on the application of the Cartesian grid data structure which is used for data transfer between the continuum and the molecular dynamics (MD) solver. We demonstrate our approach in a coupled scenario using the spatially adaptive Lattice Boltzmann framework waLBerla and the MD package LAMMPS.

**Keywords** Mesh-to-Particle · Molecular Dynamics · Lattice Boltzmann · Coupling · Macro-Micro-Coupling Tool · Molecular-Continuum

## 1 Introduction

Molecular-continuum simulations are a promising approach e.g. in fluid dynamics to allow for virtual multi-resolution of computational domains. The computational domain is split into a large region where a coarse-grained, e.g. mesh-based Lattice Boltzmann, fluid solver is applied and a (typically) small, fine-grained region where the fluid flow is described by means of molecular dynamics (MD). Both coarse-grained and MD simulation are coupled based on mass, momentum and/or energy transfer. One particular issue in molecular-continuum simulations is constituted in switching between particle- and mesh-based perspectives.

In the following, we revise the macro-micro-coupling tool [1,2] which is meant to support the developers of new coupling algorithms. In Section 2 we describe the coupling tool with particular focus on the underlying data structures and the mapping from mesh- to particle-based descriptions. We

---

Philipp Neumann  
Boltzmannstr. 3  
Tel.: +49-89-289-18600  
Fax: +49-89-289-18607  
E-mail: [neumanph@in.tum.de](mailto:neumanph@in.tum.de)

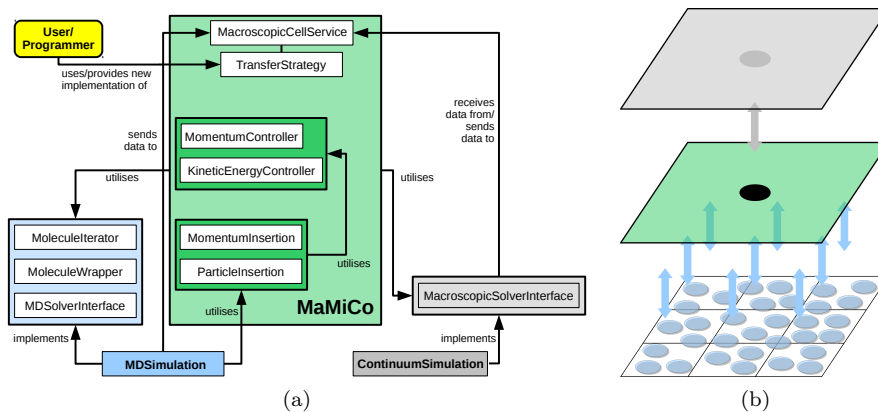


**Fig. 1** Design of the macro-micro-coupling tool (a) and mesh-to-particle mapping (b)[1].

subsequently provide results for hybrid Lattice Boltzmann-molecular dynamics (LB-MD) simulations in Sec. 3 using our coupling tool.

## 2 The Macro-Micro-Coupling Tool: Mesh-to-Particle Mapping

Fig. 1 gives an overview of the overall design and functionality of the macro-micro-coupling tool [1]. A Cartesian grid data structure is encapsulated inside the coupling tool and is used for the transfer of hydrodynamic quantities (such as mass or momentum) between macro- and microscopic simulations. The respective grid cells are referred to as *macroscopic cells* in the following. The data structure is designed such that the macroscopic cells always reside on the same process as the corresponding computational domain of the MD simulation.

This is advantageous for several reasons. First, linked cell data structures which are often used in MD simulations to speedup computations can immediately be re-used by the macro-micro-coupling tool, e.g. to iterate over the molecules (`MoleculeIterator`, see Fig. 1(a)). In this case, the size of the macroscopic cells (see green cell in Fig. 1(b)) needs to be a multiple of the linked cell size. Alternatively, a different `MoleculeIterator` (see Fig. 1(a)) can be defined by the MD simulation which allows for more flexibility in the choice of the cell size. Still, in order to yield consistent force evaluations or particle insertions, the macroscopic cell size needs to be larger than or equal to the cut-off radius used in the respective MD simulation.

Second, interpolation and sampling is established strictly locally on each MD process in parallel scenarios; currently, up to second-order interpolation is possible while retaining the strict locality [2]. If the macroscopic cells resided on other processes, significant communication overhead would be introduced. For example, in case of local sampling of mass or momentum from the molecule configurations inside each macroscopic cell, the sampled quantities would need to be sent to the respective process in each sampling step.

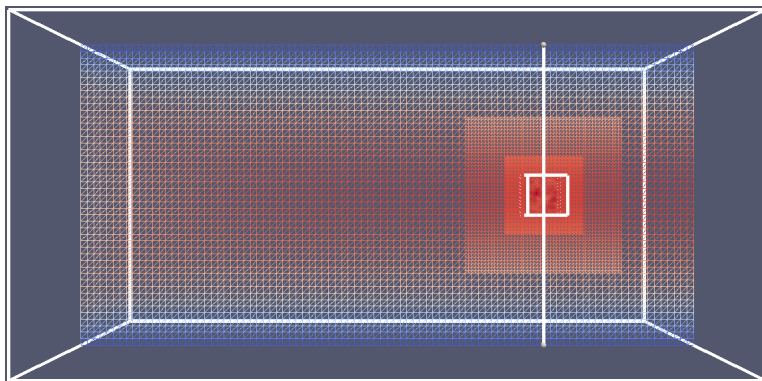


**Fig. 2** Velocity field in a channel flow experiment. The MD region is embedded near the outlet in the middle of the channel (white cubic box). Three levels of refinement are applied around the MD region. The white line through the center of the MD box corresponds to the cross-section for the evaluation of velocity profiles, see Fig. 3(a).

In order to have consistent data/molecule configurations on all processes, `synchronise()` methods need to be implemented by the `MDSolverInterface` (see Fig. 1(a)) and thus provided to the coupling tool. This step is strongly dependent from the MD implementation. For example, in case of particle insertion/deletion due to mass transfer, a synchronisation may be achieved by updating the molecule information close to the process boundaries on all processes of the MD simulation.

### 3 Molecular-Continuum Channel Flow Simulation

A coupling of the spatially adaptive Lattice Boltzmann framework `walBerla`<sup>1</sup> [3] and the MD package `LAMMPS`<sup>2</sup> [4] was established using the macro-micro-coupling tool. Figure 2 shows the setup of a channel flow scenario: the inner white cubic box is resolved by MD whereas the whole computational domain is covered and solved by the Lattice Boltzmann method; for details on the underlying steady-state coupling algorithm, see [2]. The parameters required for the coupling are listed in Tab. 1.

The velocity profiles of the pure LB and the LB-MD solution are shown in Fig. 3(a). They are in good agreement, with thermal fluctuations visible in the LB-MD solution. Strong scaling experiments for the underlying scenario were conducted on the bulldozer partition of the MAC-cluster<sup>3</sup>. Good scaling behaviour is observed for the coupling on up to 1024 cores, corresponding to 16 bulldozer nodes, cf. Fig. 3(b).

<sup>1</sup> [www.walberla.net](http://www.walberla.net)

<sup>2</sup> [lammps.sandia.gov](http://lammps.sandia.gov)

<sup>3</sup> For details on the hardware architecture, see [http://www.mac.tum.de/wiki/index.php/MAC\\_Cluster](http://www.mac.tum.de/wiki/index.php/MAC_Cluster).

Channel size	$1920 \times 960 \times 960$
MD domain size	$120 \times 120 \times 120$
MD model	Single-centered Lennard-Jones, $\epsilon = 1$ , $\sigma = 1$ , cut-off radius $r_c = 2.5$
Thermodynamic state	$(\rho, T) = (0.6, 1.8)$
Kinematic viscosity	$\nu = 1.5$
Relaxation time (BGK) in LB	$\tau = 0.65$
Time steps LB per coupling cycle	$n^{LB} = 80\,000$
Time steps MD per coupling cycle	$n^{MD} = 4\,000\,000$
Time step size in MD	$dt^{MD} = 0.002$
LB velocity relaxation factor, cf. Eq. (17.5) in [2]	$\lambda^{LB} = 0.1$
MD velocity relaxation factor, cf. Eq. (13.11) in [2]	$\lambda^{MD} = 0.05$
Coarsest mesh size in LB	$dx^{coarse} = 10.0$
Finest mesh size in LB	$dx^{fine} = 2.5$

**Table 1** Parameter settings for the LB-MD channel flow simulation.

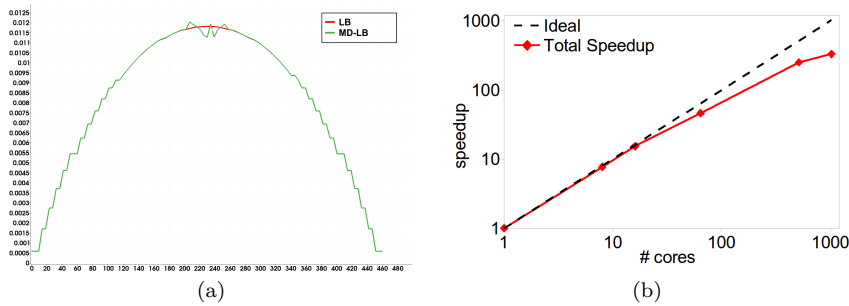


**Fig. 3** Velocity profile along the cross-section of the channel flow for pure LB and hybrid LB-MD simulation (a) and strong scaling of this scenario (b).

## Acknowledgement

This publication is partially based on work supported by Award No. UK-C0020, made by King Abdullah University of Science and Technology (KAUST). We thank Piet Jarmatz for his implementations within waLBerla and Florian Schornbaum for his support on technical aspects in waLBerla.

## References

1. P. Neumann and N. Tchipev, A Coupling Tool for Parallel Molecular Dynamics–Continuum Simulations, Proceedings of the International Symposium on Distributed and Parallel Computing 2012, 2012
2. P. Neumann. Hybrid Multiscale Simulation Approaches for Micro- and Nanoflows. PhD thesis, Dr. Hut, 2013
3. C. Feichtinger, J. Götz, S. Donath, K. Iglberger and U. Rüde, WaLBerla: Exploiting Massively Parallel Systems for Lattice Boltzmann Simulations, Parallel Computing: 241–260, 2009
4. S. Plimpton, Fast Parallel Algorithms for Short-Range Molecular Dynamics J. Comp. Phys. 117:1–19, 1995

MS II.4: Local Time-Stepping Along Coastlines for  
Tsunami Simulations

Authors: Unterweger, Kristof, Wittmann, Roland

---

# Local Time-Stepping Along Coastlines For Tsunami Simulations

Kristof Unterweger · Roland Wittmann

**Abstract** To cope with the different occurring scales in Tsunami simulations—the global propagation of the wave and the local effects of the coastline impact—often adaptive mesh refinement (AMR) is used. Explicit time integration demands here usually for finer time steps in the finer parts of the grid compared to coarser parts. However, along coastlines, the shallower bathymetry leads to a slower wave speed and, hence, allows for larger time steps. Classical AMR schemes apply the same time step size for all cells of the same resolution. In this work a different approach for local time-stepping is tested in coastline scenarios to investigate the benefit of exploiting larger time step sizes in these areas.

**Keywords** Adaptive Mesh Refinement · Complex Geometries · Local Time-Stepping

## 1 Introduction

The simulation of large-scale waves is an important tool to get a better understanding of the creation, propagation, and effects of Tsunamis. For this purpose usually the shallow water equations are used that reduce the three-dimensional ocean domain to a two-dimensional representation which allows an efficient computation.

The propagation of a wave across an ocean takes place at scales of thousands of kilometers with wavelengths of up to several hundreds of kilometers. Hence, resolutions in the order of kilometers are sufficient to yield reasonable results. However, when a Tsunami wave approaches the coast and the water is getting shallower, the wavelength decreases down to hundreds of meters. For this wavelength, the bathymetry of the sea floor as well as the geometry of the coastline needs to be resolved with resolutions in the order of meters [1, 2]. This gap between resolutions is usually bridged by using dynamically adaptive grids.

---

Kristof Unterweger and  
Roland Wittmann  
Technische Universität München,  
Boltzmannstr. 3, 85748 Garching  
Tel.: +49-89-289 18 634  
Fax: +49-89-289 18 607  
E-mail: unterweg@in.tum.de, wittmanr@in.tum.de

## 2 Local Time-Stepping

Wave propagation simulations demand for explicit time integration schemes which are restricted in the allowed time step size due to stability. The maximally allowed time step size depends on the resolution: Fine cells lead to small time step sizes. Global time-stepping schemes apply the global minimum of the allowed time step size on every cell in the simulation. This provides a stable solution, but has two major disadvantages: The computational effort is much larger than necessary and the numerical diffusion is increased if the taken time step size for a cell is far below the maximally allowed time step size for this cell [3]. Local time-stepping schemes are used to circumvent these disadvantages, so to compute simulations faster and to yield a better solution.

### 2.1 Resolution-Based Local Time-Stepping

The classical approach for local time-stepping is based on the resolution of a cell or a certain part of the grid. That means, if a part of the grid (called subgrid in the following) is refined in space, the same refinement factor is applied to the time step size within this subgrid. One central aspect is that integer refinement factors are required between all cells. The general idea is described in [4] and the according implementation can be found in [5].

While this approach has been proven to work very well in many cases [6, 7], it has a significant drawback when applied on Tsunami simulations: As described before, in real-world scenarios the grid has a much finer resolution along the coastline, which leads to very fine timesteps in this area. However, the wave speed corresponds to  $\sqrt{gh}$ , where  $g$  is the gravitational constant and  $h$  is the water height above the sea floor. Hence, close to the coastline, where the grid has a fine resolution,  $h$  is relatively small and, thus, the wave speed becomes small as well. So, larger time steps would be possible here, compared to the time step size stemming from the resolution-based local time-stepping.

In a mere resolution-based approach, this can only be treated by choosing different refinement factors for time and space [2, 8]. However, these refinement factors apply globally for the given resolution. So, a careful selection of the refinement factors throughout the grid's hierarchy is required, which also depends heavily on the used refinement criterion and, thus, on the shape of the coastline's geometry.

### 2.2 Stability-Based Local Time-Stepping

We proposed a different approach to local time-stepping in [9] and implemented this scheme in the software PeanoClaw<sup>1</sup>. Here, the time step is not chosen with respect to the local resolution but the actual stability criterion for the numerical scheme is evaluated for a certain subgrid. Hence, a time step size is taken so that a certain CFL number is reached.

The main difference to the classical approach is that the refinement factors in time are decoupled from the refinement factors in space and that the temporal refinement factors do not have to be integer ratios. Furthermore, cells with the same resolution do not have to take the same time step size, but can take time steps of arbitrary length. That means, that parts of the grid can advance with a different time resolution than others, independent of the actual spatial resolution. This allows Tsunami simulations to use a larger time step size for a fine resolution if the stability criterion allows this due to a lower wave speed.

<sup>1</sup> <https://github.com/www5scs/peanoclaw>

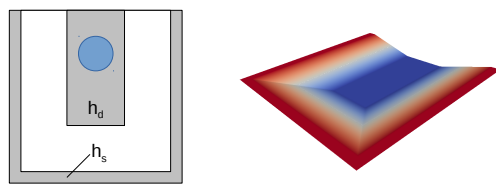


**Fig. 1** A schematic view of the scenario is given on the left. Here, the gray areas represent areas of constant depth ( $h_d$ : deep area,  $h_s$ : shallow area), while the blue circle represents the radial breaking dam. On the right the bathymetry is shown in a perspective view. Colors represent the depth.

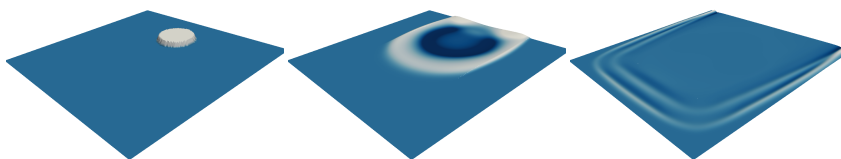


**Fig. 2** The scenario in the initial state (left), during the deep-water propagation of the waves (middle), and towards the end of the simulated time (right).

### 3 Benchmark Scenario

To show the benefit of the stability criterion-based local time-stepping, an artificial ocean scenario is used: The simulated domain contains a deep water area with constant depth ( $h_d = 100m$ ) and a shallow water ( $h_s = 10m$ ) area representing the coastal region along three of the four sides of the domain. There are linear ramps as transition between the deep and the shallow part as can be seen in Figure 1. The domain size is  $1,000 \times 1,000$  meters.

The initial ocean surface has the same absolute height throughout the domain but for a cylindrical area that is elevated above the rest of the domain. That means, the scenario represents a classical radial breaking dam with a piece-wise linear bathymetry. It is simulated until the first wave front hits the coastline boundary (see Figure 2).

### 4 Results

The described scenario is simulated with three different grids. In all cases, every cell is flagged for refinement that represents the shallow part of the domain. The coarsest cells always have a size of about  $6 \times 6$  meters, while the spatial refinement factors between two grid levels is always 3. So, for one level of adaptivity the fine cells have a size of about  $2 \times 2$  meters, for two levels of adaptivity about  $0.69 \times 0.69$  meters, and for three levels about  $0.23 \times 0.23$  meters. The cells are assembled into subgrids of  $18 \times 18$  cells each.

For every grid  $g$  the number of performed cell updates  $c_g$  is measured and the theoretical number of cell updates required by an optimal resolution-based AMR simulation  $r_g$  is computed. The potential speedup for grid  $g$  is computed as  $s_g = \frac{r_g}{c_g}$ . Figure 3 shows these ratios of cell updates. The number of cell updates can be reduced by a factor of 1.8 for one level of adaptivity, by a factor of 2.8 for two, and by a factor of 4 for three levels of adaptivity.

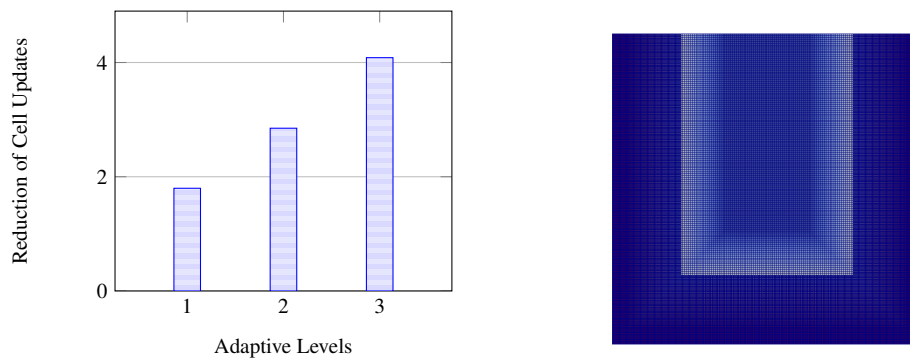


**Fig. 3** The speedup achieved with different adaptivity patterns (left) and the resulting grid with one level of adaptivity (right).

## 5 Conclusion

The results are artificial as the used scenario does not resemble a real geometry and the potential speedup is determined against a theoretical model. Additionally, the results were found to be sensitive with respect to the scenario setup. However, the estimation of the cell update reduction ratio was done conservatively and show a significant potential for improving the simulation performance. Furthermore, the simulated scenario only represents a local wave propagation system, were the ratio between shallowest and deepest region is only ten. In global systems, the differences in depth and, thus, wave speeds can be significantly larger.

For massive parallel simulations, the stability-based approach reduces the global dependency of the time-stepping scheme. This can reduce the global communication demand and, hence, may result in better scalability. However, investigations on real-world setups would be required to get reliable information.

## References

1. Z. Kowalik, *Introduction to Numerical Modeling of Tsunami Waves* (Institute of Marine Science, University of Alaska, Fairbanks, 2012)
2. D.L. George, Augmented riemann solvers for the shallow water equations over variable topography with steady states and inundation. Ph.D. thesis, University of Washington (2006)
3. J.J. Quirk, S. Karni. On the dynamics of a shock-bubble interaction (1994)
4. M.J. Berger, P. Colella, *Journal of Computational Physics* **82**, 64 (1989)
5. M.J. Berger, R.J. LeVeque, *SIAM J. Numer. Anal.* **35**, 2298 (1998)
6. K.T. Mandli, C.N. Dawson, *Ocean Modelling* **75**(0), 36 (2014). DOI <http://dx.doi.org/10.1016/j.ocemod.2014.01.002>. URL <http://www.sciencedirect.com/science/article/pii/S1463500314000031>
7. M.J. Berger, D.L. George, R.J. LeVeque, K.T. Mandli, *Advances in Water Resources* **34**(9), 1195 (2011). DOI <http://dx.doi.org/10.1016/j.advwatres.2011.02.016>. URL <http://www.sciencedirect.com/science/article/pii/S0309170811000480>. New Computational Methods and Software Tools
8. R.J. LeVeque, in *Proc. Int. Cong. Math.* (2006), pp. 1227–1254. URL <http://faculty.washington.edu/rjl/pubs/icm06>
9. K. Unterweger, T. Weinzierl, D.I. Ketcheson, A. Ahmadi, Technical Report (2013)

MS II.5: Spacetree-Based Adaptive Meshing of  
Complex Geometries

Authors: Wittmann, Roland, Unterweger, Kristof

---

# Spacetree-based adaptive meshing of complex geometries

Roland Wittmann · Kristof Unterweger

**Abstract** We study adaptive mesh refinement in flood simulations where we have to deal with complex geometries like terrain data or buildings. For this, we use both structured and unstructured meshes in a geometric multigrid scheme to allow efficient and accurate simulations on large scenarios. We present strategies for data exchange between different mesh types and different grid levels while maintaining computational efficiency.

**Keywords** adaptive mesh refinement · domain decomposition · geometric multigrid · mesh coupling

Adaptive mesh refinement (AMR) is a valuable technique to reduce computational effort and preserve numerical accuracy. It yields regions with a rather high cell density, where accuracy demands for it, while other areas of the computational domain hold a coarse mesh. Furthermore, if areas of high refinement change dynamically over time, the assignment of computational resources has to be adopted to the new mesh constellations permanently. A good example for codes benefiting from AMR are hyperbolic equation solvers: Regions of the computational domain where the wave runs through require high refinement and hence a lot of computational resources. In contrast, the remaining regions with low activity require far less computational work. Ideally, most resources should be assigned at the wave front throughout the whole simulation while keeping the amount of work balanced to some extent on all involved resources. In Figure 1, we simulate rainfall with an intensity of 50 mm/h in the Mecca mountain area to determine which areas might be affected by flooding. We are using the FullSWOF2D[2] solver package, which solves the shallow water equations with added rainfall and friction terms. Additionally, the solver was specifically designed for simulating rainfall in agricultural areas. There-

---

Roland Wittmann\* - Kristof Unterweger  
Boltzmannstr. 3, D-85748 Garching  
Tel.: +49-89-18626  
Fax: +49-89-18607  
E-mail: wittmanr@in.tum.de - unterweg@in.tum.de

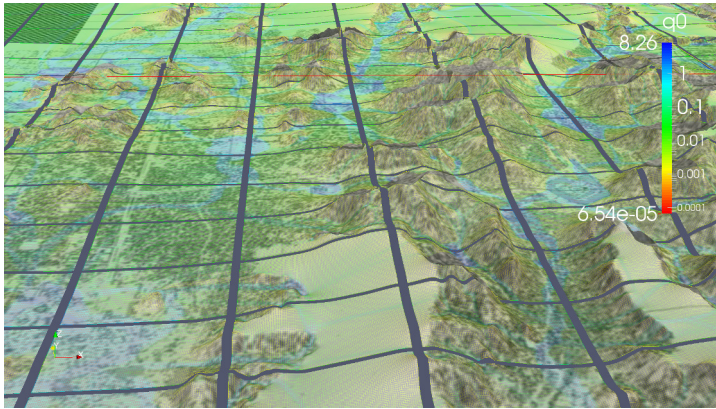


**Fig. 1** Rainfall simulation with an intensity of 50 mm/h in the Mecca mountain area.

fore, it is able to handle dry-wetting effects which is a very essential feature for our scenario.. The computational domain for the Mecca mountain area has a size of 16 km x 9 km and our topography dataset has a resolution of 1m. The corresponding dataset was kindly provided by the Visual Computing Center at KAUST. Due to the size of the domain and due to the fact that the FullSWOF2D solver software was designed for regular grids, we integrated this solver into PeanoClaw[6]. This allows us to enhance the original solver by adaptive local time stepping and we also get free parallelism through the Peano framework[8] on which PeanoClaw is based. The basic idea is to decompose a domain into a hierarchy of sub-domains, where each sub-domains is made of a fixed number of rectilinear cells. The interfaces between these sub-domains are then handled through exchange of halo-layers as well as through spatial and temporal interpolation or extrapolation. However, the solver cannot simply use the dataset because we are dealing with different mesh types: Both the FullSWOF2D solver as well as PeanoClaw expect a rectilinear mesh while the terrain dataset is a triangular mesh, which was generated through a restricted quadtree triangulation method. An overview for quadtree based triangulations can be found for instance in [4]. Though it is easily possible to use interpolation and sampling techniques to map grid points from one mesh type to the other, this approach ignores the valuable properties like the hierarchical structure of the underlying triangular mesh. Moreover, in this particular scenario we are not only dealing with terrain data but also with buildings which are given by models, created by Computer-aided design, or point cloud data. While there might not be a notable difference for the solution when we use a rectangular approximation for the terrain surface due to rather large scales, there is a notable difference for buildings with complex surfaces, which have to be represented as accurately as possible in the simulation. Even if we would represent it with a very fine mesh, this would also decrease our possible time steps due to the CFL condition of the underlying solver. Hence, our objective is to represent complex geometries and terrain data as accurately as possible

while using a mesh which is as coarse as possible. Therefore, we are able to benefit from adaptive local time stepping, which in turn allows us to run our simulations in a time-efficient manner.

In our approach, we extend the PeanoClaw domain concept in two ways: First, we implement support for arbitrary coordinate frames as proposed by Chen et al[1]. The authors present a method for coupling multi-block domains through a common parent block, which has a coordinate frame on its own. It is possible to translate data between different coordinate frames without knowing the coordinate frames of the neighboring domains. However, arbitrary coordinate frames may still lead to domain interfaces which might not fit exactly. To solve this issue, we adapt a method proposed by Nguyen et al[3]. Using this method, the authors are able to couple two and three dimensional non uniform rational b-splines (NURBS) patches, though they have different mesh properties at the patch interfaces. Second, we present different strategies how to handle the data exchange between structured and unstructured meshes, based on work of Turnbull et al[5], and how to switch between these two mesh types in an AMR context. Our goal is to maximize the number of sub-domains with structured meshes while limiting the number of unknowns per sub-domain to benefit from cache-efficiency, as shown in[7]. All together, these concepts fit naturally into the geometric multigrid context of the Peano framework..

Finally, we will show the effectiveness and flexibility of our approach with respect to our large-scale flood simulation scenario with complex geometries.

## References

1. Chen, W., Lien, F., Leschziner, M.: Local mesh refinement within a multi-block structured-grid scheme for general flows. *Computer Methods in Applied Mechanics and Engineering* **144**(34), 327 – 369 (1997). DOI [http://dx.doi.org/10.1016/S0045-7825\(96\)01187-5](http://dx.doi.org/10.1016/S0045-7825(96)01187-5). URL <http://www.sciencedirect.com/science/article/pii/S0045782596011875>
2. Delestre, O., Darboux, F., James, F., Lucas, C., Laguerre, C., Cordier, S.: FullSWOF: A free software package for the simulation of shallow water flows. *ArXiv e-prints* (2014)
3. Nguyen, V.P., Kerfriden, P., Brino, M., Bordas, S.P., Bonisoli, E.: Nitsches method for two and three dimensional nurbs patch coupling. *Computational Mechanics* **53**(6), 1163–1182 (2014)
4. Pajarola, R.: Overview of quadtree-based terrain triangulation and visualization. Department of Information & Computer Science, University of California, Irvine (2002)
5. Turnbull, M., Borthwick, A., Taylor, R.E.: Wavestructure interaction using coupled structuredunstructured finite element meshes. *Applied Ocean Research* **25**(2), 63 – 77 (2003). DOI [http://dx.doi.org/10.1016/S0141-1187\(03\)00032-4](http://dx.doi.org/10.1016/S0141-1187(03)00032-4). URL <http://www.sciencedirect.com/science/article/pii/S0141118703000324>
6. Unterweger, K., Weinzierl, T., Ketcheson, D.I., Ahmadi, A.: PeanoClaw - a functionally-decomposed approach to adaptive mesh refinement with local time stepping for hyperbolic conservation law solvers. Tech. Rep. TUM-I1332, Technische Universität München (2013)
7. Weinzierl, T., Wittmann, R., Unterweger, K., Bader, M., Breuer, A., Rettenberger, S.: Hardware-aware block size tailoring on adaptive spacetime grids for shallow water waves. (2014)
8. Weinzierl, T., et al.: Peano—a Framework for PDE Solvers on Spacetree Grids (2012). URL <http://www.peano-framework.org>. [Http://www.peano-framework.org](http://www.peano-framework.org)

MS II.6: Multi-Scale High-Performance Fluid Flow  
Simulations Through Porous Media

Authors: Perović, Nevena, Frisch, Jérôme, Mundani, Ralf-Peter, Rank, Ernst, Salama, Amgad, Sun,  
Shuyu

---

# Multi-Scale High-Performance Fluid Flow Simulations Through Porous Media

Nevena Perović<sup>1</sup> · Jérôme Frisch<sup>1</sup> ·  
Ralf-Peter Mundani<sup>1</sup> · Ernst Rank<sup>1</sup> ·  
Amgad Salama<sup>2</sup> · Shuyu Sun<sup>2</sup>

## 1 Introduction

In petroleum production and engineering, the subsurface formation that surrounds the well screen gets, in many cases, deteriorated with time in relation to its hydraulic conductivity. As a consequence, well production declines with time and this limits to a large extent its efficiency. Since well installation is a major production operation that usually requires a large capital, it is always important to revive the use of the installed wells rather than abandoning them. One of the methods that have been proposed to alleviate this problem is to inject chemicals that dissolve, in a sense, the formation materials and open channels to ease the flow of the oil. Most of the research work that has been reported on this topic appeals to experimental correlations that are to a large extent specific to certain types of porous media (e. g., granular, consolidated porous media) and therefore not applicable to the wide range of soil material types. In this work, we provide an alternative route, thanks to the advancement in the CFD simulations of complex pore scale structures. The idea is to update the permeability based on pore scale simulations rather than based on experimental correlations. The main challenge beside coupling two different spatial scales is to handle the differences in time scales required to perform porous media simulations (which are relatively fast) versus the time required to update the permeability based on CFD simulations (which are relatively slow). This goal can be achieved through the generation of offline database data of permeability values with a direct access from a porous media simulator, which triggers the transmission whenever a new calculated value is available.

---

<sup>1</sup> Chair for Computation in Engineering, Technische Universität München, Germany  
E-mail: nevena.perovic@tum.de (corresponding Author: Nevena Perović)

<sup>2</sup> King Abdullah University of Science and Technology, Saudi Arabia

In order to present our concept and some first findings, this extended abstract will shortly describe established and implemented governing laws and equations, the applied high-performance parallel computing techniques, and an application example enlightening the usability and efficiency of our implemented approach.

## 2 Groundwater Flow Through Porous Medium

### 2.1 Governing Equations

As stated before, two models are introduced in order to make such numerical simulations as efficient as possible – a macro model based on Darcy’s Law, described through the following equations:

$$\frac{Q}{A} = -\frac{k}{\mu} \cdot \frac{\Delta H_p}{L}, \quad K = \frac{k\rho g}{\mu}, \quad \text{and} \quad U_{darcy} = -K \frac{\Delta P}{L}, \quad (1)$$

where the ratio  $Q/A$  is often referred to as Darcy flux,  $U$  the fluid velocity  $\mathbf{u}$  [m/s],  $k$  denotes the permeability,  $\mu$  the dynamic viscosity of the fluid [kg/(m·s)],  $K$  the hydraulic conductivity [m/s],  $\Delta H_p$  [Pa] the pressure drop.

A second micro model is based on the Navier-Stokes conservation of mass and momentum equations that can be written in their vector forms as follows:

$$\nabla \cdot \mathbf{u} = 0, \quad (2)$$

$$\frac{\partial u_i}{\partial t} + \nabla \cdot (u_i \mathbf{u}) = \nabla \cdot (\nu \nabla u_i) - \frac{1}{\rho} \nabla \cdot (p \mathbf{e}_i) + b_i \quad (3)$$

for  $i \in \{x, y, z\}$ , where  $\mathbf{u} = (u_x \ u_y \ u_z)^T$  denotes the velocity field in [m/s] in the three spatial dimensions,  $t$  the current time of the simulation in [s],  $\nu$  the kinematic viscosity in [m<sup>2</sup>/s],  $\rho$  the density in [kg/m<sup>3</sup>] and  $p$  the pressure in [Pa].

Since the description of the governing equations is kept quite brief here, the interested reader is referred to standard literature such as [2] or [6] for further information on the derivation of both laws.

### 2.2 High-Performance Computing Concept for CFD Simulations

In order to solve the Navier-Stokes equations described previously, a discretisation of the physical domain is performed, resulting in a complex data structure that consists of sets of non-overlapping block-structured orthogonal Cartesian grids as depicted in figure 1. While the logical grid structure contains topological and geometrical information such as parentage, the data grids themselves contain the actual variables such as velocity, pressure, permeability, temperature etc. necessary for performing any numerical calculations.

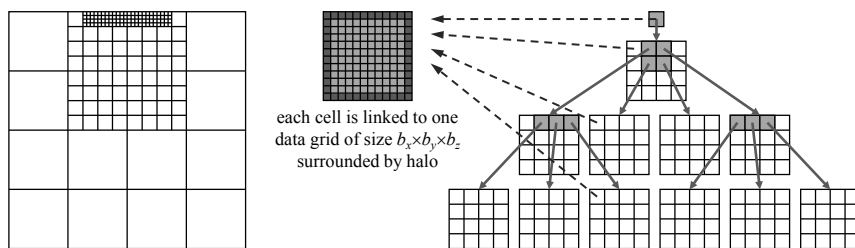


Fig. 1: Logical data structure layout in tree form (on right-hand side) and in overlaid grid form (on left-hand side). Each logical grid holds a pointer to a data grid containing the actual data surrounded by a halo of ghost cells (mid of picture). (Source: [4])

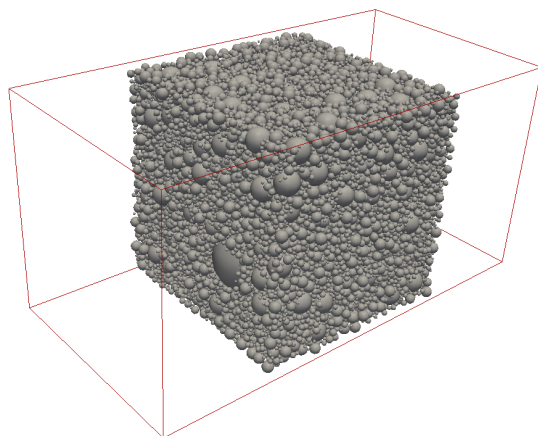


Fig. 2: Generated geometry based on sieve curve input data

Having generated such complex data structures, a fractional step method proposed by Chorin [1] is applied while using numerical discretisation based on a finite volume scheme in space and a second order explicit Adams-Bashforth method in time [5]. An efficient multi-grid like solver is applied in order to solve the arising pressure Poisson equation. For detailed information on the realisation of the structure or the MPI exchange routines in order to ensure proper communication, the reader is referred to [4] or [3] for instance.

### 3 Application Example

For the purpose of a CFD simulation on the micro scale, the physical domain of a porous medium is generated as a set of spheres of different diameter randomly positioned in a predefined domain and depicted in figure 2.

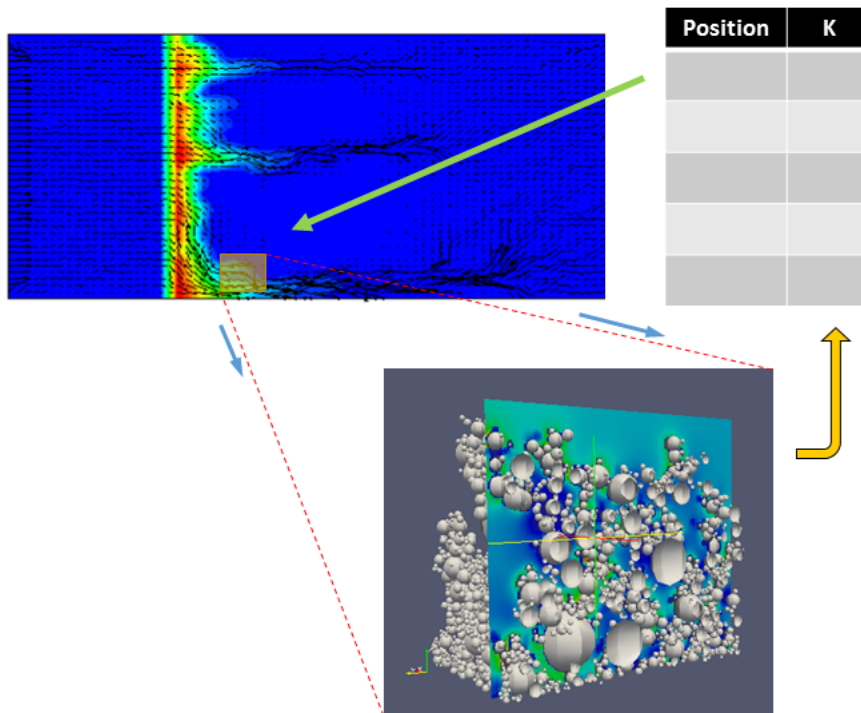


Fig. 3: Representation of an established iteration routine between two models of a different scale

Such domain represents just a small part of the domain (cf. figure 3) at which the macro-scale simulation is performed. In order to overcome the problem raised due to two different spatial and time scales, an offline database is generated and updated with values of permeability that are calculated on a micro level for several different scenarios. At this point, it is important to mention that coupling between these two models is exclusively done over the permeability value, as when the velocity and pressure values on the micro-scale are known, the permeability value can be calculated with almost no effort and upscaled for the macro-scale calculations. The later model is linked to the database, in such way to be able to take over calculated values of permeability for a specific case, whereas if the required value is not presented, to trigger a new micro-scale calculation.

Once the adequate coupling value is available, the fast macro-scale calculation of necessary amount of chemicals, inserted into the underground area in the vicinity of an existing well, can be performed. Within this calculation, the output parameters which describe the rate of soil degradation on a porous scale (also called, macro scale) are stored at some share memory medium. This medium can be a part of the database, but it might be also completely inde-

pendent of it. Having calculated this degradation value, a micro scale model is triggered once again to perform a completely new simulation, starting from discretisation of degraded geometry domain, setting all necessary boundary conditions, up to the calculation of new value of permeability, which will be then stored in the previously generated database.

Taking into account that Darcy equations are derived by means of volume averaging from the physical Navier-Stokes equations, the same principle is applied in order to achieve the permeability value at the micro scale that would fit into macro scale model. Having done that, additional analyses were performed, so to define a deviation of particular value of permeability at the micro scale comparing to the mean value calculated for the macro scale model. Such a deviation is a measure of how those two models can be coupled together and can be set to some specific value, depending on particular goals of research work.

**Acknowledgements** This publication is partially based on work supported by Award No. UK-c0020, made by King Abdullah University of Science and Technology (KAUST).

## References

1. Chorin, A.: Numerical solution of the Navier-Stokes equations. *Mathematics of Computation* **22**(104), 745–762 (1968)
2. Ferziger, J., Perić, M.: *Computational Methods for Fluid Dynamics*, 3rd rev. edn. Springer (2002)
3. Frisch, J., Mundani, R.P., Rank, E.: Parallel multi-grid like solver for the pressure Poisson equation in fluid flow applications. In: *Proc. of the IADIS International Conference - Applied Computing*, pp. 139–146. Fort Worth, Texas, USA (2013)
4. Frisch, J., Mundani, R.P., Rank, E.: Adaptive multi-grid methods for parallel CFD applications. *Scalable Computing: Practice and Experience* **15**(1), 33–48 (2014)
5. Schwarz, H.R., Köckler, N.: *Numerische Mathematik*, 8th rev. edn. Vieweg + Teubner (2011)
6. Vadlamudi, R.: *Darcy's Law*. University of Central Oklahoma (1997)

**MS III Towards Exascale  
Simulations and Applications**

MS III.1: Towards a Fault-Tolerant, Scalable  
Implementation of GENE

Authors: Hinojosa, Alfredo Parra, Heene, Mario, Kowitz, Christoph, Pflüger, Dirk

---

# Towards a fault-tolerant, scalable implementation of GENE

Alfredo Parra Hinojosa · Mario Heene ·  
Christoph Kowitz · Dirk Pflüger

**Abstract** We consider the HPC challenge of fault tolerance in the context of plasma physics simulations using the sparse grid combination technique. We follow an algorithm-based strategy and present initial convergence results, current bottlenecks, and future strategies based on recent theoretical results. This work is a building block of the project *EXAHD* in the DFG's Priority Programme "Software for Exascale Computing" (SPPEXA).

**Keywords** sparse grids · combination technique · computational plasma physics · algorithm-based fault tolerance

## 1 Introduction

This project stands on the intersection of two major upcoming scientific endeavors: the sustainable generation of fusion energy, for which a deep understanding of plasma turbulence phenomena is crucial, and the approaching era of exascale computations. In the former, numerical simulations of hot plasma fusion are expected to provide further insights into the turbulent processes that characterize the flow. This task requires the solution of a 5D partial differential equation (PDE), the so-called gyrokinetic Vlasov equation, that depends on three spatial coordinates  $(x, y, z)$ , the velocity parallel to the magnetic field line  $v_{\parallel}$ , and the magnetic moment  $\mu$ . Both time-evolution and eigenvalue problems within this context can be numerically treated with the robust code GENE [1]. In particular, the code solves an equation of the form  $\frac{\partial \mathbf{g}}{\partial t} = \mathcal{L}(\mathbf{g}) + \mathcal{N}(\mathbf{g})$ , where  $\mathcal{L}$  and  $\mathcal{N}$  represent the linear and nonlinear terms of the Vlasov model, respectively.

---

A. Parra Hinojosa acknowledges the financial support of *CONACYT*, Mexico.

A. Parra Hinojosa, C. Kowitz  
Chair of Scientific Computing, Technische Universität München  
E-mail: {hinojosa,kowitz}@in.tum.de

M. Heene, D. Pflüger  
Institute for Parallel and Distributed Systems, University of Stuttgart  
E-mail: {mario.heene,dirk.pflueger}@ipvs.uni-stuttgart.de

The second pillar of our project is the potential implementation of GENE on exascale, for which new software paradigms have to be introduced. Given the excellent scaling properties of the code on current HPC systems, an additional level of parallelism based on the sparse grid combination technique (CT) [2] has been proposed to target exascale. The idea is to approximate a  $d$ -dimensional function  $f_{\mathbf{n}}$  (e.g., the solution of the Vlasov equation) defined on a regular Cartesian grid  $\Omega_{\mathbf{n}}$  by a weighted sum of functions  $f_{\mathbf{l}}$  defined on smaller, anisotropic Cartesian grids,

$$f_{\mathbf{n}}(\mathbf{x}) \approx f_{\mathbf{n}}^{(c)} = \sum_{\mathbf{l} \in \mathcal{I}} c_{\mathbf{l}} f_{\mathbf{l}}(\mathbf{x}), \quad (1)$$

with appropriate coefficients  $c_{\mathbf{l}}$ . Here,  $\Omega_{\mathbf{l}}$  (with the multi-index  $\mathbf{l} = (l_1, l_2, \dots, l_d)$ , also called level vector) denotes a grid with mesh size of  $2^{-l_k}$  in dimension  $k = 1, \dots, d$ , and  $\mathcal{I}$  is the set of level vectors of the grids used for the combination. The choice

$$f_{\mathbf{n}}^{(c)}(\mathbf{x}) = \sum_{q=0}^{d-1} (-1)^q \binom{d-1}{q} \sum_{\mathbf{l} \in \mathcal{I}_{\mathbf{n}}} f_{\mathbf{l}}(\mathbf{x}) \quad (2)$$

yields the classical sparse grid combination technique, with  $\mathcal{I}_{\mathbf{n}}$  given by

$$\mathcal{I}_{\mathbf{n}} = \{\mathbf{l} \in \mathbb{N}^d : |\mathbf{l}|_1 = |\mathbf{l}_{\min}|_1 + d - q - 1 : l_{\min,i} \leq l_i \leq n_i\}, \quad (3)$$

where  $\mathbf{l}_{\min}$  specifies a minimal resolution level in each direction. The resulting approximation requires considerably fewer discretization points at a small increase in the approximation error, assuming certain regularity properties of  $f_{\mathbf{n}}$ . However, the combination coefficients  $c_{\mathbf{l}}$  and index set  $\mathcal{I}$  can be chosen differently, adding to the flexibility of the combination technique [8]. To interpolate among grids, we use  $d$ -linear interpolation with piecewise  $d$ -linear functions. The fact that all  $f_{\mathbf{l}}$  in Eq. (1) are of considerably smaller size than  $f_{\mathbf{n}}$  and can be computed independently of each other is the main idea behind the two-level parallelism approach. This will potentially allow us to exploit exascale resources, but it also presents various challenges. Important advances have been made in the context of load balancing [7] and communication schemes [9] for the combination technique, and we now address the issue of resilience for our specific application.

## 2 Fault Tolerance with the Combination Technique

Developing the theory of a fault-tolerant combination technique (FTCT) has required great efforts in the last few years [4, 5, 10], and only recently has it been generalized within a more formal mathematical framework [6].

Figure 1 illustrates the problem in 2D, using a CT with  $\mathbf{l}_{\min} = (1, 1)^T$  and  $\mathbf{n} = (6, 6)^T$ . For simplicity, assume that we attempt to calculate the solution to our problem on each of the 11 grids shown in Fig. 1a, and that all grids are computed in parallel on independent nodes. We are interested in finding suitable combination coefficients when one or more of these grids are no longer available to due processor failures. This is illustrated in Fig. 1b for grids (2, 4) and (4, 3) (marked with  $\times$ ). Our goal is to avoid recomputing these lost solutions (if possible), especially on the largest grids, which are the most expensive. Additionally, recomputing them will interfere with the load balancing. A straightforward strategy is to remove all

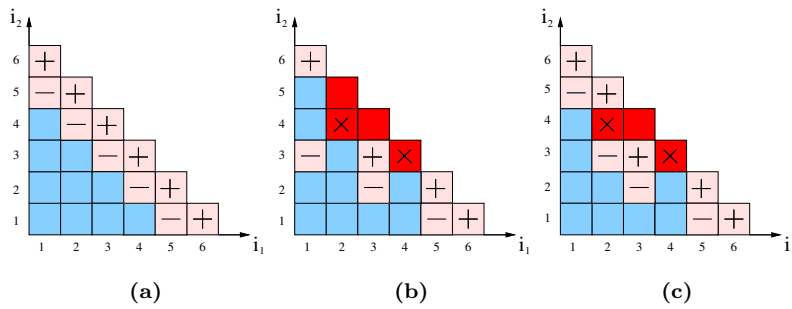


**Fig. 1** (a) Usual 2D combination; (b) Simple recovery strategy; (c) A better recovery strategy.

subspaces larger than the lost subspaces<sup>1</sup> (marked red) and then use the principle of Inclusion/Exclusion with the remaining grids to obtain a new combination [4, 5]. This approach has two main disadvantages: many grids can be lost (especially in higher dimensions), thus increasing the error of the combination, and many grids from lower subspaces are required (in Fig. 1b, we additionally need grids (1, 3) and (3, 2)). The solution on these extra grids should thus be available in advance. Alternatively, note from Fig. 1c that not all subspaces have to be removed in order to obtain a consistent CT. Here, grid (2, 5) can still be used and the resulting scheme is consistent, since it excludes the faulty grids and satisfies the Inclusion/Exclusion principle. However, checking which subspaces can be removed until a consistent CT is obtained is not a trivial task. Nevertheless, our initial implementations already show promising results.

### 3 Numerical Experiments

We carried out two sets of simulations of GENE (standard test case 1: ITG instability) to test the fault tolerance ideas described in Sec. 2: a small combination ran on a desktop, and a larger solution ran on 16 nodes of the supercomputer *Hermit*. In both cases, we performed linear, time-evolution runs of GENE. In the following, the coordinates of the 5D grid follow the ordering  $(\mu, v_{\parallel}, z, y, x)$ , and the faults were simulated “offline”, i.e., after having successfully carried out the simulations<sup>2</sup>.

For the smaller run, a combination solution with  $\mathbf{l}_{\min} = (2, 3, 2, 1, 1)^T$  and  $\mathbf{n} = (6, 7, 6, 1, 1)^T$  was performed, with a total of 31 independent combination grids. Note that fixing the values of  $\mathbf{l}_{\min}$  and  $\mathbf{n}$  to 1 in the  $y$  and  $x$  directions reduces the combination space to only three effective dimensions, which is reflected in the speed of the fault tolerance algorithms. Fig. 2a shows the error of the combination solution with respect to our reference full grid  $\Omega_{\mathbf{n}}$ . We simulated 1 to 5 faults chosen randomly, and for each number of faults, ten simulations were carried out. The error shown is thus the mean value of the ten simulations. The norm used is the  $L_1$  error divided by the number of unknowns. In all of the simulations, only the available (successfully calculated) solutions were used. This means that no recalculation was performed, and no additional (coarser) grids were calculated. However, the probability of finding a consistent combination scheme through this approach decreases dramatically as the number of faults increases.

<sup>1</sup> Two subspaces  $\alpha, \beta$  satisfy  $\alpha \geq \beta$  if  $\alpha_i \geq \beta_i, \quad \forall i \in \{1, \dots, d\}$

<sup>2</sup> For real-time, parallel simulation of faults, see [3, 6].

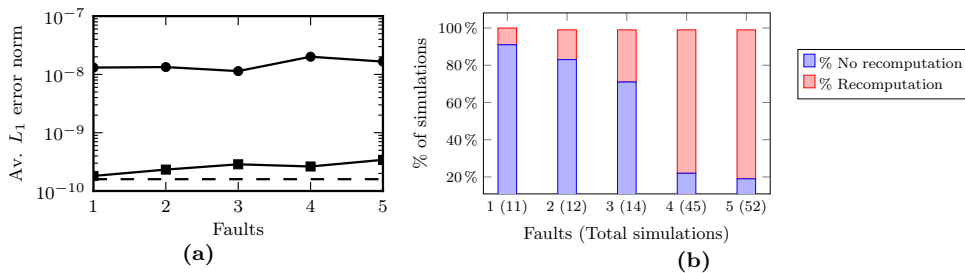


**Fig. 2** (a) Error of the combination grid without faults (*dashed*), with faults (*circles*), and after recovery (*squares*); (b) Percentage of fault simulations whose recovery scheme required recomputation.

This is illustrated in Fig. 2b, where we once again simulated faults randomly and counted in how many occasions recalculation of failed grids or calculation of new grids was required. We see that, as the number of faults increases, it becomes very unlikely that a consistent combination scheme is obtained only with the available grids. It is thus preferable to combine often in order to reduce the number of faults that can occur between each combination [6].

A second simulation was carried out with  $\mathbf{l}_{\min} = (2, 3, 2, 1, 2)^T$  and  $\mathbf{n} = (6, 7, 6, 1, 6)^T$ . In this (effective) 4D space, the problems described for the smaller become worse: either too many grids are lost (using the naïve strategy, Fig. 1b), or the recombination algorithms take prohibitively long times (larger than recalculating the solutions). The latest results on the FTCT specify under which conditions the recomputation of lost solutions or the computation of additional coarser solutions comes into question [6]. We could, for example, choose to recompute faulty solutions of level  $\mathbf{l} \in \mathcal{I}_{\mathbf{n}}$  with  $q \in \{1, \dots, d-1\}$ , and allow the set  $\mathcal{I}_{\mathbf{n}}$  to additionally include grids with level  $\mathbf{l}$  s.t.  $|\mathbf{l}|_1 = |\mathbf{l}_{\min}|_1 - 1$ , in which case the recomputation of the coefficients  $c_1$  is trivial [6]. The extra effort involved in calculating these additional grids is at most  $\frac{1}{2(2^d-1)}$  (1.6% in 5D).

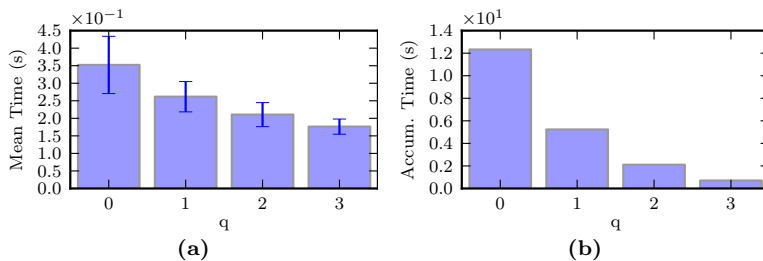


**Fig. 3** For  $q = \{0, 1, 2, 3\}$ , the CT generates  $\{35, 20, 10, 4\}$  grids, resp. (a) Mean and STD, and (b) total accumulated computation times required by the CT grids.

The GENE solution on the smallest grids ( $q = 3$ ) requires roughly half of the time needed by the largest grids ( $q = 0$ ), Fig. 3a, and all solutions on grids for which  $q = 3$  require 5.7% of the resources needed by all grids with  $q = 0$ , Fig. 3b. This will be reflected in the probability of failure of the corresponding computing nodes.

For our future steps, we will choose to recompute faulty solutions for which  $q \in \{2, \dots, d-1\}$ , allowing the set  $\mathcal{I}_{\mathbf{n}}$  to include grids with  $|\mathbf{l}|_1 = |\mathbf{l}_{\min}|_1 - 2$ . This

---

choice seems to offer the best compromise in terms of complexity [6], and we plan to incorporate the load balancing schemes described in [7].

## References

1. GENE Development Team: URL <http://www.ipp.mpg.de/fsj/gene/>
2. Griebel, M., Schneider, M., Zenger, C.: A combination technique for the solution of sparse grid problems. In: *Iterative Methods in Lin. Alg.*, pp. 263–281 (1992)
3. Harding, B., Hegland, M.: A parallel fault tolerant combination technique. In: *PARCO*, pp. 584–592 (2013)
4. Harding, B., Hegland, M.: A robust combination technique. *ANZIAM Journal* **54**, C394–C411 (2013)
5. Harding, B., Hegland, M.: Robust solutions to PDEs with multiple grids. In: *Sparse Grids and Applications-Munich 2012*, pp. 171–193. Springer (2014)
6. Harding, B., Hegland, M., Larson, J., Southern, J.: Scalable and fault tolerant computation with the sparse grid combination technique. [arXiv:1404.2670 \[math.NA\]](https://arxiv.org/abs/1404.2670) (2014)
7. Heene, M., Kowitz, C., Pflüger, D.: Load balancing for massively parallel computations with the sparse grid combination technique. In: *PARCO*, pp. 574–583 (2013)
8. Hegland, M.: Adaptive sparse grids. *ANZIAM Journal* **44**, C335–C353 (2003)
9. Hupp, P., Jacob, R., Heene, M., Pflüger, D., Hegland, M.: Global communication schemes for the sparse grid combination technique. In: *PARCO*, pp. 564–573 (2013)
10. Larson, J.W., Hegland, M., Harding, B., Roberts, S., Stals, L., Rendell, A.P., Strazdins, P., Ali, M.M., Kowitz, C., Nobes, R., et al.: Fault-tolerant grid-based solvers: Combining concepts from sparse grids and mapreduce. *Procedia Computer Science* **18**, 130–139 (2013)

MS III.2: New Approaches to Nonlinear Domain  
Decomposition

Authors: Klawonn, Axel, Lanser, Martin, Rheinbach, Oliver

---

# New Approaches to Nonlinear Domain Decomposition

Axel Klawonn · Martin Lanser · Oliver Rheinbach

**Abstract** The numerical solution of nonlinear partial differential equations on modern supercomputers requires fast and highly scalable parallel solvers. Domain Decomposition methods as FETI-DP (Finite Element Tearing and Interconnecting - Dual Primal) are well known and efficient parallel methods for this kind of problems, discretized by finite elements. In this paper, we describe the inexact reduced Nonlinear FETI-DP (irNonlinear FETI-DP) method. In this recently introduced nonlinear Domain Decomposition approach, the decomposition is done before linearizing the problem with a Newton type method. This strategy can localize the computational work and can reduce communication. Additionally, the FETI-DP coarse problem is solved inexactly and is preconditioned by an AMG (Algebraic Multigrid) method. Finally, weak scalability results for the p-Laplace equation up to 262K cores on Mira BlueGene/Q will be presented.

**Keywords** Nonlinear FETI-DP · FETI-DP · inexact FETI-DP · Nonlinear Domain Decomposition

## 1 Introduction

In contrast to classical Newton-Krylov methods, nonlinear domain decomposition methods are based on decomposing the computational domain before linearization of the nonlinear equation. These approaches are strategies to localize computational work in order to improve scalability for future supercom-

---

Axel Klawonn, Martin Lanser  
Universität zu Köln, Mathematisches Institut, Weyertal 86-90, 50931 Köln  
E-mail: {axel.klawonn, martin.lanser}@uni-koeln.de

Oliver Rheinbach  
Technische Universität Bergakademie Freiberg, Fakultät für Mathematik und Informatik,  
Institut für Numerische Mathematik und Optimierung, 09596 Freiberg  
E-mail: oliver.rheinbach@math.tu-freiberg.de

puter architectures. Different nonlinear domain decomposition methods have been developed in recent years, as, e.g., ASPIN (Additive Schwarz Preconditioned Inexact Newton) by Cai and Keyes [9], Nonlinear FETI-1 by Pebreil et al. [10] and nonlinear Neumann-Neumann methods by Bordeu et al. [11]. Linear FETI-DP domain decomposition, first introduced by Farhat et al. in [12], belong to a family of nonoverlapping domain decomposition methods. The absence of an overlap reduces communication in comparison to overlapping methods as, e.g., overlapping Schwarz. In this paper, we describe a nonlinear FETI-DP method (inexact reduced nonlinear FETI-DP), which can further reduce communication. Additionally, the global coupled FETI-DP coarse problem is solved inexactly and we use an AMG method as a preconditioner.

## 2 Nonlinear FETI-DP

Let  $\Omega \subset \mathbf{R}^d$ ,  $d = 2, 3$  be a computational domain, discretized by finite elements and let  $V^h$  be the corresponding finite element space. We consider a nonlinear problem on  $\Omega$ . In nonlinear as in linear FETI-DP methods we decompose  $\Omega$  into  $N$  nonoverlapping subdomains  $\Omega_i, i = 1, \dots, N$ . We consider the minimization of a nonlinear energy,  $J : V^h \rightarrow \mathbf{R}$ ,  $\min_{u \in V^h} J(u)$ . For standard problems, such as hyperelasticity, discretized by finite elements, this global energy can be represented by a sum  $J(u) = \sum_{i=1}^N J_i(u_i)$  of local energies on the nonoverlapping subdomains; for details, see [1]. So, in contrast to standard Newton-Krylov approaches, the decomposition into subdomains is done before linearizing the problem. Using the decomposition of energy, the linear jump constraint  $B\tilde{u} = 0$  and the standard FETI-DP partial assembly operator  $R_\Pi^T$  (see, e.g., [2,3] for the notation), we can derive and introduce the nonlinear FETI-DP master system

$$\begin{aligned} \tilde{K}(\tilde{u}) + B^T \lambda - \tilde{f} &= 0 \\ B\tilde{u} &= 0. \end{aligned} \quad (1)$$

For more details how to obtain system (1) see, e.g., [4,1]. We assume that the operator  $\tilde{K}$  is continuously differentiable and locally invertible.

### 2.1 Inexact Nonlinear FETI-DP - Solution Phase

Partition of  $\tilde{u}$  into primal variables  $\tilde{u}_\Pi$  and dual variables  $u_B$  in (1), subsequent Newton linearization of the resulting system with respect to  $(u_B, \tilde{u}_\Pi, \lambda)$ , and finally one step of block Gauss elimination of  $\delta u_B$  leads to the reduced linear system

$$\begin{bmatrix} \tilde{S}_{\Pi\Pi} & -(D\tilde{K}(\tilde{u}))_{\Pi B} (D\tilde{K}(\tilde{u}))_{BB}^{-1} B_B^T \\ (sym.) & -B_B (D\tilde{K}(\tilde{u}))_{BB}^{-1} B_B^T \end{bmatrix} \begin{bmatrix} \delta \tilde{u}_\Pi \\ \delta \lambda \end{bmatrix} = \begin{bmatrix} \mathcal{F}_\Pi \\ \mathcal{F}_\lambda \end{bmatrix}, \quad (2)$$

with the Schur complement

$$\tilde{S}_{\Pi\Pi} = (D\tilde{K}(\tilde{u}))_{\Pi\Pi} - (D\tilde{K}(\tilde{u}))_{\Pi B} (D\tilde{K}(\tilde{u}))_{BB}^{-1} (D\tilde{K}(\tilde{u}))_{\Pi B}^T. \quad (3)$$

In the inexact reduced nonlinear FETI-DP method, we solve the block system (2) iteratively using a block-triangular preconditioner. We use cycles of BoomerAMG [8] to precondition  $\tilde{S}_{\Pi\Pi}$  and also include one of the standard FETI-DP preconditioners operating on the Lagrange multipliers  $\delta\lambda$ . This new approach, along with some preliminary results, was first presented in [6]. It combines the inexact approach from [5,7] with the Nonlinear-FETP-DP method [4,1].

## 2.2 Inexact Nonlinear FETI-DP - Computation of an Initial Value

A good initial value can be essential for a fast convergence of Newton-type methods. A suitable initial value  $\tilde{u}^{(0)}$  for the Nonlinear FETI-DP method has to be continuous in all primal variables  $\tilde{u}_{\Pi}^{(0)}$  and should provide a good local approximation of the given problem. A possible initial value  $\tilde{u}^{(0)}$  can be obtained from solving the nonlinear problem  $\tilde{K}(\tilde{u}^{(0)}) = \tilde{f} - B^T\lambda^{(0)}$ .

Newton linearization, partitioning of  $\delta\tilde{u}$  in  $(\delta u_B^T, \delta\tilde{u}_{\Pi}^T)^T$ , and elimination of  $\delta u_B$  leads again to a Schur complement system  $\tilde{S}_{\Pi\Pi} \delta\tilde{u}_{\Pi} = \tilde{d}_{\Pi}$  which is solved iteratively, again using BoomerAMG as a preconditioner.

## 3 Numerical Results

In Fig. 1 one can find a graph of scalability results on the MIRA BlueGene/Q supercomputer. Here, we solve a nonlinear differential equation including the p-Laplace operator. See also the caption of Fig. 1 for more details. Let us mention that inexact reduced nonlinear FETI-DP needs four or five Newton iterations in the first phase, where the initial value is calculated (depending on the problem size) and one iteration in the final solution phase. The runtimes presented in Fig. 1 are average values over the iterations. All in all we see good scalability results up to 262K cores, a reduction of Krylov iterations, and an increase of local work in the first phase where the initial value is computed.

## References

1. Axel Klawonn, Martin Lanser, and Oliver Rheinbach. Nonlinear FETI-DP and BDDC methods. *SIAM J. Sci. Comput.*, 36(2):A737–A765 (2014).
2. Axel Klawonn, and Oliver Rheinbach. Robust FETI-DP methods for heterogeneous three dimensional elasticity problems. *Comput. Methods Appl. Mech. Engrg.*, 196(8):1400–1414 (2007).
3. Andrea Toselli, and Olof B. Widlund. *Domain Decomposition Methods - Algorithms and Theory*, volume 34 of Springer Series in Computational Mathematics. Springer, 2004.

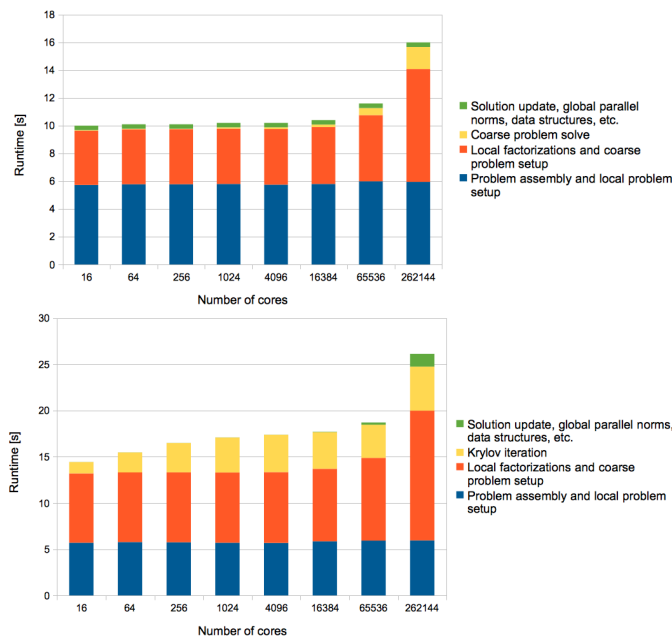


**Fig. 1** Bar plot of initial value calculation (upper) and solution phase (lower) of the inexact nonlinear FETI-DP algorithm. Performed on the Mira supercomputer at Argonne National Laboratory;  $\Delta u + 4\Delta_4 u, H/h = 180$ ; zero dirichlet boundary.

4. Axel Klawonn, Martin Lanser, Patrick Radtke, and Oliver Rheinbach. On an Adaptive Coarse Space and on Nonlinear Domain Decomposition. In *Domain Decomposition Methods in Science and Engineering, Proceedings of the 21st International Conference on Domain Decomposition Methods*, Rennes, France, June 25-29 2012. Springer-Verlag, Lecture Notes on Computational Science and Engineering, 2014. Accepted for publication. 12p.
5. Axel Klawonn, and Oliver Rheinbach. Inexact FETI-DP methods. *Internat. J. Numer. Methods Engrg.*, 69(2):284–307 (2007).
6. Axel Klawonn, Martin Lanser, and Oliver Rheinbach. A Nonlinear FETI-DP Method with an Inexact Coarse Problem. Submitted to the proceedings of the 22th International Conference on Domain Decomposition Methods, Sept. 16-20, 2013, Universita della Svizzera italiana, Lugano, Switzerland (2014).
7. Axel Klawonn, and Oliver Rheinbach. Highly scalable parallel domain decomposition methods with an application to biomechanics. *ZAMM Z. Angew. Math. Mech.*, 90(1):5–32 (2010).
8. Van E. Henson, and Ulrike M. Yang. Boomeramg: A parallel algebraic multigrid solver and preconditioner. *Applied Numerical Mathematics*, 41:155–177 (2002).
9. Xiao Chuan Cai, and David Keyes: Nonlinearly Preconditioned Inexact Newton Algorithms. *SISC*, 2003.
10. Julien Pebrel, Christian Rey, and Pierre Gosselet: A nonlinear dual-domain decomposition method: Application to structural problems with damage. *Inter. J. Multiscale Comp. Eng.* 6(3):251–262 (2008).
11. Felipe Bordeu, Pierre-Alain Boucard, and Pierre Gosselet, *Proceedings of the First International Conference on Parallel, Distributed and Grid Computing for Engineering. Balancing Domain Decomposition with Nonlinear Relocalization: Parallel Implementation for Laminates*. Civil-Comp Press, Stirlingshire, UK (2009).
12. Charbel Farhat, Michel Lesoinne, and Kendall Pierson: A scalable dual-primal domain decomposition method. *Numer. Lin. Alg. Appl.*, 7: 687–714 (2000).

MS III.3: Towards Fluid-Acoustics Interaction on  
Massively Parallel Systems

Authors: Gatzhammer, Bernhard, Klimach, Harald, Krupp, Verena, Lindner, Florian, Mehl, Miriam,  
Roller, Sabine, Uekermann, Benjamin

---

# Towards Fluid-Acoustics Interaction on Massively Parallel Systems

Bernhard Gatzhammer · Harald Klimach · Verena Krupp · Florian Lindner · Miriam Mehl · Sabine Roller · Benjamin Uekermann

**Abstract** In this work, we present first scaling results for a partitioned Euler-acoustics coupling, an important milestone towards fluid-structure-acoustic interaction.

**Keywords** Fluid-Structure-Acoustics Interaction · Exa-Scale · Partitioned Coupling

## 1 Introduction

Simulation of fluid-structure-acoustics interaction will bring new insight into different applications, as, for example, the sound design of aircrafts or wind energy plants. The immense computational costs of a fully 3D simulation demand to make efficient use of today's massively parallel supercomputers. To achieve this, different challenges have to be tackled, including a scalable communication scheme, and the treatment of a huge amount of data.

We aim to develop a partitioned simulation, reusing existing software for each individual discipline. This allows to benefit from prior experience on how to scale up each single simulation. Furthermore, we avoid the rising complexity of a monolithic simulation if more and more physical fields should be captured. On the other hand, the coupling between each pair of physical solvers needs

---

V. Krupp  
Universität Siegen  
Hölderlinstr. 3  
D - 57068 Siegen  
E-mail: verena.krupp@uni-siegen.de

B. Uekermann  
Technische Universität München  
Institute for Advanced Study  
Lichtenbergstrae 2 a  
D - 85748 Garching b. München  
E-mail: uekerman@in.tum.de

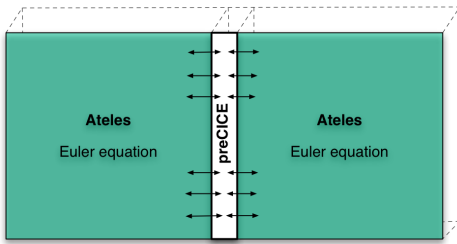


**Fig. 1** Simulation of a density pulse – Simulation setup

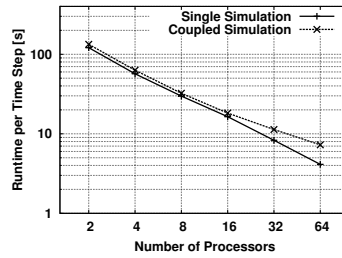


**Fig. 2** Simulation of a density pulse – Communication Bottleneck

to be carried out carefully, to get a stable overall simulation, while not degrading the scalability. For this purpose, we developed the coupling library `preCICE` ([1]). The library approach allows for a very flexible coupling of different solvers, taking full advantage of the partitioned approach. `preCICE` offers a high-level application interface, making the incorporation into a solver code minimally invasive. Different mapping techniques, including such based on radial basis functions, as well as sophisticated coupling algorithms ranging from simple explicit to quasi-Newton-based implicit schemes, are implemented.

In [1], each parallel solver uses a single server process to gather coupling data. This approach limits the scalability as the gathering represents a serial step in the overall algorithm. We are working on a point-to-point communication scheme that should overcome this bottleneck. In this paper, we study first, in Section 2, the aforementioned bottleneck on a simple test case. Afterwards, in Section 3, we describe an application that shows the necessity of a better scalability of the overall simulation. At the CE 2014, we plan to present first results for this application with an improved communication scheme of `preCICE`.

## 2 A Scalability Test Case

To test the scalability of the server-based communication scheme in `preCICE`, we set up a simple test case. We simulate a travelling density pulse in the non-linear Euler equations with the discontinuous Galerkin solver `Ateles` ([2]). The shape of the pulse does not vary over time, validating our coupling approach. `Ateles` uses an 8th order scheme, leading to a relatively small amount of data that needs to be communicated per element. We compare a single `Ateles` simulation on the whole domain, with one where we used `preCICE` to couple between two `Ateles` instances over an artificial coupling interface (cf. Figure 1).

Figure 2 shows strong scaling results (already shown in [3]) for a total of 512 mesh elements, corresponding to 1310720 degrees of freedom. We run

the simulation on the MAC Cluster<sup>1</sup> in Munich. Full nodes, comprised of 16 physical processors, are reserved also for smaller runs. Runs with more than 16 processors use multiple nodes. The `preCICE` server processes always run on different full nodes and are not taken into account for Figure 2. The single `Ateles` run shows a nearly perfect scaling while the bottleneck, stemming from `preCICE`, in the coupled simulation can be observed clearly. Changing the current communication scheme of `preCICE`, based on a single server process per solver that gathers the coupling data, to a point-to-point scheme, should overcome this bottleneck.

### 3 Euler-Acoustics Coupling

An important component in the fluid-structure-acoustics interaction is the coupling of fluid and acoustic domains. This coupling builds the outermost interface and needs to properly capture flow perturbations to ensure accurate propagation of acoustic waves. To show the principal setup as targeted by the project, we use a flow around an obstacle to generate sound in a fluid domain and append a far field domain, which is modelled by the isothermal acoustic wave equations. For the domain of the flow around the obstacle we use inviscid compressible Euler equations, which matches with the targeted simulation scenario, where an inviscid domain should interface with the acoustic domain. However, in the final setup a further inner level with viscid flow phenomena will be considered, which we neglect for now. The flow domain requires a high resolution to properly capture all important phenomena. In the acoustic domain, on the other hand, the usage of simplified equations as well as a coarser resolution drastically reduces the computational costs. Figure 3 depicts this scenario setup, note that we make use of local refinement towards the obstacles. The obstacle is impinged by a circular subsonic jet that is prescribed with a inlet velocity of Mach 0.3. Both domains are computed with `Ateles` and the coupling is realized via `preCICE`.

As shown in Section 2, the amount of data exchanged at the `preCICE` interface is important for the performance with the current server-based communication procedure. This argument, however, still holds true for an efficient point to point communication procedure. Higher order discretization schemes reduce the amount of data that needs to be exchanged at the interfaces in relation to the computational effort spent in the volume. Yet, due to geometrical requirements and to allow for parallel processing in general, there needs to be a certain amount of elements present in the flow domain. Thus, a compromise between higher order and the number of elements needs to be found. Therefore, we use more elements in the flow domain, but increase the order in the acoustic domain to allow similar resolution in both domains. Furthermore, for the required resolution of the fluid phenomena, multiple refinement levels are placed in the flow domain (cf. Figure 3). This allows us to achieve a high

---

<sup>1</sup> [http://www.mac.tum.de/wiki/index.php/MAC\\_Cluster](http://www.mac.tum.de/wiki/index.php/MAC_Cluster)

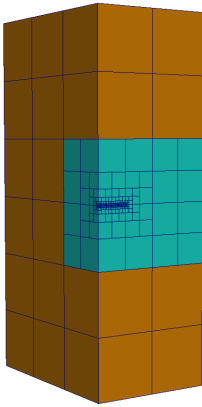


**Fig. 3** Simulation of a subsonic jet impinging an obstacle – Cut through the scenario setup. The Euler domain is marked in blue, the acoustic domain in other yellow.

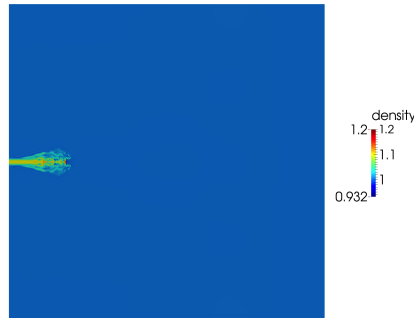


**Fig. 4** Subsonic jet in the Euler domain.

resolution in the vicinity of jet and obstacle, while reducing the resolution at the outside, therefor reducing the amount of data, that needs to be exchanged at the `preCICE` interface.

The question remains, if the server-based communication scheme still hampers the simulation of such applications despite the reduced amount of communication data. To obtain some estimate, we compare the setup of the subsonic jet with the test case of Section 2. For the subsonic jet, we use 1068 elements to discretize the fluid domain, while, due the spatial adaptivity only 64 elements are located at the coupling interface. In contrast, both domains of the test case in Section 2, use 512 elements in total, 64 of them adjacent to the coupling interface on either side. For a proper resolution of the flow, we need to use at least an 16th order scheme for our chosen mesh. For the setup in section 2 we need to communicate roughly 160 MB of data in each time step, while in the setup for the subsonic jet we will need around 525 MB per time step. For a theoretical throughput of 14 Gbit/s<sup>2</sup> this would result in a theoretical minimal time for data transfer of 0.093 s in the scaling analysis or 0.3 s in the subsonic jet. Thus, roughly a factor of 3 increased data transfer time is expected. However, the computational effort is increased by a factor around 16 and we therefore do not expect the server based `preCICE` coupling to be a worse bottleneck than in the previous scaling analysis.

We conclude that a coupled scenario with the realistic testcase should be feasible with the server-based communication of `perCICE`. However, since we

<sup>2</sup> LRZ, `SuperMUC`, thin nodes, with an individual island FRD10 Infiniband network <http://www.lrz.de/services/compute/supermuc/systemdescription/>

are aiming for more complex testcases and larger problemsizes, we need to speed up the overall runtime. Therefore, we would like to speed up the communication time and the server-based communication is definitely not feasible. As already stated in the introduction, at the CE 2014, we plan to show coupled simulations for both, the server-based and a point-to-point communication scheme.

**Acknowledgements** The financial support of the Institute for Advanced Study (IAS) of the Technische Universität München, and of SPPEXA, the German Science Foundation Priority Program 1648 – Software for Exascale Computing are thankfully acknowledged.

## References

1. B. Gatzhammer, Efficient and Flexible Partitioned Simulation of Fluid-Structure Interactions. Dissertation, TU München, Institut für Informatik, to be published (2014)
2. J. Zudrop, H. Klimach, M. Hasert, K. Masilamani, and S. Roller, A fully distributed cfd framework for massively parallel systems. In Cray User Group, Stuttgart (2012)
3. H. Bijl, T. Ertl, M. Mehl, S. Roller, and D. Sternel, ExaFSA – Exascale Simulation of Fluid-Structure-Acoustics Interactions, inSiDE, 12, 78–81 (2014)
4. H.Klimach, K.Jain, S.Roller, End-to-end Parallel Simulations with APES, International Conference on Parallel Computing - ParCo2013, Munich, Germany (2013)

MS III.4: Node-Level Performance Optimization of  
the Fast Multipole Method

Authors: Beckmann, Andreas, Kabadshow, Ivo

---

# Node-level Performance Optimization of the Fast Multipole Method

Andreas Beckmann · Ivo Kabadshow

**Abstract** The goal of this presentation is to show how the most time-consuming near and far field kernels of a fast multipole method can be optimized towards node-level peak performance. Most of the presented optimization schemes allow a generic, hence platform-independent algorithmic description within the chosen C++ framework for the GROMEX project.

**Keywords** Fast multipole method · node-level optimization · GROMEX · SPPEXA

## 1 Introduction

Classical simulations in the field of molecular dynamics or astrophysics [1] are mostly limited by the number of long-range particle interactions. A straightforward computation is limited to small particle numbers due to the  $\mathcal{O}(N^2)$  scaling. Fast summation methods like [2–4] are capable of reducing the complexity to  $\mathcal{O}(N \log N)$  or even  $\mathcal{O}(N)$ . The development of parallel computers in the last decades accelerated this development further. Now simulation codes can handle multi-billion particle simulations [5] easily. However, every fast summation method has auxiliary parameters, data structures and memory requirements which need to be supplied. The overall performance of such

---

GROMEX is funded by the German Research Foundation (DFG) under the priority programme 1648 “Software for Exascale Computing – SPPEXA”.

A. Beckmann  
Jülich Supercomputing Centre  
Tel.: +49 2461/61-8713  
Fax: +49 2461/61-6656  
E-mail: a.beckmann@fz-juelich.de

I. Kabadshow  
Jülich Supercomputing Centre  
E-mail: i.kabadshow@fz-juelich.de

algorithms on the node-level strongly depends on the provided features of the underlying hardware architecture.

## 2 The Fast Multipole Method in a Nutshell

The Fast Multipole Methods allows to compute the pairwise interactions of  $N$  particles with charge or mass  $q_i$  with  $\mathcal{O}(N)$  complexity. The Coulomb energy for such a system with open boundary conditions can be written as

$$E_C = \frac{1}{2} \sum_{i=1}^N \sum_{j=1}^N \frac{q_i q_j}{r_{ij}} \quad (i \neq j). \quad (1)$$

The inverse distance can be factorized by a bipolar expansion [6] into three individual parts. A multipole expansion  $\omega_{lm}(\mathbf{a})$  around a first coordinate system's center  $O_1$ , a multipole expansion  $\omega_{jk}(\mathbf{b})$  around a second coordinate system's center  $O_2$  and an operator  $M2L_{j+l,m+k}(\mathbf{R})$  to translate the multipole expansions into Taylor coefficients  $\mu_{lm}$ . The energy of the expanded coordinates reads

$$E_{FF} = \sum_{l=0}^p \sum_{j=0}^p \sum_{m=-l}^l \sum_{k=-j}^j (-1)^j \omega_{lm}(\mathbf{a}) M2L(\mathbf{R}) \omega_{jk}(\mathbf{b}). \quad (2)$$

However, convergence conditions of equation 2 demand  $|\mathbf{a}| + |\mathbf{b}| < |\mathbf{R}|$ . To avoid convergence issues, the FMM tree can be subdivided until the condition is met, or interactions violating the convergence condition can be performed directly in the so called near field. Thus, in general the computation is split up into a far field (FF) part where the interactions take place via the expansion and a near field (NF) part, where the interaction is computed classically

$$E_C = E_{NF} + E_{FF}. \quad (3)$$

## 3 Hardware Features and Node-Level Performance

Current processors (and accelerators) come with a variety of features that can and should be exploited to maximize performance in time-critical parts of applications: multi-core (and many-core) CPUs, SMT (simultaneous multi-threading), SIMD-operations, ILP (instruction level parallelism), out-of-order execution (or lack thereof), large register sets, cache hierarchies, NUMA (non-uniform memory access), etc. To ease application development and adaptation to new platforms these features need to be accessed through some abstraction layer. To identify the time critical computational kernels profiling tools may be used. Evaluating a kernel to find its current limiting factor as well as unused resources requires much manual work, in-depth knowledge of the architecture and the algorithm. Performance counters that are provided by the hardware can be utilized by e.g. PAPI[7]. An inspection at assembly level is required (the

two kernels presented here need less than 40 instructions for their innermost loops). Once a kernel fully uses some resource in an optimal way it may be considered as fully optimized.

## 4 Optimizing kernels from the Fast Multipole Method

### 4.1 The Near Field kernel on Blue Gene/Q

The SIMD capabilities can be exploited easily by processing several particles concurrently, ideally using a Struct-of-Arrays (SoA) format for the particle information.

Part of this is the computation of the inverse distance between two particles which require SQRT (square root) and DIV (divide) instructions which either have a long latency and are not pipelined or are not even available (as SIMD instructions). Instead a platform may provide an estimate for reciprocal square root (RSQRTE) which has to be followed by one (or more) Newton-Raphson (NR) iteration(s) to increase the accuracy as needed. That results in 4 additional multiplications and 1 subtraction (with some data dependencies) per iteration. The quality of these estimates varies significantly between platforms, but using such an estimate also adds the flexibility to do less (or even no) NR-iterations in case the requested accuracy is less than machine precision.

The time for computing force and potential contribution for a pair of particles is largely dominated by the dependencies in the critical instruction path. To increase the number of available instructions and fill unused slots an out-of-order (ooo) architecture will issue instructions from the next iteration(s) while waiting for the dependencies that block progress in the current iteration. Since the data dependencies between loop iterations are minimal (only the accumulator at the end is shared) this is easily handled by e.g. Intel CPUs.

For in-order platforms like Blue Gene/Q this has to be realized by the compiler (ideally) or the software engineer. Loop unrolling can be applied to interweave two (or more) subsequent iterations. Scheduling the registers and instructions for the interleaved iterations may be a nontrivial task.

Threads are used to load the individual cores with work. The execution model on the Blue Gene/Q cores requires use of SMT to leverage ILP which can easily be achieved using thread oversubscription.

Due to compilers insufficiencies we implemented a manually interleaved and scheduled SIMD-inline-assembly kernel. Running this kernel in 4-way SMT on one core issues  $4 \times 21 = 84$  floating point instructions over 86.8 cycles which is near the limit of issuing 1 FP op per cycle.

### 4.2 The Far Field kernels

We focus on a slightly simplified version of the most frequent (and time consuming) computational kernel executed during the far field computation:

**Table 1** Tradeoff for value reuse in subsequent iterations for read/write operations (higher is better) and minimal cache requirement (lower is better). There are  $\mathcal{O}(p^4)$  iterations.

loop order	<b>input</b> (read)	<b>B</b> (read)	<b>result</b> (write)	cache requirement
1-m-j-k	1	1	$\mathcal{O}(p^2)$	$\mathcal{O}(p^2)$
j-k-l-m	$\mathcal{O}(p^2)$	1	1	$\mathcal{O}(p^2)$
1-j-m-k	1	1	$\mathcal{O}(p)$	$\mathcal{O}(p)$

```

for (l = 0; l <= p; ++l)
  for (m = -1; m <= 1; ++m)
    for (j = 0; j <= p; ++j)
      for (k = -j; k <= j; ++k)
        result[l, m] += B[j + 1, k + m] * input[j, k]

```

This example is also representative for several other similarly structured kernels with the same complexity of  $\mathcal{O}(p^4)$ . Variables **input** and **result** are triangular arrays containing complex numbers at elements  $(l, m) : 0 \leq l \leq p, |m| \leq l$ . The input **B** has the same structure, but extends up to  $2p$ .

The access pattern suggests to use a column-major memory layout for the data structures. The summation order is not important for numeric stability, therefore the loops can be interchanged arbitrarily and partial results can be temporarily accumulated in registers. Exchanging loops trades cache locality between the three data structures, see Table 1.

- The 1-m-j-k-order (as shown above) can perform  $\mathcal{O}(p^2)$  subsequent accumulations for the same **result** element in registers followed by a single memory update. But reuse of elements from **input** and **B** only happens after  $\mathcal{O}(p^2)$  steps. This is a good choice for small  $p$  where  $\mathcal{O}(p^2)$  elements fit in cache.
- The j-k-l-m-order would gain optimal reuse of the elements from **input** at the cost of not caching any memory update for the result in registers. Turning reads into writes usually results in a performance loss.
- The 1-j-m-k-order splits the computation of a **result** element into  $\mathcal{O}(p)$  phases with one memory update per phase, but improves the locality and reuse in **input** and **B** to a set of only  $\mathcal{O}(p)$  hot elements. This is a better choice for larger  $p$  values.

## References

1. V. Springel, inSiDE **8**(2), 20 (2010)
2. J. Barnes, P. Hut, Nature **324**, 446 (1986)
3. L. Greengard, V. Rokhlin, J. Comput. Phys. **73**(2), 325 (1987)
4. J.W. Eastwood, R.W. Hockney, D.N. Lawrence, Comput. Phys. Commun. **19**(2), 215 (1980)
5. A. Rahimian, et al., in *Proceedings of the 2010 ACM/IEEE International Conference for High Performance Computing, Networking, Storage and Analysis* (IEEE Computer Society, Washington, DC, USA, 2010), SC '10, pp. 1–11

- 
6. C.A. White, M. Head-Gordon, *J. Chem. Phys.* **101**, 6593 (1994)
  7. S. Browne, J. Dongarra, N. Garner, G. Ho, P. Mucci, *Int. J. High Perform. Comput. Appl.* **14**(3), 189 (2000)

MS III.5: Node-Level Performance Engineering for  
an Advanced Density Driven Porous Media Flow  
Solver

Authors: Müthing, Steffen, Bastian, Peter, Göttsche, Dominik, Ribbrock, Dirk

---

# Node-level performance engineering for an advanced density driven porous media flow solver

Steffen Müthing · Peter Bastian ·  
Dominik Göddeke · Dirk Ribbrock

**Abstract** We present a scalable solver for density driven flow in porous media based on operator splitting and a Discontinuous Galerkin discretization using the frameworks DUNE and PDELab. In particular, we focus on the efficient exploitation of current and next generation HPC architectures. For this purpose, we extend the existing parallel computation support in DUNE (based on classical MPI domain partitioning) to a hybrid model with shared memory parallelism on multi-threaded CPU nodes and accelerators like GPGPUs or Intel MIC. Moreover, we investigate the effects of leveraging the SIMD capabilities of current hardware at the different solver stages (assembly / linear algebra).

## 1 Introduction

In the EXADUNE project, we pursue a framework approach toward software development to facilitate code reuse and thus cut down on development

---

S. Müthing  
Interdisciplinary Center for Scientific Computing  
Heidelberg University  
E-mail: steffen.muething@iwr.uni-heidelberg.de

P. Bastian  
Interdisciplinary Center for Scientific Computing  
Heidelberg University  
E-mail: peter.bastian@iwr.uni-heidelberg.de

D. Göddeke  
Department of Mathematics  
TU Dortmund  
E-mail: dominik.gueddeke@math.tu-dortmund.de

D. Ribbrock  
Department of Mathematics  
TU Dortmund  
E-mail: dirk.ribbrock@math.tu-dortmund.de

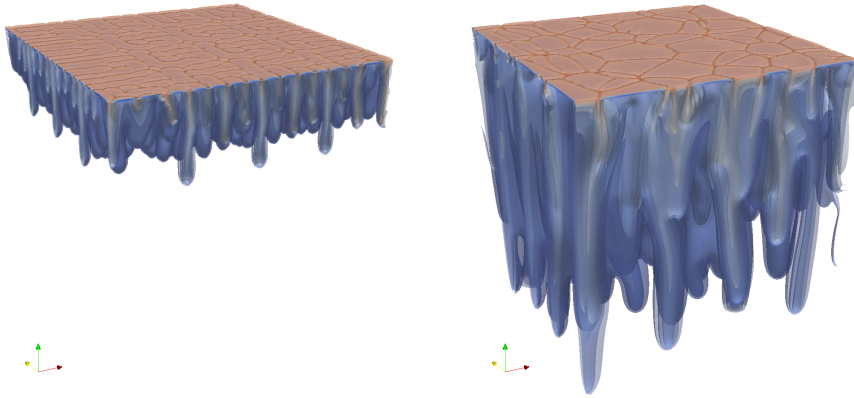


**Fig. 1** Density driven flow for  $Ra = 8000$ . Concentration after the onset of instability and after the development of persistent fingers.

time, an important metric in the current fast-paced research environment. For this purpose, we layer our work on top of existing frameworks, in particular DUNE [2, 1], which already provides us with high-performance abstractions for PDE simulation as well as large-scale MPI parallelism and combine it with the hardware-specific adaptations developed as part of the FEAST project [14].

A more complete overview of the EXADUNE project, in particular its higher-level concepts like multi-scale approaches, model order reduction and Monte-Carlo simulations, can be found in [3].

## 2 Problem

We will demonstrate the capabilities of our framework approach on a three-dimensional model problem of density driven flow problem in a porous medium, which serves as a model for the dissolution of  $\text{CO}_2$ . Due to gravity and the different densities, the model exhibits an unstable flow behaviour with enhanced mixing.

Our problem is given by an elliptic equation for pressure  $p(x, y, z, t)$  coupled to a parabolic equation for concentration  $c(x, y, z, t)$ :

$$-\nabla \cdot (\nabla p - c \mathbf{1}_z) = 0, \quad (1)$$

$$\partial_t c - \nabla \cdot \left( (\nabla p - c \mathbf{1}_z) c + \frac{1}{Ra} \nabla c \right) = 0, \quad (2)$$

which we regard in a non-dimensional formulation governed exclusively by the Raleigh number  $Ra$  on the unit cube  $\Omega = (0, 1)^3$ . Details can be found in [12].

In order to solve the problem, we perform an operator splitting to decouple the resulting system. For the pressure equation (1), we employ a cell centered finite volume discretisation and reconstruct the velocity field with lowest order

Raviar-Thomas elements. The transport equation (2) is discretised in space with the symmetric weighted interior penalty DG finite element method [6]. The time domain is discretised using strong stability preserving explicit Runge-Kutta methods [13], which allows us to solve the transport without matrix assembly, yielding an increased arithmetic intensity. Figure 1 shows some of the features we are able to observe, in particular a very pronounced fingering and the formation of Voronoi-like patterns at the upper (inflow) boundary.

### 3 Assembly

DG methods have a lot of beneficial properties in the context of porous media applications. We increase the efficiency of the problem assembly by exploiting the tensor product structure of the polynomial basis functions and the quadrature rules on cuboid element and are able to reduce the associated computational by performing sum factorisation ([9,10]).

We present performance numbers for our assembly procedure on CPUs and Xeon Phi for discretisations up to order 10, which clearly show that high order methods offer a way to exploit modern multicore architectures and their SIMD capabilities.

### 4 Linear Algebra

At the linear algebra level, we present some of the enhancements aimed at improving node-level performance that we have recently added to the DUNE framework. In particular, we have added new containers and algorithms that fully exploit the capabilities of modern CPUs and accelerators like GPGPUs and Xeon Phi. In order to facilitate simulation in heterogeneous hardware environments (e.g. assembly on host CPUs / linear algebra on CUDA) and due to the non-applicability of standard sparse matrix formats like CSR to SIMD-dependent architectures like Xeon Phi / GPUs, we implemented a uniform matrix format (introduced in [8]) that provides adequate performance across our target architectures. As our DG discretisations yield block-structured matrices, we extended that format to support arbitrary block sizes while retaining the ability to vectorise operations by interleaving data from multiple blocks [11].

We present those extensions as well as benchmarks that demonstrate the relative performance of CPUs and accelerators, the advantage of using a blocked format, which reduces the required memory bandwidth, and the importance of limiting shared-memory parallelism to hardware partitions with uniform memory access.

**Acknowledgements** This research was funded by the DFG SPP 1648 Software for Exascale Computing.

## References

1. Bastian, P., Blatt, M., Dedner, A., Engwer, C., Klöfkorn, R., Kornhuber, R., Ohlberger, M., Sander, O.: A generic grid interface for parallel and adaptive scientific computing. part II: Implementation and tests in DUNE. *Computing* 82(2-3), 121–138 (2008)
2. Bastian, P., Blatt, M., Dedner, A., Engwer, C., Klöfkorn, R., Ohlberger, M., Sander, O.: A generic grid interface for parallel and adaptive scientific computing. part I: Abstract framework. *Computing* 82(2-3), 103–119 (2008)
3. Bastian, P., Engwer, C., Göttsche, D., Iliev, O., Ippisch, O., Ohlberger, M., Turek, S., Fahlke, J., Kaulmann, S., Müthing, S., Ribbrock, D.: EXA-DUNE: Flexible PDE Solvers, Numerical Methods and Applications. Submitted to: Proceedings of Euro-Par 2014
4. Choi, J., Singh, A., Vuduc, R.: Model-driven autotuning of sparse matrix-vector multiply on GPUs. In: *Principles and Practice of Parallel Programming*. pp. 115–126 (2010)
5. Engwer, C., Fahlke, J.: Scalable hybrid parallelization strategies for the DUNE grid interface. In: *Proceedings of ENUMATH 2013* (2014)
6. Ern, A., Stephansen, A., Zunino, P.: A discontinuous Galerkin method with weighted averages for advection-diffusion equations with locally small and anisotropic diffusivity. *IMA Journal of Numerical Analysis* 29(2), 235–256 (2009)
7. Kretz, M., Lindenstruth, V.: Vc: A C++ library for explicit vectorization. *Software: Practice and Experience* 42(11), 1409–1430 (2012)
8. Kreuzer, M., Hager, G., Wellein, G., Fehske, H., Bishop, A.: A unified sparse matrix data format for modern processors with wide SIMD units. *SIAM Journal on Scientific Computing* (2013), accepted, Preprint: arXiv 1307.6209
9. Kronbichler, M., Kormann, K.: A generic interface for parallel cell-based finite element operator application. *Computers & Fluids* 63, 135–147 (2012)
10. Melenk, J., Gerdes, K., Schwab, C.: Fully discrete hp-finite elements: fast quadrature. *Computer Methods in Applied Mechanics and Engineering* 190(32-33), 4339–4364 (2001)
11. Müthing, S., Ribbrock, D., Göttsche, D.: Integrating multi-threading and accelerators into DUNE-ISTL. In: *Proceedings of ENUMATH 2013* (2014)
12. Riaz, A., Hesse, M., Tchelepi, H., Orr, F.: Onset of convection in a gravitationally unstable diffusive boundary layer in porous media. *Journal of Fluid Mechanics* 548, 87–111 (2006)
13. Shu, C.: Total-variation-diminishing time discretizations. *SIAM Journal on Scientific and Statistical Computing* 9, 1073–1084 (1988)
14. Turek, S., Göttsche, D., Becker, C., Buijssen, S., Wobker, S.: FEAST – Realisation of hardware-oriented numerics for HPC simulations with finite elements. *Concurrency and Computation: Practice and Experience* 22(6), 2247–2265 (2010)

**MS IV Optimal Control Based on  
Reduced Order Models**

MS IV.1: Optimal Flow Control Based on POD  
and MPC and an Application to the Cancellation of  
Tollmien-Schlichting Waves

Authors: Ghiglieri, Jane, Ulbrich, Stefan

---

# Optimal Flow Control based on POD and MPC and an Application to the Cancellation of Tollmien-Schlichting Waves

Jane Ghiglieri · Stefan Ulbrich

**Abstract** We present a reduced-order model based on Proper Orthogonal Decomposition (POD) which is suitable for active control for fluid dynamical systems. We propose a special snapshot ensemble which can be generated beforehand and is applicable to optimal control problems. Additionally, we obtain a corresponding a-priori error estimate.

We combine the reduced order model with a Model Predictive Control (MPC) approach for the cancellation of Tollmien-Schlichting waves in the boundary layer of a flat plate with a body force induced by a plasma actuator.

**Keywords** Navier-Stokes equations · flow control · model reduction · Proper Orthogonal Decomposition · Model Predictive Control · error estimates

## 1 Optimal Control Problem

With increasing Reynolds number, laminar flows become unstable and transition to turbulence occurs. Turbulent flow leads to an increased drag at the flow boundaries. Thus, a natural engineering problem is to develop methods of flow control which can delay or eliminate transition to turbulence.

The onset of transition is characterized by the formation of growing disturbances inside the boundary layer, which form two-dimensional waves, the Tollmien-Schlichting waves. Successful damping of the amplitude of these waves

---

Jane Ghiglieri · Stefan Ulbrich  
Research Group Optimization  
Department of Mathematics  
Technische Universität Darmstadt  
Dolivostraße 15  
D-64293 Darmstadt  
Tel.: +49-6151-16-2960  
Fax: +49-6151-16-4459  
E-mail: ghiglieri,ulbrich@mathematik.tu-darmstadt.de

can delay transition for a significant distance downstream, lowering the skin friction drag of the body.

We consider plasma actuators for flow control. These actuators induce a body force which leads to a fluid acceleration, such that the velocity profile changes next to the surface. Experiments and simulations have indicated that plasma actuators can dampen Tollmien-Schlichting waves and are able to move their occurrence downstream [5].

The optimal control problem is given by

$$\begin{aligned} \min \quad & J(y, u) \\ \text{subject to} \quad & y_t - \nu \Delta y + (y \cdot \nabla) y + \nabla p = f_a + f_c(u) \quad \text{in } \Omega \times (0, T] \\ & \nabla \cdot y = 0 \quad \text{in } \Omega \times (0, T] \\ & y(0) = y_0 \quad \text{in } \Omega \\ & y = y_b \quad \text{on } \Gamma \times (0, T]. \end{aligned} \quad (1)$$

with velocity field  $y : [0, T] \times \Omega \rightarrow \mathbb{R}^2$  and pressure  $p : [0, T] \times \Omega \rightarrow \mathbb{R}$ . The viscosity of the fluid is given by a parameter  $\nu > 0$ , the kinematic viscosity.

A time-dependent body force  $f_a(x, t)$  generates the desired disturbances which develop to mono-frequency Tollmien-Schlichting waves after a short transient oscillation length.

The body force induced by the plasma actuator is given by  $f_c(u) = u(t)g(x)$ , whereas  $g(x)$  is an experimentally based body force field and  $u : [0, T] \rightarrow [0, 1]$  is the time-dependent control amplitude.

The cost functional  $J$  assesses the cancellation of the Tollmien-Schlichting waves by

$$J(y, u) = \int_0^T \left( \frac{d}{dt} \int_{\Omega_c} y_1(x, t) dx \right)^2 dt + \frac{\alpha}{2} \int_0^T |u(t)|^2 dt. \quad (2)$$

with regularization parameter  $\alpha > 0$ .

## 2 Model Reduction

Proper Orthogonal Decomposition (POD) serves in many cases as promising model reduction tool for simulation purposes, see e.g. [1], [3], [7], [8]. However, the POD approach highly depends on the snapshot set used to generate it, such that the POD may suffer when the system is under the action of control. There have been techniques introduced to enlarge the computational database in order to accurately capture the system behavior for various control trajectories during optimization, see [1], [2], [3], [12], [11]. In most of these techniques an adaptive procedure is used to generate new snapshots which is costly since these snapshots are determined using expensive codes like finite-element codes, which can have many thousands of degrees of freedom.

We propose a special snapshot ensemble that can be generated beforehand and is applicable to optimal control problems. The snapshots can be generated

off-line, so that their costs can be neglected during the optimization. Even the POD basis can be generated off-line which after all requires the solution of an eigenvalue problem which is of the size of the cardinality of the snapshot set. The optimization uses the corresponding reduced order model based on the POD basis to determine the state and the adjoint solutions needed by the optimizer.

In the proposed method the POD basis is built based on finite-element snapshots  $y_k^h$ ,  $k = 1, \dots, n$  of the uncontrolled state and impulse response snapshots. The impulse response snapshots give a characterization of the input-output behavior for the actuation. Therefore, the resulting ROM can predict how the system will behave for varying control inputs.

Based on POD approximations in space with this special snapshot ensemble and a semi-implicit Euler discretization in time, we extend the techniques used in [9] and [10] to obtain an error estimate, see [4]. Due to the choice of the snapshot ensemble we can quantify the approximation properties of POD based schemes under control.

The error  $\sum_{k=1}^n \delta t \|y_k^l - y(t_k)\|_{H_0^1}^2$  between the reduced order model state  $y_k^l$  and the solution of the PDE  $y(t_k)$  can be estimated by a constant depending on  $\|u\|_{L^2}$ ,  $\|(y_k^h)\|_{L^\infty(I; H^1)}$  and  $\|y^h\|_{L^\infty(I; H^1)}$  multiplied by the projection error in the initial data, the distance to the steady state  $y_s^h$  by  $\|(y_k^h - y_s^h)\|_{L^4(I; H_0^1)}^4$  and the projection error in the snapshots.

### 3 Optimization and Numerical Results

For the optimization, the reduced order model based on POD is coupled with a Model Predictive Control scheme, see e.g. [6]. In MPC, the control actions are obtained by solving the optimal control problem over finite time intervals. Since only a first part of the resulting optimal control sequence is applied and the whole procedure is repeated, this gives a feedback control. The optimization of the finite time optimal control problem is finally carried out by a limited memory BFGS algorithm adapted to large problem sizes and bound constraints.

The effectiveness of our proposed POD-based MPC algorithm is shown in numerical experiments for the cancellation of Tollmien-Schlichting waves by plasma actuators. The optimized finite-element velocity values in the middle of the sensor area  $\Omega_o$  can be found in Figure 1. As comparison the values for the uncontrolled finite-element simulation are plotted.

**Acknowledgements** The work of Jane Ghiglieri and Stefan Ulbrich is supported by the 'Excellence Initiative' of the German Federal and State Governments and the Graduate School of Computational Engineering at Technische Universität Darmstadt.

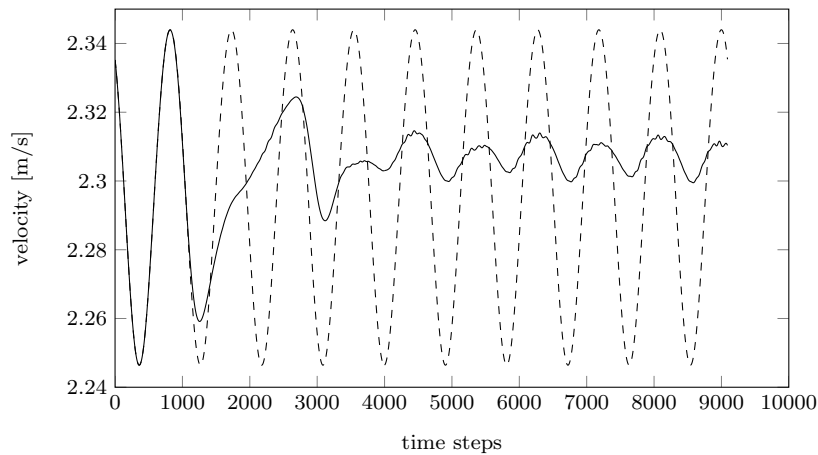


**Fig. 1** Cancellation result - uncontrolled velocity (dashed), optimized velocity (continuous).

## References

1. Afanasiev, K., Hinze, M.: Adaptive control of a wake flow using proper orthogonal decomposition. Preprint No. 648 (1999)
2. Arian, E., Fahl, M., Sachs, E.W.: Trust-Region Proper Orthogonal Decomposition for Flow Control. Technical Report (2000)
3. Diwoky, F., Volkwein, S.: Nonlinear boundary control for the heat equation utilizing proper orthogonal decomposition. In: K.H. Hoffmann, R. Hoppe, V. Schulz (eds.) Fast solutions of Discretized Optimization Problems, Internat. Ser. Numer. Math. 138, pp. 73–87. Birkhäuser, Basel (2001)
4. Ghiglieri, J., Ulbrich, S.: Optimal flow control based on POD and MPC and an application to the cancellation of Tollmien-Schlichting waves. *Optimization Methods and Software* **29**(5), 1042–1074 (2014)
5. Grundmann, S.: Transition Control using Dielectric Barrier Discharge Actuators. Ph.D. thesis, Technische Universität Darmstadt (2008)
6. Grüne, L., Pannek, J.: Nonlinear Model Predictive Control. Theory and Algorithms. Springer, London (2011)
7. Hinze, M., Kunisch, K.: On Suboptimal Control Strategies for the Navier-Stokes Equations. *ESAIM: Proceedings*, Vol. 4, Paris (1998)
8. Kunisch, K., Volkwein, S.: Control of the Burgers equation by a reduced-order approach using proper orthogonal decomposition. *J. Optim. Theory Appl.* **102**(2), 345–371 (1999)
9. Kunisch, K., Volkwein, S.: Crank-Nicolson Galerkin Proper Orthogonal Decomposition Approximations for a General Equation in Fluid Dynamics. 18th GAMM Seminar on Multigrid and related methods for optimization problems, Leipzig pp. 97–114 (2002)
10. Kunisch, K., Volkwein, S.: Galerkin Proper Orthogonal Decomposition Methods for a General Equation in Fluid Dynamics. *SIAM Journal on Numerical Analysis* **40**(2), 492–515 (2002)
11. Kunisch, K., Volkwein, S.: Proper Orthogonal Decomposition for optimality systems. *ESAIM: Mathematical Modelling and Numerical Analysis* **42**, 1–23 (2008)
12. Ravindran, S.S.: Reduced-Order Adaptive Controllers for Fluid Flows Using POD. *Journal of Scientific Computing* **15**, 457–478 (2000)

MS IV.2: Parameter Identification for Nonlinear  
Elliptic-Parabolic Systems

Authors: Lass, Oliver, Volkwein, Stefan

---

# Parameter identification for nonlinear elliptic-parabolic systems

Oliver Lass · Stefan Volkwein

**Abstract** In this work a parameter estimation problem for nonlinear systems is considered. For the numerical realization of the optimization a combination of the finite element method and a reduced order model based on proper orthogonal decomposition (POD) is utilized in an adaptive manner. Numerical examples show the efficiency of the proposed approach.

## 1 Introduction

In this work we consider a parameter estimation problem governed by a system of nonlinear coupled elliptic-parabolic partial differential equations (PDE). Systems of this type can be viewed as generalizations of mathematical models for lithium-ion batteries; see, e.g., [3, 12]. The investigated nonlinear system is motivated by the modeling of lithium-ion batteries and consists of one parabolic equation for the concentration and two elliptic equations for the

---

The authors gratefully acknowledge support by the German Science Funds *Numerical and Analytical Methods for Elliptic-Parabolic Systems Appearing in the Modeling of Lithium-Ion Batteries* (Excellence Initiative) and DFG grant VO 1658/2-1 *A-posteriori-POD Error Estimators for Nonlinear Optimal Control Problems governed by Partial Differential Equations*.

---

Oliver Lass  
Technische Universität Darmstadt  
Department of Mathematics  
Dolivostraße 15  
D-64293 Darmstadt, Germany  
E-mail: lass@mathematik.tu-darmstadt.de

Stefan Volkwein  
University of Konstanz  
Department of Mathematics and Statistics  
Universitätsstraße 10  
D-78457 Konstanz, Germany  
E-mail: stefan.volkwein@uni-konstanz.de

potentials. The measurements are given as boundary values for one of the potentials. The nonlinear systems arising from these models contain a variety of parameters. To identify those parameters and calibrate the model we formulate the following nonlinear least squares problem for the observation function  $\eta(t, \mu) = q(t, b)$  and admissible set  $\mathcal{M}_{ad}$  as

$$\min_{\mu \in \mathcal{M}_{ad}} J(\mu) = \frac{1}{2} \int_0^T |\eta(t, \mu) - q^d(t)|^2 dt, \quad (1a)$$

subject to the nonlinear PDE system

$$y_t(t, \mathbf{x}) - (c_1(\mathbf{x})y_{\mathbf{x}}(t, \mathbf{x}))_{\mathbf{x}} + \mathcal{N}(\mathbf{x}, y(t, \mathbf{x}), p(t, \mathbf{x}), q(t, \mathbf{x}); \mu) = 0, \quad (1b)$$

$$-(c_2(y(t, \mathbf{x}); \mu)p_{\mathbf{x}}(t, \mathbf{x}))_{\mathbf{x}} + \mathcal{N}(\mathbf{x}, y(t, \mathbf{x}), p(t, \mathbf{x}), q(t, \mathbf{x}); \mu) = 0, \quad (1c)$$

$$-(c_3(\mathbf{x})q_{\mathbf{x}}(t, \mathbf{x}))_{\mathbf{x}} - \mathcal{N}(\mathbf{x}, y(t, \mathbf{x}), p(t, \mathbf{x}), q(t, \mathbf{x}); \mu) = 0 \quad (1d)$$

for almost all (f.a.a.)  $(t, \mathbf{x}) \in (0, T) \times (a, b)$  together with homogeneous Neumann boundary conditions for  $y$  and  $p$ , Dirichlet-Neumann conditions for  $q$ ,  $q(t, a) = 0$  and  $q_{\mathbf{x}}(t, b) = \mathcal{I}(t)$  f.a.a.  $t \in (0, T)$ , the initial condition  $y(0, \mathbf{x}) = y_o(\mathbf{x})$  f.a.a.  $\mathbf{x} \in (a, b)$  and the target  $q^d$ . The nonlinearity under investigation is given by

$$\mathcal{N}(\mathbf{x}, z, p, q; \mu) = \begin{cases} \mu_2 \sqrt{y} \sinh(\mu_1(q - p) - \ln y) & \text{for } \mathbf{x} \in [a, s_1], \\ 0 & \text{for } \mathbf{x} \in [s_1, s_2], \\ \mu_3 \sqrt{y} \sinh(\mu_1(q - p) - \ln y) & \text{for } \mathbf{x} \in (s_2, b]. \end{cases}$$

Note that for this particular nonlinearity  $\mathcal{N}$  the system (1b) - (1d) possesses a unique weak solution for piecewise constant positive diffusion coefficients  $c_1$  and  $c_3$  and some assumptions on the admissible set  $\mathcal{M}_{ad}$  and the nonlinear diffusion coefficient  $c_2(y; \mu)$  [8, 11, 12].

## 2 Methodology

To solve the nonlinear optimization problem (1) we discretize the PDE using the finite element (FE) method. This leads to a discrete system of large dimension that is expensive to solve. In the multi-query context of an optimization strategy this will result in long runtimes. Therefore, the spatial approximation is replaced by a Galerkin scheme using proper orthogonal decomposition (POD) [7]. The basis obtained by the POD method is specifically tailored to the problem under investigation. This leads to much smaller problems. The POD basis is computed by a singular value decomposition from the solution of the nonlinear system by the method of snapshots. The reduced order model (ROM) is then obtained by projecting the FE model in the obtained subspace. Since the basis is computed with respect to one specific parameter  $\mu$  during the optimization it might be required to update the basis in order to capture the dynamics of the nonlinear system. For this an adaptive strategy is applied. This strategy uses the residual as an error indicator, i.e., the residual of the FE

model upon inserting the ROM solution. This error indicator is motivated by error estimator developed for the reduced basis method [4]. The POD basis is changed whenever the dual norm of the residual exceeds a given tolerance. In the case that the ROM is of poor quality in every iteration of the optimization process we end up using only the FE model. To obtain an efficient ROM for the nonlinear system the nonlinear term  $\mathcal{N}$  and  $c_2$  have to be affinely decomposed. Therefore, in this work the empirical interpolation method (EIM) is applied [4, 9]. The presented approach combines the FE method with a ROM. This strategy is used to speed up the computation in an optimization strategy.

To compute the necessary derivatives in optimization process we utilize the sensitivity analysis. Compared to the approach using the adjoint equation this strategy is computationally more expensive since for each parameter a linear sensitivity equation has to be solved [5]. In parametrized dynamical systems not all parameters are equally sensitive. To eliminate non identifiable parameters from problem (1) we utilize a subset selection method [1]. This method uses the obtained information from the sensitivities and the QR factorization with pivoting to extract suited parameters for the optimization. For the optimization we use a Gauss-Newton method. Note that also here the computed sensitivities are utilized.

Finally, after the optimization method terminates successfully an a posteriori error is computed to verify the solution [2, 6, 10]. This estimator only has to be evaluated if the last optimization step is performed by the ROM. In the case of a FE step this can be omitted.

### 3 Numerical results

To demonstrate the efficiency of the proposed strategy we present some numerical results. For this we briefly introduce the problem under consideration. The spatial domain is set to  $[0, 5]$  and the end time  $T = 1$ . By discretizing using the FE method we end up with a system of 6997 unknowns in space, a ROM of dimension 48 and 100 points in time. The nonlinear diffusion coefficient is set to  $c_2(y; \mu) = (1 + \mu_4 y)^3 + 1$  and the initial guess is set to  $y_0 = 1$ . Additionally the excitation term is set to  $\mathcal{I}(t) = \frac{t}{2} \sin(2\pi t)$ . For more details on the settings we refer the reader to [8, 10]. As an initial guess for the parameter estimation we choose  $\bar{\mu}^k = [1.87, -0.7k, -0.1k, 0.4k]$ ,  $k \in \{1.5, 2\}$ . The target  $q^d$  is generated numerically with  $\mu^* = [1.1, -0.7, -0.1, 0.4]$ . For the adaptive strategy we choose  $10^{-4}$  as the tolerance for the dual norm of the residuals. The optimal solution obtained by the FE and ROM are denoted by  $\mu^{N,*}$  and  $\mu^{\ell,*}$ , respectively.

In Table 1 the efficiency of the proposed strategy can be seen. For the initial guess  $\bar{\mu}^2$  the basis has to be recomputed one time, hence we end up with 2 finite element solves of the nonlinear system. Note that the optimization using the ROM, excluding the required FE solve for the basis generation, requires approximately 9 seconds. In both cases a good reduction in the computational time can be achieved. Comparing the solution obtained by the two methods

**Table 1** Optimal solution obtained by the FE approach and the adaptive algorithm using ROM. The † indicates the parameter fixed by the subset selection. In the last two columns the total expenses of the two approaches is compared by the number of nonlinear FE model solves and computation time in seconds. In parenthesis the number of linear sensitivity equation solves is indicated.

Initial	Method	$\mu^{N,*}$ and $\mu^{\ell,*}$	FE solves	CPU time
$\bar{\mu}^{1.5}$	FE	(1.100000, $-0.7^\dagger$ , $-0.100000$ , 0.400000)	8(21)	260
$\bar{\mu}^{1.5}$	ROM	(1.100003, $-0.7^\dagger$ , $-0.100000$ , 0.399995)	1( 0)	36
$\bar{\mu}^2$	FE	(1.100000, $-0.7^\dagger$ , $-0.100000$ , 0.400000)	10(21)	315
$\bar{\mu}^2$	ROM	(1.099997, $-0.7^\dagger$ , $-0.100001$ , 0.399998)	2( 0)	64

**Table 2** A posteriori error estimator for the ROM solutions obtained by the adaptive optimization strategy.

Initial	$\ \mu^{N,*} - \mu^{\ell,*}\ _2$	[6]	[2]
$\bar{\mu}^{1.5}$	0.000005	0.005945	0.008495
$\bar{\mu}^2$	0.000004	0.006375	0.002471

we can see that they perform equally well. The error estimators in Table 2, verify these results.

## References

1. M. Burth, G.C. Verghese and M. Véléz-Reyes, Subset selection for improved parameter estimation in on-line identification of a synchronous generators, *IEEE Transactions on Power Systems*, 14(1), 218–225 (1999)
2. M. Dihlmann and B. Haasdonk, Certified PDE-constrained parameter optimization using reduced basis surrogate models for evolution problems, Submitted, (2013)
3. T. Fuller, M. Doyle and J. Newman, Modeling of galvanostatic charge and discharge of the lithium ion battery/polymer/insertion cell, *Journal of the Chemical Society*, 140(6), 1526–1533 (1993)
4. M. Grepl, Certified reduced basis method for nonaffine linear time-varying and nonlinear parabolic partial differential equations, *WSPC: Mathematical Models and Methods in Applied Sciences*, 22(3), 40 (2012)
5. M. Hinze, R. Pinnau, M. Ulbrich, and S. Ulbrich, *Optimization with PDE Constraints*, Springer, Netherlands (2009)
6. E. Kammann, F. Tröltzsch and S. Volkwein, A method of a-posteriori error estimation with application to proper orthogonal decomposition. *ESAIM: M2AN*, 47, 555–581 (2013)
7. K. Kunisch and S. Volkwein, Galerkin proper orthogonal decomposition methods for parabolic problems, *Numerische Mathematik*, 90, 117–148 (2001)
8. O. Lass, Reduced-order modeling and parameter identification for coupled nonlinear PDE systems, Ph.D thesis, University of Konstanz (2014)
9. O. Lass and S. Volkwein, POD Galerkin schemes for nonlinear elliptic-parabolic systems, *SIAM Journal on Scientific Computing*, 35(3), A1271–A1298 (2013)
10. O. Lass and S. Volkwein, Parameter identification for nonlinear elliptic-parabolic systems with application in lithium-ion battery modeling, Submitted, (2013)
11. T. Seger, *Elliptic-Parabolic Systems with Application to Lithium-Ion Battery Models*, PhD thesis, University of Konstanz (2013)
12. J. Xu, J. Wu and H. Zou, On the well posedness of mathematical model for lithium-ion battery systems, *Methods and Applications of Analysis*, 13, 275–298 (2006)

MS IV.3: A-Posteriori Error Analysis and  
Optimality-System POD for Constrained Optimal  
Control

Authors: Grimm, Eva, Gubisch, Martin, Volkwein, Stefan

---

# A-Posteriori Error Analysis and Optimality-System POD for Constrained Optimal Control

Eva Grimm · Martin Gubisch · Stefan Volkwein

**Keywords** PDE constrained optimization · state constraints · model-order reduction · a-posteriori error · optimality system POD

**The state constrained optimal control problem.** Let  $V$  and  $H$  be real, separable Hilbert spaces and suppose that  $V$  is dense in  $H$  with compact embedding. By  $\langle \cdot, \cdot \rangle_H$  we denote the inner products in  $H$ . Let  $t_f > t_o \geq 0$  be the fixed end and initial times. For  $t \in [t_o, t_f]$  we introduce a time-dependent symmetric bilinear form  $a(t; \cdot, \cdot) : V \times V \rightarrow \mathbb{R}$  which is assumed to be continuous and coercive. Recall the Hilbert space  $W(t_o, t_f) = \{\varphi \in L^2(t_o, t_f; V) \mid \varphi_t \in L^2(t_o, t_f; V')\}$ . Let  $\mathcal{D}$  be an open and bounded subset of  $\mathbb{R}^d$  with  $d \in \mathbb{N}$ . Then the control space is given by  $U = L^2(\mathcal{D}; \mathbb{R}^m)$  for  $m \in \mathbb{N}$ . By  $U_{\text{ad}} \subset U$  we define the closed, convex and bounded subset

$$U_{\text{ad}} = \{u \in U \mid u_a \leq u \leq u_b \text{ in } \mathbb{R}^m \text{ almost everywhere (a.e.)}\},$$

where “ $\leq$ ” is understood componentwise in  $\mathbb{R}^m$  and  $u_a, u_b \in U$  holds with  $u_a \leq u_b$  in  $\mathbb{R}^m$  a.e. In particular, we identify  $U$  with its dual space  $U'$ . For  $u \in U_{\text{ad}}$ ,  $y_o \in H$  and  $f \in L^2(t_o, t_f; V')$  we consider the linear evolution problem

$$\begin{aligned} \frac{d}{dt} \langle y(t), \varphi \rangle_H + a(t; y(t), \varphi) &= \langle (f + \mathcal{B}u)(t), \varphi \rangle_{V', V} \quad \forall \varphi \in V \text{ a.e. in } (t_o, t_f], \\ y(t_o) &= y_o \quad \text{in } H, \end{aligned} \quad (1)$$

where  $\langle \cdot, \cdot \rangle_{V', V}$  stands for the dual pairing between  $V$  and its dual space  $V'$  and  $\mathcal{B} : U \rightarrow L^2(t_o, t_f; V')$  is a continuous, linear operator. Let us define the set of admissible states

$$\tilde{Y}_{\text{ad}} = \{y \in W(t_o, t_f) \mid y_a \leq \mathcal{I}y \leq y_b \text{ in } \mathbb{R}^n \text{ a.e.}\},$$

---

Eva Grimm, Martin Gubisch, Stefan Volkwein  
University of Konstanz, Dep. of Mathematics and Statistics, Universitätsstr. 10, 78457 Konstanz, Germany; E-mail: {Eva.Grimm, Martin.Gubisch, Stefan.Volkwein}@uni-konstanz.de

where  $\mathcal{I} : L^2(t_o, t_f; V) \rightarrow L^2(t_o, t_f; \mathbb{R}^n)$  is a bounded, linear operator with  $n \in \mathbb{N}$ ,  $y_a, y_b \in L^2(t_o, t_f; \mathbb{R}^n)$  with  $y_a \leq y_b$  in  $\mathbb{R}^n$  a.e. We introduce the Hilbert space  $\tilde{X} = W(t_o, t_f) \times U$  endowed with the natural product topology. Moreover, we define the closed and convex subset  $\tilde{X}_{\text{ad}} = \tilde{Y}_{\text{ad}} \times U_{\text{ad}} \subset \tilde{X}$ . Moreover, the cost function  $\tilde{J} : \tilde{X} \rightarrow \mathbb{R}$  is given by

$$\tilde{J}(y, u) = \frac{1}{2} \int_{t_o}^{t_f} \sigma_Q \|y(t) - y_Q(t)\|_H^2 + \sigma_u \|u(t)\|_{\mathbb{R}^m}^2 dt + \frac{\sigma_\Omega}{2} \|y(t_f) - y_\Omega\|_H^2$$

for  $x = (y, u) \in \tilde{X}$ , where  $\sigma_Q, \sigma_\Omega$  are nonnegative weighting parameters,  $\sigma_u \geq 0$  is a regularization parameter and  $y_Q \in L^2(t_o, t_f; H)$ ,  $y_\Omega \in H$  are given desired states. Then, we consider the following convex optimal control problem

$$\min \tilde{J}(x) \text{ subject to } x \in \mathcal{F}(\mathbf{P}) = \{(y, u) \in \tilde{X}_{\text{ad}} \mid (y, u) \text{ satisfies (1)}\} \quad (\mathbf{P})$$

with the set  $\mathcal{F}(\mathbf{P}) = \{x = (y, u) \in \tilde{X}_{\text{ad}} \mid (y, u) \text{ satisfies (1)}\}$  of feasible solutions.

**The Lavrentiev regularization.** It is well-known that the (sufficient) first-order optimality conditions for  $(\mathbf{P})$  involve a measure-valued Lagrange multiplier associated with the state constraint  $\bar{y} \in \tilde{Y}_{\text{ad}}$ ; see [4, Section 1.7.3]. To develop a fast numerical solution methods (by combining semismooth Newton techniques with reduced-order modelling) we apply a Lavrentiev regularization of the state constraints. For that purpose we introduce an additional (artificial) control variable and approximate the pure state by mixed control-state constraints, which enjoy  $L^2$ -regularity; see, e.g., [9]. Instead of the Hilbert space  $\tilde{X}$  we consider the Hilbert space  $X = W(t_o, t_f) \times U \times L^2(t_o, t_f; \mathbb{R}^n)$ , again supplied with the product topology. For  $\varepsilon > 0$  the subset  $\tilde{X}_{\text{ad}}$  is replaced by the closed and convex subset

$$X_{\text{ad}}^\varepsilon = \{(y, u, w) \in X \mid y_a \leq \varepsilon w + \mathcal{I}y \leq y_b \text{ in } \mathbb{R}^n \text{ a.e., } u \in U_{\text{ad}}\}.$$

For a chosen weight  $\sigma_w > 0$  we replace  $\tilde{J}$  by  $J : X \rightarrow \mathbb{R}$  with

$$J(y, u, w) = \tilde{J}(y, u) + \frac{\sigma_w}{2} \int_{t_o}^{t_f} \|w(t)\|_{\mathbb{R}^n}^2 dt, \quad x = (y, u, w) \in X.$$

Now the regularized optimal control problem has the following form

$$\min J(x) \text{ subject to } x \in \mathcal{F}(\mathbf{P}^\varepsilon) = \{(y, u) \in X_{\text{ad}}^\varepsilon \mid (y, u) \text{ satisfies (1)}\}. \quad (\mathbf{P}^\varepsilon)$$

**The POD method.** Optimal control problems for partial differential equations (like  $(\mathbf{P}^\varepsilon)$ ) are often hard to tackle numerically because their discretization leads to very large scale optimization problems. Therefore different techniques of model reduction were developed to approximate these problems by smaller ones that are tractable with less effort. We apply the method of *Proper orthogonal decomposition* (POD), where the basis functions contain information from the solutions of the dynamical system at pre-specified time-instances,

so-called snapshots. Due to a possible linear dependence or almost linear dependence the snapshots themselves are not appropriate as a basis. Hence a singular value decomposition is carried out and the leading generalized eigenfunctions are chosen as a basis, referred to as the POD basis.

**A-posteriori error analysis.** In contrast to methods of balanced truncation type, the POD method is somehow lacking a reliable a-priori error analysis. Unless its snapshots are generating a sufficiently rich state space, it is not a-priorly clear how far the optimal solution of the POD problem is from the exact one. On the other hand, the POD method is a universal tool that is applicable also to problems with time-dependent coefficients or to nonlinear equations. Moreover, by generating snapshots from the real (large) model, a space is constructed that inherits the main and relevant physical properties of the state system. This, and its ease of use makes POD very competitive in practical use, despite of a certain heuristic flavor. Based on a perturbation argument [1] a computationally a-posteriori error estimate is derived how far the suboptimal (POD) solution to  $(\mathbf{P}^\varepsilon)$  is from the (unknown) exact optimal solution for chosen regularization  $\varepsilon > 0$ . The error analysis is related to the results in [3, 5, 10].

**Optimality system POD.** The accuracy of the reduced-order model can be controlled by the a-posteriori error analysis presented in the previous subsection. However, if the POD basis is created from a reference trajectory containing features which are quite different from those of the optimally controlled trajectory, a rather huge number of POD ansatz functions have to be included in the reduced-order model. This fact may lead to non-efficient reduced-order models and numerical instabilities. To avoid these problems the POD basis is generated in an initialization step utilizing *optimality system POD* (OS-POD); see [6] and [7, 8]. In OS-POD the POD basis is updated in the direction of the minimum of the cost. We propose to consider an extended problem, has the property that the associated POD reduced system is computed from the trajectory corresponding to the optimal control and thus the problem of unmodelled dynamics is removed. Hence, the POD basis is changed during the optimization; see Figure fig1. We investigate the combination of OS-POD and a-posteriori error analysis; compare [2, 3, 11]; see Figure 2.

## References

1. A.L. Dontchev, W.W. Hager, A.B. Poore, and B. Yang. Optimality, stability, and convergence in nonlinear control. *Applied Math. and Optimization*, 31:297–326, 1995.
2. E. Grimm. *Optimality System POD and A-Posteriori Error Analysis for Linear-Quadratic Optimal Control Problems*. Master thesis, University of Konstanz, 2013.
3. M. Gubisch and S. Volkwein. POD a-posteriori error analysis for optimal control problems with mixed control-state constraints. *Comput. Optim. Appl.*, 58:619–644, 2014.
4. M. Hinze, R. Pinnau, M. Ulbrich, and S. Ulbrich. *Optimization with PDE Constraints*. Springer-Verlag, Berlin, 2009.
5. E. Kammann, F. Tröltzsch, and S. Volkwein. A method of a-posteriori error estimation with application to proper orthogonal decomposition. *ESAIM Math. Modell. Numer. Anal.*, 47:555–581, 2013.

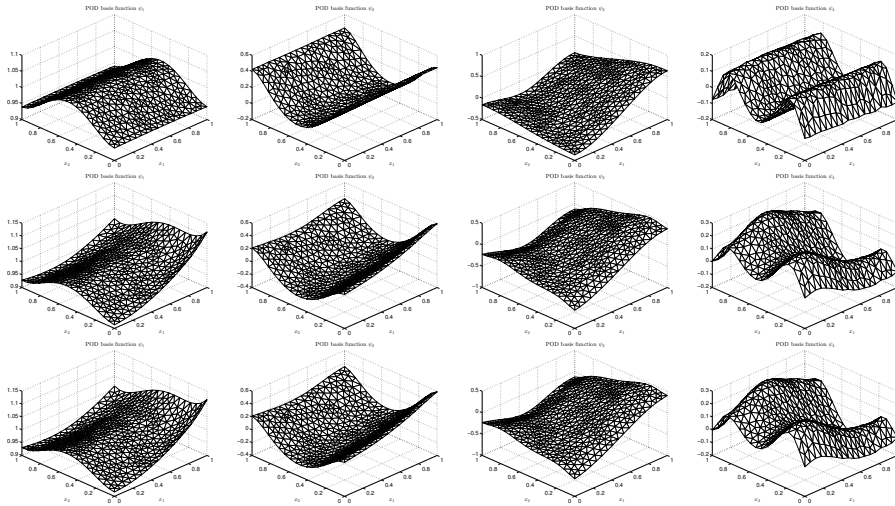


**Fig. 1** First four POD basis functions associated with the uncontrolled heat equation (top), with the control (middle) and with the control after two OS-POD gradient steps.

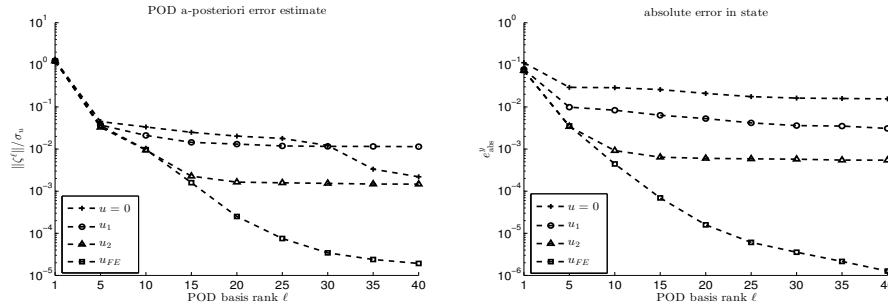


**Fig. 2** Comparison of errors for POD suboptimal solutions (left: a-posteriori error, right: absolute error in the state). The snapshots for the POD basis are generated either with  $u = 0$ ,  $u_k$  after  $k$  OS-POD gradient steps or the exact solution  $u_{FE}$ .

6. K. Kunisch and S. Volkwein. Proper orthogonal decomposition for optimality systems. *ESAIM Math. Modell. Numer. Anal.*, 42:1–23, 2008.
7. K. Kunisch and M. Müller. Uniform convergence of the POD method and applications to optimal control. Submitted, 2014. [math.uni-graz.at/kunisch/papers/KK\\_281.pdf](http://math.uni-graz.at/kunisch/papers/KK_281.pdf)
8. M. Müller. *Uniform Convergence of the POD Method and Applications to Optimal Control*. Ph.D thesis, University of Graz, 2011.
9. F. Tröltzsch. Regular Lagrange multipliers for control problems with mixed pointwise control-state constraints. *SIAM Journal on Optimization*, 22:616–634, 2005.
10. F. Tröltzsch and S. Volkwein. POD a-posteriori error estimates for linear-quadratic optimal control problems. *Comput. Optim. Appl.*, 44:83–115, 2009.
11. S. Volkwein. Optimality system POD and a-posteriori error analysis for linear-quadratic problems. *Control and Cybernetics*, 40:1109–1125, 2011.

MS IV.4: Interfacing between Dynamics and Optics  
for Reduced Models of Deformable Optical Elements

Authors: Wengert, Nicolai, Eberhard, Peter

---

# Interfacing between dynamics and optics for reduced models of deformable optical elements

Nicolai Wengert · Peter Eberhard

**Abstract** High-precision optical systems have extremely small tolerances. Even very small perturbations can yield unacceptable errors in a projected image. To avoid this, it is necessary to estimate the influence of dynamical excitations and elastic deformations of lenses on the imaging. If it is possible to determine this influence, procedures can be developed to react on the perturbations. Controlling an imaging process of high-performance optics requires systematic interfacing between the mechanical model and the optical model. Here, an overview is provided on basic issues concerning deformable lenses.

## 1 Introduction

During the last decades, optical systems have been developed which allow higher and higher resolutions. These systems are especially used in the mass production of microchips, i.e. in optical lithography. Lithography objectives project the structures of integrated circuits on a light resistive coating. In a next step, it is possible to process the projected structures. Since the structure size is supposed to decrease with any newly designed objective, accuracy demands increase correspondingly. Unfortunately, also the sensitivities to dynamical perturbations increase.

There are different possibilities to make the imaging process more robust, e.g. by introducing active and passive vibration damping. However, the higher the accuracy demands, the higher the effort to meet them. Consequently, the dynamical-optical performance should be included during developing the mechanical part of new objectives. This requires methods to combine the two different fields dynamics and optics.

In the following, also image quality criteria will be summarized. These criteria are required to both qualify and quantify the performance for certain states of the dynamical-optical system. Next, interfacing between dynamics and optics will be discussed. According to this, an example will be given where a single optical component will be investigated.

## 2 Quality criteria for dynamical-optical systems

An optical system projects an object from the object plane to the image plane. If the optical system is perturbed, it produces two characteristic aberrations, i.e. im-

---

Nicolai Wengert, Peter Eberhard  
Pfaffenwaldring 9, 70569 Stuttgart  
Tel.: +49-711-685-66627  
E-mail: [nicolai.wengert, peter.eberhard]@itm.uni-stuttgart.de

age errors, see Fig. 1. For a mathematical description of the aberrations, the object is discretized into point light sources, so-called fields. A point light source is represented by a ray bundle. Typically, the center ray of the ray bundle is called the chief ray. The first characteristic aberration is the image shift which is quantified by chief ray deviation (CRD) in the first instance. The other aberration type is blurring which is quantified by wavefront aberration (WFA).

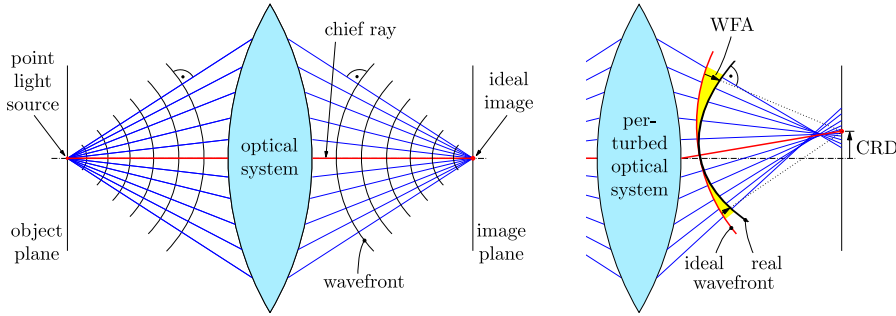


**Fig. 1** Ideal imaging (left) and imaging of a perturbed optical system yielding chief ray deviation (CRD) and wavefront aberration (WFA).

Wavefront aberrations can be described by means of polynomials. In the case of a circular pupil, Zernike polynomials are commonly used [1, 2]. Here, the notation of [3] is chosen, see also [4]. The wavefront aberration reads

$$\Delta W = W_{real} - W_{ideal} = \sum_j c_j Z_j, \quad (1)$$

where  $W_{real}$  is the real wavefront,  $W_{ideal}$  is the ideal wavefront, and  $c_j$  is the amplitude of the  $j$ -th Zernike polynomial  $Z_j$ . In addition to the chief ray deviation, a deviation of the intensity centroid is included in the wavefront aberration. The intensity centroid is named line of sight (LOS). Its deviation is the sum of the chief ray deviation and the small additional shift,

$$\begin{bmatrix} \Delta x_{los} \\ \Delta y_{los} \end{bmatrix} = \begin{bmatrix} \Delta x_{crd} \\ \Delta y_{crd} \end{bmatrix} - 2 \frac{\lambda}{NA} \begin{bmatrix} c_2 \\ c_3 \end{bmatrix}, \quad (2)$$

where  $\lambda$  is the wavelength of the light and  $NA$  the numerical aperture. The aberrations of a single field  $i$  can be summarized in

$$\mathbf{a}_i = [\Delta x_{los}, \Delta y_{los}, c_4, c_5, c_6, \dots]^T. \quad (3)$$

The coefficients  $c_1, c_2, c_3$  are not required since they have no influence on blurring.

### 3 Interfacing between dynamics and optics

For the mechanical modeling, Elastic Multibody Systems (EMBS) can be used. Due to the very small vibration amplitudes, the equations of motion are linear [6],

$$\mathbf{M} \cdot \ddot{\mathbf{q}}(t) + \mathbf{D} \cdot \dot{\mathbf{q}}(t) + \mathbf{K} \cdot \mathbf{q}(t) = \mathbf{B} \cdot \mathbf{u}(t), \quad (4)$$

$$\mathbf{a}(t) = \mathbf{C}_a \cdot \mathbf{q}(t), \quad (5)$$

with the generalized coordinates  $\mathbf{q}$ , mass matrix  $\mathbf{M}$ , damping matrix  $\mathbf{D}$ , stiffness matrix  $\mathbf{K}$ , input matrix  $\mathbf{B}$ , inputs  $\mathbf{u}$ , and the dynamical-optical output matrix  $\mathbf{C}_a$ .

The matrix  $\mathbf{C}_a$  allows a direct computation of the aberrations. Since all generalized coordinates cause specific aberrations, these dynamical-optical sensitivities can be summarized in the matrix

$$\mathbf{C}_a = \begin{bmatrix} \mathbf{a}_{1,1} & \dots & \mathbf{a}_{1,n_q} \\ \vdots & & \vdots \\ \mathbf{a}_{n_f,1} & \dots & \mathbf{a}_{n_f,n_q} \end{bmatrix}, \quad (6)$$

where  $\mathbf{a}_{i,j}$  are the aberrations at the  $i$ -th field for a unit amplitude of the  $j$ -th generalized coordinate exclusively. It is regardless whether the type of generalized coordinate represents a rigid or elastic degree of freedom (DOF). In the case of elastic DOFs,  $\mathbf{a}_{i,j}$  corresponds to a certain shape function resulting from model order reduction. It should be noted that the type of model reduction has no influence on the computation procedure of  $\mathbf{C}_a$ . Nevertheless, it does influence the accuracy of the mechanical model.

Computing the sensitivity matrix  $\mathbf{C}_a$  requires ray tracing. As long as there are only spherical surfaces and rigid body motion, the ray paths can be calculated analytically. For considering deformations, the intersections of rays and surfaces have to be computed numerically by means of a Newton-Raphson method. Here, an important issue is the surface approximation. Surfaces are discretized due to the Finite Element modeling. However, discrete surfaces yield artefacts in ray tracing simulations. To ensure a smooth surface, polynomial interpolation can be used. For this, an appropriate set of polynomials has to be chosen depending on the shape of the surface. For example, for circular-shaped surfaces, Zernike polynomials are a good choice. Rectangular-shaped surfaces could be approximated by means of B-Splines.

If a lens gets deformed and its optical properties are sensitive to stresses, the 2D case of surfaces has to be enhanced to a 3D case. Since most lenses have a circular base, cylindrical polynomials could be used, see [5]. In this case, the path of the ray paths through a lens have to be solved by means of differentiation. This procedure is called gradient index ray tracing.

#### 4 Example

For testing interfacing methods between dynamics and optics, it is helpful to investigate and understand a small system first. Figure 2 shows a single component belonging to a lithography objective. This model enables benchmark simulations to compare different approaches for surface approximation methods, or to compute the influence of stress effects yielding a refraction index variation.

A deformed state considered in the optical model can be seen in Fig. 3. The figure also shows the resulting wavefront aberration map and an image simulation of the letter 'F' which is, obviously, blurred.

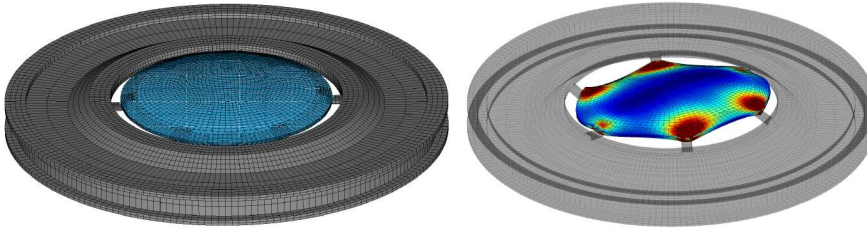


**Fig. 2** Optical component consisting of a lens and its holding device: initial configuration (left) and 2nd mode with visualization of the refraction index variation (right).

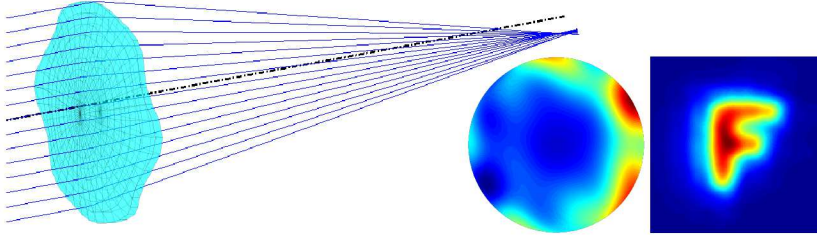


**Fig. 3** The lens in a deformed state (left) with the resulting wavefront aberration (center) and an image simulation of the letter 'F' (right).

## 5 Conclusions

Combining dynamics and optics by means of the dynamical-optical output matrix  $C_a$  appears to be a promising method. It provides a direct correlation between degrees of freedom and aberrations. In combination with the Floating Frame of Reference Approach,  $C_a$  has to be computed only once for a certain optical system, independent of model reduction techniques. This is a clear advantage of this method, especially for developing active aberration suppression.

**Acknowledgements** The authors would like to thank the German Research Foundation (DFG) for financial support of the project within the Cluster of Excellence in Simulation Technology (EXC 310, SimTech) at the University of Stuttgart. Special thanks for useful discussions and advice go to the Institute of Applied Optics (ITO), Holger Gilbergs and Wolfgang Osten. All this support is highly appreciated.

## References

1. Born, M., Wolf, E.: Principles of Optics. Cambridge University Press, Cambridge (1999)
2. Gross, H. (ed.): Handbook of Optical Systems Vol. 3 - Aberration Theory and Correction of Optical Systems. Wiley, Weinheim (2005)
3. Noll, R.: Zernike polynomials and atmospheric turbulence. *Journal of the Optical Society in America* **66**(3), 207–211 (1976)
4. Wengert, N., Eberhard, P.: Optimization of the dynamical behavior of high-performance lens systems to reduce dynamic aberrations. *The Archive of Mechanical Engineering* **58**(4), 407–423 (2011)
5. Wengert, N., Eberhard, P.: Using dynamic stress recovery to investigate stress effects in the dynamics of optical lenses. *Proceedings of the 7th ICCSM, Zadar, Croatia* (2012)
6. Wengert, N., Nefzi, M., Eberhard, P., Geuppert, B.: Dynamics in lithographic projection objectives. *Multibody System Dynamics* **30**(2), 233–245 (2013)

MS IV.5: Fast Evaluation of Implied Volatility  
Surfaces with Reduced Order Models

Authors: Sachs, Ekkehard, Schneider, Marina

---

# Fast Evaluation of Implied Volatility Surfaces with Reduced Order Models

Ekkehard Sachs · Marina Schneider

**Abstract** Implied volatility is a key value in financial mathematics. We discuss some of the pros and cons of the standard ways to compute this quantity, i.e. numerical inversion of the well-known Black-Scholes formula or asymptotic expansion approximations, and propose a new way to directly calculate the implied variance in a local volatility framework based on the solution of a quasilinear degenerate parabolic partial differential equation. Since the numerical solution of this equation may lead to large nonlinear systems of equations and thus high computation times compared to the classical approaches, we apply model order reduction techniques to achieve computational efficiency. Our method of choice for the derivation of a reduced-order model will be Proper Orthogonal Decomposition (POD). This strategy is additionally combined with the Discrete Empirical Interpolation Method (DEIM) to deal with the nonlinear terms.

**Keywords** Implied volatility · local volatility models · partial differential equations · model order reduction · proper orthogonal decomposition · discrete empirical interpolation method

## 1 Introduction

Volatility is a crucial input parameter in the famous Black-Scholes pricing formula and therefore the problem of inverting this relation is of great practical interest to traders. The resulting *implied volatility* is often seen as an estimated

---

E. Sachs  
Department of Mathematics, University of Trier, 54286 Trier, Germany  
Tel.: +49-651-201-3474  
Fax: +49-651-201-3973  
E-mail: sachs@uni-trier.de

M. Schneider  
Department of Mathematics, University of Trier, 54286 Trier, Germany

average future volatility and a widely used factor in financial markets research. As it is not directly observable at the market and there is no exact analytic formula available, the efficient numerical computation of this quantity is an important task.

In this work, we present a new way to efficiently calculate the implied variance in a local volatility framework based on the solution of a quasilinear parabolic partial differential equation. In general, the solution of this equation via Finite-Differences or Finite-Element methods will result in the solution of large nonlinear systems. These systems are expensive to solve and lead to high computation times compared to the classical approaches for the computation of the implied volatility. Therefore we propose to use model order reduction techniques to approximate the problem in a lower-dimensional subspace.

In the following we first review the existing methods to calculate the implied volatility, before we introduce the reduced order model approach.

## 2 Existing methods to compute the implied volatility

In the present paper, we address the problem of computing the implied volatility surface in a local volatility framework. Local volatility models, as proposed by [6] replace the constant Black-Scholes volatility by a deterministic function depending on state and time. It is assumed that the dynamics of the price  $S_t$  of the underlying asset at time  $t$  are governed by the stochastic differential equation

$$dS_t = rS_t dt + \bar{\sigma}(S_t, t)S_t dW_t, \quad S_0 = s_0. \quad (1)$$

Here  $r$  denotes the risk-free interest rate and  $W$  is a standard Brownian motion. For a given local volatility function  $\bar{\sigma}$  we are interested in computing the implied volatility of European call options as a function of strike and maturity. The classical approaches for its calculation can be divided into two main categories: Iterative approaches and approximation formulas.

Iterative methods present the most common approach. They use the fact that, by definition, the implied volatility can be inferred from computed option prices in a given model by inversion of the analytic Black-Scholes pricing formula for European call options. Obviously, the iterative approach is split into two steps. In a first step, the corresponding call price for each strike price and each maturity has to be calculated. It is well-known that these prices can be computed efficiently as the solution of a linear partial differential equation, as explained in [1]. After the determination of the option prices, the next step is the inversion of the Black-Scholes formula which has to be done numerically, using root finding algorithms like Newton's method. One drawback of the iterative approach is that the inversion is known to be computationally difficult near expiry and far from the money. These difficulties are caused by the low vega of the corresponding options. Furthermore, this procedure can be time-consuming if many implied volatilities have to be provided, since the numerical inversion has to be done for all strike prices and maturities.

Another way to compute the implied volatility is represented by the approximation formula approach. There has been considerable interest in these methods over the last years, cf. [2]. One approach especially suited for local volatility models is presented in [8]. There, the heat-kernel expansion of the transition density function of the pricing process is used to obtain an expansion in time-to-expiration of the implied volatility  $\sigma^I(T, K)$  of an option with expiry date  $T$  and strike  $K$  at time  $t$  of the form

$$\sigma^I(T, K) \approx c^0(K) + c^1(K) \cdot (T - t) + c^2(K) \cdot (T - t)^2 + o((T - t)^2). \quad (2)$$

This formula is straightforward to implement and can be evaluated quickly. Unfortunately, it is not suited for longer maturities and the local volatility function is required to be smooth to obtain good results.

### 3 A Reduced Order Model for the Implied Variance

Let  $\sigma^I(K, T)$  denote the implied volatility of a European call option with strike price  $K$  and maturity  $T$  at a fixed time  $t$  with spot price  $S_t = s$ . In the following we will use as transformed variables the time to expiration  $\tau := T - t$  and the log forward moneyness  $x := \ln(\frac{K}{F_\tau})$ , where  $F_\tau = e^{r\tau}s$  denotes the forward price of the underlying. Furthermore, we define a function  $\varphi$  such that  $\sigma^I(K, T) = \varphi(\ln(K/F_\tau), \tau) = \varphi(x, \tau)$  for all  $K > 0, T \in (0, \infty)$ . This function is given as the solution of a partial differential equation, see [3].

**Theorem 1** *Let the local volatility function  $\sigma$  be a globally bounded uniformly continuous function and  $\underline{\sigma}, \bar{\sigma}$  constants such that  $0 < \underline{\sigma} \leq \sigma(x, \tau) \leq \bar{\sigma} < \infty$  for all  $x \in \mathbb{R}, \tau \in [0, \tau_{max}]$ . Then:*

i)  $\varphi$  lies in  $W_{loc}^{2,1;p}(\Omega)$  for all  $1 < p < \infty$  and satisfies

$$\begin{aligned} 2\tau\varphi\varphi_\tau + \varphi^2 - \sigma^2(x, \tau) \left(1 - x \frac{\varphi_x}{\varphi}\right)^2 \\ - \sigma^2(x, \tau)\tau\varphi\varphi_{xx} + \frac{1}{4}\sigma^2(x, \tau)\tau^2\varphi_x^2 = 0 \end{aligned} \quad (3)$$

a. e. in  $\Omega$ .

ii) In the limit  $\tau \rightarrow 0$ , the implied volatility is the harmonic mean of the local volatility  $\lim_{\tau \rightarrow 0} \varphi(x, \tau) = \left(\int_0^1 \frac{1}{\sigma(sx, 0)} ds\right)^{-1}$  uniformly in  $x \in \mathbb{R}$ .

iii) Given continuous functions  $\sigma_+$  and  $\sigma_-$  such that  $\lim_{x \rightarrow \infty} \sigma(x, \tau) = \sigma_+(\tau)$  and  $\lim_{x \rightarrow -\infty} \sigma(x, \tau) = \sigma_-(\tau)$  locally uniformly in  $\tau$ , then

$$\lim_{x \rightarrow \pm\infty} \varphi(x, \tau) = \sqrt{\frac{1}{\tau} \int_0^\tau \sigma_\pm^2(s) ds}.$$

Equation (3) will hereafter be referred to as the implied volatility partial differential equation (IV PDE). To simplify equation (3), one can alternatively consider the implied variance  $\psi = \varphi^2$ .

For the numerical solution of this partial differential equation a finite difference scheme can be applied. Therefore we have to replace the space domain

by a bounded domain and choose a partition of the space interval with  $N$  discretization points. Applying central difference quotients in space direction for the diffusion term plus an upwinding scheme to avoid oscillation issues for the convection term results in a nonlinear,  $N$ -dimensional system of ordinary differential equations (ODEs) of the form

$$\dot{y}(\tau) = A(\tau)y(\tau) + f(\tau, y(\tau)) \quad \forall \tau \in (0, T_{max}], \quad y(0) = y^0 \quad (4)$$

with  $A(\tau) \in \mathbb{R}^{N \times N}$  and a nonlinear function  $f : (0, T_{max}] \times \mathbb{R}^N \rightarrow \mathbb{R}^N$ . To solve the system (4) an appropriate time-stepping scheme is necessary. For stability reasons it is advisable to utilize implicit discretization methods which require the solution of a nonlinear system of  $N$  equations in each time step. For this purpose root-finding algorithms like Newton's method can be used. If the number of space discretization steps is high, the solution of the large nonlinear systems is expensive and leads to high computation times compared to the classical approaches. Therefore we propose to use model order reduction techniques to approximate the problem in a lower-dimensional subspace.

A popular model reduction technique is *proper orthogonal decomposition* (POD), see e.g. [10], [11], [12]. This method is very efficient for affine systems, but for nonlinear systems it has the drawback that the evaluation of the projected nonlinear term in general still depends on the complexity of the evaluation of the original system. This effect can be circumvented by means of the *Discrete Empirical Interpolation Method* (DEIM), see [4], which provides an approximation of the nonlinear term in a separate low-dimensional subspace.

Compared to other approaches for the computation of the implied volatility, as the inversion of the Black-Scholes formula and asymptotic expansion approximations, the reduced order model (ROM) approach has the advantage that it gives good results for all option maturities. In contrast, the inversion of the Black-Scholes formula will be numerically difficult for very small maturities, because of the low vega of the corresponding options, and the asymptotic expansion formula is not suited for longer maturities.

Furthermore the computation time of the ROM approach is independent of the number of requested implied volatilities. One solution of equation (3) gives the implied volatilities on the whole discretization grid. In contrast, the computation times of the asymptotic expansion approach and the iterative approach increase with the requested number of implied volatilities, since the inversion of the Black-Scholes formula has to be done for each strike and each maturity and the coefficients of the expansion formula have to be computed for all different strikes. Nevertheless, the asymptotic expansion approach is always much faster than the other ones, but one has to keep in mind that, in many examples, it fails for longer maturities. Comparing the inversion of the Black-Scholes formula and the ROM approach, the inversion takes less time for a small number of requested implied volatilities, but for large numbers it will be clearly slower.

## References

1. Y. Achdou & O. Pironneau: *Computational Methods for Option Pricing*. Philadelphia: SIAM (2005)
2. L. Andersen & A. Lipton: Asymptotics for exponential Lévy processes and their volatility smile: Survey and new Results, *International Journal of Theoretical and Applied Finance* 16 (1), 1350001.1 – 1350001.98 (2013)
3. H. Berestycki, J. Busca & I. Florent: Asymptotics and calibration of local volatility models, *Quantitative Finance* 2 (1), 61–69 (2002)
4. S. Chaturantabut & D. C. Sorensen: Nonlinear model reduction via discrete empirical interpolation, *SIAM Journal on Scientific Computing* 32 (5), 2737–2764 (2010)
5. R. Cont, N. Lantos & O. Pironneau: A reduced basis for option pricing, *SIAM Journal on Financial Mathematics* 2 (1), 287–316 (2011)
6. B. Dupire: Pricing with a smile, *Risk Magazine* 7 (1), 18–20 (1994)
7. J. Gatheral: *The Volatility Surface: A Practitioner's Guide*. Hoboken, NJ : Wiley (2006)
8. J. Gatheral, E. P. Hsu, P. Laurence, C. Ouyang & T.-H. Wang: Asymptotics of implied volatility in local volatility models, *Mathematical Finance* 22 (4), 591–620 (2012)
9. P. Henry-Larbodère: *Analysis, Geometry, and Modeling in Finance: Advanced Methods in Option Pricing* (Financial mathematics series) New York: Chapman and Hall/CRC Taylor and Francis Group (2009)
10. K. Kunisch & S. Volkwein: Galerkin proper orthogonal decomposition methods for parabolic problems, *Numerische Mathematik* 90 (1), 117–148, (2001)
11. M. Rathinam & L. R. Petzold: A new look at proper orthogonal decomposition, *SIAM Journal on Numerical Analysis* 41 (5), 1893–1925, (2003)
12. E. W. Sachs & S. Volkwein: POD-Galerkin approximations in PDE-constrained optimization, *GAMM-Mitteilungen* 33 (2), 194–208 (2010)

MS IV.6: Certified Parameter Optimization for  
Parametrized PDEs with Reduced Basis Surrogate  
Models

Authors: Dihlmann, Markus, Haasdonk, Bernard

---

# Certified Parameter Optimization for Parametrized PDEs with Reduced Basis Surrogate Models

Markus Dihlmann · Bernard Haasdonk

**Abstract** Solving PDE-constrained parameter optimization problems with arbitrary output functionals may be quite expensive when using standard PDE-solvers. Instead, we use Reduced Basis (RB) surrogate models for approximately solving the optimization problem. Ingredients of our scheme comprise RB-spaces for the solution and its sensitivity derivatives as well as rigorous a-posteriori error bounds for the solution, derivatives, output functional and the suboptimality of the parameters. Experiments on a stationary diffusion and an instationary convection-diffusion problem demonstrate the benefits of the approach.

**Keywords** Reduced Basis Methods · Parameter Optimization · PDE-Constrained Optimization · A-Posteriori Error Estimation

## 1 Introduction

We consider the parameter optimization problem

$$(\mathbb{P}) = \begin{cases} \min_{\boldsymbol{\mu}} J(u(\boldsymbol{\mu})) \\ \text{s.t.} \\ \mathbb{E}(\boldsymbol{\mu}) \text{ is solved.} \end{cases}$$

---

We acknowledge the Baden-Württemberg Stiftung gGmbH for funding as well as the German Research Foundation (DFG) for financial support of the project within the Cluster of Excellence in Simulation Technology (EXC 310/1) at the University of Stuttgart.

---

M. Dihlmann · B. Haasdonk  
Institute of Applied Analysis and Numerical Simulation  
Pfaffenwaldring 57  
D-70569 Stuttgart  
Germany  
Tel.: +49-(0)711-685-65542  
Fax: +49-(0)711-685-65507  
E-mail: dihlmann,haasdonk@mathematik.uni-stuttgart.de

where the functional  $J$  evaluates the solution  $u(\boldsymbol{\mu})$  to a parametrized partial differential equation (P<sup>2</sup>DE) denoted by  $\mathbb{E}(\boldsymbol{\mu})$  depending on the parameter  $\boldsymbol{\mu} \in \mathbb{R}^p$  with  $p \in \mathbb{N}$ . We successfully treated different PDE settings with our approach. In [4] we handled the case of  $\mathbb{E}(\boldsymbol{\mu})$  being a general parameterized linear evolution equation with linear output functional. In [5] we considered general parametrized stationary elliptic PDEs with nonlinear output functionals.

This kind of parameter optimization problem with a PDE-constraint can be found in numerous engineering applications. If the underlying model is complex, a discretization of the governing equation can lead to a large-scale discrete optimization problem causing extensively long computation times for solving the optimization problem. In other cases the problem may not be solvable under real-time requirements.

In order to accelerate the optimization, one possible approach is to replace the discretized PDE model by a reduced order surrogate model obtained by a model reduction technique like POD or reduced basis (RB) methods, cf. [18,9]. In the optimization context POD as well as RB methods have already been introduced, namely to solve optimal control problems, e.g., [3,6,19,20] and parameter optimization problems, e.g., [14,16,17]. In our work we will use a reduced basis surrogate model to approximate the behaviour of the P<sup>2</sup>DE, but in contrast to the latter references we will also provide a more detailed error estimation, including as a main result the certification of the optimal parameters found by the reduced optimization in an online-efficient way, i.e. the error estimator does not require any high dimensional operations.

The work we present here is not limited to one specific numerical optimization scheme and many techniques can be applied (gradient descent, SQP, trust region, etc). For some optimization schemes derivative information of the functional, e.g. the gradient or the Hessian, is needed. Essentially, there are two ways to obtain this information efficiently: the adjoint approach, see for example [2,7,11,12] and the sensitivity approach, cf. [1,15,13]. When using the adjoint approach in combination with the reduced basis method, one would have to build up a new reduced basis for every new functional [3,6,10]. Therefore, in our work we use the second possibility to calculate the functional gradient by solving sensitivity PDEs. Using the sensitivity approach gives us more flexibility in the use of the reduced model. In contrast to the adjoint approach the reduced basis surrogate model once constructed can be used for all choices of functionals. Furthermore we easily obtain higher order derivative information of the functional like Hessians for example. This approach comprises additional RB spaces for the sensitivity derivatives, all constructed via variants of the Greedy/POD-Greedy procedure, cf. [8].

Although solving the optimization problem with a reduced basis surrogate model is in general much faster, the found solution can be suboptimal due to the approximative nature of the surrogate model. In order to control this suboptimality we will not only provide rigorous error bounds for the functional and the functional gradient as in [16] but we will also derive rigorous error bounds for the derivative solutions and the optimal parameters. Thereby

we can provide a certification of the optimal parameters obtained by the optimization process with the reduced basis surrogate model. Experiments on a parametrized linear time-variant diffusion-advection problem and a linear elliptic problem with nonlinear output demonstrate the applicability of the approach. For more details we refer to [4,5].

## References

1. Borggaard, J. and Burns, J. (1997). A PDE sensitivity equation method for optimal aerodynamic design. *Journal of Computational Physics*, 136, 366–384.
2. Bui-Thanh, T., Willcox, K., and Ghattas, O. (2008). Model reduction for large-scale systems with high-dimensional parametric input space. *SIAM Journal on Scientific Computing*, 30(6), 3270–3288.
3. Dede, L. (2011). Reduced basis method and a posteriori error estimation for parametrized optimal control problems with control constraints. *Journal of Scientific Computing*.
4. Dihlmann, M. and Haasdonk, B. (2013). Certified pde-constrained parameter optimization using reduced basis surrogate models for evolution equations. Technical report, University of Stuttgart.
5. Dihlmann, M. and Haasdonk, B. (2013). Certified Nonlinear Parameter Optimization with Reduced Basis Surrogate Models. *Proc. Appl. Math. Mech.*, 13, 3–6.
6. Grepl, M. and Kärcher, M. (2011). Reduced basis a posteriori error bounds for parametrized linear-quadratic elliptic optimal control problems. *C.R. Acad. Sci. Paris, Ser. I*, 349, 873–877.
7. Griesse, R. and Vexler, B. (2007). Numerical sensitivity analysis for the quantity of interest in PDE-constrained optimization. *SIAM J. of Scientific Computing*, 29(1), 22 – 48.
8. Haasdonk, B. (2013). Convergence rates of the POD-Greedy method. *ESAIM: Mathematical Modelling and Numerical Analysis*, 47, 859 – 873.
9. Haasdonk, B. and Ohlberger, M. (2008). Reduced basis method for finite volume approximations of parametrized linear evolution equations. *M2AN, Math. Model. Numer. Anal.*, 42(2), 277–302.
10. Hay, A., Akhtar, I., and Borggaard, J. (2011). On the use of sensitivity analysis in model reduction to predict flows for varying inflow conditions. *International Journal for Numerical Methods in Fluids*.
11. Hinze, M., Pinnau, R., Ulbrich, M., and Ulbrich, S. (2009). *Optimization with PDE Constraints*, volume 23 of *Mathematical Modelling: Theory and Applications*. Springer.
12. Hinze, M. and Tröltzsch, F. (2010). Discrete concepts versus error analysis in PDE-constrained optimization. *GAMM-Mitteilungen*, 33, 148 – 162.
13. Lass, O. (2014). Reduced order modeling and parameter identification for coupled nonlinear PDE systems. PhD Thesis, University of Konstanz, Germany.
14. Lassila, T. and Rozza, G. (2010). Parametric free-form shape design with PDE models and reduced basis method. *Computer Methods in Applied Mechanics and Engineering*, 199, 1583–1592.
15. Lewis, R., Patera, A., and Peraire, J. (2000). A posteriori finite element bounds for sensitivity derivatives of partial-differential-equation outputs. *Finite Elements in Analysis and Design*, 34, 271–290.
16. Oliveira, I. and Patera, A. (2007). Reduced-basis techniques for rapid reliable optimization of systems described by affinely parametrized coercive elliptic partial differential equations. *Optim Eng*, 8, 43–65.
17. Quarteroni, A., Rozza, G., and Quaini, A. (2006). Reduced basis methods for optimal control of advection-diffusion problems. In *Advances in Numerical Mathematics*, MOX 79, 193–216.
18. Rozza, G., Huynh, D., and Patera, A. (2008). Reduced Basis approximation and a posteriori error estimation for affinely parametrized elliptic coercive partial differential equations: application to transport and continuum mechanics. *Arch. Comput. Meth. Eng.*, 15(3), 229–275.

19. Sachs, E. and Volkwein, S. (2010). POD-Galerkin approximations in PDE-constrained optimization. *GAMM-Mitteilungen*, 33, No.2, 194–208.
20. Tröltzsch, F. and Volkwein, S. (2009). POD a-posteriori error estimation for linear-quadratic optimal control problems. *Computational Optimization and Applications*, 44(1), 83–115.

**MS V High Order Methods for  
Unsteady Flows**

MS V.1: On the Aliasing of Discrete Kinetic  
Energy in a Nodal Discontinuous Galerkin Method

Authors: Gassner, Gregor J.

---

# On the Aliasing of discrete Kinetic Energy in a Nodal Discontinuous Galerkin Method

Gregor J. Gassner

**Abstract** We use the connection of Gauss-Lobatto-Legendre based nodal discontinuous Galerkin methods to the summation-by-parts finite difference framework to derive the discrete kinetic energy balance for the compressible Euler equations. In this paper, we identify a non-linear source term, inconsistent to the continuous kinetic energy balance, which may either act as a sink or as a source and thus driving the instability.

**Keywords** Gauss-Lobatto · Nodal DG · summation-by-parts · kinetic energy preservation · Euler equations · skew-symmetry

## 1 Introduction

In [3] it was shown that the favorable dissipation and dispersion properties of very high order DG methods (in this case, a polynomial degree of 15) give highly accurate results in the case of underresolved turbulence. It is worth noting that the standard nodal DG formulation had instabilities issues due to aliasing of the kinetic energy. In case of a very high order discretisation, the artificial dissipation provided by the Riemann solver based surface fluxes is not large enough to get rid of the aliasing driven instabilities. Hence, to resolve this issue either an ad hoc filtering approach or an approach based on polynomial projection rather than polynomial interpolation is used. While the former is unsatisfactory due to its parameter dependent nature the second approach, while yielding accurate results, comes at a vastly increased computational price. The aim of this paper is to demonstrate the issue for a nodal based discretisation and analyse the associated discrete kinetic energy balance.

---

Gregor J. Gassner  
Mathematical Institute, University of Cologne, Weyertal 86-90, 50931 Cologne  
Tel.: +49-221-470-2954  
E-mail: ggassner@math.uni-koeln.de

## 2 The Compressible Euler Equations

The conservative form of the equation reads as

$$U_t + F_x(U) = 0, \quad (1)$$

where the conservative variables and fluxes are

$$U = \begin{pmatrix} u_1 \\ u_2 \\ u_3 \end{pmatrix} := \begin{pmatrix} \rho \\ \rho v \\ \rho e + \rho v^2/2 \end{pmatrix}, \quad F = \begin{pmatrix} f_1 \\ f_2 \\ f_3 \end{pmatrix} := \begin{pmatrix} \rho v \\ \rho v^2 + p \\ \rho v e + \rho v^3/2 + v p \end{pmatrix}, \quad (2)$$

where  $\rho$ ,  $v$ ,  $p$ ,  $e$  are density, velocity, pressure and specific inner energy respectively. Assuming a perfect gas, we have the relation  $\rho e = p/(\kappa - 1)$  with the constant adiabatic coefficient  $\kappa$ .

## 3 The Numerical Method

Our numerical method of choice is the Gauss-Lobatto based nodal collocation spectral element discontinuous Galerkin method (DGSEM), see e.g. [5, 4, 1, 2] for a detailed derivation. We subdivide the domain into non-overlapping grid cells and map each of the cells to a reference element. For each element, a nodal based ansatz spanned by the Gauss-Lobatto points is made. Using a variational approach and replacing the integrals with the numerical quadrature associated to the Gauss-Lobatto points, we get the following condensed discretisation

$$\frac{\Delta x}{2} \partial_t \underline{u}_k + \underline{D} \underline{f}_k = -\underline{M}^{-1} \underline{B} (\underline{f}_k^* - \underline{f}_k), \quad k = 1, 2, 3, \quad (3)$$

where the components of the flux vector  $\underline{f}_k$  are computed via the collocation principle as

$$\begin{aligned} f_1^j &= \rho^j v^j, \\ f_2^j &= \rho^j (v^j)^2 + p^j, \\ f_3^j &= \rho^j v^j e^j + \rho^j (v^j)^3/2 + v^j p^j, \end{aligned} \quad (4)$$

for each Gauss-Lobatto node  $j = 0, \dots, N$ .  $f^*$  denotes the numerical flux function, e.g. [11], which resolves the discontinuity at the grid cell interfaces. The operators are given by the mass matrix

$$\underline{M} := \text{diag}([\omega_0, \dots, \omega_N]), \quad (5)$$

where the  $\omega_j$  are the associated quadrature weights. The differentiation matrix

$$D_{ij} := \ell_j'(\xi_i), \quad i, j = 0, \dots, N, \quad (6)$$

where the  $\ell_j$  are the Lagrange polynomials associated to the Gauss-Lobatto points. The boundary operator is given by

$$\underline{B} := \text{diag}([-1, 0, \dots, 0, 1]). \quad (7)$$

These operators satisfy the so-called summation-by-parts (SBP) property, originally introduced in the finite difference framework [6–10],

$$(\underline{\underline{M}}\underline{\underline{D}}) + (\underline{\underline{M}}\underline{\underline{D}})^T = \underline{\underline{B}}. \quad (8)$$

#### 4 The discrete Kinetic Energy Balance

The first step to derive the balance is to multiply the discrete continuity equation by the velocity field  $\underline{v}/2$ . We subtract this from the discrete momentum equation of the standard DGSEM formulation (3) to get

$$\frac{\Delta x}{2} \left( \partial_t \underline{u}_2 - \frac{1}{2} \underline{v} \partial_t \underline{u}_1 \right) + \underline{\underline{D}} \underline{f}_2 - \frac{1}{2} \underline{v} \underline{\underline{D}} \underline{\rho} \underline{v} = S.T. \quad (9)$$

where

$$S.T. = -\underline{\underline{M}}^{-1} \underline{\underline{B}} \left( \underline{f}_2^* - \underline{f}_2 \right) + \frac{1}{2} \underline{v} \underline{\underline{M}}^{-1} \underline{\underline{B}} \left( \underline{f}_1^* - \underline{f}_1 \right). \quad (10)$$

Assuming time continuity, the first term can be reformulated as

$$\frac{\Delta x}{2} \left( \partial_t \underline{u}_2 - \frac{1}{2} \underline{v} \partial_t \underline{u}_1 \right) = \frac{\Delta x}{2} \frac{1}{2} \left( \partial_t \underline{u}_2 + \underline{\rho} \partial_t \underline{v} \right). \quad (11)$$

We insert this into equation (9) and multiply the resulting equation by the velocity field  $\underline{v}$

$$\frac{\Delta x}{2} \frac{1}{2} \left( \underline{v} \partial_t \underline{u}_2 + \underline{u}_2 \partial_t \underline{v} \right) + \underline{v} \underline{\underline{D}} \underline{f}_2 - \frac{1}{2} \underline{v}^2 \underline{\underline{D}} \underline{\rho} \underline{v} = \underline{v} S.T. \quad (12)$$

The first term gives us the time derivative of the discrete kinetic energy

$$\frac{1}{2} \left( \underline{v} \partial_t \underline{u}_2 + \underline{u}_2 \partial_t \underline{v} \right) = \partial_t (\underline{\rho} \underline{v}^2 / 2). \quad (13)$$

We furthermore extend the formulation by adding and subtracting the volume term of the transport flux  $\frac{1}{2} \underline{\underline{D}} \underline{\rho} \underline{v}^3$  to get

$$\frac{\Delta x}{2} \partial_t (\underline{\rho} \underline{v}^2 / 2) + \frac{1}{2} \underline{\underline{D}} \underline{\rho} \underline{v}^3 + \underline{v} \underline{\underline{D}} \underline{p} + \underline{s}_{kin} = \underline{v} S.T., \quad (14)$$

where the source term in the kinetic energy is given by

$$\underline{s}_{kin} = \frac{1}{2} \left[ -\underline{\underline{D}} \underline{\rho} \underline{v}^3 + 2 \underline{v} \underline{\underline{D}} \underline{\rho} \underline{v}^2 - \underline{v}^2 \underline{\underline{D}} \underline{\rho} \underline{v} \right]. \quad (15)$$

The continuous kinetic energy balance (derived directly from the Euler equations) reads as

$$\partial_t (\rho v^2 / 2) + \partial_x (\rho v^3 / 2) + v \partial_x p = 0. \quad (16)$$

Comparing both, we realise that the two differ only in the additional source term  $\underline{s}_{kin} := s - \tilde{s}$ , as the other terms have a one-by-one discretisation. An

analysis of the source term reveals that it is the sum of a consistent and conservative part

$$s := \frac{1}{2} \left[ -\underline{\underline{D}} \underline{\underline{\rho}} v^3 + \underline{\underline{v}} \underline{\underline{D}} \underline{\underline{\rho}} v^2 + \underline{\underline{\rho}} v^2 \underline{\underline{D}} v \right] \quad (17)$$

and a non-conservative term

$$\tilde{s} := \frac{1}{2} \underline{\underline{v}} \left[ -\underline{\underline{D}} \underline{\underline{\rho}} v^2 + \underline{\underline{\rho}} \underline{\underline{v}} \underline{\underline{D}} v + \underline{\underline{v}} \underline{\underline{D}} \underline{\underline{\rho}} v \right]. \quad (18)$$

It is exactly this second term generated due to aliasing that can act either as a source or as a sink, thus being responsible for instabilities in under resolved turbulence computations with high order nodal DG methods.

## 5 Discussion

We showed that for a nodal DG method, an aliasing driven source term is introduced in the kinetic energy balance. This term is responsible for the aliasing instability observed in marginally resolved turbulence computations. In [2], the author shows how to construct an alternative formulation based on the skew-symmetric form of the Euler equations to get rid of the second problematic source term  $\tilde{s}$ , resulting in a kinetic energy consistent nodal DG method.

## References

1. Gassner, G.: A skew-symmetric discontinuous Galerkin spectral element discretization and its relation to SBP-SAT finite difference methods. *SIAM Journal on Scientific Computing* **35**(3), A1233–A1253 (2013)
2. Gassner, G.: A kinetic energy preserving nodal discontinuous galerkin spectral element method. accepted in *IJNMF* (2014)
3. Gassner, G.J., Beck, A.D.: On the accuracy of high-order discretizations for underresolved turbulence simulations. *Theoretical and Computational Fluid Dynamics* (2012). DOI: 10.1007/s00162-011-0253-7
4. Hindenlang, F., Gassner, G., Altmann, C., Beck, A., Staudenmaier, M., Munz, C.D.: Explicit discontinuous Galerkin methods for unsteady problems. *Computers and Fluids* **61**, 86–93 (2012). URL <http://dx.doi.org/10.1016/j.compfluid.2012.03.006>
5. Kopriva, D.A.: *Implementing Spectral Methods for Partial Differential Equations: Algorithms for Scientists and Engineers*, 1st edn. Springer Publishing Company, Incorporated (2009)
6. Kreiss, H.O., Scherer, G.: Finite element and finite difference methods for hyperbolic partial differential equations. In: *Mathematical Aspects of Finite Elements in Partial Differential Equations*, pp. 195–212. Academic Press (1974)
7. Nordström, J., Carpenter, M.H.: Boundary and interface conditions for high-order finite-difference methods applied to the Euler and NavierStokes equations. *Journal of Computational Physics* **148**(2), 621 – 645 (1999)
8. Olsson, P.: Summation by parts, projections, and stability. I. *Math. Comput.* **64**(211), 1035–1065 (1995)
9. Olsson, P.: Summation by parts, projections, and stability. II. *Mathematics of Computation* **64**(212), pp. 1473–1493 (1995)
10. Strand, B.: Summation by parts for finite difference approximations for  $d/dx$ . *Journal of Computational Physics* **110**(1), 47 – 67 (1994)
11. Toro, E.: *Riemann Solvers and Numerical Methods for Fluid Dynamics*. Springer (1999)

MS V.2: GPU-Accelerated High-Order  
Aeroacoustics Using the Flux Reconstruction  
Approach

Authors: Ntemos, George, Vincent, Peter E.

---

# GPU-Accelerated High-Order Aeroacoustics using the Flux Reconstruction Approach

G. Ntemos · P.E. Vincent

**Abstract** In this talk we will demonstrate the utility of using a multi-GPU accelerated high-order accurate CFD solver to undertake simulations of flow over a tandem rod-aerofoil configuration. Specifically, simulations will be undertaken using the open-source solver PyFR, which is based on the Flux Reconstruction approach, and can target a range of accelerator based hardware platforms. Various quantities will be extracted from the simulation data, and compared with experimental results; including time-averaged velocity distributions and acoustic spectra.

**Keywords** Fluid Dynamics · High Order · Flux Reconstruction · GPU · Unstructured Grid · DNS · Aeroacoustics · Numerical Methods · Rod · Aerofoil

## 1 Introduction

High-order flow solvers for unstructured grids have begun to be used for fundamental fluids research, and are also considered by many as a next-generation tool for industrial design. Accurate and efficient simulation of flow around complex geometries is a major issue that arises in many modern aerospace applications. Examples of such applications include reliable noise calculations from high speed flow entering turbomachinery or passing over aircraft landing gear. The rod-aerofoil benchmark test case considered here can reproduce many of the underlying flow characteristics present in such cases, making it an appropriate proof-of-concept and validation test. A robust and computationally efficient method for fully resolving the dynamics of such flows is critical. The objective of this study is to demonstrate the utility of using a multi-GPU accelerated high-order accurate CFD solver to undertake such simulations.

## 2 Problem Specification

The test case considers flow over a rod-aerofoil configuration at a Reynolds number of 480,000 (based on the chord  $C$  and the free-stream velocity  $U_{in}$ ), and a Mach number of 0.21 [7, 8, 9]. The symmetrical

---

G. Ntemos  
Department of Aeronautics  
Imperial College London  
South Kensington  
London  
SW7 2AZ  
Tel.: +44 (0)755 1519 447  
E-mail: george.ntemos11@imperial.ac.uk

P. E. Vincent  
Department of Aeronautics  
Imperial College London  
South Kensington  
London  
SW7 2AZ  
Tel.: +44 (0)20 7594 1975  
E-mail: p.vincent@imperial.ac.uk

NACA 0012 aerofoil is positioned at zero incidence relative to the incoming free-stream velocity. The rod has a diameter of  $0.1C$ . The distance between the rod centre and the aerofoil leading edge is equal to  $C$ . A illustration of the layout can be seen in Figure 1.

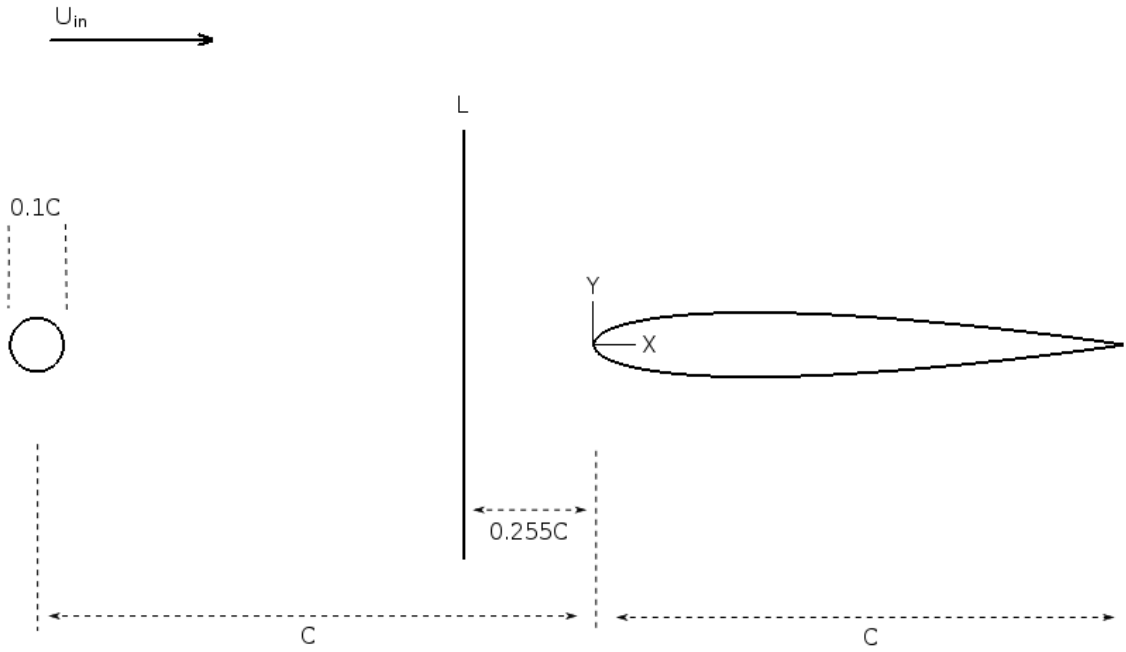


**Fig. 1** Rod-Aerofoil layout.

## 2.1 Computational Method

The study was undertaken using PyFR [2], version 0.2.1. PyFR utilizes the Flux Reconstruction approach and it has been specifically designed to run on a range of different hardware, including GPUs. One of its main features is the fact that it is written almost entirely in the Python scripting language, with all the compute-intensive operations executed from kernels produced at runtime and in low level languages targeting specific platforms, eg. CUDA, OpenCL and OpenMP. This is a design that Python can very conveniently support. PyFR solves the full system of the compressible Navier-Stokes equations, with no sub-grid scale modelling (i.e. a DNS/ILES approach). It is easily configurable in terms of fundamental numerical parameters, such as polynomial order or the type of Riemann solver for the inter element fluxes. Perhaps most importantly, it is able to efficiently apply the FR method on unstructured grids, which greatly facilitate the meshing of complex geometries. PyFR is explicit in time, utilizing multi-stage Runge-Kutta methods for time advancement. A rigorous description of PyFR, the theory behind it and proofs of a number of its properties can be found in [1, 2, 3, 4, 5, 6].

## 3 Simulation Parameters and Results

The studies were performed in 3D. The aerofoil chord had a value of  $C = 0.1m$  and the free-stream velocity was  $U_{in} = 72.0m/s$ . Meshing was performed using Gmsh, an open-source, high-order meshing

application [10]. Specifically the computational domain was meshed with approximately 350,000 unstructured hexahedra, and solution polynomials of degree three were used to represent the solution within each element - thus the simulation had  $\sim 5 \times 10^7$  degrees of freedom. The computational domain had a cylindrical boundary on which Riemann-Invariant, Characteristic BCs [11] were imposed. Time advancement used a five-stage, fourth-order order, explicit Runge-Kutta scheme (RK45) [12]. The simulation start-up procedure consisted of two phases. Phase one advanced the solution to 0.03 time units using a polynomial order in space equal to one. Phase two advanced the solution to 0.06 time units with an order of two. Results were then acquired from a third phase, which utilized a spatial order of 3 and advanced to 0.09 time units with a time-step of  $10^{-8}s$ . Total simulation time on 20 Nvidia K20 GPUs was of the order of 8 days for 10 passes over the chord (corresponding to 0.03 physical time units or 3 million time steps) and a polynomial order of 3.



**Fig. 2** Instantaneous pressure isosurfaces,  $Re=480,000$ ,  $Ma=0.21$ . Coloured by velocity magnitude.

Figure 2 illustrates an instantaneous state of the flow field. Figure 3 plots the time-averaged stream-wise velocity  $\bar{u}$  (normalized with respect to  $U_{in}$ ) along the line  $L$  marked in Figure 1.

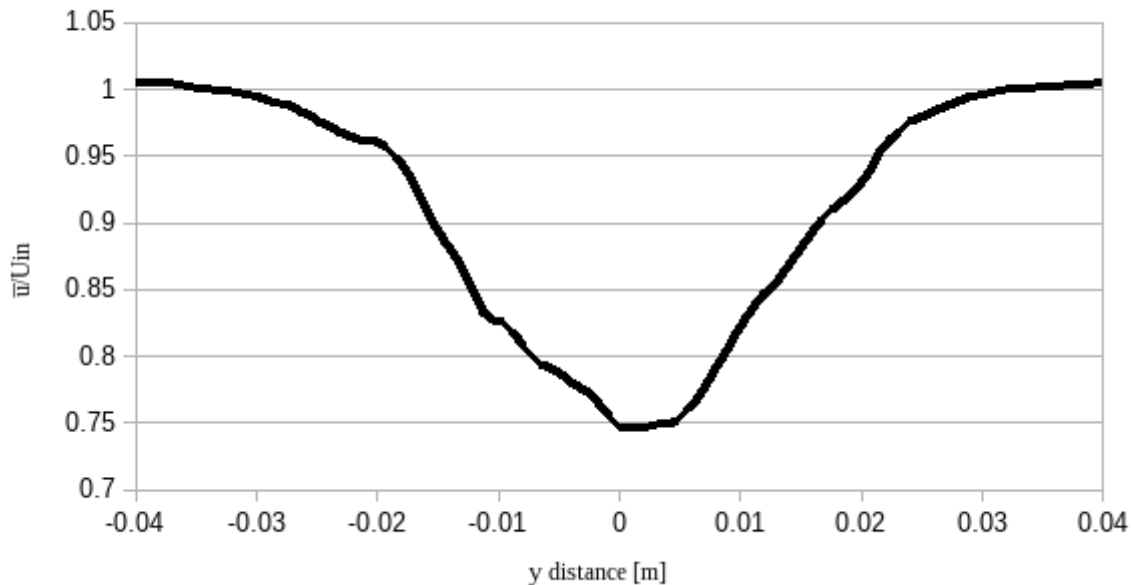


**Fig. 3** Time-averaged streamwise velocity profile along line L (see fig. 1),  $Re=480,000$ ,  $Ma=0.21$ .

Agreement with the experimental benchmark and previous numerical studies will be investigated, placing particular emphasis on its sensitivity to fundamental simulation parameters such as mesh refinement and polynomial order. The ultimate goal of CFD development is the reduction of simulation time required for a given accuracy. This study attempts to demonstrate advances towards this aim achieved within the PyFR framework and its potential as a robust design and simulation tool.

## References

1. HT Huynh, A flux reconstruction approach to high-order schemes including discontinuous Galerkin methods, AIAA paper, 4079, 2007
2. FD Witherden - AM Farrington - PE Vincent, PyFR: An open source framework for solving advection-diffusion type problems on streaming architectures using the Flux Reconstruction approach, 2014
3. PE Vincent - P Castonguay - A Jameson, A new class of high-order energy stable flux reconstruction schemes, Journal of Scientific Computing, 47(1), 50-72, 2011
4. P Castonguay - PE Vincent - A Jameson, A new class of high-order energy stable flux reconstruction schemes for triangular elements, Journal of Scientific Computing, 2011
5. P Castonguay - PE Vincent - A Jameson, Application of high-order energy stable flux reconstruction schemes to the Euler equations, 49th AIAA Aerospace Sciences Meeting, 686, 2011
6. P Castonguay - DM Williams - PE Vincent - A Jameson, Energy stable flux reconstruction schemes for advection-diffusion problems, Computer Methods in Applied Mechanics and Engineering, 2013
7. MC Jacob - J Boudet - D Casalino - M Michard, A rod-airfoil experiment as benchmark for broadband noise modeling, Theoretical and Computational Fluid Dynamics, 19, 171-196, 2005
8. JC Giret - A Sengissen - S Moreau - M Sanjose - JC Jouhaud, Prediction of the sound generated by a rod-airfoil configuration using a compressible unstructured LES solver and a FW-H analogy, 2012
9. J Berland - P Lafon - F. Crouzet - F. Daude - C. Bailly, Numerical insight into sound sources of a rod-airfoil flow configuration using direct noise calculation, 16th AIAA/CEAS Aeroacoustics Conference, 2010
10. C Geuzaine - JF Remacle, Gmsh: a three-dimensional finite element mesh generator with built-in pre- and post-processing facilities, International Journal for Numerical Methods in Engineering 79(11), 1309-1331, 2009
11. A Jameson - TJ Baker, Solution of the Euler Equations for complex Configurations, AIAA paper, 1983-1929-869
12. MH Carpenter - CA Kennedy, Fourth-order 2N-Storage Runge-Kutta schemes, NASA Technical Memorandum 109112, 1994

MS V.3: Development of a High-Resolution,  
Scalable DGM Solver for DNS and LES of  
Turbomachinery Flows

Authors: Carton de Wiart, Corentin, Hillewaert, Koen

---

# Development of a high-resolution, scalable DGM solver for DNS and LES of turbomachinery flows

Corentin Carton de Wiart · Koen Hillewaert

**Abstract** This work is part of the development of a new generation of CFD solvers on the basis of the discontinuous Galerkin Method (DGM), specifically targeted towards accurate, adaptive, reliable and fast DNS and LES of industrial aerodynamic flows. In this study, the ability of the method to perform accurate implicit LES is investigated. The method is applied on several advanced benchmarks (studied in the European project IDIHOM), performed at moderate Reynolds number. The 2D periodic hill flow, the low pressure turbine blade T106C and the JEAN nozzle benchmarks are considered. Encouraging results have been obtained, paving the way to the use of the method for industrial applications.

**Keywords** Discontinuous Galerkin Method · Direct Numerical Simulation · Large Eddy Simulation · Turbomachinery

Nowadays, *Computational Fluid Dynamics (CFD)* has become an indispensable tool for both academic and industrial studies. The increase of computational power next to the industrialisation of the methods opened the way to the use of CFD in many sectors. CFD is now daily used for the design of aircraft, cars, energy production units, production processes and even building physics. Nevertheless, a large gap still remains between the accuracy of the solvers used in industry and those developed by the academic community. Indeed, the academic community is more focused on fundamental aspects of fluid flow or the development of physical models, thereby considering relatively simple setups on which very accurate methods can be used. On the other hand, the industrial applications target a large range of flow regimes in complex configurations. Therefore, the CFD solvers used in the industry often sacrifice

---

Rue des Freres Wright, 29  
6041 Gosselies Belgium  
Tel.: +32 71 910956  
Fax: +32 71 910931  
E-mail: corentin.carton@cenaero.be

accuracy for higher flexibility, robustness and a lower computational cost. As a consequence, less accurate numerical schemes together with significant and important physical modelling, mainly RANS, are the current industry standard. Indeed, most of the time, the complexity of the geometry is such that only the mean flow can be captured with strong modelling contributions.

For the last decade, the field of computational fluid dynamics has seen the advent of new unstructured, finite element-like high order methods, such as the *discontinuous Galerkin method (DGM)* [1], *spectral element method (SEM)* [2], flux reconstruction (FR) [3] or *spectral difference method (SDM)* [4]. These methods appear to provide a compromise between the flexibility of industrial *finite volume methods (FVM)* [5] and the accuracy of academic solvers, such as high order *finite difference methods (FDM)* [6] or *pseudo-spectral methods (PSM)* [7]. Due to their computational compactness, most of these methods - in particular those with discontinuous interpolation - also provide an excellent serial and parallel computational efficiency. In view of these advantages, it is mainly in the field of scale-resolving simulations that these methods offer the best perspectives. Indeed, as these simulations require a nearly flawless representation of the turbulent scales, current industrial solvers require huge computational resources to provide sufficient accuracy, and hence, most computations appear to be under-resolved so far (see Tucker [8,9] for a recent review in turbomachinery).

One of those novel methods, the discontinuous Galerkin method with symmetric interior penalty (DGM/SIP) has been firstly implemented in Argo, the multiphysics platform of Cenaero, during the thesis of Koen Hillewaert [10], in collaboration with the *Université catholique de Louvain (UCL)*. The solver has been subsequently applied on the scale-resolving simulations of moderate Reynolds flows during the thesis of Corentin Carton de Wiart (Cenaero/UCL) [11].

During the IDIHOM project, the compressible flow module of Argo, the DGM solver developed at Cenaero, has been applied on the scale-resolving simulations of canonical and industrial flows, putting forward the ability of this new generation of high-order methods to handle large cases on unstructured meshes. Several ambitious cases - occurring at moderate Reynolds numbers - were investigated, including the well-known 2D periodic hill (figure 1), the JEAN nozzle (figure 2) and the T106 low pressure turbine blade (figure 3).

Those results, next to those of the more fundamental work, have shown the viability of the method, at least for a small ranges of industrial applications, occurring at moderate Reynolds numbers. The results of the test cases and the comparison with reference numerical or experimental results will be presented at the workshop.

**Acknowledgements** The authors gratefully acknowledge the support by the Walloon Region, by the European regional development fund (ERDF) contract N° ECV12020022015F and finally through the FP7 research project IDIHOM.

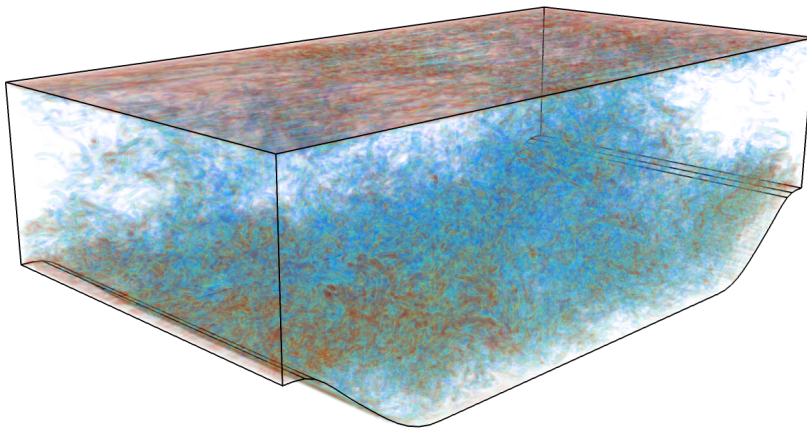


**Fig. 1** Simulation of the flow over a 2D periodic hill configuration at  $Re_b = \frac{u_b h}{\nu} = 10595$  with  $u_b = \frac{1}{2.035h} \int_h^{3.035h} u(y) dy$  and  $h$  the hill height . Volume rendering of the instantaneous Q criterion field.

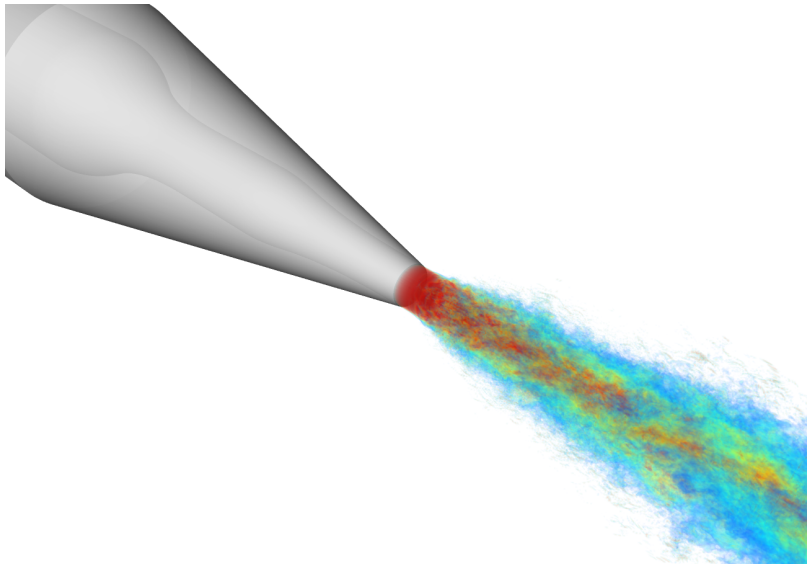


**Fig. 2** JEAN nozzle.  $Re_{D, is} = 5 \times 10^4$  and  $M_{is} = 0.75$ , based on the isentropic expansion from inlet total to free stream static pressure and the exhaust diameter  $D$ . Volume rendering of the velocity.

## References

1. J. Hesthaven, T. Warburton, *Nodal Discontinuous Galerkin Methods; Algorithms, Analysis and Applications*. Text in Applied Mathematics (Springer Verlag, 2008)
2. G. Karniadakis, S. Sherwin, *Spectral/hp element methods for computational fluid dynamics* (Oxford University Press, 2005)
3. H.T. Huynh, in *18th AIAA Computational Fluid Dynamics Conference* (2007), AIAA-2007-4079

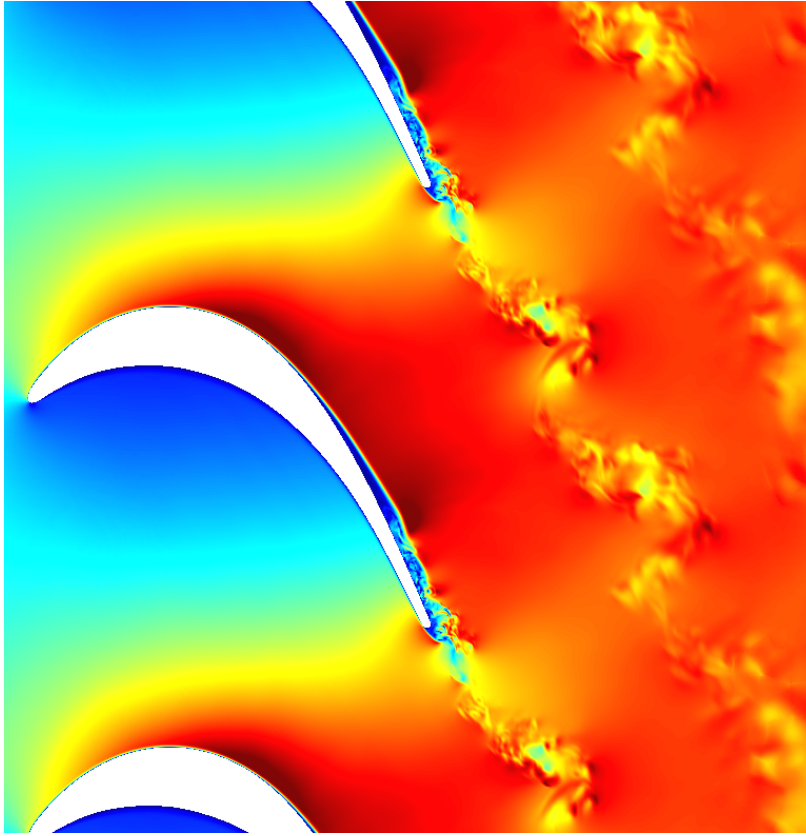


**Fig. 3** Transitional flow past the low pressure turbine blade T106C at  $M_{2,is} = 0.59$  and  $Re_{2,is} = 80.000$  (based on isentropic exit conditions). Global overview of the Mach number field on the spanwise periodic plane. The passage has been duplicated for clarity.

4. Y. Sun, Z. Wang, Y. Lia, *Communication in Computational Physics* **2**(2), 310
5. E.F. Toro, *Riemann Solvers and Numerical Methods for Fluid Dynamics: A Practical Introduction* (Springer-Verlag, 1999)
6. O. Vasilyev, *Journal of Computational Physics* **157**(2), 746 (2000)
7. C. Canuto, M.Y. Hussaini, A. Quarteroni, T.A. Zang, *Spectral Methods in Fluid Dynamics* (Springer-Verlag, 1988)
8. P. Tucker, *Progress in Aerospace Sciences* **47**, 522 (2011)
9. P. Tucker, *Progress in Aerospace Sciences* **47**, 546 (2011)
10. K. Hillewaert, Development of the Discontinuous Galerkin Method for high-resolution, large scale CFD and acoustics in industrial geometries. Ph.D. thesis, Ecole polytechnique de Louvain/iMMC (2013)
11. C.C. de Wiart, Towards a discontinuous Galerkin solver for scale-resolving simulations of moderate reynolds number flows, and application to industrial cases. Ph.D. thesis, Ecole polytechnique de Louvain/iMMC (2014)

MS V.4: An Application of High-Order DGSEM to  
Large Eddy Simulation

Authors: Bolemann, Thomas, Beck, Andrea D., Munz, Claus-Dieter

---

# An Application of High-Order DGSEM to Large Eddy Simulation

Thomas Bolemann · Andrea D. Beck ·  
Claus-Dieter Munz

**Abstract** In this work we apply an explicit CFD code based on the Discontinuous Galerkin Spectral Element Method (DGSEM) to under-resolved turbulent flows. We demonstrate that our framework is highly accurate, efficient and scalable and is thus well suited for scale-resolving tasks like Large Eddy Simulation and Direct Numerical Simulation. Considering a near-incompressible, moderate Reynolds number regime we pick two classical benchmark cases for LES: a channel flow across a configuration with streamwise periodic hills at different Reynolds numbers and a flow around a circular cylinder. We compare with state-of-the-art low order simulations from literature and show that we obtain equal to better results with significantly less degrees of freedom.

**Keywords** Discontinuous Galerkin Spectral Element Method · High-Order Methods · Large Eddy Simulation · Direct Numerical Simulation · Under-resolved Turbulence · Polynomial Dealiasing

In recent years the role of Computational Fluid Dynamics has changed from being a tool for experts to a tool closely linked to the design process. This was on one hand caused by the increase of computational resources, on the other hand solvers for steady flows have become very mature and are highly optimized, RANS-type simulations can thus be carried out within a few hours on modest hardware. In contrast scale-resolving simulations are less widespread, as tackling unsteady turbulent flows remains resource intensive due to its very nature. In the past a considerable amount of progress has been made in this field, leading to a number of accurate and efficient research codes. However, these do mostly not support complex geometries and thus lack the flexibility required for industrially relevant applications. A great deal of LES research

---

T. Bolemann, A. D. Beck, C.-D. Munz  
Institute for Aerodynamics and Gasdynamics  
University of Stuttgart, Pfaffenwaldring 21, 70550 Stuttgart, Germany.  
Tel.: +49-711-685 69973  
E-mail: bolemann/beck/munz@iag.uni-stuttgart.de

focuses on modeling the effects of small scales using standard second order Finite Volume schemes as a basis.

For LES however Discontinuous Galerkin methods seem to be a viable alternative to FV methods. While providing a high-order of accuracy they can be using on unstructured, hybrid meshes and thus promise to deliver academic accuracy on an industrial scale. In addition their low dispersion and dissipation errors [7] are favorable in an LES setup.

High-order DG methods for CFD have received an increased amount of interest since the turn of the millennium, where most research was in the field of RANS, however only few could report a benefit in computational efficiency over FV methods. One of the first attempts to apply DG methods on LES was by Collis in 2002 [4,5]. More recently contributions are by Uranga et al. [11] and Carton de Wiart [3,12]. In [6] Gassner and Beck performed very high-order DGSEM computations of isotropic turbulence and obtained results on par with FV methods, but using only a fraction of degrees of freedom (DOFs). In [1] Beck et al. reported successful simulations of various benchmark cases.

For the simulations the DGSEM framework Flexi is used, consisting of an unstructured solver and a complete pre- and postprocessing toolchain. As already mentioned LES usually comes with high computational cost, which necessitates the use of massively parallel computing architectures. Due to the locality of the operator explicit DG methods can be parallelized very efficiently, for Flexi efficient strong scaling for 100,000+ cores is possible. In this work we rely on a model-free approach and do not use any explicit turbulence model or filter. We apply however, polynomial dealiasing to reduce the effects of aliasing. Two benchmark cases are used to demonstrate our LES strategy:

The first one consists of an incompressible flow through a stream- and spanwise periodic channel with hill-shaped restrictions in streamwise direction, which has been thoroughly investigated by Breuer et al. [2]. Here we perform simulations at a Reynolds number of  $Re = 2,800$  and  $Re = 10,595$ , on a mesh with solely 8,192 elements. For each case we have three simulations for polynomial degrees from  $N = 3$  up to  $N = 9$ . In the separation region, depicted in fig. 1, we observe that time-averaged velocities nearly match the reference solution and even turbulent kinetic energy agrees very well. Fig. 2 gives an impression of the instantaneous turbulent structures in the flow field. We note that for the highest polynomial degree we use 8,192 cores and thus have one single element per core, while still retaining efficient scaling.

The other benchmark case, depicted in fig. 3, is a subcritical flow over a circular cylinder at  $Re_D = 3900$ , which has been studied by Kravchenko [8]. We can observe that the pressure coefficient of our simulation agrees well to reference DNS and experimental data.

We conclude that we achieved results on par with or superior to the reference results from literature, while using considerably less DOFs and thus being more efficient. Thereby we did not use any explicit subgrid-scale model whatsoever and rely on polynomial dealiasing, providing a clean numerical basis. The results clearly indicate that high-order DG methods as the Flexi framework

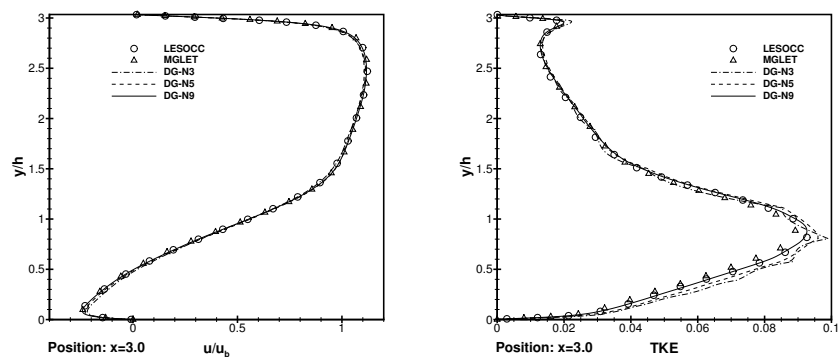


**Fig. 1**  $Re = 2,800$ : Spatial and time averaged streamwise velocity  $\langle u \rangle / u_b$  and turbulent kinetic energy in the separation region ( $x = 3.0$ ).

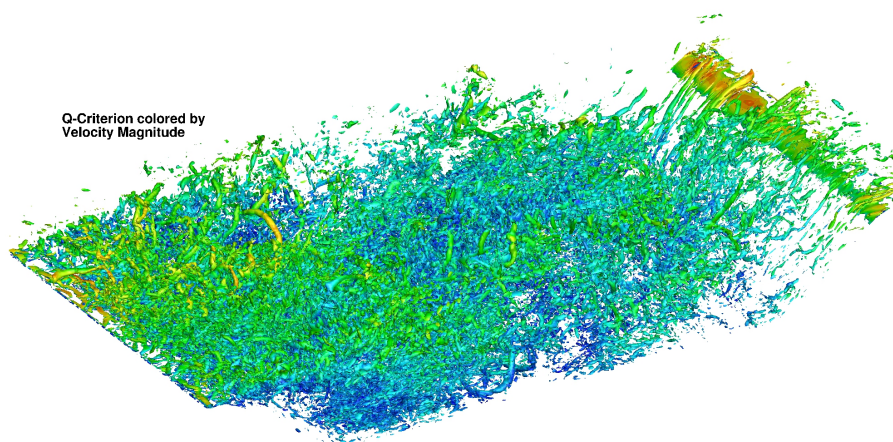


**Fig. 2**  $Re = 10595$ : Instantaneous snapshot: Q-criterion colored by velocity magnitude

perform very well in an LES setup and are for these type of problems superior to classical FV methods.

**Acknowledgements** This research has partially been funded by the European Union through the FP7 project IDIHOM and the DFG priority program Metström.

## References

1. Beck, A., Bolemann, T., Flad, D., Frank, H., Gassner, G., Hindenlang, F., Munz, C.D.: High order discontinuous galerkin spectral element methods for transitional and turbulent flow simulations. Accepted for publication in International Journal of Numerical Methods in Fluids, to appear 2014 (2014)

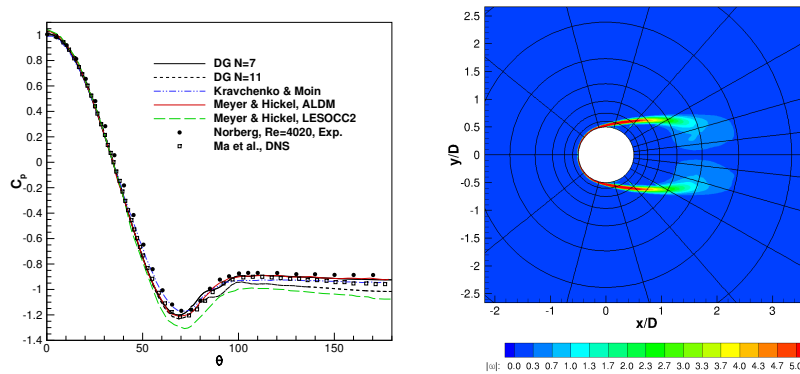


**Fig. 3** LES of cylinder at  $Re_D = 3900$ . *left*: Comparison of averaged pressure coefficient, results for DNS and experimental data of Norberg taken from [9], results for Meyer et al. from [10] and Kravchenko from [8], *right*: Computational grid and averaged vorticity magnitude.

2. Breuer, M., Peller, N., Rapp, C., Manhart, M.: Flow over periodic hills numerical and experimental study in a wide range of Reynolds numbers. *Computers and Fluids* **38**(2), 433 – 457 (2009). DOI <http://dx.doi.org/10.1016/j.compfluid.2008.05.002>. URL <http://www.sciencedirect.com/science/article/pii/S0045793008001126>
3. Carton de Wiart, C., Hillewaert, K.: DNS and ILES of transitional flows around a SD7003 using a high order discontinuous Galerkin method. In: *Seventh International Conference on Computational Fluid Dynamics (ICCFD7)* (2012)
4. Collis, S.: Discontinuous Galerkin methods for turbulence simulation. In: *In Proceedings of the 2002 Center for Turbulence Research Summer Program*, pp. 155–167 (2002)
5. Collis, S.: The DG/VMS method for unified turbulence simulation. In: *32nd AIAA Fluid Dynamics Conference and Exhibit* (2002)
6. Gassner, G., Beck, A.: On the accuracy of high-order discretizations for underresolved turbulence simulations. *Theoretical and Computational Fluid Dynamics* **27**(3-4), 221–237 (2013)
7. Gassner, G., Kopriva, D.: A comparison of the dispersion and dissipation errors of Gauss and Gauss-Lobatto discontinuous Galerkin spectral element methods. *SIAM J. Scientific Computing* **33**(5), 2560–2579 (2011)
8. Kravchenko, A.G., Moin, P.: Numerical studies of flow over a circular cylinder at  $Re_D=3900$ . *Physics of Fluids* **12**, 403–417 (2000). DOI 10.1063/1.870318
9. Ma, x., Karamanos, g.s., Karniadakis, g.E.: Dynamics and low-dimensionality of a turbulent near wake. *Journal of Fluid Mechanics* **410**, 29–65 (2000). DOI 10.1017/S0022112099007934
10. Meyer, M., Hickel, S., Adams, N.: Assessment of implicit large-eddy simulation with a conservative immersed interface method for turbulent cylinder flow. *International Journal of Heat and Fluid Flow* **31**(3), 368 – 377 (2010). DOI <http://dx.doi.org/10.1016/j.ijheatfluidflow.2010.02.026>. URL <http://www.sciencedirect.com/science/article/pii/S0142727X10000597>
11. Uranga, A., Persson, P.O., Drela, M., Peraire, J.: Implicit large eddy simulation of transition to turbulence at low Reynolds numbers using a discontinuous Galerkin method. *International Journal for Numerical Methods in Engineering* **87**(1-5), 232–261 (2011)
12. Carton de Wiart, C., Hillewaert, K., Duponcheel, M., Winckelmans, G.: Assessment of a discontinuous Galerkin method for the simulation of vortical flows at high Reynolds number. *International Journal for Numerical Methods in Fluids* (2013). DOI 10.1002/fl.3859. URL <http://dx.doi.org/10.1002/fl.3859>

## **MS VI Simulation-based Identification**

MS VI.1: Optimization of the Strainer Design in  
the Extrusion Process of Visco-Plastic Materials

Authors: Hoffmann, Wolfgang

---

## Optimization of a strainer design in the extrusion process of visco-plastic materials

Wolfgang Hoffmann

**Abstract** In ceramic and plastic production plants shaping plays an important role, it is the fundament of high quality products. Typically, auger extruders (screw extruders) are used for continuous extrusion and piston or ram extruders are deployed for intermittent extrusion. Here our focus lies on de-airing screw extruders combined with vacuum devices incorporated in the extruder barrel. Auger extrusion processes are mostly used for endless string products with rotationally symmetric components and a small cross section relative to their length.

For modern ceramic or plastic production processes it is expected that the shaping process guarantees strength of shape and produce flawless surfaces and crack-free, filigree structures. All these requirements depend a lot on the quality of shaping. Thus, stress-relieved extrusion is the main precondition for column-drawn products. Combined with this process there is also the need to avoid excessive shear stresses. Consequently, the basis for a high quality ceramic or plastic product takes place mainly in the forming devices, i.e. in the strainer, the pressure head and the die.

Screw extruders have in addition to many advantages one important drawback. The screw of the auger induces in the formed pastes a pulsating effect in the column, which is often referred to as a pulsating memory effect. Therefore, a strainer is used to counterbalance or at least minimize these memory effect. But also the other components play a crucial role during the forming process. The pressure head should optimize the passage of the paste from strainer to die and needs an inter-coordinated design between strainer and die. Finally, the die forms the final product depending on the previous forming process.

The requirements to a successful production yields to a design of the strainer, the pressure head and die in that way that the ceramic body shows an optimal speed-and-stress profile passing the extrusion device. The key criterion to ensure the quality is consequently a uniform, constant velocity profile over the cross-section of the column.

---

Wolfgang Hoffmann

SiCo-Solutions Scientific and Technical Solutions Lehenstrasse 30 70180 Stuttgart, Germany  
Tel.: +49-0-711-1206247 Fax: +49-0-711-1206254 E-mail: wolfgang.hoffmann@sico-solutions.de

Our focus lies on the geometric optimization of the strainer. Hence, we require a constant velocity profile at the exit of the strainer, i.e. at the inflow part of the pressure head.

Due to the complexity of the optimization problem we use the non-linear gradient free Nelder-Mead method to find an optimal velocity profile at the exit of the strainer. Therefore, we want to optimize the shape of the strainer and, according to this, we define an upstream flow angle and a diameter as parameters for our objective function.

**Keywords** Numerical optimization · non-linear least square problems · Nelder-Mead method · Non-Newtonian fluids · high-viscosity flow · Bingham fluid · Herschel-Bulkley fluid · flow of visco-plastic materials with wall slip · non-linear boundary conditions · rheology · extrusion technology

## 1 Introduction

Extrusion of soft solids is a forming process for a great number of products like pharmaceutical tablets [4], catalyst monoliths [6]. [5], pasta [9], rubber, compounds, alumina profiles etc..

Typically pastes and compounds will be formed in extrusion devices as endless string products. The quality of the string is essential for the quality of the final product, for example ceramic monoliths for catalysts in the automotive sector. In general, a forming device is splitted into a pressure head with strainer and a die. Here the quality of the extrusion string depends significantly on the velocity field of the flow passing the extruder, strainer and the forming pressure head and die. The velocity field will also effect strains and stresses influencing the quality of the final product. For the production of peak-quality, wet-shaped products, which we denominate as extrudates, it is important to produce a well-prepared body of constant, uniform consistency. Also two more prerequisites are an optimized vacuum and a non-pulsating column.

Even there are well-known technical processes in extrusion technology in practice every new product needs a modified or new process technology. Extrusion involves very high pressures up to 200 bar or higher and also bodies which are difficult to extrudate. Consequently, this requires extrusion tools considering the influence of the extruder itself to the die exit in a hydraulically optimized design. Also the extrudates and honeycomb elements for technical applications need a high level of accuracy. For instance, the engineering of a honeycomb die for thin-walled honeycombs, i.e. ceramic monoliths with wall thickness of 0.09 mm and less requires a degree of precision only guaranteed with state-of-the-art machine tools in combination with state-of-the-art simulation and optimization techniques.

In fig. 1 typical designs of forming devices are shown. In fig. 1 on the upper left side are examples for forming cores inside a die, in the upper right part are combinations of pressure head and dies and the lower part shows some typical extrudated products.

The extrusion body in the entire shaping process must be kept uniformly shaped, guided and finally moulded into the geometry of the end product. Thus we consider the forming process in more detail. There are two type of extrusion processes. Auger

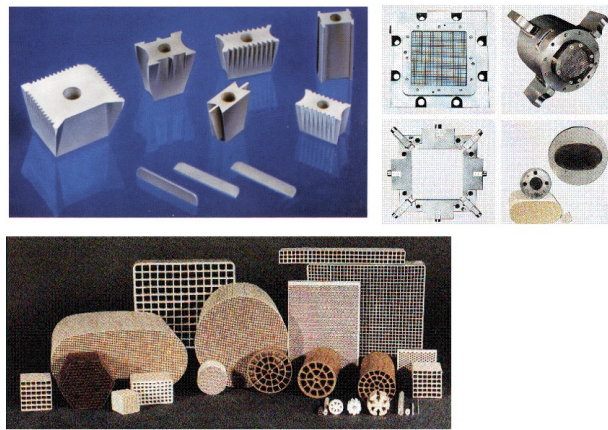


**Fig. 1** Examples of forming devices of the die (upper left), selection of pressure heads and dies (upper right) and a selection of products

or screw extruders are used for continuous extrusion while piston or ram extruders are employed for intermittent extrusion. Here we focus augers respectively screw extruders and their influence on the forming process. The characteristics of the extruder in question has to be incorporated into the design of the forming device. Especially for auger extruders the nature of the barrel, the auger and the end auger has to be included. Typically this is combined with the extrusion velocity profile, i.e. the velocity profile of the extruder as inflow profile of the strainer.

The strainer is in direct contact to the extruder and its purpose is to compensate the memory effect and to ensure a balanced, equilibrated velocity profile. At this first step of the forming process the quality of the product is influenced dramatically.

Thus we want to optimize the velocity field in the sense of a nearly equi-distributed velocity profile at the exit of strainer into the pressure head. Here we consider the flow in forming devices as a non-Newtonian flow with wall slip. The most important influence is due to the shape of the strainer and also the pressure head. But in our optimization we restrict our focus on the strainer due to the complexity of the problem. Therefore we want to find an optimal shape of the strainer under consideration yielding in the desired velocity profile.

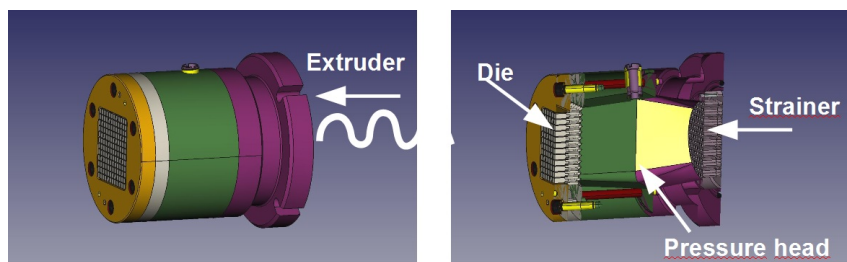


**Fig. 2** Typical design of a highly complex die with pressure head and strainer

## 2 Non-Newtonian material behaviour

Non-Newtonian fluids completely different from Newton-fluids. In Non-Newtonian fluids the viscosity depends on the shear rate and the shear rate history. Nevertheless some non-Newtonian fluids will show shear-independent viscosity. Examples are many salt solutions, coal tar, noodles, ketchup, toothpaste, blood, paint, heavy clay and technical ceramics.

In a Newtonian fluid the relation between shear stress and shear rate is linear, passing the origin and the proportional factor is the linear viscosity. A Non-Newtonian fluid shows a non-linear relation between shear stress and shear rate resulting in a non-linear viscosity function. Here the viscosity depends on the shear stress and shear rate while the relation between shear stress and shear rate can be time-dependent.

Furthermore, Non-Newtonian fluids have a yield stress, i.e. below a initial stress, the yield stress  $\tau_F$ , they behave like a rigid body. Trespassing the yield stress will change the material behaviour completely, the fluid shows plastic deformation.

There are a lot of other effects, which will discussed shortly. A shear thickening or dilatant fluid has a viscosity, which increases with increasing shear rate. Shear thinning or pseudo-plastic fluids have a viscosity function decreasing with rising shear rate, an example is paint but also ceramics and many polymers. For our purpose, Bingham-fluids play the important role. Bingham fluids are characterized by a linear shear stress to shear strain relationship and a yield stress  $\tau_F$  to start with plastic deformation. The linear proportional factor between shear strain and shear strain is denominated as Bingham viscosity  $\eta_B$ . Furthermore Bingham fluids are shear thinning, pseudo-plastic fluids. There exist a lot of textbooks for non-linear viscoplastic fluids and for more details we refer to [1] and [10].

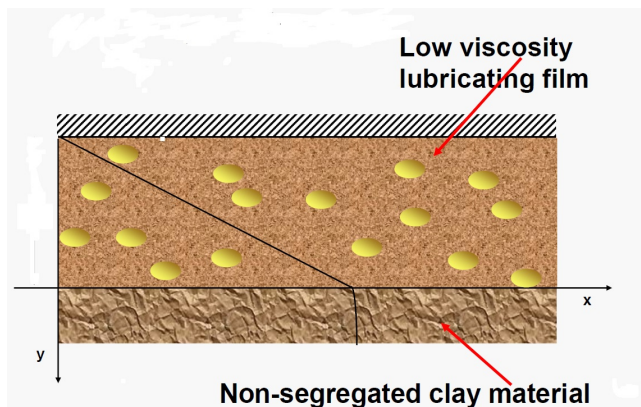


Fig. 3 Wall slip behaviour of a non-Newtonian fluid

It is important to describe the deformation process not only as shear rate dependent process, it is essential to involve also the wall slip of Non-Newtonian materials [2], [3], [5]. Neglecting wall slip will result in non-realistic modelling of the flow behaviour and simulations of deforming processes will not describe reality.

Wall slip is an effect caused by the disintegration of the fluid close to the walls. Due to the pressure a thin low viscosity lubricating film occurs splitting the fluid in two regions with different flow behaviour (see fig. 3). A segregated material and a thin film will describe the flow behaviour at the walls, a non-segregated material determines the flow behaviour in the within. The flow parameters for the flow within are the yield stress  $\tau_f$  and the Bingham viscosity  $\eta_B$ .

Additionally we introduce two parameters for the wall slip, the yield stress  $\tau_w$ , describing when walls slip will start and the  $k$ -factor, describing the flow behaviour close to the wall. The yield stress  $\tau_w$  is directly related to yield stress  $\tau_f$ , its magnitude is 10 - 100 times smaller than the yield stress  $\tau_f$ . The  $k$ -factor represents the tribology of the wall and the viscosity close to the wall. For more details we refer to [5].

Thus we have 4 material parameters to describe the behaviour of an incompressible non-Newtonian fluids with wall slip (see table 1). The four material parameters have to be determined by measurement.

$\tau_f$	yield stress	[Pa]
$\eta_B$	Bingham viscosity	[Pa · s]
$\tau_w$	wall slip stress	[Pa]
$k$	k-factor	[Pa · s/m]

**Table 1** Characteristic material parameters for Bingham fluids

As constitutive partial differential equation for the flow of a Bingham fluid within the domain  $\Omega \subset R^3$  we have (details for the derivation of the system of partial differential equations see in [6]):

$$-\nabla T = \nabla(-2\mu(v)D + p\mathbb{1}) = 0 \quad (1)$$

$$\Delta v = 0 \quad (2)$$

$$(3)$$

The viscosity function  $\mu$  is:

$$-\mu(D) = \eta_B + \tau_f \sqrt{4I_2} \quad \text{with} \quad (4)$$

$$I_2 = \frac{1}{2} \text{trace}(D^2) + (\text{trace}(D))^2 \quad (5)$$

Here  $T$  is the stress tensor,  $p\mathbb{1}$  the pressure multiplied with the unit matrix,  $D$  the strain rate tensor,  $\mu$  the viscosity function and  $v$  the velocity field.

The non-Newtonian fluid moves along fixed walls with the wall slip velocity  $v_{wall}$  as a function of wall stress  $\tau_w$ . Thus, we can formulate the boundary conditions for the walls as function of  $\tau_w$  with wall slip velocity  $v_{slip}$ :

$$v_{slip} = f(|\tau_w|) \tau_w \quad (6)$$

The boundary conditions for the other boundaries are the usual inflow and outflow boundary conditions.

### 3 An optimization method for Bingham fluids will wall slip in a strainer

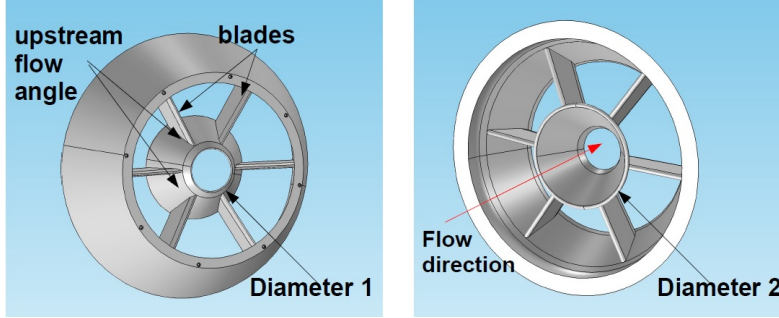


Fig. 4 Initial shape of the strainer with 6 blades

The geometry to optimize is shown in fig. 4. Here we have 6 blades for minimizing the pulsating memory effect. Furthermore we use diameter 1,  $d_1$ , and the upstream flow angle  $\alpha$  of the blades for optimization. The flow direction is in x-direction in a cartesian coordinate system. Hence, we have to find a nearly equi-distributed velocity profile at the outlet of the strainer. Therefore we have to ensure that the velocity components perpendicular to the flow direction yield into a minimum at the outlet of the strainer,  $|v_y| + |v_z| \rightarrow \min$ .

We define the objective function  $f_{objective} = \tilde{f}$  as:

$$\tilde{f}(\alpha, d_1) = \sum_{\text{grid points}} |v_y| + |v_z| \rightarrow \min \quad (7)$$

The index set of the sum in equation 7 means the finite volume solution for the flow at all grid points of the exit of the strainer.

As optimization algorithm we use the Nelder-Mead method [12]. A comprehensive description of the Nelder-Mead algorithms can be found in many textbooks for numerical optimization, for example in [11].

We use this method because we have a highly non-linear partial differential equation system (see (3) and (5)) and it is not guaranteed to find a gradient for the optimization problem. Thus, we use the most important property of the Nelder-Mead method, the fact that Nelder-Mead does not need a gradient of the objective function. Even the objective function has not to be continuous.

The Nelder-Mead method is easy to implement but very little is known about its convergence properties. It is not a priori clear, that the algorithm will find a solution and heuristic motivated regularisation has to be implemented. There is done some research in convergence theory for Nelder-Mead and more details are to find for example in [7] or [8].

## References

1. Barnes, H.A., Hutton, J.F., Walters, K. An introduction to rheology, Rheology series, 3, Elsevier New York (1989)
2. Barnes, H. A., A review of the wall slip (wall depletion) of polymer solutions and particle suspensions in viscosimeters: its cause, character and cure, *J. Non-Newton Fluid Mech.*, 56, 221 - 251 (1996)
3. Barnes, E. C., Wilson, D.I., Johns, M.I. Velocity profiling inside a ram extruder using magnetic resonance (MR) techniques, *Chemical Engineering Science*, 61, 1357 - 1367 (1996)
4. Harrison, P.J., Newton, J.M., Rowe, R.C., Flow defects in wet powder mass extrusion, *Journal of Pharmacy and Pharmacology*, 37, 81 - 83 (1985)
5. Hoffmann, Wolfgang, Berger, Harald, Rheology of a heavy clay extrusion body, *J ZI Ziegelindustrie International*, 4, 27 - 34 (2001)
6. Hoffmann, Wolfgang, Flow Simulation of Plastic Ceramic Bodies - Part 1, *Keramische Zeitschrift*, 54, 194 - 198 (2002)
7. Kelley, C.T., Iterative methods for optimization, *Frontiers in Applied Mathematics*, SIAM Publications, Philadelphia, PA, 18, (1999)
8. Lagarias, J.W., Reeds, J.A., Wright, M.H., Wright, P.E., Convergence properties of the Nelder-Mead simplex algorithm in low dimensions, *SIAM Journal on Optimization*, 9, 112 - 147 (1998)
9. Lucisiano, M., Pagani, M.A., Mariotti, M., Locatelli, D.P., Influence of die material on pasta characteristics, *Food Research International*, 41, 646 - 652 (2008)
10. Macosko, C.W., Rheology, principles, measurement and applications, VCH New York (1994)
11. Nocedal, J., Wright, S.J., Numerical optimization, Springer Series in Operations Research, Springer New York, (2006)
12. Nelder, J.A., Mead, R., A simplex method for function minimization , *The Computer Journal*, 8, 308 - 313 (1965)

MS VI.2: Wavelet Methods for a Weighted Sparsity  
Penalty for Region of Interest Tomography

Authors: Klann, Esther, Quinto, Eric Todd, Ramlau, Ronny

---

# Wavelet Methods for a Weighted Sparsity Penalty for Region of Interest Tomography

Esther Klann · Eric Todd Quinto ·  
Ronny Ramlau

**Abstract** We consider region of interest (ROI) tomography of piecewise constant functions. We apply a Haar-wavelet reconstruction algorithm that uses a weighted  $\ell_p$ -penalty with weights that depend on the relative location of wavelets to the ROI. The proposed method is a regularization method, i.e., the regularized solutions converge to the exact piecewise constant solution if the noise tends to zero. We provide tests on phantoms that demonstrate the efficacy of the method and compare it to the method proposed in [4].

**Keywords** region of interest tomography · wavelets · sparsity · regularization

**Mathematics Subject Classification (2000)** MSC2010 34A55 · MSC2010 65T60 · MSC2010 62P10

## 1 Introduction

We consider the *interior problem* or *region of interest (ROI) tomography*; tomographic data are given only over lines meeting a region of interest  $\Omega$  inside an object, and the goal is to image that region. ROI data of a function  $f$  are the integrals  $Rf(\ell)$  for all lines  $\ell$  that intersect  $\Omega$ ,  $R$  denotes the Radon transform and data limitations are referred to by the subscript ‘lim’. Already the full data problem of solving  $Rf = z$  in  $L_2$  is ill-posed [2, 3], and regularization methods have to be applied. We consider the ROI problem for piecewise

---

The first author was supported by FWF grant T 529-N18. The second author was supported in part by NSF Grants DMS 0908015 and DMS 1311558. The third author was supported partly by Doctoral Program “Computational Mathematics”.

E. Klann (and R. Ramlau)

Industrial Mathematics Institute, Johannes Kepler University Linz, Altenberger Strasse 69, A-4040 Linz, Austria. E-mail: esther.klann@jku.at

E.T. Quinto

Department of Mathematics, Tufts University, 503 Boston Av., Medford, MA 02155, USA

constant (PC) functions that can be written as the finite linear combination of characteristic functions:  $f(x) = \sum_{n=1}^N a_n \chi_{\Omega_n}(x)$ .

We use a weighted wavelet reconstruction scheme which leads to the minimization of the functional

$$\|R_{\text{lim}}f - z_{\text{lim}}^\delta\|_{L_2(S^1 \times \mathbb{R})}^2 + \alpha \|Ff\|_{p,\omega}^p \quad (1)$$

where

$$\|Ff\|_{p,\omega}^p = \sum_{j,k} \omega_{jk} |c_{jk}|^p$$

is a weighted  $\ell_p$ -norm with strictly positive weights  $0 < C \leq \omega_{jk}$  and the operator  $F$  maps  $f$  to its Fourier coefficients with respect to the Haar basis. For  $p < 2$ , such an approach is known to promote sparsity; and for  $p > 1$  the functional is strictly convex and has a unique minimizer. For the minimization of the functional we use the method of surrogate functionals [1, 5]. The novelty of the proposed method is the choice of weights.

## 2 The weights

For the choice of weights we consider three types of basis functions.

1. The first type are basis functions with support either containing the region of interest (approximation, coarse wavelets), or being contained in the region of interest (detail, fine wavelet). These basis functions assemble the reconstruction *in the ROI* and hence, the coefficients should be computed as accurately as possible. We choose the weight to be equal to 1 for these basis functions.
2. The second type are basis functions whose support does not overlap the region of interest (details, fine wavelets and coarser wavelets away from the ROI). These functions only have an indirect influence on the reconstruction. We choose a fixed value for the corresponding weights. In the numerical examples we experiment with different values for this *outside weight*, e.g., 2, 5 and 10.
3. The last type of basis functions are those that overlap the region of interest without belonging to the first type. For these functions we define intermediate weights depending on the size of the intersection (the size of the shared support). The weight interpolates between 1, the inside weight, and the value chosen for the outside weight (empty intersection).

Splitting the weighted sum according to the position of the basis functions with respect to the ROI in three sets, namely  $\Gamma_{\text{in}}$ ,  $\Gamma_{\text{out}}$  and  $\Gamma_{\text{rim}}$ , the regularization term in (1) can be written as

$$\|Ff\|_{p,\omega}^p = \sum_{jk \in \Gamma_{\text{in}}} |c_{jk}|^p + \sum_{jk \in \Gamma_{\text{rim}}} \omega_{jk} |c_{jk}|^p + \omega_{\text{out}} \sum_{jk \in \Gamma_{\text{out}}} |c_{jk}|^p. \quad (2)$$

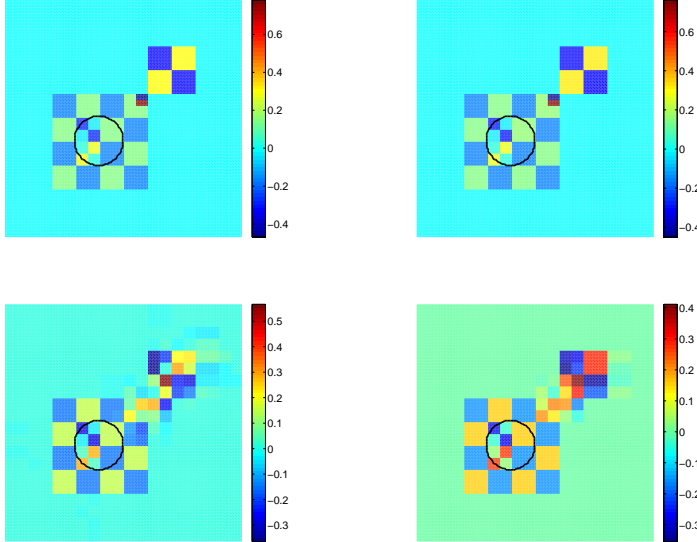


**Fig. 1** A very sparse wavelet example with ROI. First row: Left: Original. Right: reconstruction from region of interest data with regularization parameter  $\alpha = 5 \cdot 10^{-7}$  and outer weight equal to 10. Second row: Reconstructions with the linear shrinkage reconstruction as in [4]; outside of the ROI the 2 finest detail levels are missing. Left:  $\alpha = 1 \cdot 10^{-6}$ , right:  $\alpha = 5 \cdot 10^{-6}$ .

### 3 Example Reconstructions

We use an academic example built from 8 wavelets of different size, see Figure 1. An important feature is the small wavelet, corresponding to a fine detail with high intensity, outside the ROI. Our proposed method allows the reconstruction of fine details outside the ROI; and Figure 1 and Table 1 demonstrate that this is beneficial. Table 1 shows that the proposed method is able to achieve a very small relative reconstruction error both in the region of interest and in the whole image domain.

In [4] a wavelet based method is proposed that deletes fine detail levels outside the ROI in order to get a regularized and sparse solution in the ROI. With this method, the small detail in our example cannot be reconstructed as soon as more than 1 detail level outside the ROI are deleted, see the second row of Figure 1. Also with this approach a very small reconstruction error in the ROI can be achieved, see the reconstruction errors given in Table 2. This happens, however, at the cost of the sparseness of the reconstruction (Table 2).

**Table 1** Reconstructions with the proposed weighted wavelet method. Relative  $L_2$ -error in the ROI and in the image domain for different values of the regularization parameter and  $\omega_{\text{out}} = 5$  and 10.

$\alpha$	$\omega_{\text{out}}$	nnz	$\delta_{\text{ROI}}$ in %	$\delta_{\text{D}}$ in %
$5 \cdot 10^{-7}$	10	8	0.379	1.114
$1 \cdot 10^{-6}$	10	8	0.758	2.221
$1 \cdot 10^{-6}$	5	8	0.417	1.115
$5 \cdot 10^{-6}$	5	8	2.084	5.560

**Table 2** Reconstructions with the linear shrinkage method of [4]. Relative  $L_2$ -error in the ROI and in the image domain for different values of the regularization parameter and different numbers of deleted detail levels outside the ROI.

$\alpha$	no. of deleted levels	nnz	$\delta_{\text{ROI}}$ in %	$\delta_{\text{D}}$ in %
$5 \cdot 10^{-7}$	1	247	0.195	42.3
$1 \cdot 10^{-6}$	1	133	0.226	32.41
$5 \cdot 10^{-6}$	1	8	0.864	1.153
$1 \cdot 10^{-6}$	2	109	0.683	53.552
$5 \cdot 10^{-6}$	2	33	1.030	39.433

## References

1. Daubechies, I., Defrise, M., De Mol, C.: An iterative thresholding algorithm for linear inverse problems with a sparsity constraint. *Comm. Pure Appl. Math.* pp. 1413–1457 (2004)
2. Engl, H.W., Hanke, M., Neubauer, A.: *Regularization of Inverse Problems*. Kluwer Academic Publishers, Dordrecht (1996)
3. Louis, A.: *Inverse und schlecht gestellte Probleme*. Teubner Verlag, Stuttgart (1988)
4. Niinimäki, K., Siltanen, S., Kolehmainen, V.: Bayesian multiresolution method for local tomography in dental X-ray imaging. *Physics in Medicine and Biology* **52**, 6663–6678 (2007)
5. Ramlau, R.: Regularization properties of Tikhonov regularization with sparsity constraints. *ETNA. Electronic Transactions on Numerical Analysis [electronic only]* **30**, 54–74 (2008). URL <http://eudml.org/doc/130630>

MS VI.3: Colored Buzz, or Glottal Inverse Filtering

Authors: Siltanen, Samuli

---

# Colored Buzz, or Glottal Inverse Filtering

Samuli Siltanen

**Abstract** The structure of vowel sounds in human speech can be divided into two independent components. One of them is the *excitation signal*, which is a kind of buzzing sound created by the vocal folds flapping against each other. The other is the *filtering effect* caused by resonances in the vocal tract, or the confined space formed by the mouth and throat. The Glottal Inverse Filtering (GIF) problem is to (algorithmically) divide a microphone recording of a vowel sound into its two components. This *blind deconvolution* type task is an ill-posed inverse problem. Good-quality GIF filtering is essential for computer-generated speech needed for example by disabled people (think Stephen Hawking). Also, GIF affects the quality of synthetic speech in automatic information announcements and car navigation systems. Accurate estimation of the voice source from recorded speech is known to be difficult with current glottal inverse filtering (GIF) techniques, especially in the case of high-pitch speech of female or child subjects. In order to tackle this problem, the present study uses Bayesian inversion for GIF. The proposed method takes advantage of the Markov chain Monte Carlo (MCMC) modeling in defining the parameters of the vocal tract inverse filter. The filtering results are found to be superior to those achieved by the standard iterative adaptive inverse filtering (IAIF).

**Keywords** Glottal inverse filtering · MCMC

## 1 Introduction

The structure of vowel sounds in human speech can be divided into two independent components. One of them is the *excitation signal*, which is a kind of

---

S. Siltanen  
Department of Mathematics and Statistics  
PO Box 68  
FI-00014 University of Helsinki  
Tel.: +358-40-5943560  
E-mail: samuli.siltanen@helsinki.fi

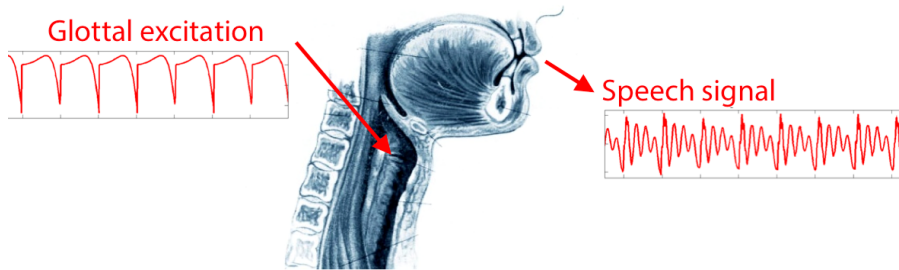


**Fig. 1** Acoustic pressure between periodically closing vocal folds creates the glottal excitation signal. The resonances in the vocal tract filter the signal that can be recorded using a microphone.

buzzing sound created by the vocal folds flapping against each other. The other is the *filtering effect* caused by resonances in the vocal tract, or the confined space formed by the mouth and throat. See Figure 1.

The Glottal Inverse Filtering (GIF) problem is to (algorithmically) divide a microphone recording of a vowel sound into its two components. This *blind deconvolution* type task is an ill-posed inverse problem. Good-quality GIF filtering is essential for computer-generated speech needed for example by disabled people (think Stephen Hawking). Also, GIF affects the quality of synthetic speech in automatic information announcements and car navigation systems.

Accurate estimation of the voice source from recorded speech is known to be difficult with current glottal inverse filtering (GIF) techniques, especially in the case of high-pitch speech of female or child subjects. In order to tackle this problem, the present study uses Bayesian inversion for GIF. The method proposed in [2] takes advantage of the Markov chain Monte Carlo (MCMC) modeling in defining the parameters of the vocal tract inverse filter.

## 2 Materials and methods

Computational solution of the inverse problem requires a model for both the excitation signal and for the vocal tract effects. We use the so-called Klatt model for parameterizing the air flow through the glottis illustrated in Figure 2. The Klatt model has only one real parameter taking values between zero and one.

The vocal tract is modelled using the Z-transform. It turns out that simple piecewise-constant rotationally symmetric tube models provide a good-enough model for the human vocal tract. Furthermore, the filtering effect of such a tube takes a convenient form of an all-pole filter in the Z-transform domain. Two of the poles are the most significant and practically determine the vowel. Accordingly, the degrees of freedom in our vocal tract model are the radii and angles of two poles expressed in polar coordinates.

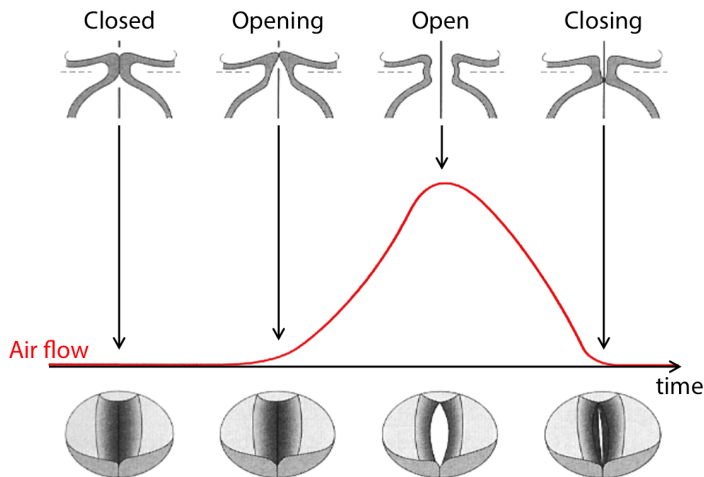


**Fig. 2** Airflow through the glottis (the gap between the vocal folds) is shown here (red line) as a function of time. This is just one period of the movement of the vocal folds during phonation. Vocal folds are shown in the coronal plane (top) and in the transversal plane (bottom). The derivative of the red line (physically the pressure) is the excitation signal.

Summarizing, our simple model of vowel sounds depends on five real parameters: the Klatt parameter and the two polar coordinates of two points in the complex plane.

Computational inversion is performed using Bayesian inversion [3]. Incomplete measurement information is inserted in a likelihood model. Everything we know about the possible and probable values of our five parameters is modelled using a prior model. The Bayes formula combines those two models into the *posterior distribution*. Finally, the solution of the ill-posed glottal inversion problem is recast in a well-posed task of exploring a probability distribution in a five-dimensional space. For this we use a Markov Chain Monte Carlo (MCMC) method called the Metropolis-Hastings algorithm.

Our sound samples are provided by Professor Brad Story. Magnetic resonance imaging is used to estimate the geometry of the vocal tract very accurately. This allows one to create a very realistic computational vocal tract model. Furthermore, since the excitation signals are simulated, we have ground truth available for measuring quantitatively the errors in the reconstructions.

### 3 Results

We apply both Iterative Adaptive Inverse Filtering [1] and the proposed MCMC method to the synthetic dataset we have available. The result for one representative case is shown in Figure 3; for a comprehensive statistical analysis of a larger set of results see [2].

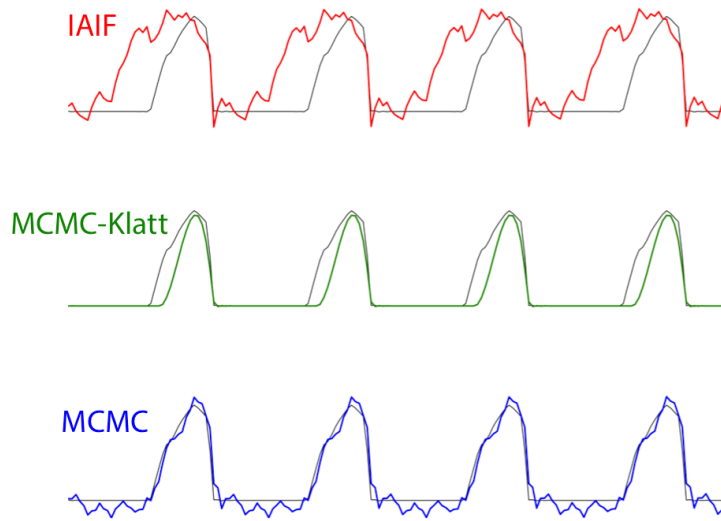


**Fig. 3** Inversion results. With a difficult sound sample the MCMC-based method performs better than the state-of-the-art IAIF method. Here the exactly known true airflow is shown as a gray line.

#### 4 Discussion

The MCMC-based filtering results are found to be superior to those achieved by the standard iterative adaptive inverse filtering (IAIF). This paves the way for

- High-quality speech prostheses allowing natural synthetic speech for disabled persons, even for women and children with high fundamental speech frequency.
- Clearer information announcements for railway stations and car navigation systems.
- Better automatic speech recognition in noisy environments.

#### References

1. Alku, P., 1992. Glottal wave analysis with pitch synchronous iterative adaptive inverse filtering. *Speech Communication* 11 (2/3), 109-118.
2. Harri Auvinen, Tuomo Raitio, Manu Airaksinen, Samuli Siltanen, Brad H. Story and Paavo Alku, Automatic glottal inverse filtering with the Markov chain Monte Carlo method, *Computer Speech & Language*, Volume 28, Issue 5, September 2014, Pages 1139–1155
3. J. KAIPIO AND E. SOMERSALO, *Statistical and Computational Inverse Problems*, vol. 160 of Applied Mathematical Sciences, Springer Verlag, 2004.

MS VI.4: A Resolution Guarantee for Anomaly  
Detection within a Realistically Modeled EIT Setting

Authors: Harrach, Bastian, Ullrich, Marcel

---

# A resolution guarantee for anomaly detection within a realistically modeled EIT setting

Bastian Harrach · Marcel Ullrich

**Abstract** We consider the problem of detecting anomalies in a conductive object from boundary current-to-voltage measurements. For a realistically modeled electrode measurement setting, we discuss the possibility of a resolution guarantee that guarantees to detect anomalies of a certain size without detecting false positives in the anomaly-free case. Based on a monotonicity relation for the measurement operator, we state a simple test criterion to check if a measurement setting contains enough information to ensure this guarantee.

**Keywords** Inverse parameter identification for PDEs · electrical impedance tomography (EIT) · monotonicity relation · resolution guarantees

## 1 Introduction

**Notations:**  $\chi_M$  denotes the characteristic function of a set  $M$  and  $\text{eig}(A)$  the set of eigenvalues of a square matrix  $A$ .

The aim of anomaly detection (aka. inclusion detection) in electrical impedance tomography (EIT) is to reconstruct areas of a conductive object  $\Omega$  where the conductivity  $\sigma$  differs from an approximately known background conductivity  $\sigma_B$ . For this purpose, current-voltage measurements are taken on the object's surface.

Mathematically, the potential distribution  $u$  in a conductive object  $\Omega \subseteq \mathbb{R}^n$  (with  $n \in \{2, 3\}$ ) is modeled by the solution of

$$\text{div}(\sigma \nabla u) = 0 \quad \text{in } \Omega, \quad (1)$$

$$\sigma \partial_\nu u|_{\partial\Omega} = g \quad \text{on } \partial\Omega, \quad (2)$$

---

B. Harrach and M. Ullrich  
Department of Mathematics - IMNG  
Chair of Optimization and Inverse Problems  
Allmandring 5b  
70569 Stuttgart  
Germany  
Tel.: +49 711 685-68401  
Fax: +49 711 685-51075  
E-mail: harrach@math.uni-stuttgart.de and marcel.ullrich@mathematik.uni-stuttgart.de

and the boundary measurements (applied boundary current to corresponding boundary potential) are modeled by the Neumann-to-Dirichlet Operator

$$\Lambda(\sigma) : g \mapsto u|_{\partial\Omega}.$$

For  $\sigma \in L_+^\infty(\Omega)$ , the operator  $\Lambda(\sigma) : L_\diamond^2(\partial\Omega) \rightarrow L_\diamond^2(\partial\Omega)$  is linear and self-adjoint, whereas the subscripts “+” and “ $\diamond$ ” denote the subset of functions with positive (essential) infima and vanishing integral mean, respectively.

We assume that  $\sigma$  differs on  $D \subseteq \Omega$  from a constant background conductivity  $\sigma_B \in \mathbb{R}$  with anomaly conductivity  $\sigma_D$ , i.e.

$$\sigma : \Omega \rightarrow \mathbb{R}, \quad \sigma(x) = \sigma_B \chi_{\Omega \setminus D}(x) + \sigma_D(x) \chi_A(x) \quad (3)$$

In addition, we assume that a contrast condition

$$\inf_{x \in A} \sigma_D(x) \geq \sigma_{D\min} > \sigma_B \quad (4)$$

for some constant  $\sigma_{D\min}$  is fulfilled. Then, the problem of anomaly detection is to reconstruct the area  $D$ .

For a realistically modeled electrode measurement setting (see section 2) including a finite amount of modeling and measurement errors, our main result in section 3 shows the possibility of the following resolution guarantee.

**Resolution guarantee (RG):** Let  $(\omega_1, \omega_2, \dots, \omega_N)$  be a resolution partition of  $\Omega$  (see fig. 1). A measurement setting fulfills the RG if it yields enough information to implement an anomaly detection method that guarantees:

- (a) A resolution element  $\omega_i$  will be marked if  $\omega_i \subseteq D$ .
- (b) No resolution element will be marked if  $D = \emptyset$ .

## 2 The measurement setup

The setting is given by current-voltage measurements on a finite number of electrodes  $E_1, E_2, \dots, E_L$ . We assume that the electrodes are almost perfectly conductive so that the electrical potential inside each electrode is constant. In addition, we assume that a contact layer between each electrode  $E_i$  and  $\Omega$  leads to a contact impedance  $z^{[i]}$ . This setting is mathematically modeled by the complete electrode model (CEM), cf. [4]. For this model, the boundary condition (2) has to be replaced by

$$u|_{\partial\Omega} + z_i \sigma \partial_\nu u|_{\partial\Omega} = U_i = \text{const. on } E_i \quad \forall i \in S := \{1, 2, \dots, L\}, \quad (5)$$

$$\sigma \partial_\nu u|_{\partial\Omega} = 0 \quad \text{on } \partial\Omega \setminus \bigcup_{i \in S} E_i, \quad (6)$$

$$\int_{E_i} \sigma \partial_\nu u|_{\partial\Omega} dS = I_i \quad \forall i \in S, \quad (7)$$

This boundary condition models the mapping of an applied current pattern  $(I_i)_{i=1}^L \in \mathbb{R}^L$  to the corresponding potential pattern  $(U_i)_{i=1}^L \in \mathbb{R}_\diamond^L$ , whereas the subscript “ $\diamond$ ” denotes the subspace of vectors with vanishing component sum.

For a conductivity distribution  $\sigma$  and contact impedances given by the components of  $z \in \mathbb{R}^L$ , we define a measurement matrix

$$R(\sigma, z) = \left( R^{[i,j]}(\sigma, z) \right)_{i,j=1}^{L-1} \in \mathbb{R}^{L-1 \times L-1}, \quad (8)$$

where the components  $R^{[i,j]}(\sigma, z)$  are given by the measurements as in fig. 1. The matrix  $R(\sigma, z)$  is symmetric, cf. [4].

To allow for **modelling and measurement errors**:

- (a) Background conductivity  $\sigma_B$  is approximately known by  $\sigma_0$  with  $|\sigma_B - \sigma_0| \leq \varepsilon$ .
- (b) Contact impedances  $z$  are approximately known by vector  $z_0$  with  $\|z - z_0\|_\infty \leq \gamma$ .
- (c) Noisy measurements  $R_\delta$  are given with  $\|R(\sigma, z) - R_\delta\|_2 \leq \delta$ . Possibly replacing  $R_\delta$  by its symmetric part, we can assume that  $R_\delta$  is symmetric.

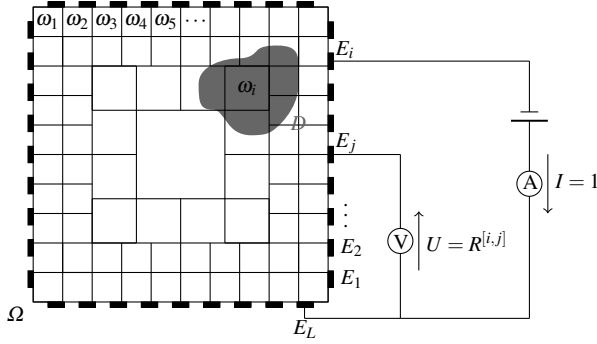


Fig. 1 Measurement setting with a sample resolution for  $\Omega$  (unit square).

### 3 Monotonicity-based verification of resolution guarantee

Let  $\sigma_0$ ,  $z_0$ ,  $\varepsilon$ ,  $\gamma$ ,  $\delta$  (of section 2) and  $\sigma_{D_{\min}}$  of (section 1) be given. We define

$$\sigma_B^\pm := \sigma_0 \pm \varepsilon, \quad (9)$$

$$z^\pm := z_0 \pm \gamma(1, \dots, 1), \quad (10)$$

$$\tau_i(x) := \sigma_B^- \chi_{\Omega \setminus \omega_i}(x) + \sigma_{D_{\min}} \chi_{\omega_i}(x) \quad \text{for } i \in \{1, 2, \dots, N\}. \quad (11)$$

**Theorem 1 (Verification of resolution guarantee)** *The RG is possible if*

$$\max_{i=1}^N \min \text{eig} (R(\tau_i, z^+) - R(\sigma_B^+, z^-)) < -2\delta. \quad (12)$$

*Proof (sketch)* The proof is based on the monotonicity relation

$$\sigma_1 \leq \sigma_2, z_1 \geq z_2 \quad \Rightarrow \quad R(\sigma_1, z_1) - R(\sigma_2, z_2) \geq 0. \quad (13)$$

The main idea is to consider (12) as a worst-case scenario test for the algorithm below (cf. [2, 3]).

**Algorithm 1:** Mark element  $\omega_i$  if

$$\min \operatorname{eig}(R(\tau_i, z_{\max}) - R_\delta) \geq -\delta. \quad (14)$$

□

*Remark 1* For idealized noise-free continuous boundary measurements and piecewise analytic conductivity functions, the results of [1] show that monotonicity-based methods (as algorithm 1) are able to reconstruct the exact outer shape of anomalies.

## 4 Numerical results

We consider the measurement setup and the resolution partition of fig. 1. Furthermore, let  $\sigma_0 \equiv 1$  and  $z_0 = (1, \dots, 1) \in \mathbb{R}^L$  be approximations of the background conductivity  $\sigma_B(x)$  and the vector  $z$  (contact impedances), respectively. Additionally, let  $\sigma_{D_{\min}} = 10$  be a lower bound of the inclusion conductivity.

Then, algorithm 1 fulfills (12) for a background error bound of  $\varepsilon = 1/4\%$ , a contact impedance error bound of  $\gamma = 1/4\%$  and an absolute measurement noise level of  $\delta = 8\%$ . Hence, the **RG** holds.

## 5 Conclusion

Based on monotonicity arguments, the possibility of a rigorous resolution guarantee can be shown for a realistically modeled electrode measurement setting. Even a finite amount of modeling and measurement errors is covered by this result. By checking a simple test criterion, the resolution guarantee can be verified and tolerable bounds for the errors can be calculated.

## 6 Acknowledgements

The authors Bastian Harrach and Marcel Ullrich would like to thank the German Research Foundation (DFG) for financial support of the project within the Cluster of Excellence in Simulation Technology (EXC 310/1) at the University of Stuttgart.

## References

1. Harrach, B., Ullrich, M.: Monotonicity-based shape reconstruction in electrical impedance tomography. *SIAM Journal on Mathematical Analysis* **45**(6), 3382–3403 (2013)
2. Harrach, B., Ullrich, M.: Monotony based inclusion detection in EIT for realistic electrode models. In: *Journal of Physics: Conference Series*, vol. 434, p. 012076. IOP Publishing (2013)
3. Harrach, B., Ullrich, M.: Resolution Guarantees in Electrical Impedance Tomography (submitted for publication)
4. Somersalo, E., Cheney, M., Isaacson, D.: Existence and uniqueness for electrode models for electric current computed tomography. *SIAM J. Appl. Math.* **52**(4), 1023–1040 (1992)

# Contributed Talks

# **C 1 Extrapolation in Time in Thermal Fluid Structure Interaction**

Authors: Birken, Philipp, Gleim, Tobias, Kuhl, Detlef, Meister, Andreas

---

# Extrapolation in time in thermal fluid structure interaction

Philipp Birken · Tobias Gleim · Detlef Kuhl · Andreas Meister

**Abstract** We consider time dependent thermal fluid structure interaction. The respective models are the compressible Navier-Stokes equations and the nonlinear heat equation. A partitioned coupling approach via a Dirichlet-Neumann coupling and a fixed point iteration is employed. As a reference solver a previously developed efficient time adaptive higher order time integration schemes is used.

To improve upon this, we explore the idea of extrapolation based on data given from the time integration. This allow to reduce the number of fixed point iterations significantly further with the linear version performing better than the quadratic one.

**Keywords** Thermal Fluid Structure Interaction · Dirichlet-Neumann iteration · Extrapolation · Time adaptivity

## 1 Introduction

Thermal interaction between fluids and structures plays an important role in many applications. One example is quenching, an industrial heat treatment

---

Part of this work was financed by the German Research Foundation (DFG) as part of the collaborative research area SFB-TRR 30, projects C1, C2.

---

P. Birken  
Lund University, Centre for the Mathematical Sciences, Numerical Analysis, Box 118, 22100 Lund, Sweden  
Tel.: +46-46-2223165  
Fax: +46-46-2224213  
E-mail: philipp.birken@na.lu.se

T. Gleim · D. Kuhl  
Inst. of Mechanics and Dynamics, University of Kassel, Mönchebergstr. 7, 34109 Kassel, Germany

A. Meister  
Inst. of Mathematics, University of Kassel, Heinrich-Plett-Str. 40, 34132 Kassel, Germany

of metal workpieces. There, the desired material properties are achieved by rapid local cooling, which causes solid phase changes, allowing to create graded materials with precisely defined properties. This recently received a lot of industrial and scientific interest [8] and thus one is interested in simulating this.

For the solution of the coupled problem, we prefer a partitioned approach, where different codes for the sub-problems are reused and the coupling is done by a master program which calls interface functions of the other codes. Our goal is to find a fast solver in this partitioned setting. One approach would be to speed up the subsolvers, see [3] for the current situation for fluid solvers. However, we want to approach the problem from the point of view of a partitioned coupling method, meaning that we use the subsolvers as they are. As a reference solver, we use the time adaptive higher order time integration method suggested in [2]. Namely, the singly diagonally implicit Runge-Kutta (SDIRK) method SDIRK2 is employed.

To improve upon this, one approach would be to define the tolerances in the subsolver in a smart way and recently, progress has been made for steady problems [4]. However, it is not immediately clear how to transfer these results to the unsteady case. Thus, the most promising way is to reduce the number of fixed point iterations. The idea we follow is that of extrapolation based on knowledge about the time integration scheme [1]. Hereby, we use linear and quadratic extrapolation of old values from the time history applied specifically to SDIRK2.

## 2 Model, Discretization and Solver

In the fluid, we employ the compressible Navier-Stokes equations, discretized using a finite volume method. In particular, the DLR TAU-Code is used [5].

In the structure, the nonlinear heat equation is employed. Thereby, to model the steel 51CrV4, the coefficient functions for the heat conductivity and the specific heat capacity from [7] are implemented. The PDE is discretized using quadratic finite elements in the form of the in house code NATIVE.

For the time integration, the time adaptive SDIRK2 scheme is used, as described in the context of a partitioned coupling solver in [2]. There, the used has to supply a tolerance TOL for the desired error in the time integration, which is then used to steer the time step size.

Regarding the coupling, a Dirichlet-Neumann iteration in the form of a Gauß-Seidel process is applied. Following Giles [6], temperature is prescribed for the fluid and the heat flux for the structure.

The Dirichlet-Neumann iteration is terminated when the norm of the interface residual is smaller than  $TOL/5$ . This leads to a situation where for engineering tolerances, only two iterations are necessary. To nevertheless improve upon this, we use the technique of extrapolation in time.

At the first stage, we have the old time step size  $\Delta t_{n-1}$  with value  $\Theta_{n-1}$  and the current time step size  $\Delta t_n$  with value  $\Theta_n$ . We are looking for the value

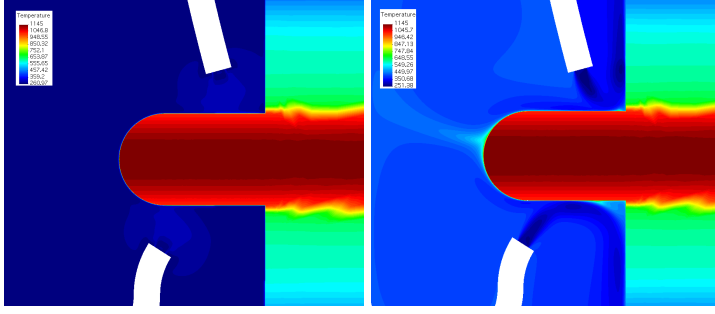


**Fig. 1** Temperature distribution in fluid and structure at  $t = 0s$  (left) and  $t = 1s$  (right).

$\Theta_1$  at the next stage time  $t_n + c_1 \Delta t_n$ . Linear extrapolation results in

$$\Theta_1 = \Theta_n + c_1 \Delta t_n (\Theta_n - \Theta_{n-1}) / \Delta t_{n-1}. \quad (1)$$

Regarding quadratic extrapolation, it is reasonable to choose  $t_n$ ,  $t_{n-1}$  and the intermediate temperature vector  $\Theta_{n-1/2}$  from the previous stage  $t_{n-1} + c_1 \Delta t_{n-1}$ . This results in

$$\begin{aligned} \Theta_1 = \Theta_{n-1} & \frac{(c_1 \Delta t_n + (1-c_1) \Delta t_{n-1}) c_1 \Delta t_n}{c_1 \Delta t_{n-1}^2} - \Theta_{n-1/2} \frac{(c_1 \Delta t_n + \Delta t_{n-1}) c_1 \Delta t_n}{c_1 \Delta t_{n-1}^2 (1-c_1)} \\ & + \Theta_n \frac{(c_1 \Delta t_n + \Delta t_{n-1}) (c_1 \Delta t_n + (1-c_1) \Delta t_{n-1})}{(1-c_1) \Delta t_{n-1}^2}. \end{aligned} \quad (2)$$

When applying this idea at the second stage when trying to find the value at  $t_n$ , it is better to use values from the current time interval. Thus, we linearly extrapolate  $\Theta_n$  at  $t_n$  and  $\Theta_1$  at  $t_n + c_1 \Delta t$ . In the quadratic case we employ  $\Theta_n$ ,  $\Theta_1$  and  $\Theta_{n-1}$ . The resulting formulae are analogous to the previous ones.

### 3 Numerical Results

We now look at the cooling of a flanged shaft by cold high pressured air coming out of small tubes as examined experimentally in [8]. A two dimensional cut through the domain is considered, resulting in one half of the flanged shaft and two tubes blowing air at it. We assume that the air leaves the tube in a straight and uniform way at a Mach number of 1.2. Furthermore, we assume a freestream in  $x$ -direction of Mach 0.005. The Reynolds number is  $Re = 2500$  and the Prandtl number  $Pr = 0.72$ .

The grid consists of 279212 cells in the fluid, which is the dual grid of an unstructured grid of quadrilaterals in the boundary layer and triangles in the rest of the domain, and 1997 quadrilateral elements in the structure.

To obtain initial conditions, we use the following procedure: We define a first set of initial conditions by setting the flow velocity to zero throughout and choose the structure temperatures at the boundary points to be equal to temperatures that have been measured by a thermographic camera. Then, setting the  $y$ -axis on the symmetry axis of the flange, we set the temperatur at

**Table 1** Total number of iterations for 1 sec of real time for different extrapolation methods

<i>TOL</i>	none	lin.	quad.
$10^{-2}$	52	42	47
$10^{-3}$	127	97	99
$10^{-4}$	433	309	312

each horizontal slice to the temperature at the corresponding boundary point. Finally, to determine the actual initial conditions, we compute  $10^{-5}$  seconds of real time using the coupling solver with a fixed time step size of  $\Delta t = 10^{-6}s$ . This means, that the high pressured air is coming out of the tubes and the first front has already hit the flanged shaft. This solution is illustrated in figure 1 (left).

Now, we compute 1 second of real time using the time adaptive algorithm with different tolerances and an initial time step size of  $\Delta t = 10^{-6}s$ . During the course of the computation, the time step size is increased until it is on the order of  $\Delta t = 0.1s$ , which demonstrates the advantages of the time adaptive algorithm and reaffirms that it is this algorithm that we need to compare to. In total, the time adaptive method needs between 22 and 130 time steps to reach  $t = 1s$ , compared to the  $10^6$  steps the fixed time step method would need. The solution at the final time is depicted in figure 1 (right). As can be seen, the stream of cold air is deflected by the shaft.

We then compare the total number of iterations for the different extrapolation methods. In table 1, the total number of iterations for 1 second of real time is shown. The extrapolation methods cause a noticeable decrease in the total number of fixed point iterations, with linear extrapolation performing better than the quadratic version. The speedup from linear extrapolation is between 20% and 30%, compared to the results obtained without extrapolation.

## References

1. M. Arnold, Stability of Sequential Modular Time Integration Methods for Coupled Multi-body System Models, *J. Comput. Nonlinear Dynam.* 5, pp. 1–9 (2010)
2. Birken, P., Quint, K. J., Hartmann, S., Meister, A., A Time-Adaptive Fluid-Structure Interaction Method for Thermal Coupling, *Comp. Vis. in Science*, 13, pp. 331–340 (2011).
3. P. Birken, Numerical Methods for the Unsteady Compressible Navier-Stokes Equations, Habilitation Thesis, University of Kassel (2012).
4. P. Birken, Termination criteria for inexact fixed point schemes, *Numer. Linear Algebra Appl.*, submitted.
5. T. Gerhold, O. Friedrich, J. Evans, and M. Galle, Calculation of Complex Three-Dimensional Configurations Employing the DLR-TAU-Code, AIAA Paper, 97-0167 (1997).
6. M. B. Giles, Stability Analysis of Numerical Interface Conditions in Fluid-Structure Thermal Analysis, *Int. J. Num. Meth. in Fluids*, 25, pp. 421–436 (1997).
7. K. J. Quint, S. Hartmann, S. Rothe, N. Saba, and K. Steinhoff, Experimental validation of high-order time integration for non-linear heat transfer problems, *Comput. Mech.* 48, pp. 81–96 (2011).
8. U. Weidig, N. Saba, and K. Steinhoff, Massivumformprodukte mit funktional gradierten Eigenschaften durch eine differenzielle thermo-mechanische Prozessführung, *WT-Online*, pp. 745–752 (2007).

**C 2 Parallel Algorithm for  
Solution-Adaptive Grid Movement in  
the Context of Fluid Structure  
Interaction**

Authors: Kneißl, Stefan, Sternel, Dörte C., Schäfer, Michael

---

# Parallel algorithm for solution-adaptive grid movement in the context of fluid structure interaction

S. Kneißl, D. C. Sternel, M. Schäfer

**Abstract** We demonstrate a new grid movement strategy, exemplified with a generic fluid-structure interaction (FSI) test case. A flat plate with a prescribed rotational movement in a channel flow is investigated. The transient turbulent flow field is calculated with a low-Re RANS model and two different grid movement methods. Using transfinite interpolation with a grid-point distribution fitted to the stationary starting conditions as grid moving method, leads to errors for the drag-coefficient. By employing a normalized wall distance adaptive method, it is possible to fulfill the near-wall resolution requirements within every time step and thereby getting more accurate results.

**Keywords** Coupled Problems, Fluid-Structure Interaction, Moving Grid, Grid Adaptivity.

---

S. Kneißl  
Graduate School of Computational Engineering, TU Darmstadt, Dolivostraße 15, 64293 Darmstadt  
Tel.: +49 6151 16-7445  
Fax: +49 6151 16-4459  
E-mail: kneissl@gsc.tu-darmstadt.de

D. C. Sternel  
Institute of Numerical Methods in Mechanical Engineering, TU Darmstadt, Dolivostraße 15, 64293 Darmstadt  
Tel.: +49 6151 16-5524  
Fax: +49 6151 16-4479  
E-mail: sternel@fmb.tu-darmstadt.de

M. Schäfer  
Institute of Numerical Methods in Mechanical Engineering, TU Darmstadt, Dolivostraße 15, 64293 Darmstadt  
Tel.: +49 6151 16-2877  
Fax: +49 6151 16-4479  
E-mail: schaefer@fmb.tu-darmstadt.de

## 1 INTRODUCTION

For many engineering problems the interaction between a moving structure and a turbulent flow is of importance. Numerical models are used to predict the behavior of such systems. The overall solution fidelity strongly depends on the quality of the turbulent flow model used to calculate the forces acting on the structure. We employ the finite volume method with an URANS (Unsteady Reynolds Averaged Navier Stokes) modeling approach. Here the underlying spatial discretization is decisive for efficiency and accuracy. Furthermore the grid resolution has to fulfill validity requirements implied by the turbulence model in the near wall regions. These are formulated in terms of a velocity normalized wall distance  $y^+$  for the wall adjacent cells.

The need to change the grid that represents the deforming fluid domain within a FSI Simulation, poses a conflict of aims between geometrical cell quality and resolution requirements. Standard techniques for calculating the movement of grid points, like spring analogy methods or interpolation methods (see, for example [1–3]), are designed to keep the initial distribution constant relatively to the structure. These do not address the conflict of aims explicitly and may produce wrong flow solutions if the resolution requirements change.

## 2 METHOD

In this contribution we want show that it is possible to meet the near wall resolution requirements of a RANS model in a generic test case by relocating grid-points according to the flow situation. The idea is, since it is necessary to solve a grid movement problem for the deforming domain anyway, one could also incorporate solution information for a more suited fluid grid. We use the Target-Matrix-Paradigm (TMP) introduced in [4] to formulate the grid movement problem as an optimization problem. It offers the possibility to express different aspects of cell quality within a uniform principle. Here, quality is defined as a deviation from an optimal cell. In the near wall region we define the optimal cells as rectangular and scaled in wall normal direction according to the  $y^+$  requirements. In the rest of the field optimal cells are chosen to be just rectangular with an arbitrary size.

For the parallelization overlapping domain decomposition is used to divide the grid movement problem into independent subproblems. The same decomposition as for the fluid solver can be used. An iteration process using averaged displacements on the interfaces between adjacent subdomains solves the problem for the whole domain.

## 3 RESULTS AND DISCUSSION

### 3.1 Description of the test case

As test case we employ a two-dimensional channel flow with a length of 2 m and a height of 0.45 m. In it's center a flat plate with a length of 0.12 m and a

height of 0.006 m and rounded edges, which inclines with a constant angular velocity of  $175 \text{ s}^{-1}$ , serves as obstacle. At the inflow a parabolic profile was chosen to avoid high gradients triggering the refine mechanism at the edges. The Reynolds number based on the channel height and center inflow velocity  $u_{max} = 4 \text{ m/s}$  equals  $Re = 2.21 \cdot 10^5$ .

The initial grid shown in figure 1 is an O-Grid type mesh consisting of 74880 cells. The treatment of turbulence in wall proximity is based on the first control volume being located in the viscous sub-layer. Thus  $y^+$  should not exceed 5. The initial grid has been chosen accordingly as visible from Figure 2d.

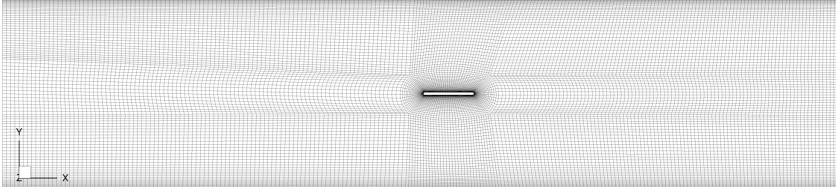


Fig. 1: Starting grid

### 3.2 Evaluation and Discussion

In order to demonstrate that the near wall resolution can be controlled, Figure 2 contains plots of  $y^+$  on the plate's top wall for an interpolation method and the adaptive method at different simulation times. The reference method does not change the near wall resolution. So in consequence of the accelerated flow towards the trailing edge the  $y^+$  values surpass the model limit of 5. For the  $y^+$  adaptive method we can not observe a raising tendency.

It has to be mentioned that the exceeding  $y^+$  values could be avoided by choosing a finer initial mesh. But such a trial and error strategy might not be feasible for more complex FSI scenarios.

## 4 CONCLUSION

We have presented a turbulent test case with prescribed structural motion for which we applied a  $y^+$  adaptive and a non-solution-adaptive grid movement strategy. The conducted numerical experiments showed, that it is important to control the grid resolution for simulations with changing flow conditions as occurring for FSI scenarios. The grid moving strategy outlined in this work in principle is not restricted to just limiting  $y^+$ . Other solution dependent criteria are possible as for example velocity gradients aiming to reduce discretization errors.

## ACKNOWLEDGMENT

This work is supported by the 'Excellence Initiative' of the German Federal and State Governments and the Graduate School of Computational Engineering at Technische Universität Darmstadt.

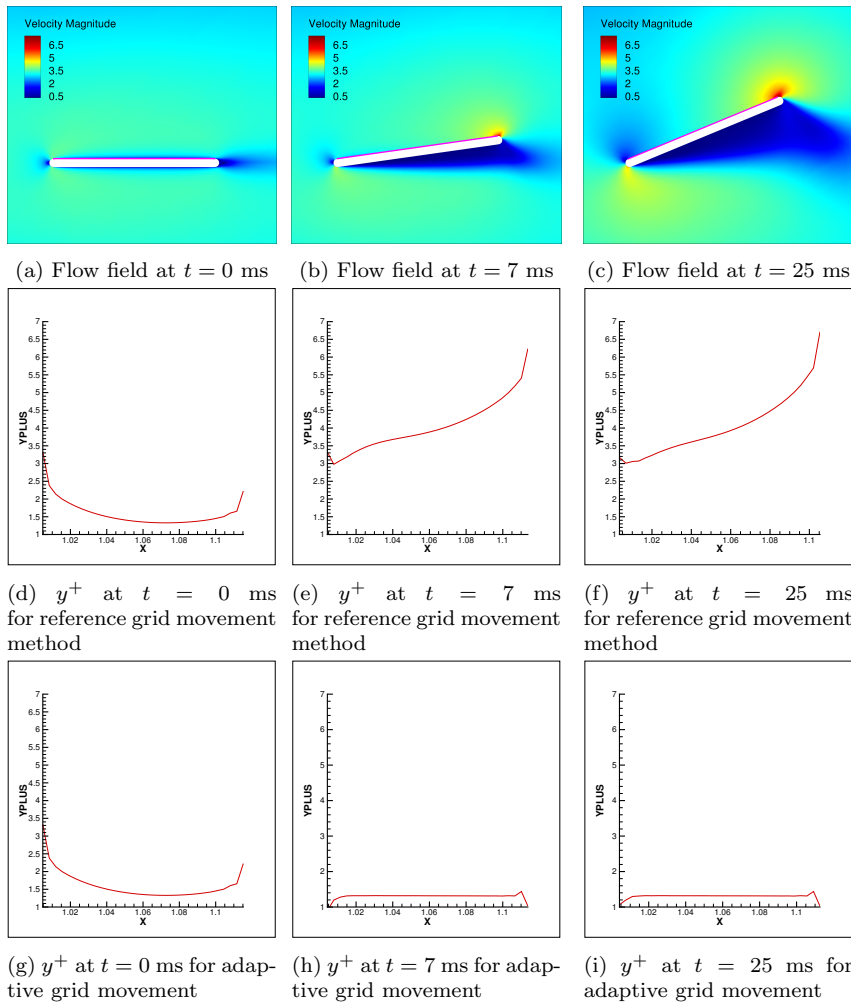


Fig. 2: Comparison of  $y^+$  values on the purple marked lines in a,b,c for different simulation times between the reference grid movement method (d-e) and the  $y^+$  adaptive method (g-i)

## References

1. C. Degand and C. Farhat. A three-dimensional torsional spring analogy method for unstructured dynamic meshes. *Comput. Struct.*, Vol. **80**(3-4), 305-316, 2002.
2. A. de Boer, M. van der Schoot and M. Bijl. Mesh deformation based on radial basis function interpolation. *Comput. Struct.*, Vol. **85**(11-14), 784-795, 2007.
3. S. P. Spekreijse, B. B. Prananta and J. C. Kok. A simple, robust and fast algorithm to compute deformation of multi-block structured grid,. *Technical Report - National Aerospace Laboratory NLR*, NLR-TP-2002-105, 2002.
4. P. Knupp. Introducing the target-matrix paradigm for mesh optimization via node-movement. *Engineering with Computers.*, Vol. **28**(4), 419-429, 2012.
5. P. Pironkov. Numerical Simulation of Thermal Fluid-Structure Interaction. PhD thesis, Technische Universität Darmstadt, 2010.

# **C 3 Simulation of Wave Propagation and Impact Damage in Brittle Materials Using the Peridynamics Technique**

Authors: Diehl, Patrick, Schweitzer, Marc Alexander

---

# Simulation of Wave Propagation and Impact Damage in brittle materials using the Peridynamics technique

Patrick Diehl · Marc Alexander Schweitzer

**Abstract Keywords** Wave Propagation · Impact Damage · Peridynamics · Applications · Edge-On-Impact (EOI) Experiment.

We present the simulation of wave propagation and impact damage in brittle materials, e.g. ALON or fused silica.

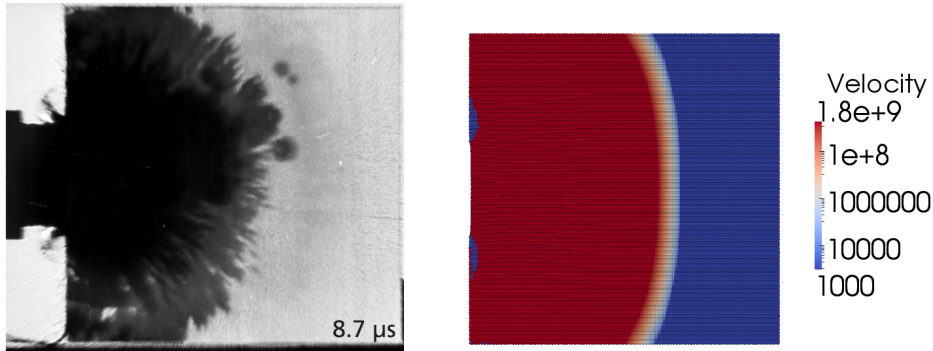
For the visualization of impact damage in ceramics the Ernst-Mach-Institute (EMI) developed the Edge-On Impact (EOI) technique [1]. In this experiment a steel projectile impacts a ceramic plate and the growth of the primary crack is observed with a high-speed camera. The results from the EOI experiment are shadow graphs (figure 1(a)) of the evolving wave and the wave front velocity.

To simulate the evolving of the wave the Peridynamic technique [4], an alternative non local theory in solid mechanics is used. This theory formulates the problem with integral equations instead of partial differential equations. This allows discontinuities in the displacement fields and the branching of cracks is directly possible. Figure 1(b) shows the first simulation results with an simple material model of the wave velocity at  $t=8.7\mu s$ . With the first simulation the extracted wave front velocity converge to an numerical value of

---

P. Diehl  
Institute for Numerical Simulation  
Wegelerstr. 6  
53115 Bonn  
Tel.: +49 228 733846  
Fax: +49 228 733979  
E-mail: diehl@ins.uni-bonn.de

M. A. Schweitzer  
Institute for Numerical Simulation  
Wegelerstr. 6  
53115 Bonn  
E-mail: schweitz@ins.uni-bonn.de



(a) Shadow graph of the ALON specimen at  $t=8.7\mu\text{s}$ . Image taken from [3].

(b) The velocity of the evolving wave at  $t=8.7\mu\text{s}$ .

**Fig. 1** Shadow graph of the evolving wave of the EOI experiment and the velocity of the evolving wave at  $t=8.7\mu\text{s}$ .

the front wave velocity. The numerical value differs by 10% to 20% from the measured wave front velocity in the experiments.

We implemented two extensions for the Peridynamic technique to improve the convergence of the wave front velocity to the measured wave front velocity of the EOI experiment. The first extension is to use the normalized bond-based Peridynamics model for the energy density  $W^{\text{PD}}$ . With this model the deficit of the Energize is reduced compared to the density. The second extension is to replace the contact potential between particles with an hertzian potential.

With these extensions we hope to improve the convergence of the numerical value of the wave front velocity.

## References

1. E. Strassburger. Visualization of Impact Damage in Ceramics Using the Edge-On Impact Technique. *Int. J. Appl. Ceram. Technol.*, Vol. **10**, 235–242, 2004.
2. E. Strassburger, P. Patel, J. W. McCauley and D. W. Tempelton. Visualization of Wave Propagation and Impact Damage in a Polycrystalline Transparent Ceramic – ALON 22<sup>th</sup> International Symposium on Ballistics.
3. E. Strassburger and et al. *HIGH-SPEED PHOTOGRAPHIC STUDY OF WAVE PROPAGATION AND IMPACT DAMAGE IN FUSED SILICIA and ALON USING THE EDGE-ON IMPACT (EOI) METHOD*.
4. S. A. Silling and E. Askari. A meshfree method based on the peridynamic model of solid mechanics. *Computer & Structures*, Vol. **38** 1526–1535, 2005.

## **C 4 Using Instancing to Efficiently Render Super Carbon Nanotubes**

Authors: Burger, Michael, Bischof, Christian

---

# Using Instancing to efficiently render Super Carbon Nanotubes

Michael Burger · Christian Bischof

**Abstract** In this paper, we present an efficient way to visualize Super Carbon Nanotubes (SCNTs). SCNTs are complex, hierarchical structures and their models easily consist of more than 1 million atoms. Our SCNTs are modeled as graphs of uniform nodes and edges. We show that OpenGL instancing is a very suitable technique for rendering such large graphs, because they only consist of two different types of geometry. Our visualizer software exploits this property and we demonstrate that it allows to render the tubes in a fashion that is time- and space-effective. We implemented auto-tuning of the model to the underlying graphics card through adaptive mesh-resolution-choices. We also designed and implemented our own shading programs in the OpenGL Shading Language (GLSL) to realize a sufficient but performant and configurable lighting computation. This allows us to render big models even on laptop GPUs and to cope with models that consist of 150 million triangles, which is still a challenging amount for most of today's graphics cards.

## 1 Introduction to Super Carbon Nanotubes and OpenGL Instancing

Carbon Nanotubes (CNTs) are an interesting field of research, because they can be used in a lot of applications. New synthesis approaches allow the composition of tubes with Y-shaped junctions to structures that possess again the

---

Michael Burger  
FG Scientific Computing, TU Darmstadt  
Mornewegstrasse 30, 64293 Darmstadt  
Tel.: +49 6151 16-76991  
E-mail: michael.burger@sc.tu-darmstadt.de

Christian Bischof  
FG Scientific Computing, TU Darmstadt  
Tel.: +49 6151 16-71001  
E-mail: christian.bischof@sc.tu-darmstadt.de

shape of a tube. The resulting tubes are called Super Carbon Nanotubes (SCNTs) ([SW13]). This process can be repeated an arbitrary number of times. Figure 1 shows a CNT. A Y-shaped junction to construct tubes of level 1 is depicted in figure 2.

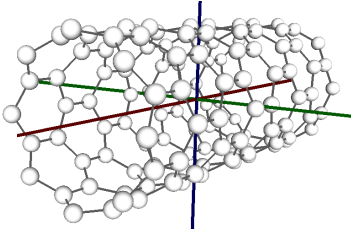


**Fig. 1** SCNT of level 0

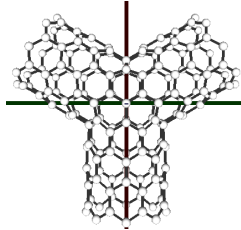


**Fig. 2** Junction as basic building block of a SCNT of level 1.

The shape is defined by a quadruple of values  $(D_0, L_0, D_X, L_X)$  which determines the following properties:

- $D_0$ : Diameter of the resulting SCNT,  $L_0$ : Length of the resulting SCNT
- $D_X$ : Thickness of the Y-junction arms,  $L_X$ : Length of the junction arms

Each valid combination of these parameters, together with the tube level, results in a unique tube. Even for small CNTs this procedure leads very fast to structures with high atom-count. This makes it challenging to cope with such a high amount of data and to render these structures.

Our visualization tool uses OpenGL and instancing [SSK13, p. 128 - 139]. This allows to draw several elements with the same geometry with slight differences. The technique makes it possible to reduce the OpenGL API-calls by only using one instanced draw-call for  $n$  instances of an object. This drastically reduces the CPU load, as the host only needs to pass the mesh itself and additional information like the position of the models, their material, etc.

## 2 Features of our tool

Our program is able to zoom into and to arbitrarily rotate the scene. It can interactively visualize the constructed tubes within the main program by exploiting the graph properties that are suitable for instancing. Compared to a data export to a general purpose visualization tool, this saves time and memory.

### 2.1 Auto-performance-tuning by adaptive meshes

The graph is rendered in a two step approach. First, the connections between the nodes are drawn as `GL_LINES`, a primitive within OpenGL. `GL_LINES` are

determined by their end points and the graphics driver and card are responsible for rasterizing the line. The second step adds the atoms. These are represented as spheres, modeled by a triangle-mesh. To be able to run on different systems, the visualizer adapts the resolution of the triangle meshes, depending on the graphics card it is executing on. This change is transparent to the user. Our visualizer monitors the frame rate and automatically reduces the details if it is too slow for a predefined time interval. The current version includes five levels of detail for the spheres, plus a sixth level that draws no spheres at all.

Example screenshots for this procedure are shown in figure 3 and figure 4. Figure 3 shows a scene with the highest resolution, e.g. level 5, while figure 4 represents the same scene with detail-level 1.

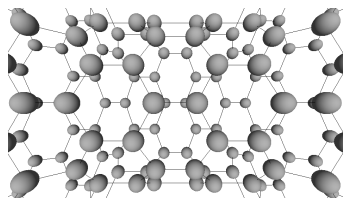


**Fig. 3** Full detail

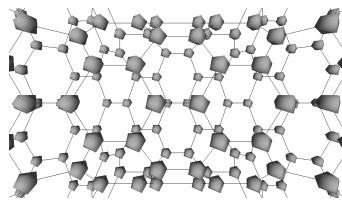


**Fig. 4** Reduced detail

The visualizer is configured to target about 12 frames per second (fps). From experiments we noticed that this rate is sufficient for practical use.

## 2.2 GLSL shading programs

The model-transformations are applied within our GLSL-vertex-shader programs by the GPU. This moves work load from the CPU to the graphics card.

Lighting is also done by our shading programs. We developed two different shaders for the two distinct components of the model. The one for spheres is based on Phong-shading-model. The lines are drawn in a predefined color.

## 3 Test Systems and Results

The tests show that our visualization software is able to render all structures that are of relevance for us. For the measurements we used a desktop system equipped with an Intel Xeon 1230v2 processor, 16 GB of DDR3 RAM and a AMD R280x graphics card. For comparison, a laptop with an Intel i7-3520M, integrated HD4000 graphics and 8 GB of DDR3 main memory is employed.

The visualizer is able to render a (16, 16, 1, 2) tube of level 2 on a R280x with 24 fps with detail level 1 and still 11 fps with detail level 2. The HD4000 is able to reach a frame rate  $> 12$  when falling back to detail-level 0. In that case the scene is rendered with about 20 fps. This scene consists of 50 million triangles for the spheres in detail level 1. This value rises to about 150 million

triangles for the detail level 2. This tube is also one of the most complex structures that our software package for constructing SCNTs can cope with at the moment. Table 1 summarizes the results for two smaller tubes.

level 2 (6, 6, 1, 3) tube, 1179648 atoms						
	L5	L4	L3	L2	L1	L0
<b>R280x</b>	1.99	5.61	14.97	27.07	63.76	284.35
<b>HD4000</b>	0.45	1.33	3.51	5.62	11.19	23.04
level 1 (10, 8, 1, 11) tube, 81920 atoms						
	L5	L4	L3	L2	L1	L0
<b>R280x</b>	28.57	80.21	211.53	380.66	868.03	3336.66
<b>HD4000</b>	6.48	18.15	45.01	66.13	113.38	177.91

**Table 1** Summary of the achieved frames per second for a two different tubes.

As can be seen in table 1, the R280x allows the use of detail-level 3 for the level 2 (6, 6, 1, 3) tube case. For HD4000, the visualizer chooses level 1. It can be noticed that the scaling between the distinct level of details of the R280x is much better than the one of the HD4000. This can be explained with the performance for rasterizing lines. Considering the change from level 1 to 0, the rendering speed of the R280x increases by the factor of 3 when completely disabling sphere-rendering, the frame rate of the HD4000 only doubles.

Another test is the (10, 8, 1, 11) level 1 tube. As figure 5 shows, it has the property that some parts of it are very dense (the „dark lines“), while the others contain no atoms (the rest). Figure 6 depicts such a „dark line“ in detail.

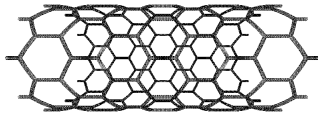


**Fig. 5** Level 1 tube with longer arms at the junctions

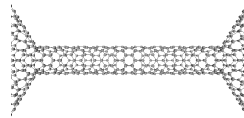


**Fig. 6** Single line within the tube

The R280x has no problems in visualizing the tube at all. The fact of higher line-rendering speed of the R280x is confirmed. While the performance when neglecting spheres triples for the R280x, the HD4000 increases by a factor of 1.57. The overlaying lines in the dense parts seem to be the reason.

## References

- [SSKLLK13] SHREINER, Dave ; SELLERS, Graham ; KESSENICH, John ; LICEA-KANE, Bill: *OpenGL Programming Guide: The Official Guide to Learning OpenGL, Version 4.3*. 8th. Boston, MA, USA : Addison-Wesley Longman Publishing Co., Inc., 2013. – ISBN 978-0-321-77303-6
- [SW13] SCHROEPPEL, Christian ; WACKERFUSS, Jens: Constructing meshes based on hierarchically symmetric graphs. In: *Internal Report, TU Darmstadt* 0 (2013)

## **C 5 An Efficient Algorithm to Include Sub-Voxel Information in FFT-Based Homogenization**

Authors: Merkert, Dennis, Andrä, Heiko, Kabel, Mathias, Schneider, Matti, Simeon, Bernd

---

# An Efficient algorithm to include sub-voxel information in FFT-based homogenization

Dennis Merkert · Heiko Andrä ·  
Mathias Kabel · Matti Schneider ·  
Bernd Simeon

**Abstract** Recently, FFT-based methods to solve the equations of elasticity in homogenization have become quite popular. The voxel-based methods are parallelizable, fast and can handle a very large number of degrees of freedom with ease. However, regular voxel grids cannot resolve interfaces exactly.

In this paper we identify a class of mixing rules for interface voxels to cure this deficiency. Adding mixing rules is inexpensive in terms of computational time and increases the accuracy of the calculated effective properties significantly, as will be demonstrated by several numerical examples.

## 1 Introduction

In the last years, when solving the equations of static elasticity, the FFT-based method proposed by Moulinec and Suquet in 1998 [1, 2] has attracted much attention.

Given a stiffness tensor  $C$  and a constant tensor  $C^0$  of fourth order, the differential equation is reformulated as Lippmann-Schwinger equation

$$\epsilon = E - \Gamma^0 * ((C - C^0) : \epsilon).$$

---

{D. Merkert, Bernd Simeon}  
TU Kaiserslautern Paul-Ehrlich-Straße 31  
67663 Kaiserslautern Tel.: +49-631-205-5316,5310  
Fax: +49-631-205-5308  
E-mail: {dmerkert,simeon}@mathematik.uni-kl.de

{H. Andrä, M. Kabel}  
Fraunhofer Institut für Techno- und Wirtschaftsmathematik ITWM  
Fraunhofer-Platz 1  
67663 Kaiserslautern

M. Schneider  
TU Chemnitz  
Reichenhainer Straße 31/33  
09126 Chemnitz

```

1:  $\epsilon \leftarrow E$ 
2: repeat
3:    $\epsilon \leftarrow \text{MSiterate}(\epsilon, C, C^0, E)$ 
4: until Convergence
5: return  $\epsilon$ 
MSiterate( $\epsilon, C, C^0, E$ )
1:  $\epsilon \leftarrow C : \epsilon - C^0 : \epsilon$ 
2:  $\epsilon \leftarrow \text{FFT}(\epsilon)$ 
3:  $\epsilon \leftarrow -\hat{I}^0 : \epsilon, \quad \epsilon(0) = E$ 
4:  $\epsilon \leftarrow \text{FFT}^{-1}(\epsilon)$ 
5: return  $\epsilon$ 
a)

```

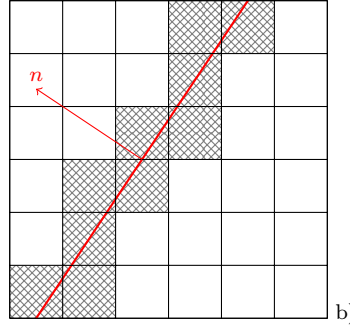


**Fig. 1** a) basic scheme, b) red: interface with normal  $n$ , hatched: interface voxels

The second order tensor  $E$  is the prescribed macroscopic strain and  $\Gamma^0$  is Green's operator, easily described by its Fourier coefficients. The operation  $*$  is the convolution. Then, one usually is interested in the effective matrix, a fourth order tensor given by  $C^{\text{eff}}E = |\Omega|^{-1} \int_{\Omega} C : \epsilon dx$  and  $\Omega$  the domain.

The Lippmann-Schwinger equation is solved by the so called basic scheme in Fig. 1 a). As the required operations in real space and Fourier space are voxel-wise operations, this algorithm allows for easy parallelization. With a parallel implementation of the FFT [3], it is scalable and can perform on very large geometries with ease. While being very fast and memory efficient, the scheme cannot resolve the material interfaces correctly.

This paper will present a method to use additional information in interface voxels to greatly increase the quality of the effective matrix for reasonable computational costs. As the proposed operations are again applied voxel-wise, the algorithm stays fully parallelizable.

## 2 Mixing formulas

To incorporate information about the interface voxels, we introduce the concept of mixing formulas. Given an interface voxel  $V \subset T^n$  (see Fig. 1 b)), one sets its new stiffness to be a mixture of the material laws around the interface.

As information to use, we take the volume fractions of the materials in the interface voxel and a normal on the linearized interface. One way to obtain these is to use the exact values of voxels in computer tomography images for the volumes and image processing techniques to determine the interface. When downsampling a higher-resolution image, the normal can be easily obtained by stable estimators [4]. This can be done in advance for each geometry and is cheap in comparison to the actual calculation.

First, taking only volume fractions into account, we introduce the Voigt mixing formula  $|V|^{-1} \int_V C dx$  and the Reuss mixing formula  $(|V|^{-1} \int_V C^{-1} dx)^{-1}$ . Using additionally the normal on the interface, we can use rotated laminates. There, we use as new stiffness the effective matrix of a laminate consisting of the materials in the interface voxel with their respective volume fractions.

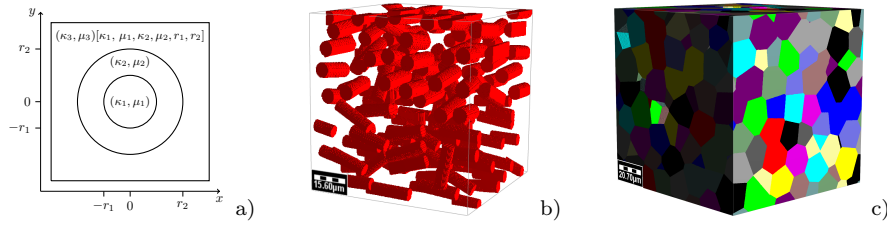


**Fig. 2** Example geometries: a) Hashin structure, b) fiber structure, c) polycrystal

The direction of lamination is given by the normal on the linearized interface. Formulas for this can be found in [5].

One can show that after introducing mixing formulas, the effective matrix still converges to the correct solution. If the composite itself is a laminate, one can even show that rotated laminates cancel the voxelization error entirely. The calculation of these mixing rules can be done while evaluating the stiffness in the voxels during the iterations of the algorithm. This allows for non-constant material laws and has a small effect on the computing time.

### 3 Numerical results

To compare the mixing formulas numerically, we consider three examples. First, we investigate the two-dimensional Hashin structure, cf. [5], that is shown in Fig. 2 a). For this structure the effective matrix is given analytically. Further, we take a look at a more realistic two-layered fiber structure, cf. Fig. 2 b), and the polycrystalline structure in Fig. 2 c).

For the Hashin structure we fix the elastic properties in the core and vary the stiffness in the coating, cf. Fig. 3. One sees, that depending on contrast one gains almost one order of magnitude in accuracy when computing the effective properties using mixing rules.

In the case of the fiber structure, we fix the stiffness to 1 MPa in the matrix material and 50 MPa in the fibers and vary the resolution, see Fig. 4 a). As soon as the resolution gets high enough for the interface in the respective voxels to be sufficiently linear, the rotated laminates exceed the other methods in accuracy.

Taking a look at the polycrystalline structure consisting of transverse isotropic magnesium in Fig. 4 b), once again mixing rules have a tremendous effect on the error.

### 4 Summary

We have seen that using additional information in the interface voxels, one can reduce the error caused by voxelization. Especially, the rotated laminates perform very well for higher resolutions. Further, the above concepts can be

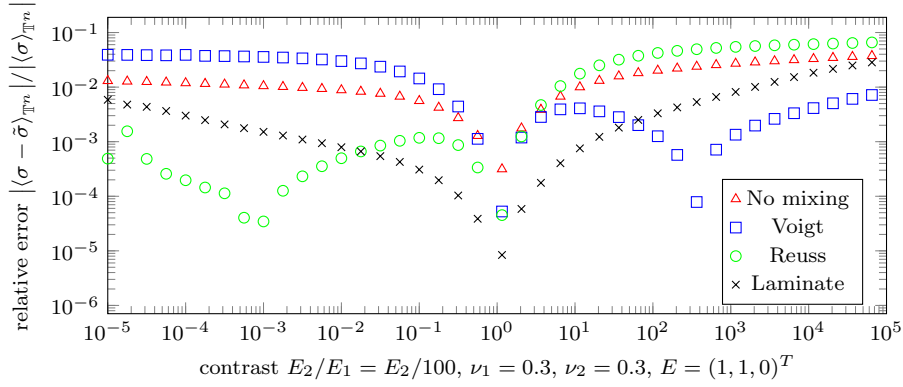


**Fig. 3** Error of the effective matrix for the Hashin structure with varying contrast

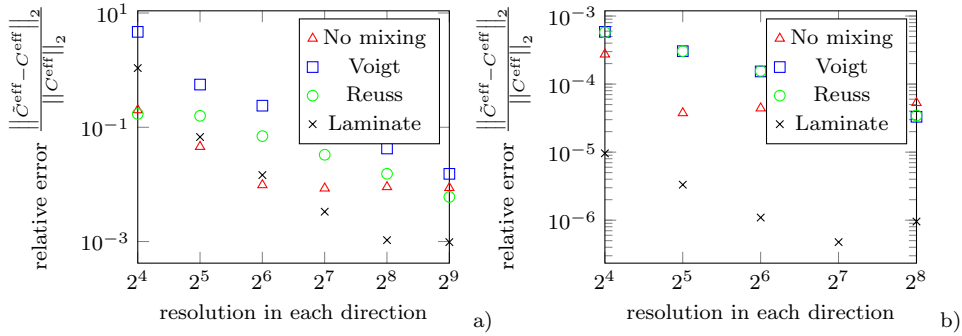


**Fig. 4** Error of the effective matrix for a) the fiber structure and b) a polycrystal with varying resolution

extended to the equations of thermoelasticity and the steady-state heat equation with similar effects.

## References

1. H. Moulinec and P. Suquet, A numerical method for computing the overall response of nonlinear composites with complex microstructure, *Comput. Methods Appl. Mech. Engrg.*, 157, 69-94 (1998)
2. M. Kabel and H. Andrä, Fast numerical computation of precise bounds of effective elastic moduli, *Berichte des Fraunhofer ITWM*, 224, 1-16 (2013)
3. M. Frigo and S. G. Johnson, The Design and Implementation of FFTW3, *Proceedings of the IEEE*, 93, 216-231 (2005)
4. T. Theile and M. Schneebeli, Algorithm to decompose three-dimensional complex structures at the necks: tested on snow structures, *IET Image Process.*, 5, 132-140 (2011)
5. G. W. Milton, *The theory of composites*. Cambridge University Press, Cambridge (2002)

## **C 6 A Multi Scale Model for Mass Transport in Arteries and Tissue**

Authors: Köppl, Tobias

---

# A multi scale model for mass transport in arteries and tissue

Tobias Köppl

**Abstract** Mathematical models have become more and more important in many applications from medicine and biology. Quite often the resulting system of equations is complex, highly nonlinear and cannot be solved analytically. Thus stable and robust numerical simulation methods play an important role in understanding phenomena like the regulatory mechanisms of the heart [6, 3] or the balancing of metabolic supply and demand in the Cerebral Blood Flow (CBF) [7–9]. By these non invasive techniques, physiological processes in the human body can be examined and understood with less effort and less danger for a patient. As a consequence scientists can get more insight into the inherent mechanisms and improve their diagnosis techniques. Moreover quantitative prediction of the distribution of a chemical compound in living tissues, which provide important contributions to the development of new medical products [1,11], will be possible by the help of numerical simulation.

Our aim is to give a reliable prediction of the distribution of certain chemicals like oxygen, carbon dioxide or lactate during the transport in blood vessels and human tissue. Furthermore the impact on organs suffering from a reduced supply of oxygen due to a stenosis can be predicted by the help of computational methods. A well known problem in this field is, e.g., to estimate the risk of ischemia caused by a carotid stenosis [4]. So both the pressure of blood flow and the concentration of these chemicals in the vessels and tissue must be computed at the same time. Therefore the development of mathematical models for pressure and velocity propagation together with mass transport are of vital interest.

Since blood flow within the network is fast compared to the flow within the tissue, we apply a domain decomposition in such a way that we separate the vessel network and the porous tissue and assign different models to them [1].

---

Tobias Köppl  
M2 - Zentrum Mathematik Boltzmannstraße 3 85748 Garching  
Tel.: +49 89 289 18413  
E-mail: koeppl@ma.tum.de

Blood flow and transport processes within the porous medium are governed by Darcy's equation and a convection diffusion equation in  $3D$ .

To model the network flow and transport,  $1D$  reduced models and  $0D$  lumped parameter models are used, which are given by transport equation systems or ODE-systems, respectively [1, 13, 10, 4, 19]. Quite often three-dimensional ( $3D$ ) models for blood flow, based on the ( $3D$ ) incompressible Navier–Stokes equations are too expensive in order to simulate the blood flow through a large network. The reduced one-dimensional models presented in [1, 13, 10] are derived from the Navier–Stokes equations, having the section area  $A$  and the mass flux  $Q$  as primary variables [14, 15]. Providing a computational complexity that is several orders of magnitude lower than that of multidimensional models, these simplified models give a good description of the pressure and velocity propagation in blood vessels and allow the simulation of the whole circulatory system [10]. Similar to the Navier–Stokes equations the convection-diffusion equation which models the mass transport can be simplified to a single transport equation having the averaged concentration  $\Gamma$  as a primary variable [1].

By means of this model, which has  $A$ ,  $Q$  and  $\Gamma$  as primary variables, we are able to take into account at the same time blood flow and the transport of chemicals (oxygen, carbon dioxide, lactate, etc.) in blood. Up to now this model was only applied to a single artery. In this talk, we focus on the modelling of mass transport at a bifurcation in this paper. To do so we use a domain decomposition approach. The branching vessel is split up into three single vessels. On each vessel, we solve a hyperbolic PDE system. The global solution is computed by coupling these PDE systems by an algebraic system of nine unknowns. For the variables  $A$  and  $Q$ , we use the already existing equations proposed in [16, 10]. The three remaining equations for the averaged concentration  $\Gamma$  are added in such a way that the number of particles which are transported through the bifurcation by the fluid is conserved.

In order to solve the PDE systems numerically, the authors of [1, 16, 10] used standard finite difference schemes, the Taylor-Galerkin method [12] or unstablized discontinuous Galerkin methods in order to solve the nonlinear transport problem. However these methods deliver only good approximations when the solution of the transport problem is sufficiently smooth. It turns out that these methods produce spurious oscillations in the vicinity of steep gradients or discontinuities or suffer from dissipation and dispersion [5]. In our application, the mass concentration might exhibit large gradients or discontinuities. On simulating the transport of oxygen in blood during one heart cycle, it can be observed that the oxygen concentration has steep gradients.

Because of such reasons we are interested in numerical schemes that provide approximations of transport problems with high accuracy on the one hand and without non physical oscillations in the vicinity of steep gradients or discontinuities on the other hand. To do so, we use a stabilized discontinuous Galerkin method originally introduced for a linear transport problem [18, 17] and generalize it to our nonlinear system.

However, the coupling conditions between the porous medium and the reduced models are not standard, since they involve the computation of average

values and the usage of Delta measures [21]. The basic coupling concepts between 1D and 3D models are introduced by taking the example of stationary diffusion-reaction models, before we derive in the next step a model for the dynamics of network flow and transport processes within a porous medium. The diffusion-reaction models are given by elliptic PDE systems, where the single equations depend on each other by some exchange terms. Such types of systems are much simpler to analyze than the time dependent systems coupling 1D transport equations and dynamic 3D models. By this mean, one can obtain a better insight into the mathematical and numerical difficulties associated with coupled 1D-3D systems [20] [1][Chapter 6].

## References

1. C. D'Angelo, Multi scale modelling of metabolism and transport phenomena in living tissues, PhD-Thesis, EPFL, Lausanne, 2007
2. S. Canic and E.H. Kim, Mathematical analysis of quasi linear effects in a hyperbolic model blood flow through compliant axi-symmetric vessels, *Math. Meth. Appl. Sci.*, 26, 1161-1186, 2003
3. G.M. Saidel and J.A. DiBella and M.E. Cabrera. In Z.M. Arnez et al., editor, *Simulations in Biomedicine*, WIT Press, 100-110, 2003
4. T. Köppl, M. Schneider, U. Pohl, B. Wohlmuth, The influence of an unilateral carotid artery stenosis on brain oxygenation, *Medical Eng. and Physics*, 2014, doi: 10.1016/j.medengphy.2014.03.020
5. D. Kuzmin, R. Löhner, S. Turek, *Flux-Corrected Transport - Principles, Algorithms and Applications*, Springer-Verlag, Berlin, 2004
6. E. Magosso, A. Feliciani, M. Ursino, A mathematical model of cardiovascular response to dynamic exercise, *Proceedings of the 23rd Annual Conference of the IEEE Engineering in Medicine and Biology Society*, 2001
7. R. Turner, How much cortex can a vein drain? Downstream dilution of activation-related cerebral blood oxygenation changes, *Neuroimage*, 16, 1062-1067, 2002
8. K.K. Kwong, J.W. Belliveau, D.A. Chesler, I.E. Goldberg, R.M. Weisskoff, B.P. Poncelet, D.N. Kennedy, B.E. Hoppel, M.S. Cohen, R. Turner, Dynamic magnetic resonance imaging of human brain activity during primary sensory stimulation, *Neuroimage*, 89, 5675-5679, 1992
9. S. Ogawa, T.M. Ledd, A.R. Kay, D.W. Tank, Brain magnetic resonance imaging with contrast dependent on blood oxygenation, *Proc Natl Acad Sci USA*, 87, 9868-9872, 1990
10. S. J. Sherwin, L. Formaggia, J. Piero, V. Franke, Computational modelling of 1D blood flow with variable mechanical properties and its application to the simulation of wave propagation in the human arterial system., *Int. J. for Numerical Methods in Fluids*, 43, 673-700, 2003
11. K. Erbertseder, J. Reichold, R. Helmig, P. Jenny, B. Flemisch, A coupled discrete / continuum model for describing cancer therapeutic transport in the lung, *Public Library of Science Online Journal*, 2012
12. J. Donea, A Taylor-Galerkin Method for convective transport problems. *Int. Journal for Num. Methods in Engineering*, 20, 101-119, 1984
13. L. Formaggia, D. Lamponi, A. Quarteroni, One-dimensional models for blood flow in arteries, *Journal of Engineering Mathematics*, 47, 251-276, 2003
14. V. Milisic, A. Quarteroni, Analysis of lumped parameter models for blood flow simulations and their realtion with 1D models, *Math. Modelling and Num. Analysis*, 38, 613-632, 2004
15. M. A. Fernandez, V. Milisic, A. Quarteroni, Analysis of a geometrical multi scale blood flow model based on the coupling of ODEs and hyperbolic PDEs, *Multi scale Model. Simul.*, 4, 215-236, 2005

16. L. Formaggia, A. Quarteroni, A. Veneziani, Cardiovascular Mathematics-Modelling and simulation of the circulatory system. Springer-Verlag, Italia, Milan, 2009
17. D. Kuzmin, Slope limiting for discontinuous Galerkin approximations with possibly non-orthogonal Taylor basis, *Int. J. Numer. Meth. Fluids*, 1, 1-12, 2011
18. D. Kuzmin, A vertex-based hierarchical slope limiter for p-adaptive discontinuous Galerkin methods, *J. Comput. Appl. Math.*, 233, 3077-3085, 2010
19. T. Köppl and B. Wohlmuth and R. Helmig, Reduced one-dimensional modelling and numerical simulation for mass transport in fluids. *Int. J. Numer. Meth. Fluids*, 72(2), 135-156, 2013
20. T. Köppl and B. Wohlmuth, Local a priori error estimates for an elliptic problem with Dirac right-hand side, *SINUM*, 2014
21. C. D'Angelo, A. Quarteroni, On the coupling of 1D and 3D diffusion-reaction equations. Applications to tissue perfusion problems, *Mathematical Models and Methods in Applied Sciences*, 18(8), 1481-1504, 2008

# **C 7 Centralized Adaptive Observation Strategy for Atmospheric Dispersion Process Estimation Using Mobile Sensors**

Authors: Ritter, Tobias, Euler, Juliane, Ulbrich, Stefan, Stryk, Oskar von

---

# Centralized Adaptive Observation Strategy for Atmospheric Dispersion Process Estimation Using Mobile Sensors

Tobias Ritter<sup>1,2,\*</sup> · Juliane Euler<sup>1,2</sup> · Stefan Ulbrich<sup>1,3</sup> · Oskar von Stryk<sup>1,2</sup>

**Abstract** Online estimating the state of dynamic dispersion processes is very important for disaster response in a number of critical applications. The estimates can be improved by the use of mobile sensor platforms which must be provided with situation-dependent trajectories. An adaptive observation strategy is presented which is based on a partial differential equation model of the process and a model-predictive control approach for multiple cooperating mobile sensors.

**Keywords** Environmental monitoring · Adaptive observation · State estimation · PDE model · Mobile sensors · Cooperative control

## 1 Introduction

The dispersion of hazardous material in the atmosphere highly affects health and well-being of nature and humankind. It is essential to repeatedly estimate the state of the dispersion process to be aware of current conditions and to be able to predict future impacts. In order to achieve this, the use of a process model is combined with measurements obtained from a network of sensors. The measurements are integrated into the model by the use of a data assimilation scheme so that the best possible estimate can be obtained. In this context, the use of multiple mobile sensor platforms is increasingly considered as they can dynamically adapt to new situations and can be guided to positions where the most amount of information can be found. Hence, the platforms must be provided with situation-dependent trajectories leading to the so-called concept of *Adaptive Observation*.

A number of adaptive observation strategies exist in literature, for example the works of Stranders et al (2009) and Simic and Sastry (2003). For the underlying process, both strategies use very simple models which can provide results in a very short time. However, as important characteristics of the process dynamics are not considered, only inaccurate approximations of the real process are possible. Using a partial differential equation (PDE) model, more accurate forecasts can be obtained since the physics and the dynamic behavior of the dispersion process are considered.

Adaptive observation strategies based on PDE models are commonly used in large-scale systems, e.g. for numerical weather prediction. In this field, a number of different approaches have been applied (Buizza and Montani, 1999; Daescu and Navon, 2003). Due to the huge system dimensions, though, vehicle dynamics are not considered in these applications.

Only a few publications focus on adaptive observation strategies combining both PDE models and vehicle dynamics. While Ucinski (2004) and Song et al (2007) work on parameter estimation, Zhang et al (2011) consider state estimation problems in conjunction with data assimilation. All these approaches involve solving a sophisticated optimal control problem subject to the process model, the covariance evolution, and the vehicle dynamics. Solving such complex problems is hard and time-consuming, especially regarding the real-time requirements of the application. Demetriou and Ucinski (2011) try to circumvent the optimal control problem and propose a Lyapunov-based sensor guidance scheme that can be applied in real-time. The resulting sensor motion allows for collision avoidance and connectivity constraints, but cannot be considered optimal with respect to vehicle cooperation.

In previous work (Ritter et al, 2014), we proposed a new

---

<sup>1</sup>Graduate School CE, TU Darmstadt, Germany

<sup>2</sup>Department of Computer Science, TU Darmstadt, Germany

<sup>3</sup>Department of Mathematics, TU Darmstadt, Germany

\*Speaker, E-mail: ritter@gsc.tu-darmstadt.de

adaptive observation strategy that combines the accuracy of PDE-based process models with the potential of a team of optimally cooperating mobile sensors for online state estimation of a dispersion process. A significant gain of computational efficiency compared to solving a complex optimal control problem was obtained since state estimation and vehicle control are considered separate problems that are linked in a repeating sequential procedure. In that approach, it was considered that measurements of the process are expensive and sophisticated so that they are only performed when the sensor vehicles have reached a target point. The present work refines this approach, especially focusing on systems providing cost-efficient measurements. This enables more frequent measurements and results in a gain of accuracy of the state estimates.

## 2 Model and State Estimation

### 2.1 Process Model

The approach presented in this work is aimed to estimate the state of a dynamic transport process that can be described by a PDE of the form

$$\frac{\partial \chi}{\partial t} = f(\chi(t), \nabla \chi(t), \Delta \chi(t), \mathbf{w}(t), \nabla \mathbf{w}(t)), \quad (1)$$

where  $\chi$  represents the dispersing entity to be estimated and  $\mathbf{w}$  the underlying velocity field. With the aid of a spatial discretization scheme, the solution of the PDE can be represented by the state vector  $\chi$ , which contains values of  $\chi$  at certain, discrete spatial positions. Applying a suitable time integration scheme, the state vector at time  $t_{i+1}$  can be calculated from a model forecast (superscript  $(\cdot)^f$ ) of the state vector at time  $t_i$  according to

$$\chi_{i+1}^f = M_i[\chi_i^f] \quad (2)$$

with the model operator  $M_i$ . It is assumed that compared to the true process state, a Gaussian and unbiased model error with known error covariance is made, introducing uncertainty into the calculations.

### 2.2 Observation Model and Data Assimilation

To alleviate uncertainty stemming from the model, the process is also measured by a network of sensors. At every time step  $t_i$ , all sensors take a measurement. The observation vector  $\psi_i^o$  is described by the relation

$$\psi_i^o = H_i[\chi_i^t] + \epsilon_i, \quad (3)$$

where  $\chi_i^t$  is the true state and  $\epsilon_i$  represents the observation error, which is also assumed to be unbiased and Gaussian with known covariance. The observation operator  $H_i$  maps vectors from the state space onto the observation space and depends on the positions the sensors take their measurements at.

To combine results obtained from simulation and from observations, a data assimilation method has to be applied. Then, the updated or analysis state vector  $\chi_i^a$  results from the combination of the forecasted state vector with a weighted innovation due to the observation

$$\chi_i^a = \chi_i^f + \mathbf{K}_i(\psi_i^o - H_i[\chi_i^f]). \quad (4)$$

Moreover, an analysis error covariance matrix  $\mathbf{P}_i^a$  is calculated describing the quality of the analysis state vector. In this work, the *Ensemble Transform Kalman Filter* (ETKF) (Bishop, 2001) is chosen as data assimilation scheme as it is especially suitable for high-dimensional problems. Furthermore, it is able to calculate the analysis error covariance matrix before the actual measurements are taken.

## 3 Cooperative Vehicle Control

The cooperative feedback control approach is able to guide multiple vehicles to a number of specified target locations that may change dynamically over time. Collision-free vehicle trajectories as well as optimal target allocation are simultaneously determined respecting the vehicles' physical characteristics. For this purpose, a discrete-time linear *Mixed Logical Dynamical* (MLD) formulation of the considered multi-vehicle system is set up (Bemporad and Morari, 1999; Kuhn et al, 2011), which has the following form:

$$\min_{U_N} |\mathbf{F}\mathbf{x}^N| + \sum_{k=0}^{N-1} (|\mathbf{G}_1\mathbf{u}^k| + |\mathbf{G}_2\boldsymbol{\delta}^k| + |\mathbf{G}_3\mathbf{z}^k| + |\mathbf{G}_4\mathbf{x}^k|) \quad (5a)$$

$$\text{s.t.} \quad \mathbf{x}^{k+1} = \mathbf{A}\mathbf{x}^k + \mathbf{B}_1\mathbf{u}^k + \mathbf{B}_2\boldsymbol{\delta}^k + \mathbf{B}_3\mathbf{z}^k \quad (5b)$$

$$\mathbf{E}_2\boldsymbol{\delta}^k + \mathbf{E}_3\mathbf{z}^k \leq \mathbf{E}_1\mathbf{u}^k + \mathbf{E}_4\mathbf{x}^k + \mathbf{E}_5. \quad (5c)$$

In this problem formulation,  $\mathbf{x} \in \mathbb{R}^{n_c}$ , is the system state and comprises the state of the vehicles and of the target points,  $\mathbf{u} \in \mathbb{R}^{m_c}$ , is the control input, and  $\boldsymbol{\delta} \in \{0, 1\}^{r_b}$  and  $\mathbf{z} \in \mathbb{R}^{r_c}$  represent auxiliary binary and continuous vectors, respectively. The prediction time step  $k = 0, \dots, N-1$  relates to the global equidistant time steps  $t_i \in \mathbb{N}$  according to  $\mathbf{x}^k = \mathbf{x}(t_{i+k})$ . As solution of problem (5), the sequence  $U_N := \{\mathbf{u}^k\}_{k=0}^{N-1}$  of control inputs is obtained.

The objective function (5a) contains terms representing

the linearly approximated distances of the vehicles to the target points (continuous part  $\mathbf{z}$ ) as well as the occupation of these positions (binary part  $\delta$ ). In addition, the vehicles are to move at a minimum control effort. The objective function has to be minimized subject to the linearized vehicle dynamics (5b), the movement of the target points (5b), the allocation of measurement points (5c) and restrictions due to collision avoidance (5c).

The problem is solved repeatedly in a receding horizon fashion to compute a sequence  $U_N$  of optimal control inputs for each vehicle. The first element of  $U_N$  is applied to the real system, then its new state is measured for computing updated control inputs at the next time step  $t_{i+1}$ . In this manner, the prediction horizon  $N$  is shifted over time.

Problem (5) is a mixed-integer linear *Constrained Finite Time Optimal Control* (CFTOC) problem. It can easily be transformed into a *Mixed Integer Linear Program* (MILP) at each time step of the model predictive control (MPC) procedure. Therefore, a numerically robust and efficient computation of control inputs can be performed.

#### 4 Adaptive Observation Strategy

While the ETKF can provide several measures of current uncertainty and of future measurements' impact on estimate quality, the controller requires discrete target points to guide the sensor vehicles to. To obtain an efficient optimization-based adaptive observation strategy, the loop has to be closed by introducing a method to generate the target points with the aid of the ETKF. The error covariance matrix provided by the ETKF is a suitable measure of the quality of a state estimate. Large entries indicate high uncertainties and, thus, high deviations between true state and estimate. The objective is to iteratively improve the state estimate of the considered dispersion process, i.e. to reduce the entries in the covariance matrix. This can be achieved by taking measurements at positions where the uncertainty in the estimate is largest and the most valuable information can be obtained. As these positions are likely to change due to the dynamic process behavior and the incorporation of gathered data, the vehicles' target points have to be updated from time to time.

In order to determine the target points, the current error covariance matrix  $\mathbf{P}_i^a$  is calculated applying the ETKF. As the covariance matrix should be reduced, the location that belongs to the maximum value of the diagonal is chosen as the first measurement location. Further target points are calculated iteratively in the same manner, but considering the analysis error covariance

matrix  $\tilde{\mathbf{P}}_i^a$ . The latter is calculated by the ETKF pretending that observations are available at all previously calculated target points, i.e. the observation matrix  $\tilde{\mathbf{H}}_i^k$  has to be determined in every iteration  $k$ . Hereby, clusterization of target points in regions with high uncertainty is avoided. The procedure is repeated until the number of target points corresponds to the number of sensor vehicles.

The sensors are supposed to take measurements at every time step. Although the new observation information is used for an update of the state estimate and the error covariance changes, the target points are not recalculated at every time step to prevent the sensors from jumping from one target direction to another. Instead, a recalculation of all destinations is only performed if one of them has been reached by a sensor. It is likely that at that time, the other sensors have not reached their targets, yet. However, the benefit of a measurement close to the optimal location and an earlier update of all observation targets is greater than waiting for them to arrive at a possibly outdated destination. As long as none of the target points has been reached, their locations are moved with wind velocity to account for the advection of the underlying process.

#### 5 Results

A simple two-dimensional test case is set up to evaluate the proposed approach. The entity to be estimated is the distribution of gas concentration whose dispersion is assumed to be governed by the source-free linear advection-diffusion equation with constant diffusion coefficient and uniform wind velocity. This PDE is discretized by the help of the finite element method so that formulation (2) is obtained.

A so-called twin experiment is performed to provide the observations considered in this test case. This means that both the estimated state *and* the true state are computed and forecasted in time. The observations are then obtained by perturbing the true state according to the observation error. Estimated and true solution differ in their initial condition: While a Gaussian pulse initializes the estimated solution, a composition of three pulses with perturbed parameters corresponds to the initial true state.

Three sensor vehicles each modeled as a point mass are employed to demonstrate the proposed approach. To be able to compare the results and the performance, four adaptive observation strategies are tested: First, the strategy presented in this work with frequent measurements and the variant proposed by Ritter et al (2014) with sporadic measurements are applied. Moreover, another scheme with three mobile sensors also taking mea-

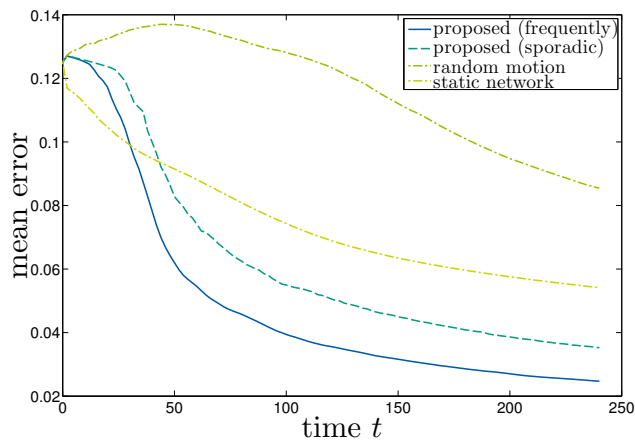


**Fig. 1** Comparison of the mean estimation error over time for four different sensor movement strategies.

surements at every time step but with random motion is investigated and finally, an approach with 16 frequently measuring static sensors is applied.

In order to achieve representative results, the test case is run 50 times, each time with a different randomly chosen initial true state. As the true state is known, the estimation error can be easily obtained from the deviation of the estimated state from the true state. Taking the mean of the estimation error over all test cases, then results in the mean error.

The evolution of the mean error over time for the different observation strategies is shown in Figure 1. At  $t = 240$  the error obtained with the proposed strategy is 3.4 times less than the error obtained with the randomly moving scheme and 2.2 times less than the estimation error of the static sensor network which takes three times more measurements. Even the strategy with only a few measurements performs better than the two simple methods. However, measuring more frequently provides the best results as it could be expected before. An additional error reduction of 30% is obtained.

## 6 Conclusion

An extension of the adaptive observation approach presented by Ritter et al (2014) was presented. While the strategy still employs a PDE-based process model, adaptive generation of observation points using the ETKF and optimal cooperation among multiple mobile sensors provided by an MLD-based model-predictive controller, the sensor vehicles now do not have to postpone measurements to times when target points are reached. Instead, measurements can be performed at every time step so that process estimates become more accurate. This is especially useful for scenarios, in which measurements can be obtained cheap, fast and simple.

**Acknowledgements** This research has been supported by the Graduate School of Computational Engineering established through the 'Excellence Initiative' of the German Federal and State Governments as well as by the GRK 1362 'Cooperative, Adaptive and Responsive Monitoring of Mixed Mode Environments' funded by the German Research Foundation (DFG).

## References

- Bemporad A, Morari M (1999) Control of systems integrating logic, dynamics, and constraints. *Automatica* 35:407–427
- Bishop C (2001) Adaptive sampling with the ensemble transform Kalman filter. Part I: Theoretical aspects. *Monthly weather review* 129(3):420–436
- Buizza R, Montani A (1999) Targeting observations using singular vectors. *Journal of the Atmospheric Sciences* 56(17):2965–2985
- Daescu DN, Navon IM (2003) Adaptive observations in the context of 4D-Var data assimilation. *Meteorology and Atmospheric Physics* 85(4):205–226
- Demetriou M, Ucinski D (2011) State estimation of spatially distributed processes using mobile sensing agents. In: *Proc. of the American Control Conf.*, pp 1770–1776
- Kuhn J, Reinl C, von Stryk O (2011) Predictive control for multi-robot observation of multiple moving targets based on discrete-continuous linear models. In: *Proc. of the 18th IFAC World Congress*, pp 257–262
- Ritter T, Euler J, Ulbrich S, von Stryk O (2014) Adaptive observation strategy for dispersion process estimation using cooperating mobile sensors. In: *Proc. of the 19th IFAC World Congress* (to appear)
- Simic SN, Sastry S (2003) Distributed environmental monitoring using random sensor networks. In: *Proc. of the 2nd Int. Workshop on Information Processing in Sensor Networks*, pp 582–592
- Song Z, Chen Y, Liang J, Ucinski D (2007) Optimal mobile sensor motion planning under nonholonomic constraints for parameter estimation of distributed systems. *Int Journal of Intelligent Systems Technologies and Applications* 3(3/4):277–295
- Stranders R, Farinelli A, Rogers A, Jennings NR (2009) Decentralised coordination of mobile sensors using the max-sum algorithm. In: *Proc. of the 21st Int. Joint Conf. on Artificial Intelligence*, pp 299–304
- Ucinski D (2004) *Optimal measurement methods for distributed parameter system identification*. CRC Press
- Zhang D, Colburn C, Bewley T (2011) Estimation and adaptive observation of environmental plumes. In: *Proc. of the American Control Conf.*, pp 4281–4286

## **C 8 Metaheuristic Based Methods for Optimum Design**

Authors: Bekdaş, Gebrail, Nigdeli, Sinan Melih

---

# Metaheuristic Based Methods for Optimum Design of RC Beams

Gebrail Bekdaş · Sinan Melih Nigdeli

**Abstract** In the design of reinforced concrete (RC) members, the design using the materials with the minimum cost cannot be found by using conventional methods since reinforced concrete is a composite of two different materials (concrete and steel reinforcement bars) with different mechanic behaviours and different costs. In this paper, two different metaheuristic based methods have been presented for optimum design of singly or doubly reinforced beams under flexural moments. The metaheuristic algorithms employed in the present study are harmony search algorithm and bat algorithm. Both methods were tested for several flexural moments. The proposed methods are effective to find optimum design with minimum cost.

**Keywords** Reinforced concrete beams · Optimization · Bat algorithm · Harmony search · Metaheuristic

## 1 Introduction

By using optimization methods, it is possible to find the best set of design variables in order to minimize or maximize an objective function. In the design of reinforcement concrete (RC) members, optimization is an important factor. The experience of the design engineers plays a great role in the best design with minimum cost. In the design of RC structures, the required reinforcements are found with respect to an assumed cross-section of RC member.

---

G. Bekdaş  
Department of Civil Engineering, Istanbul University, 34320 Avclar, Istanbul/Turkey  
Tel.: +90-212-4737070  
Fax: +90-212-4737176  
E-mail: bekdas@istanbul.edu.tr

S.M. Nigdeli  
Department of Civil Engineering, Istanbul University, 34320 Avclar, Istanbul/Turkey

Also, the required reinforcement area cannot be exactly provided by steel bars with constant sizes found in local markets. Concrete and steel are very different materials in mechanical behaviour and cost. Additionally, the cost of the materials may vary according to the location of the construction yard because of factors related with transportation. For that reason, the cost ratio of concrete and steel may also change by the location. Another factor in design of RC beams is to use a singly reinforcement design or doubly reinforcement design. Reinforcements in compressive section must be used if the yielding starts in compressive section (brittle fracture). The dimension of cross section is effective on doubly reinforcement design. Numerical search algorithms are effective on optimization of RC members in order to consider these factors. Metaheuristic based methods have been developed for optimization of several RC members [1–5].

In this paper, two metaheuristic based optimization methods are developed for design of RC beam under flexural moment. The optimum design considers cross-section design and reinforcement design including the selecting of number and size of reinforcements. The objective of optimization is to find the best design with the minimum material cost. The design procedures and constraints given in ACI 318- Building Code Requirements for Structural Concrete [6] are considered during the optimization process and the procedure checks the best of singly or doubly reinforcement design. Harmony search and bat algorithms are employed in the paper and optimum results are obtained for flexural moment values between 50 kNm and 500 kNm for selected solution ranges of design variables and design constants.

## 2 Methodology

Metaheuristic methods are the algorithms which are inspired by natural phenomena and employed for optimization of problems. Several processes in life have been imitated in developed of metaheuristic algorithms [7]. Harmony Search (HS) is a music inspired metaheuristic algorithm developed by Geem et al. [8]. It imitates the musical performances in which a musician searches the best harmony for audiences by playing random notes similar to the popular notes and memory of the musician. The bat algorithm (BA) developed by Yang [9] was developed by idealizing the echolocation behaviour of bats. Bats randomly fly with a velocity from a position with a fixed frequency varying wavelengths and loudness. The both method use a randomization procedure of generating a solution matrix containing randomly assigned design variables. Then, the solution matrix is iteratively modified by using the rules of the algorithms. In HS approach, a new solution vector is generated according to existing ones or whole solution range. The vector with the worst solution is eliminated from the solution matrix in all iterations. In BA, all vectors of the solution matrix is modified according to the velocity value used in BA or randomization from the whole solution range.

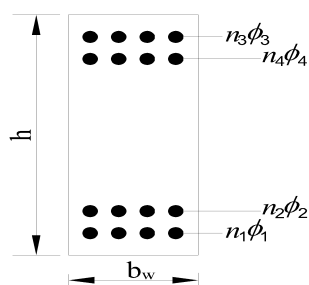


Fig. 1 Design variables

### 3 Numerical Examples

The optimum design was investigated for flexural moments between 50 kNm and 500 kNm. The optimized design variables (shown in Fig. 1) are breadth ( $b_w$ ), height ( $h$ ), number ( $n_1$ - $n_4$ ) and size ( $\phi_1$ - $\phi_4$ ) of the reinforcements in two lines of compressive and tensile sections. The clear cover of reinforcement, maximum size of aggregate diameter, specified compressive strength of concrete, specified yield strength of reinforcement, diameter of stirrup, the cost of the concrete and reinforcement bars were taken as 35 mm, 16 mm, 20 MPa, 420 MPa, 10 mm, 40\$/m<sup>3</sup> and 400\$/ton, respectively. The diameter range of the main reinforcement bars is 10-30 mm, the range of the breadth is 250-350 mm and the range of the height is 350-500 mm. The objective of the optimization is to minimize the material cost of the beam per one meter. The termination criterion is related with the approximation of the cost of best five design by 2%.

### 4 Conclusions

The optimum results of the design variables are given in Tables 1 and 2 for HS and BS based methods, respectively. For 300 kNm flexural moment or more, doubly reinforcement design is mandatory. Both approaches are effective to find the optimum values and the final material cost values are close for both algorithms. Generally, BA based method is more effective to obtain the design with minimum cost.

### References

1. C. C. Coello, F. S. Hernandez, F. A. Ferrera, Optimal Design of Reinforced Concrete Beams Using Genetic Algorithms, *Expert Syst. Appl.* 12, 101-108 (1997).
2. M. Y. Rafiq, C. Southcombe, Genetic algorithms in optimal design and detailing of reinforced concrete biaxial columns supported by a declarative approach for capacity checking, *Comput. Struct.* 69, 443-457 (1998).
3. F. Fedghouche, B. Tiliouine, Minimum cost design of reinforced concrete T-beams at ultimate loads using Eurocode2, *Eng. Struct.* 42, 4350 (2012).

**Table 1** Optimum results for HS approach

FM (kNm)	50	100	150	200	250	300	400	500
h (mm)	350	450	500	500	500	500	500	500
$b_w$ (mm)	250	250	250	250	250	250	350	350
$\phi_1$ (mm)	10	14	18	18	20	28	24	26
$\phi_3$ (mm)	26	26	30	12	12	12	10	22
$n_1$	4	4	3	3	4	3	5	5
$n_3$	0	0	0	0	0	2	3	3
$\phi_2$ (mm)	12	10	10	22	24	14	20	16
$\phi_4$ (mm)	30	24	16	10	18	16	12	14
$n_2$	2	2	4	2	2	4	3	6
$n_4$	0	0	0	0	0	0	2	0
$M_u$ (kNm)	58.61	114.35	172.61	222.87	289.16	334.85	452.99	556.40
Cost (\$/m)	5.18	6.90	8.34	9.73	11.71	13.35	18.38	22.52

**Table 2** Optimum results for BA approach

FM (kNm)	50	100	150	200	250	300	400	500
h (mm)	350	400	500	500	500	500	500	500
$b_w$ (mm)	250	250	250	250	250	300	350	350
$\phi_1$ (mm)	14	16	16	28	26	22	26	28
$\phi_3$ (mm)	30	26	26	24	14	12	12	30
$n_1$	2	3	4	2	3	5	5	5
$n_3$	0	0	0	0	2	2	6	2
$\phi_2$ (mm)	12	10	12	10	12	14	10	16
$\phi_4$ (mm)	12	10	20	26	16	26	16	22
$n_2$	2	4	2	3	2	2	3	3
$n_4$	0	0	0	0	0	0	0	0
$M_u$ (kNm)	57.31	111.22	167.71	222.42	279.29	333.48	445.15	556.17
Cost (\$/m)	5.16	6.85	8.20	9.55	11.60	13.56	18.08	22.82

4. S. Talatahari, R. Sheikholeslami, M. Shadfaran and M. Pourbaba, Optimum Design of Gravity Retaining Walls Using Charged System Search Algorithm. *Mathematical Problems in Engineering*, Vol.2012, 1-10 (2012).
5. G. Bekdas and S. M. Nigdeli, Optimization of T-shaped RC Flexural Members for Different Compressive Strengths of Concrete. *International Journal of Mechanics*, 7, 109-119 (2013).
6. ACI 318M-05, Building code requirements for structural concrete and commentary (American Concrete Institute, 2005).
7. X.-S. Yang, *Engineering Optimization: An Introduction with metaheuristic Applications*, John Wiley and Sons Inc., New Jersey, 2010.
8. Z. W. Geem, J. H. Kim, and G. V. Loganathan, A new heuristic optimization algorithm: harmony search. *Simulation* 76, 60-68 (2001).
9. X.-S. Yang, A New Metaheuristic Bat-Inspired Algorithm, in: *Nature Inspired Cooperative Strategies for Optimization (NISCO 2010)* (Eds. J. R. Gonzalez et al.), *Studies in Computational Intelligence*, Springer Berlin, 284, Springer, 65-74 (2010).

# **C 9 Source Transformation for the Optimized Utilization of the Matlab Runtime System for Automatic Differentiation**

Authors: Hück, Alexander

---

# Source Transformation for the Optimized Utilization of the Matlab Runtime System for Automatic Differentiation

Alexander Hüek

**Abstract** The ADiMat software is a tool that offers automatic differentiation of Matlab functions using a hybrid approach that combines source transformation and operator overloading. Performance tests showed a weakness with a derivative class of ADiMat. In a first step, the Matlab runtime environment is tested regarding function and method call overheads as well as property access overhead with Matlabs objects. An automatic method, transforming the XML based abstract syntax tree created with ADiMats toolchain through a set of stylesheets, was developed. The process completely removes the derivative object usage from any derivative function created with ADiMat. As a result, performance is improved considerable depending on the data container storing the derivative directions.

**Keywords** Source Transformation · Automatic Differentiation · ADiMat · Matlab · Performance Measurement · XSLT · XML AST

## 1 Introduction to Source Transformation in the Context of ADiMat

Source transformation (ST) describes the process of rewriting code of a supported programming language.

ADiMat (**A**utomatic **D**ifferentiation for **M**atlab, [1]) utilizes ST to augment the Matlab code with derivative statements by applying the chain rule of differential calculus. Listing 2 shows the result of the *forward mode* (FM) of ADiMat applied to the function in Listing 1. In general, using FM on a function  $f : \mathbb{R}^n \rightarrow \mathbb{R}^m$ , the product of the Jacobian and a seed matrix  $J \cdot S$  with

---

Alexander Hüek  
Scientific Computing, TU Darmstadt  
Mornwegstrasse 30, 64293 Darmstadt  
Tel.: +49 6151 16 75577  
Fax: +49 6151 16 72335  
E-mail: alexander.hueck@sc.tu-darmstadt.de

$J \in \mathbb{R}^{n \times m}$  and  $S \in \mathbb{R}^{n \times n_{\text{dd}}}$  is calculated. Here,  $n_{\text{dd}}$  represents the number of derivative directions. The introduced variables are called *active variables* and implicitly represent the seed matrix. Usually, ADiMat makes use of a specific prefix for these variables.

```

1 function z = F(a, b)
2   z = a * b;
3 end
4

```

**Listing 1** Matlab function F.

```

1 function [g_z, z] = g_F(g_a, a, g_b, b)
2   g_z = g_a * b + a * g_b;
3   z = a * b;
4 end

```

**Listing 2** ADiMat FM applied to F.

Derivative classes are used for a *vectorized* derivative evaluation (VDE), enabling the evaluation of multiple derivative directions with a single function invocation. Operator overloading is employed to update each derivative directions for the respective operation. In Fig. 1, the structure of the derivative class *adderiv*, including the relation to a non-active variable  $a$ , is shown.

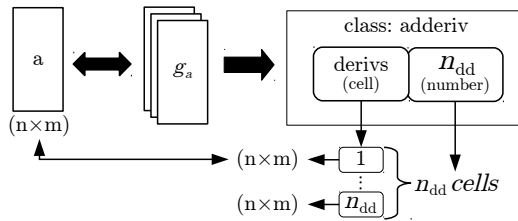


**Fig. 1** Derivative object for a  $n \times m$  matrix with  $n_{\text{dd}}$  derivative directions.

## 2 Understanding Matlab Performance

Performance tests revealed a slow VDE with *adderiv*. It was speculated that operator overloading and the class property access are the main causes. A set of general Matlab benchmarks was created in order to assess Matlabs runtime system. Additionally, the class usage of a derivative function was replaced by function calls and the timings were compared to the original. For brevity, only a subset of the collected results is shown.

Benchmarks were performed on an Intel Core 2 Duo T7200 with 3.25 GB DDR2 RAM on Ubuntu 10.04 32bit with Matlab R2012a.

In Table 1, empty method/function invocation overhead is shown. Function calls are generally faster than method calls. Functions that are placed in a different folder w.r.t. the caller suffer from significant performance loss. In contrast, the class system performance does not depend on the source location.

With Matlabs class system, our benchmarks show a substantial performance loss, in particular when accessed in a method invocation, when a *cell* or *struct* data structure is used to store the derivative directions. On the other hand, functions accessing cells or structs perform better.

Test #	Description	Mean $\pm$ Std ( $\mu$ s)
1	function	0.69745 $\pm$ 0.01849
2	function in a remote folder	9.65353 $\pm$ 0.03750
3	class method	13.53934 $\pm$ 0.03681

**Table 1** Benchmark results for method/function invocations.

The derivative of a polynomial function  $z = \sum_{i=0}^{n-1} c_i x^i$  was created and manually transformed to a functional version. The results are shown in Fig. 2. The functional version shows major speedups for a rising number of iterations. Subsequent profiling determined that the majority of the derivative evaluation time (more than 85% for  $\mathbf{c} \in \mathbb{R}^{80}$ ) is spent inside the overloaded operators (*plus* and *times*) updating the cell array.

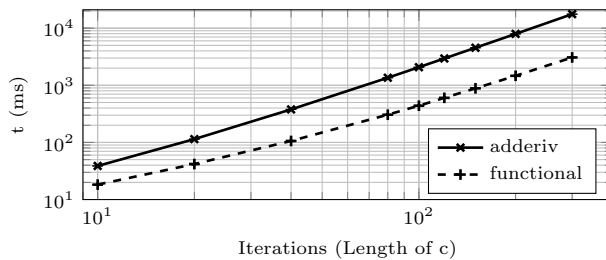


**Fig. 2** Polynomial execution time for the full Jacobian computation.

### 3 Automatic Source Transformation

ADiMat generates XML-based abstract syntax trees (AST) and utilizes a rule-based ST using XSLT. To automate class usage replacement by function calls, we also employ XSLT stylesheets. The removal of the class usage necessitates a static type inference since Matlab only provides type information during runtime. A prefix identification was utilized: Every variable starting with a specific prefix (eg. *g\_*) is assumed to be a derivative class, everything else is of type *double*.

A front-end transformation replaces the class usage in the derivative function with direct function calls. A back-end transformation encapsulates the class properties in a Matlab *struct*. Methods are converted to functions working on the new *struct*. Often, methods lack any prefix usage. Consequently, heuristics are used to identify active variables. The result of the ST of Listing 1 is shown below.

---

```

1 function [g-z, z] = ad_F(g-a, a, g-b, b)
2     g-z = ad_plus(ad_times(g-a, b), ad_times(a, g-b));
3     z = a * b;
4 end

```

---

The ST is composed of 17 XSLT stylesheets. Fig. 3 shows a detailed view of this process. The *Preprocessing* and *Postprocessing* handle AST normalization and function rename operations (6 stylesheets). *Mark Elements* identifies expressions with the prefix and tags them in the AST (7 stylesheets). *Modify Elements* transforms each expression with the inserted tag to function calls (4 stylesheets).

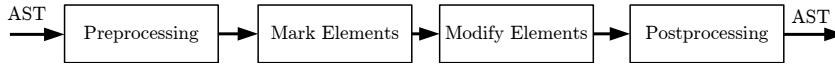


**Fig. 3** Detailed view of the ST process. ADiMat handles AST creation and AST to .m file.

## 4 Experimental Results

The system is applied to a 1D partial differential equation solver for Burgers' equation (1). It consists of 6 functions with 169 lines of code.

In addition to *adderiv*, the *arrdercont* class is tested. It uses a matrix-based storage for the derivative directions.

$$\frac{\partial u}{\partial t} + \frac{1}{2} \frac{\partial u^2}{\partial x} = 0 \quad u(x, 0) = u_0(x) \quad (1)$$

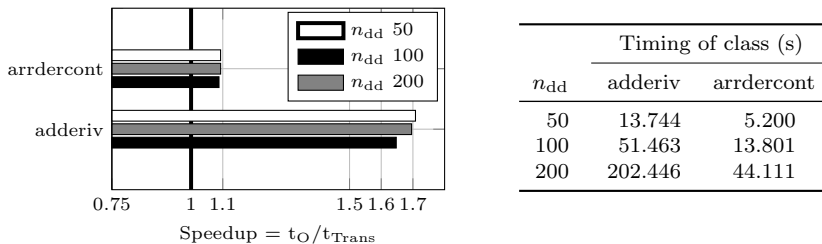


**Fig. 4** Achieved speedup after the ST process and absolute timings of the class versions for the full Jacobian ( $n_{dd} \in \{50, 100, 200\}$ ).

As shown in Fig. 4, the achieved speedup is highest for classes utilizing the cell array data structure. The performance gains for a matrix-based storage is much lower.

## References

1. Bischof, C., Bücker, H.M., Lang, B., Rasch, A., Vehreschild, A.: Combining Source Transformation and Operator Overloading Techniques to Compute Derivatives for MATLAB Programs. In: Proceedings of the Second IEEE International Workshop on Source Code Analysis and Manipulation (SCAM 2002), pp. 65–72. IEEE Computer Society (2002)

**C 10 Dynamic Two-Way  
Parallelization of Non-Intrusive  
Methods for Uncertainty  
Quantification**

Authors: Thiem, Christoph, Schäfer, Michael

---

# Dynamic two-way parallelization of non-intrusive methods for uncertainty quantification

Christoph Thiem · Michael Schäfer

**Abstract** This work deals with a two-way parallelization method of numerical flow simulations under uncertainties with sampling methods for the uncertainty quantification. In general, for such simulations there are two possibilities to distribute the computation on multiple processors in order to reduce the overall computing time. One approach is to divide the flow domain into several blocks which can be calculated by different processors. The other is that the various independent deterministic problems that arise from the sampling method for uncertainty quantification, can be solved in parallel. Both methods have advantages and disadvantages and can be applied simultaneously, depending on the provided number of processors for the simulation. The presented method assigns the available processors dynamically to both parallelization methods during the simulation of the uncertain flow problem. The aim is to reduce the overall computing time compared to a static parallelization strategy.

**Keywords** Uncertainty Quantification · Parallelization · Flow Simulation

## 1 Introduction

The calculation of numerical flow simulations under uncertainties usually is very expensive. For this reason it is necessary that complex problems are computed with multiple processors in order to achieve an acceptable computing time. This work presents a method that dynamically allocates processors

---

C. Thiem  
Institute of Numerical Methods in Mechanical Engineering  
Graduate School Computational Engineering  
Technische Universität Darmstadt  
Dolivostr. 15, D-64293, Darmstadt, Germany  
Tel.: +49-6151-16-70983  
E-mail: thiem@gsc.tu-darmstadt.de

during simulation of flow problems under uncertainties with two separate parallelization methods. For this purpose specific properties of the uncertainty quantification are used. A precondition for this method is that a sampling method for the uncertainty quantification of the flow simulation is used. To explain the basic idea of the two-way parallelization the theoretical fundamentals are described in the next section. Subsequently the concept of the idea is explained in more detail before a conclusion is made.

## 2 Theoretically fundamentals

The precondition for the two-way parallelization method is that the uncertainty quantification (UQ) is done via non-intrusive methods. In this kind of methods a stochastic problem is divided into a set of deterministic problems with slightly different values for the uncertain parameters [1]. These deterministic realizations are called sample points and can be solved by common solvers. In case of flow problems these are mainly finite-volume method (FVM) based solvers [2].

### 2.1 Parallelization strategies

For this combination of uncertainty quantification method and flow solver there exist two different approaches for parallelization. The first approach is the parallel simulation of the sample points, as these can be solved independently. This means, if the set contains  $n$  problems, the computation could be parallelized on up to  $n$  processors or clusters. The second approach is the decomposition of the flow domain into certain subdomains which can be calculated by different processors. This parallelization strategy requires data transfer between all processors in order to get an adequate result of the overall flow field [2]. In general, the second approach is less efficient because additional effort for communication is required. Nevertheless, both strategies can be combined. Thereby, it is possible to compute  $n$  sample points simultaneously with  $m$  processors.

### 2.2 Influence of the initial solution

If the finite-volume method is applied to simulate the flow problem, an algebraic system of equations is formulated which has to be solved. Due to the complexity of the system it is necessary to solve it with an iterative method. This procedure generates a sequence  $\{\phi_n\}_{n \geq 1}$  of improving approximations of the solution  $\phi$  until a convergence criterion is satisfied. The number of iterations until convergence, and hence the computing time, depends among others on the initial solution  $\phi_0$ . The process takes less time the more accurate the choice of the initial solution  $\phi_0$  is. So in case of an uncertainty quantification

an example of a good initial solution for the computation of a sample point would be a flow field of a previously calculated sample point. In [3] it has been shown that in practice it is often the case that a solution of a sample point is more suitable as initial solution for another sample point, the more similar the values of the uncertain parameters are, because the flow fields probably differ less from each other. In the dynamic two-way parallelization this property is utilized in order to define the number of processors that are used to calculate a certain sample point. For this purpose, it is assumed that the flow solver is able to save calculated flow fields and use them as an initial solution for another sample point if necessary.

### 3 Dynamic 2-way parallelization

During the initialization a minimum spanning tree (MST)  $G = (V, E)$  is generated by the algorithm of Prim [4], where  $V$  contains all sample points of the uncertain problem and  $E$  are the edges. For this purpose, the values of the uncertain parameters are interpreted as coordinates and the edge weights correspond to the Euclidean distance. The property of the shortest edge of the MST helps to get an appropriate initial solution for a flow simulation of a sample point  $V_i$ , because only flow fields are used whose corresponding sample points are connected with  $V_i$  via an edge of  $E$ . Of course, an exception of this is the first calculation. In order to describe the algorithm of the 2-way parallelization method two arrays are introduced. The array  $W$  contains all indices of sample points that have not yet been calculated and for which no flow field of an sample point exists that is connected by an edge of  $E$ . In addition, the array is sorted in descending order, with respect to the number of edges that a corresponding sample point has. The second array,  $R$ , contains all indices of sample points that have not yet been calculated, but a suitable predecessor has already been calculated. At the beginning of the algorithm  $R$  is empty and  $W$  contains the indices of all sample points. Assuming that  $m$  processors are available and a single sample point can be calculated with up to  $p_{max}$  processors, the overall computation starts with the simultaneous calculation of the first  $\text{ceil}(m/p_{max})$  points of  $W$ . Each of these problems is parallelized with  $p_{max}$  processors (if the number of processors does not fit, only the last problem will get less processors). The related indices are removed from  $W$ . The idea behind this is, that the first simulation without a good initial solution is the most time consuming one. All the following calculations converge much faster. So if the time for the first calculation is reduced, the computation time of the entire UQ can also significantly be affected. This reduction can be achieved only with the second parallelization strategy. The algorithm works according to the following scheme until all sample points are calculated:

1. Move all indices from  $W$  to  $R$  whose associated sample points have a common edge with  $V_i$ .
2. If  $R$  is not empty, distribute as many as possible idle processors uniformly the sample points in  $R$  in order to simulate the underlying problems.

3. If there are still idle processors and  $W$  is not empty, use them to calculate the first element of  $W$ .
4. If there are still idle processors, use them to support a running computation.
5. Delete all indices of sample points from  $W$  and  $R$  which are already calculated.

Preliminary tests show that the algorithm can achieve a performance enhancement compared to a static strategy. It turns out that the dynamic method is particularly well suited for problems where the ratio of sample points to the number of processors  $m$  is small. The reason for this is that time can be saved mainly for the first  $m$  and the last  $0.5m$  sample points. If the ratio of sample points to processors is very large, the computation time is similar to the time of a static parallelization. A disadvantage of the dynamic method is that the preprocessing is more complex. Further investigations that will provide more detailed results are in progress.

## 4 Conclusion

This work presents a dynamic 2-way parallelization method for numerical flow problems under uncertainty. Preliminary tests show that the method has the potential to shorten the computation time. A more detailed analysis of the efficiency of the method will be provided at the workshop.

**Acknowledgements** This work is supported by the 'Excellence Initiative' of the German Federal within State Governments and the Graduate School of Computational Engineering at Technische Universität Darmstadt.

## References

1. O. Le Maitre and O. Knio, Spectral Methods for Uncertainty Quantification: With Applications to Computational Fluid Dynamics, Springer, 2010
2. M. Schäfer, Computational Engineering, Springer (2006)
3. C. Thiem and M. Schäfer, Acceleration of Sampling Methods for Uncertainty Quantification in Computational Fluid Dynamics, Proceedings: The Ninth International Conference on Engineering Computational Technology (2014)
4. E. Horowitz and S. Sahni, Fundamentals of Computer Algorithms, Computer Science Press, 1978

**C 11 Data-Driven Uncertainty  
Quantification with Adaptive Sparse  
Grids in Subsurface Flow Simulations**

Authors: Franzelin, Fabian, Oladyshkin, Sergey, Peherstorfer, Benjamin, Pflüger, Dirk

---

# Data-driven uncertainty quantification with adaptive sparse grids in subsurface flow simulations

Fabian Franzelin · Sergey Oladyshkin ·  
Benjamin Peherstorfer · Dirk Pflüger

**Abstract** We present a novel data-driven approach to propagate uncertainty through an expensive subsurface flow simulation. We remove the gap between the subjective approximation of the input's uncertainty and the unknown real distribution by applying sparse grid density estimation. We link the estimation to the adaptive sparse grid collocation method to propagate the uncertainty and obtain new refinement criteria. Our approach excels by speed, flexibility and thus can be applied in many fields from environmental to financial sciences.

**Keywords** uncertainty quantification, environmental engineering, sparse grids, density estimation

---

Fabian Franzelin  
Dept. of Simulation Software Engineering, IPVS, University of Stuttgart  
Universitätsstr. 38, 70569 Stuttgart  
Tel.: +49 711 685 88365  
Fax: +49 711 685 70413  
E-mail: fabian.franzelin@ipvs.uni-stuttgart.de

Sergey Oladyshkin  
Dept. of Hydromechanics and Modelling of Hydrosystems, University of Stuttgart  
Pfaffenwaldring 5a (SimTech), 70569 Stuttgart  
E-mail: sergey.oladyshkin@iws.uni-stuttgart.de

Benjamin Peherstorfer  
Dept. of Aeronautics & Astronautics, Massachusetts Institute of Technology  
77 Massachusetts Avenue, Cambridge, MA 02139  
E-mail: pehersto@mit.edu

Dirk Pflüger  
Dept. of Simulation Software Engineering, IPVS, University of Stuttgart  
Universitätsstr. 38, 70569 Stuttgart  
E-mail: dirk.pflueger@ipvs.uni-stuttgart.de

## 1 Introduction

Non-intrusive stochastic collocation methods are commonly used in the quantification of uncertainties (UQ). Their main advantage is that they don't require any changes in the corresponding simulation code. They typically rely on building a surrogate model of the response function based on interpolation on selected parameters of the feature space, so called collocation nodes. The selection of the collocation nodes is of major importance and accuracy of the method depends strongly on it.

In the simulation context conventional discretization methods suffer the curse of dimensionality: The computational effort increases exponentially with the number of dimensions, which, in the context of UQ, are the uncertain variables. A straightforward ansatz to build a surrogate based on global polynomials is thus not feasible for more than typically four uncertain parameters.

## 2 Adaptive Sparse Grid Collocation Method

Our method of choice to overcome the curse of dimensionality to a large extent are spatially adaptive sparse grids, see [1,6] and Figure 1. In the context of UQ, the sparse grid discretization of the stochastic space determines the location of the collocation nodes for the stochastic collocation method, see, e.g., [3]. Using a hierarchical approach, we obtain an explicit, grid-based function representation even of high-dimensional dependencies.

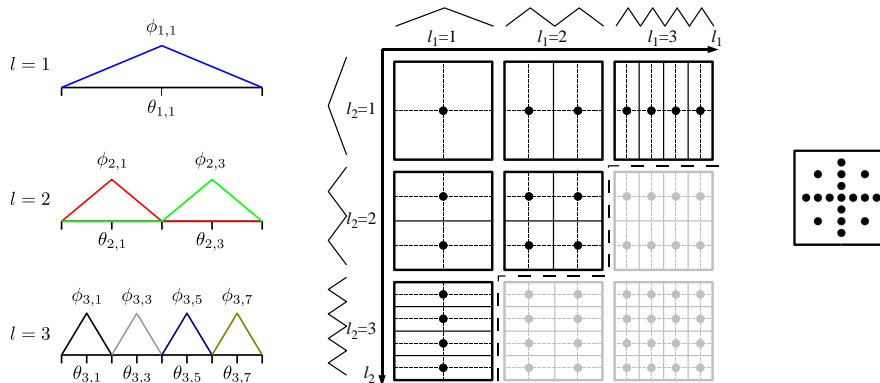


**Fig. 1** One-dimensional basis functions up to level 3 (left), and tableau of hierarchical increments  $W_1$  up to level 3 in both dimensions (center). Leaving out the grayed-out  $W_1$ , we obtain the sparse grid of level 3 (right).

As the hierarchical basis provides us a local variance estimate for free, we can use this measure to refine the stochastic domain adaptively and reduce

the number of function evaluations even more. Spatially adaptive refinement allows one to deal even with singularities and discontinuities [2].

Regarding convergence and accuracy, the sparse grid theory guarantees high convergence rates that are close to those of full grids for sufficiently smooth functional dependencies with only a moderate number of costly function evaluations. Furthermore, statistics such as moments or sensitivity values can be derived from the surrogate model directly.

### 3 CO<sub>2</sub> Leakage Benchmark

In this work, we show results of a recent project that studies the use of spatially adaptive sparse grids for the quantification of uncertainties for parameter-dependent subsurface flow simulations based on the work of [4,7]. The uncertain description of the subsurface relies on data. We present a novel, data-driven approach to describe the uncertainty by applying the sparse grid density estimation [5]. Moreover, the real-world scenario requires custom-tailored criteria for adaptive refinement to reduce the number of sampling points as well as possible, for example. The results obtained by the stochastic collocation method using spatially adaptive sparse grids are evaluated and compared to previous methods in this context.

### References

1. Bungartz, H.-J. and Griebel, M. *Sparse Grids*, Acta Numerica, 1–123, (2004).
2. Jakeman, J. D.; Archibald, R. and Xiu, D. *Characterization of discontinuities in high-dimensional stochastic problems on adaptive sparse grids*, Journal of Computational Physics, 230, 3977–3997, (2011)
3. Ma, X. and Zabaras, N. *An adaptive hierarchical sparse grid collocation algorithm for the solution of stochastic differential equations*, Journal of Computational Physics, 228, 3084–3113, (2009).
4. Oladyshkin, S.; Class, H.; Helmig, R. and Nowak, W. *An integrative approach to robust design and probabilistic risk assessment for CO<sub>2</sub> storage in geological formations*, Computational Geosciences, 15, 565–577, (2011).
5. Peherstorfer, B. and Pflüger, D. and Bungartz, H.-J. *Density Estimation with Adaptive Sparse Grids for Large Data Sets*, SIAM Data Mining 2014, SIAM, (2014).
6. Pflüger, D. *Spatially Adaptive Sparse Grids for High-Dimensional Problems*, Verlag Dr. Hut, (2010).
7. Walter, L.; Binning, P. J.; Oladyshkin, S.; Flemisch, B. and Class, H. *Brine migration resulting from CO<sub>2</sub> injection into saline aquifers - An approach to risk estimation including various levels of uncertainty*, International Journal of Greenhouse Gas Control, 9, 495–506, (2012).

# List of Authors

<b>A</b>		Harrach, Bastian .....	186
Andrä, Heiko .....	210	Heene, Mario .....	86
<b>B</b>		Heider, Yousef .....	9
Bastian, Peter .....	109	Hillewaert, Koen .....	157
Beck, Andrea D. ....	162	Hinojosa, Alfredo Parra .....	86
Beckmann, Andreas .....	103	Hoffmann, Wolfgang .....	168
Bekdaş, Gebrail .....	225	Hück, Alexander .....	230
Bijl, Hester .....	6	<b>K</b>	
Birken, Philipp .....	192	Kabadshow, Ivo .....	103
Biros, George .....	7	Kabel, Mathias .....	210
Bischof, Christian .....	205	Klann, Esther .....	176
Blaschke, Julian .....	24	Klawonn, Axel .....	92
Bolemann, Thomas .....	162	Kleinbach, Christian .....	29
Brolin, Karin .....	46	Klimach, Harald .....	97
Burger, Michael .....	205	Kneißl, Stefan .....	197
<b>C</b>		Köppl, Tobias .....	215
Carton de Wiart, Corentin .....	157	Kowitz, Christoph .....	86
<b>D</b>		Krupp, Verena .....	97
Diehl, Patrick .....	202	Kuhl, Detlef .....	192
Dihlmann, Markus .....	141	<b>L</b>	
<b>E</b>		Lanser, Martin .....	92
Eberhard, Peter .....	130	Lass, Oliver .....	120
Euler, Juliane .....	220	Lindner, Florian .....	97
<b>F</b>		<b>M</b>	
Fehr, Jörg .....	29	Markert, Bernd .....	9
Franzelin, Fabian .....	240	Mayer, Christian .....	52
Fressmann, Dirk .....	40	Mehl, Miriam .....	97
Frisch, Jérôme .....	79	Meister, Andreas .....	192
Fuchs, Therese .....	45	Merkert, Dennis .....	210
<b>G</b>		Mundani, Ralf-Peter .....	79
Gassner, Gregor J. ....	147	Munz, Claus-Dieter .....	162
Gatzhammer, Bernhard .....	97	Müthing, Steffen .....	109
Ghiglieri, Jane .....	115	<b>N</b>	
Gleim, Tobias .....	192	Neumann, Philipp .....	65
Göddeke, Dominik .....	109	Nigdeli, Sinan Melih .....	225
Grimm, Eva .....	125	Ntemos, George .....	152
Gubisch, Martin .....	125	<b>O</b>	
Guo, Yujie .....	57	Oladyshkin, Sergey .....	240
<b>H</b>		Ólafsdóttir, Jóna Marín .....	46
Haasdonk, Bernard .....	141	Östh, Jonas .....	46

<b>P</b>		Simeon, Bernd ..... 210
Peherstorfer, Benjamin ..... 240		Sternel, Dörte C. .... 197
Peldschus, Steffen ..... 45		Stryk, Oskar von ..... 220
Perović, Nevena ..... 79		Sun, Shuyu ..... 79
Pflüger, Dirk ..... 86, 240		
<b>Q</b>		<b>T</b>
Quinto, Eric Todd ..... 176		Thiem, Christoph ..... 235
<b>R</b>		<b>U</b>
Ramlau, Ronny ..... 176		Uekermann, Benjamin ..... 97
Rank, Ernst ..... 34, 79		Ulbrich, Stefan ..... 115, 220
Rheinbach, Oliver ..... 92		Ulbrich, Michael ..... 14
Ribbrock, Dirk ..... 109		Ullrich, Marcel ..... 186
Ritter, Tobias ..... 220		Unterweger, Kristof ..... 70, 75
Roller, Sabine ..... 97		
Ruess, Martin ..... 34, 57		<b>V</b>
<b>S</b>		Vincent, Peter E. .... 152
Sachs, Ekkehard ..... 135		Volkwein, Stefan ..... 120, 125
Salama, Amgad ..... 79		
Schäfer, Michael ..... 197, 235		<b>W</b>
Schmitt, Syn ..... 24		Weinzierl, Tobias ..... 61
Schneider, Matti ..... 210		Wengert, Nicolai ..... 130
Schneider, Marina ..... 135		Wille, Hagen ..... 34
Schweitzer, Marc Alexander ..... 202		Wittmann, Roland ..... 70, 75
Siltanen, Samuli ..... 181		
		<b>Y</b>
		Yosibash, Zohar ..... 16, 34